INFORMATION TO USERS

NOTE TO USERS

The original manuscript received by UMI contains pages with indistinct and/or slanted print. Pages were microfilmed as received.

This reproduction is the best copy available

UMI

University of Alberta

Absolute Permeability of McMurray Formation Oil Sands at Low Confining Stresses

By

Amin Touhidi-Baghini ©

A thesis submitted to the Faculty of Graduate Studies and Research in partial fulfillment

of the requirements for the degree of **Doctor of Philosophy**

in

Geotechnical Engineering

Department of Civil and Environmental Engineering

Edmonton, Alberta

Fall 1998

Canada

University of Alberta

Library Release Form

Name of Author: Amin Touhidi-Baghini

Title of Thesis: Absolute Permeability of McMurray Formation Oil Sands at Low Confining Stresses

Degree: Doctor of Philosophy

Year this Degree Granted: 1998

Amin Touhidi
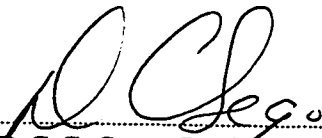
No. 61, West 176th Street, Tehranpars
Tehran 16539
Iran

Date: October 2, 1998
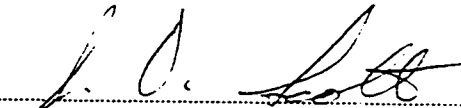
University of Alberta

Faculty of Graduate Studies and Research
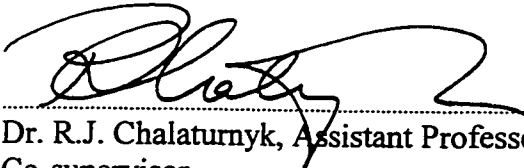
The undersigned certify that they have read, and recommend to the Faculty of Graduate Studies and Research for acceptance, a thesis entitled *Absolute Permeability of McMurray Formation Oil Sands at Low Confining Stresses* submitted by Amin Touhidi-Baghini in partial fulfillment of the requirements for the degree of Doctor of Philosophy in Geotechnical Engineering.
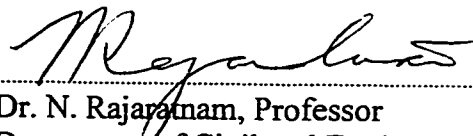
Dr. D.C.C. Sego, Professor
Committee Chair and Examiner
Department of Civil and Environmental
Engineering
University of Alberta
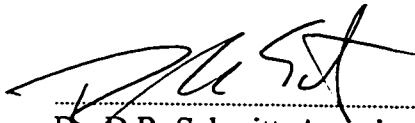
Dr. J. D. Scott, Professor Emeritus
Supervisor
Department of Civil and Environmental
Engineering
University of Alberta

Dr. R.J. Chalaturnyk, Assistant Professor
Co-supervisor
Department of Civil and Environmental
Engineering
University of Alberta

Dr. N. Rajaratnam, Professor
Department of Civil and Environmental
Engineering
University of Alberta

Dr. D.R. Schmitt, Associate Professor
Department of Physics
University of Alberta

Dr. G.E. Bauer, Professor
Department of Civil and Environmental
Engineering
Carleton University

Date: September 8, 1998

ABSTRACT

The Athabasca Deposit is the richest of the Alberta bitumen reservoirs with the majority of its recoverable reserves contained in the McMurray Formation. It has been estimated that only about 10% of Athabasca oil sands deposits are surface mineable; thus the vast majority of the bitumen will be recovered by means of in situ extraction technology. A special form of steam flooding, known as steam assisted gravity drainage (SAGD), is being used as the most promising in situ process for the McMurray Formation oil sands.

The SAGD process results in shear stresses and deformations that affect formation absolute permeability. The absolute permeability of the reservoir controls the drainage of fluids from the steam front and therefore the frontal steam advance rate and the bitumen production rate; it is one of the most important parameters in the effectiveness of the SAGD process.

An experimental study of the geomechanical behavior of McMurray Formation oil sand, specifically, the change in absolute permeability during shear at low confining pressures, was the primary objective of this thesis. Both undisturbed and reconstituted specimens were tested in this research program. The undisturbed specimens were obtained by coring a block of bitumen-free oil sand both vertically and horizontally. Since this block of locked sand is bitumen-free, no disturbance to the fabric of the cored specimens was induced by having to extract the bitumen.

Image analysis was employed to study the fabric of the undisturbed oil sand block sample. Structure anisotropy of the sand due to preferred particle orientation was identified.

A new computer controlled stress path triaxial testing system with the capability of continuous measurement of permeability during shear was developed for this study. Test procedures for the preparation of dense reconstituted specimens and for saturation of specimens were developed. A special method was derived for the analysis of permeability tests with lubricated end configuration.

The testing program included stress-strain and permeability tests on both vertical and horizontal undisturbed specimens. Inherent anisotropy was observed in strength, compressibility and permeability. A simple model for the prediction of changes in the absolute permeability is presented.

A methodology is presented in which the laboratory results can be implemented for reservoir numerical modeling of oil sands. A numerical reservoir simulator, FLAC, with strain softening behavior incorporated into the constitutive model, was used for this purpose.

In memory of my brother Ali,
a genius who did not have the opportunity to
blossom.

ACKNOWLEDGMENTS

TABLE OF CONTENTS

LIST OF TABLES

LIST OF FIGURES

LIST OF PLATES

CHAPTER 1   INTRODUCTION

1.1 Statement of problem

Oil sands are an important world energy resource by virtue of the magnitude of known reserves. A large portion of Canadian known heavy hydrocarbon reserves occurs in the oil sand deposits located in Alberta, western Canada.

Alberta's massive crude bitumen resources are contained in sand and carbonate sedimentary formations in the Athabasca, Cold Lake, and Peace River oil sands areas (Figure 1.1). The total volumes of crude bitumen in place for the designated deposits was estimated in 1993 to be 269.2 billion cubic meters (Energy Resources Conservation Board).

The Athabasca Deposit is the richest of the Alberta bitumen reservoirs. It contains 210×10^9 m^3 of bitumen in three different geologic horizons: the McMurray/Wabiskaw, Grand Rapids and Grosmont/Nisku formations. The majority of recoverable reserves is contained in the Lower Cretaceous sands of the McMurray Formation and the Wabisca Member of the Clearwater Formation; 114×10^9 m^3 of bitumen is spread over an area of 46800 km^2 with a mean thickness of 34 meters (Wightman et al. 1989). The thickness of overburden ranges from 0 to 750 meters. It has been estimated that only about 10% of Athabasca oil sands deposits are surface mineable; thus the vast majority of the bitumen will be recovered by means of in situ extraction technology.

The Alberta Oil Sands Technology and Research Authority (AOSTRA) Underground Test Facility (UTF) Phase A, located 70 km northwest of Fort McMurray (Figure 1.2), was built to test the shaft and tunnel access (SATAC) approach to in situ recovery. Because of the very high viscosity of the bitumen contained in the oil sands, hot fluid must be injected into the formation, enhancing bitumen mobility. The UTF was a field pilot for developing and evaluating methods for in situ recovery of bitumen through the use of horizontal steam injection and production wells. These wells were drilled from a shaft and tunnel system. Each well pair consisted of an injection well and a production well located approximately 7 meters and 2 meters respectively, above the base of the oil sands (Figure 1.3).

Since in situ recovery processes tend to be site specific, the steam assisted gravity drainage (SAGD) process was chosen as the most promising concept for horizontal well recovery from the McMurray Formation oil sands at the UTF site. Steam is supplied to the injector to maintain a constant pressure within the growing chamber. The steam travels to the edges of the chamber, condenses, and drains to the bottom. The condensing steam heats (by thermal conduction) a thin layer of undepleted sand near the boundary of the chamber. This mobilizes the bitumen and allows it to drain with the condensate. As the bitumen drains, steam advances into the newly depleted reservoir. The condensate and bitumen are collected at the bottom production well (Edmunds 1987).

The SAGD process described above results in a complex interaction of geomechanics and multiphase thermal flow in cohesionless porous media. The geomechanical response of an oil sands reservoir to fluid pressure changes or to temperature changes results in stress and deformations that affect formation shearing, hydraulic properties such as absolute permeability and the stability of underground openings. Most reservoir models used in simulating the steam assisted gravity drainage process do not account for this geomechanical response. Several important parameters which affect process performance are however, directly impacted by the geomechanical response of the reservoir (Chalaturnyk 1996).

Absolute permeability of the reservoir affects the drainage of fluids from the steam front and therefore the frontal advance rate and the production rate; it is one of the most important parameters in the simulation of the SAGD process. Stress change induced volume changes within the reservoir, specially within non-heated zones, will result in changes in absolute permeability (Chalaturnyk 1996). The large lateral extent of a disturbed zone, combined with a modest increase in permeability, will lead to a significant increase in productivity. This conclusion can only be drawn for a soil displaying dilation with shear, such as the Athabasca oil sands.

The above discussion shows the importance of the study of absolute permeability changes of McMurray Formation oil sands during gravity drainage recovery. The paucity of knowledge on this subject leads to the following objectives for this thesis.

1.2 Objectives

- To determine the initial absolute permeability of undisturbed specimens of McMurray Formation oil sands and how it varies with the initial porosity.

- To study the changes in the absolute permeability of oil sand during triaxial shear at low confining pressures. These triaxial tests would simulate the changes in stresses imposed by the steam assisted gravity drainage (SAGD) process employed at the Underground Test Facility.

- To investigate the anisotropy of oil sand. This includes anisotropy in permeability and stress-strain behavior.

- To illustrate a methodology through which the experimental findings can be implemented in numerical simulations of oil sand strain softening behavior.

- To present a model for the prediction of changes in the absolute permeability with changes in the stress field.

The achievement of these goals requires the following laboratory objectives:

- To produce dense uniform reconstituted specimens.

- To develop a triaxial apparatus with which different stress paths could be implemented more readily than in conventional equipment.

- To devise test procedures and methods of analysis for the triaxial permeability experiments.

1.3 Geology of McMurray Formation

A goal of this research was to study McMurray Formation core similar to the rich oil sands at the UTF site. The following describes the stratigraphy of this location.

The formal division of the Lower Cretaceous McMurray Formation into lower, middle and upper members provides a useful breakdown for the northern half of the Athabasca Deposit. At the UTF location, the lower McMurray is absent and the middle member rests unconformably on the Devonian limestone at about 163 meters (Figure 1.4). Overlying the McMurray Formation is the sandy Wabiscaw Member of the Lower Cretaceous Clearwater Formation. The rest of the Clearwater Formation is made up of thick shale. These are overlain by sands and shales of the Grand Rapids Formation and thin Quaternary gravels and tills (Rottenfusser et al. 1988). The geologic profile illustrating stratigraphy at the AOSTRA UTF site is shown in Figure 1.4.

At the Phase A site the McMurray Formation consists of mixed oil sands and shales, approximately 37 meters thick. The stratigraphic section of interest has been informally divided into 8 units, each of which can be correlated throughout the pilot site. The units cover the interval from the Wabiscaw Member (Unit A) through the McMurray Formation (Units B to G), to the Devonian Waterways Formation (Unit H). Unit E containing the best reservoir was chosen to be studied in this research program. Unit E varies from 5.6 m to 10.9 m in thickness (Figure 1.5), and consists of interbedded oil sands and shale breccia. This is the richest part of the reservoir. The breccia consists of shale fragments (<1 cm to 6 cm) suspended in the oil sands. Average porosity for the unit is 31% and water saturation is low at 13% (Rottenfusser et al. 1988). Bitumen content varies from 9% to 13%. Figure 1.6 shows the domain of Unit E grain size distribution.

1.4 Locked sand

Oil sand displays a geomechanical behavior which is different from that of a typical dense sand. In this respect the Athabasca oil sands have been studied by many researchers. The following is a summary of previous studies.

Cohesionless sands are usually classified according to their density and a common distinction that is made is whether the sand is loose or dense. Loose sands are

compressible and contract during shear. The shearing resistance increases monotonically to failure and the sand contracts to the ultimate void ratio. Dense sands are less compressible and dilate during shear at normal stresses commonly encountered in civil engineering practice. The shearing resistance falls from a peak value to the residual value as the sand dilates. The maximum shearing resistance occurs at or close to the maximum rate of dilation.

Athabasca and Cold Lake oil sands geomechanical behavior has been the object of significant study since the mid-1970's. Dusseault (1977) showed that the Athabasca oil sands has an extremely stiff structure in the undisturbed state, accompanied by a large degree of dilation when loaded to failure and therefore has peak frictional strengths considerably in excess of those displayed by a dense sand. It was suggested that another class of cohesionless sand exist in addition to loose and dense sands. These sands are called locked sands (Dusseault and Morgenstern 1979). Locked sands are composed of predominantly sand-sized particles and are commonly encountered in nature at relative densities greater than 100%. That is, they are found in situ at porosities less than can be attained by the ASTM or comparable tests for achieving minimum porosity.

The angle of shearing resistance for locked sand is greater than that of dense Ottawa sand. The locked sands contain mostly subangular, competent quartz grains. Optical and scanning electron microscope studies of locked sand specimens have indicated the source of their distinctive behavior. Locked sand displays a considerable quantity of interpenetrative (concavo-convex) and straight contacts (Figure 1.7). This fabric is the result of solution and recrystallization of quartz in a mildly diagenetic environment and results in decreased porosity, increased grain surface rugosity, decreased roundness and an increase in shear strength well beyond that expected of a dense cohesionless sand (Dusseault and Morgenstern 1978).

The strain to failure of the triaxial tests on locked sand is small. This is consistent with the hypothesis that the intimate and interpenetrative grain contacts are responsible for the dilatancy. A disruption of this fabric (interlocked structure) returns the shear-strength behavior of the material to that of an ordinary sand (Dusseault and Morgenstern 1979). The shear strength of oil sand measured in triaxial compression tests is very sensitive to the degree of specimen disturbance. Experimental results indicate that a relatively small increase in the initial sample porosity may result in a significant reduction in the measured shear strength (Agar et al. 1987).

Therefore it is pertinent that experimental studies be conducted on completely undisturbed oil sand specimens. This ensures that reliable geomechanical parameters like stress-strain and absolute permeability are obtained.

Although it has been shown that the behavior of locked sand should be studied at the stresses anticipated during steam injection (Scott et al. 1994), most triaxial tests on oil sands, so far, have been conducted at relatively high confining stresses (Chalaturnyk et al. 1991). Since the effective confining pressure is a key factor controlling geomechanical response of locked sand, and as the sand structure behaves

differently at high or low effective stresses, it is the intent of this research program to investigate the geomechanical behavior of McMurray Formation locked sand at low effective confining pressures through triaxial laboratory tests.

1.5 Problem of sampling and sample disturbance in the Athabasca oil sands

The Athabasca oil sands are an unconsolidated, water-wet (predominantly quartz) sand, bitumen and gas system. They are usually saturated with bitumen and water in situ and contain varying amounts of dissolved gas. The gas bubble pressure is typically equivalent to the in situ pore pressure. During coring and sampling the oil sand core experiences a decrease in effective stress and pore pressure. The drop in pore pressure causes gas evolution and expansion of the void space is not restricted since the effective stress has been removed (McKay 1989). Uncemented oil sand is highly susceptible to expansion and microstructure disturbance when in situ effective confining stresses are released rapidly during sampling. Cohessionless sands posses no tensile resistance to expansion and very low resistance to torsional shear. Dissolved methane, carbon dioxide and light hydrocarbon gases in the bitumen and pore water phases begin to evolve when confining stresses are released. The effective permeability of oil rich oil sand to gas is relatively low at in situ temperatures because of the extremely high viscosity of bitumen. Expansion of the oil sand structure thus occurs as dissolved gases evolve and expand but are prevented from draining. The rate and magnitude of expansion are increased due to the fact that evolving gases expand rapidly and maintain elevated pore pressure even as volumetric expansion of the oil sand occurs. The relatively large volume expansion associated with gas evolution disrupts the interlocking grain structure (Agar 1984).

Sample disturbance can adversely influence geotechnical properties in laboratory tests. Dusseault (1977) concluded that sample disturbance affects oil sand properties to varying degrees as follows:

Nonsensitive:	oil content,
Sensitive:	porosity, saturation,
More sensitive:	shear strength,
Very sensitive:	elastic modulus, compressibility and permeability.

Although there are improved coring and sampling techniques to obtain better quality samples, there exists another solution to avoid the problem of evolution of dissolved gas. Protulipac (1991) investigated the possibility of using an oil-free material to determine the constitutive behavior of an oil-saturated material, so the problem of sample disturbance could be avoided. He showed that an oil-free St. Peter sandstone (which has similar structure as McMurray Formation locked sands) behaves similarly to an oil-saturated McMurray sand, with regards to peak dilation rate, strength and stiffness.

Exposures of locked sand along rivers in the Fort McMurray area are numerous (Figure 1.8), slopes frequently stand over 70 m high, and in some places display the

entire vertical sequence of the oil-containing McMurray Formation. In some locations such as outcrops along the High Hill River and Cottonwood Creek the slopes are oil-free. A schematic cross section of the Athabasca Deposit is shown in Figure 1.9.

To obtain undisturbed specimens of the McMurray Formation locked sands, block samples of bitumen-free sand were taken along the banks of the High Hill River, approximately 60 kilometers east of Fort McMurray, Alberta (Figure 1.8). The cliff exposure that was excavated for the blocks is situated approximately one kilometer northeast of the junction of the High Hill and Clearwater rivers (Plates 1 and 2).

In this research program specimens obtained from one of these blocks were used in a series of triaxial permeability tests. Figure 1.10 shows the grain size distribution of this block. Also shown is the grain size range of Unit E at the UTF site. As the grain sizes are similar, the block sample can be considered to be representative of the rich oil sand at the UTF.

Since this block of locked sand is bitumen-free, there was no disturbance to the fabric of the locked sand specimens cored out of the block sample. Consequently the obtained specimens were truly undisturbed. These specimens provide an opportunity to investigate the results of tests on a truly undisturbed locked sand.

1.6 Reconstituted specimens

It was imperative that reconstituted specimens be included in the experimental study. Results of tests on reconstituted specimens provide an opportunity for evaluation of the testing system and experimental program. They also provide a basis for comparison with the test results on undisturbed specimens.

Producing reconstituted specimens as dense as undisturbed specimens has been attempted by many researchers (Dusseault 1977, Agar 1984, Oldakowski 1994). In this study several methods of specimen preparation were performed. A new technique was developed during the course of this study which could produce uniform dense reconstituted specimens.

Reconstituted specimens were made from McMurray Formation mixed sands. These mixed sands were made by mixing selected portions of different particle sizes. They were reconstituted to represent the grain size distribution of the block sample.

1.7 Organization of thesis

Chapter 2 describes the triaxial apparatus that was developed for stress path and permeability testing. The apparatus is described and its range and performance is discussed. The triaxial permeability test system used is discussed and explained. The method of automatic stress path testing system is presented.

The importance of the use of lubricated end platens in a triaxial permeability test is explained in Chapter 3. Since Darcy's law is not suitable for flow analysis inside a cylindrical specimen with lubricated end platens a simple approximate method for solving this problem is presented.

Chapter 4 explains different stages of a triaxial permeability test. These include different methods of triaxial specimen preparation, setting up a test and saturation procedures. Different methods of preparing a reconstituted triaxial sand specimen are described. The other steps, consolidation, permeability testing, shearing and analysis of data are also explained.

Chapter 5 describes the fabric characteristics of oil sand. Images of oil sand specimens from the McMurray Formation were obtained with the use of a scanning electron microscope (SEM). The images were analyzed with a digital image analysis software. These analyses provide the basis for the recognition of oil sand anisotropy due to preferred particle orientation.

Chapter 6 describes the laboratory testing program that was conducted to examine the geomechanical properties of oil sands. Triaxial tests were performed to replicate the stress and pore pressure conditions associated with steam stimulation. The testing program was comprised of stress-strain, strength and permeability tests. Stress-strain and strength results of this testing program are presented. However permeability test results are discussed in Chapter 8.

Chapter 7 describes a method whereby strain softening is incorporated into a constitutive model for the simulation of oil sand. A numerical simulator, FLAC was chosen for the numerical simulation of oil sand geomechanical behavior at low confining pressures. Several material input functions are necessary in order to simulate the strain softening and shear dilatancy with FLAC. Results from high quality triaxial experiments were used to provide these functions for the simulations.

Chapter 8 presents the results of the triaxial permeability tests performed. During these tests the permeability of the sand specimens were monitored when they were undergoing changes in stress and pore pressure. A simple relation for the prediction of changes in the absolute permeability during these processes is presented.

Chapter 9 summarizes the findings in the thesis and provides conclusions on the geomechanical behavior of McMurray Formation oil sand under low confining stresses. These include the issues of absolute permeability changes and numerical simulation of oil sand. Topics of further research are identified and discussed.
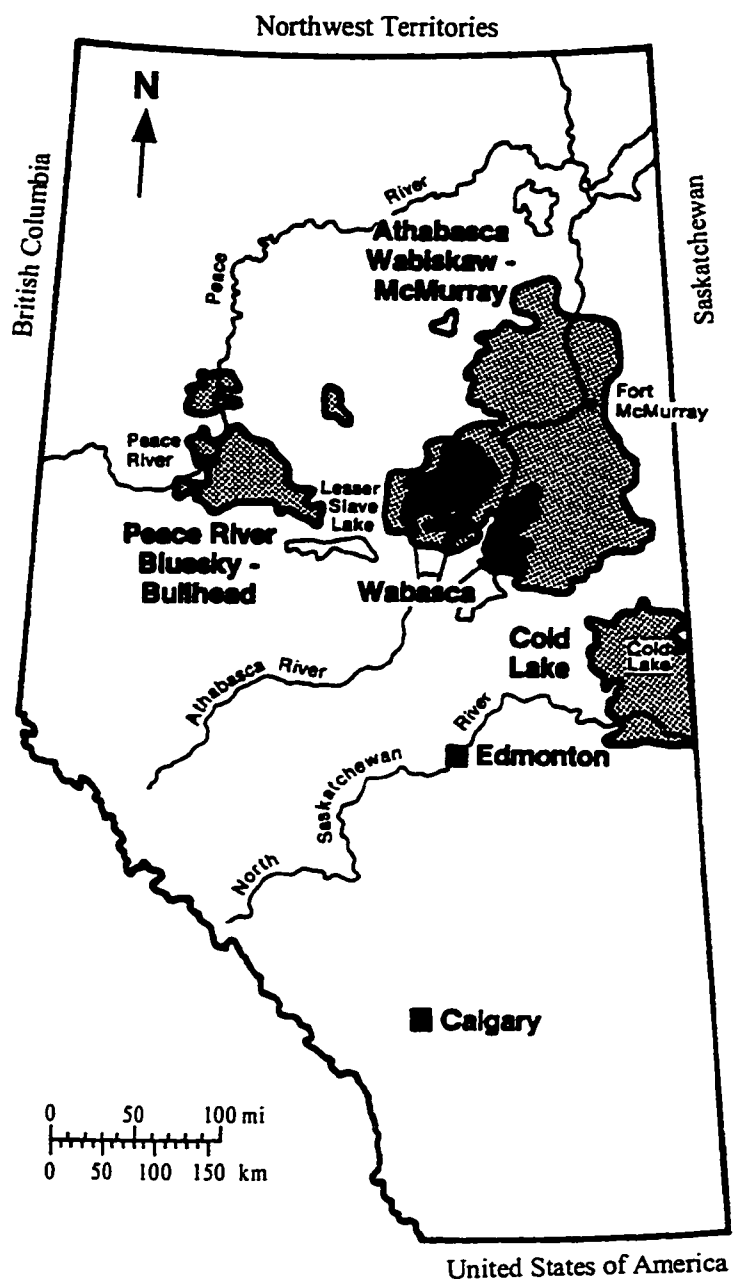
Figure 1.1 Distribution of Alberta oil sands

(Modified from Morgenstern et al., 1988
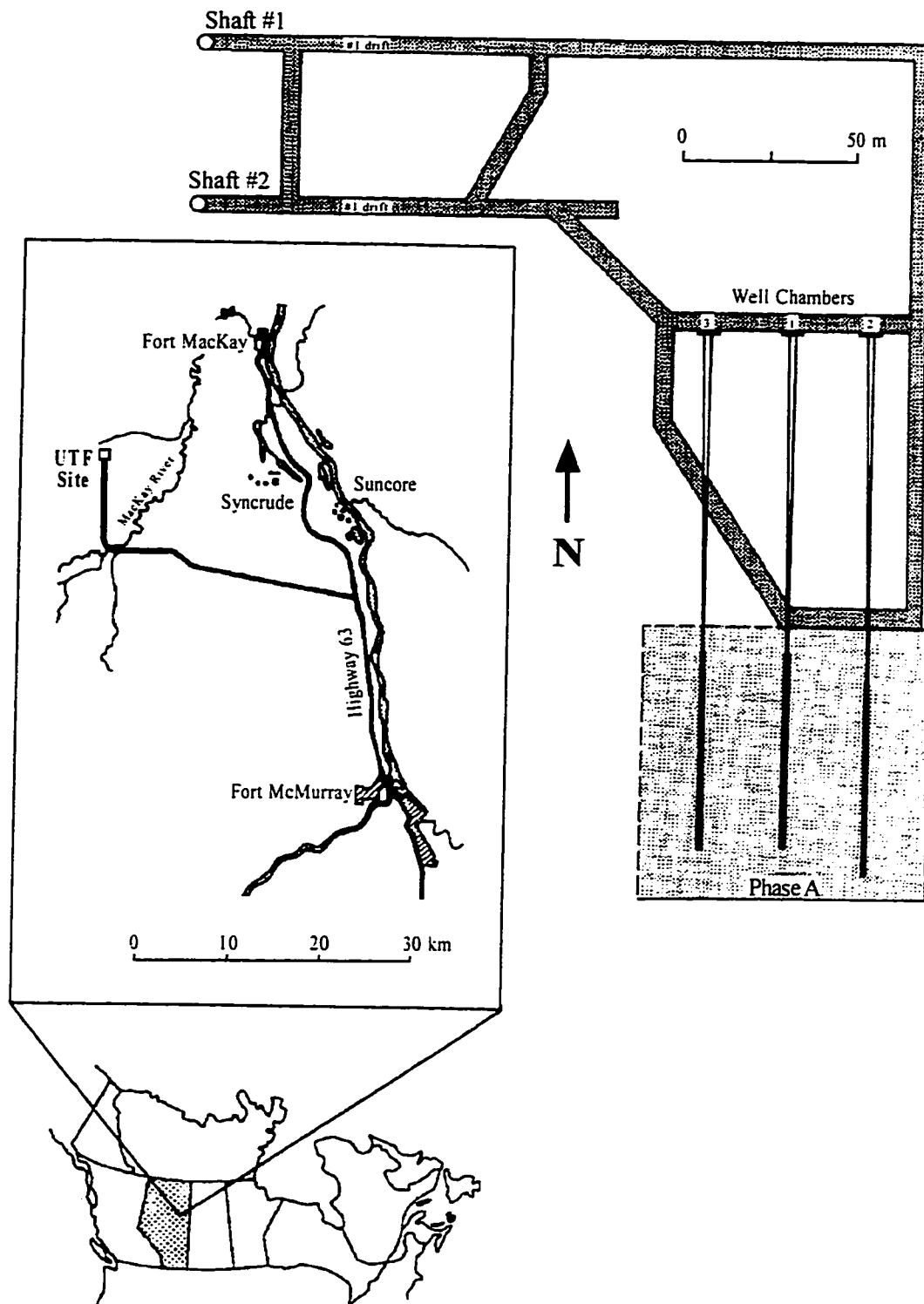
Figure 1.2 Location of the UTF site and layout of shafts, tunnels and Phase A horizontal well pairs

(Modified from Rottenfusser et al. 1988)

Wabiskaw Member Sandstone

Clearwater Formation Shale   309   124

McMurray Formation

308   125
Shale and Sandy Shale   Elevation (m) Depth (m)
298   135

Interbedded Rich Oil Sands and Shales
291   142

10
5

0   5   10   15   20   25m

Rich Oil Sand

Injection Well

Production Well   Slotted Section

270   163

Waterways Formation

Well Chamber

No. 2 Drift

253.5   176.5
251   182
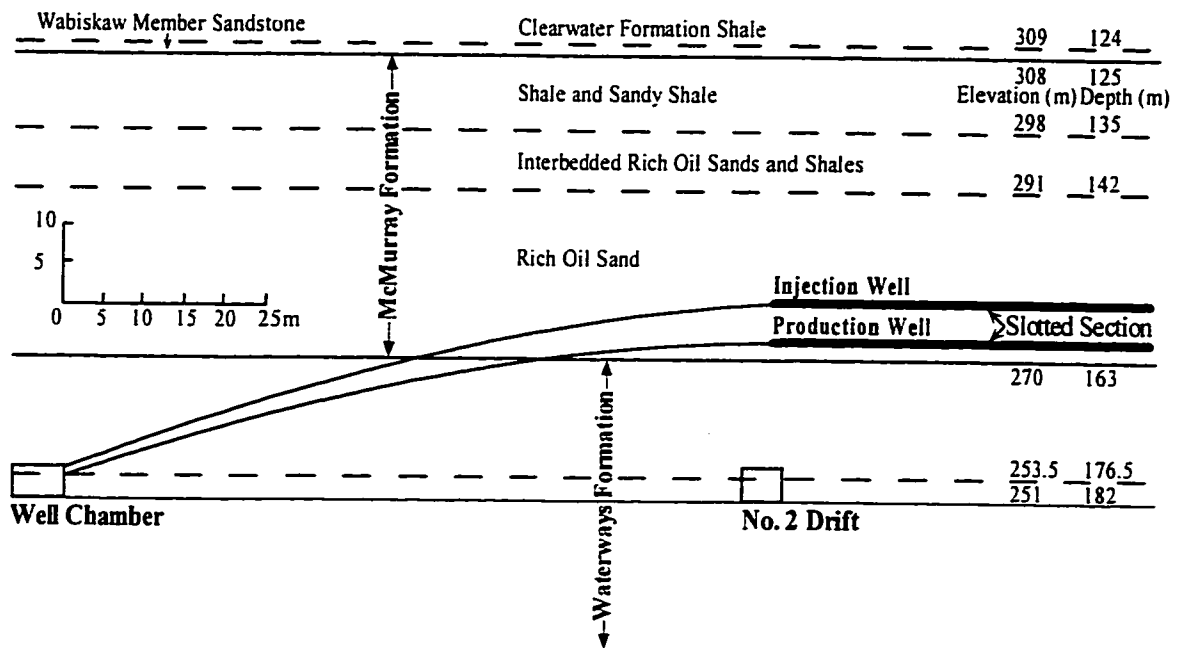
Figure 1.3 Generalized north-south cross-section through Phase A

(Showing positions of tunnels relative to the injection and production wells)
(Modified from Rottenfusser et al. 1988)

Elavation, m	Depth, m	Age	Formation	Lithology				Unit				
433		Quate-mary	Pleist.-Recent	gravels and tills								
418	15											
		Upper Cretaceous	Grand Rapids Formation	sands and shales		306	127		B	shale and sandy shale		
338	80					298	135					
		Lower Cretaceous	Clearwater Formation	marine shale		293	140		C	interbedded rich oil sands and shales		
			Wabiscaw Member						D	rich oil sands with various amount of shales which reduce in frequency with depth		
308	125			sands			149					
306	127		McMurray Formation	oil sands with clay shales					E			
							158					
							160		F	shale		
270	163								G			
		Upper Devonian	Waterways Formation	limestone		270	163					

Figure 1.4 Geology of Athabasca oil sands at UTF site (Phase A)

(Modified from Oldakowski 1994)
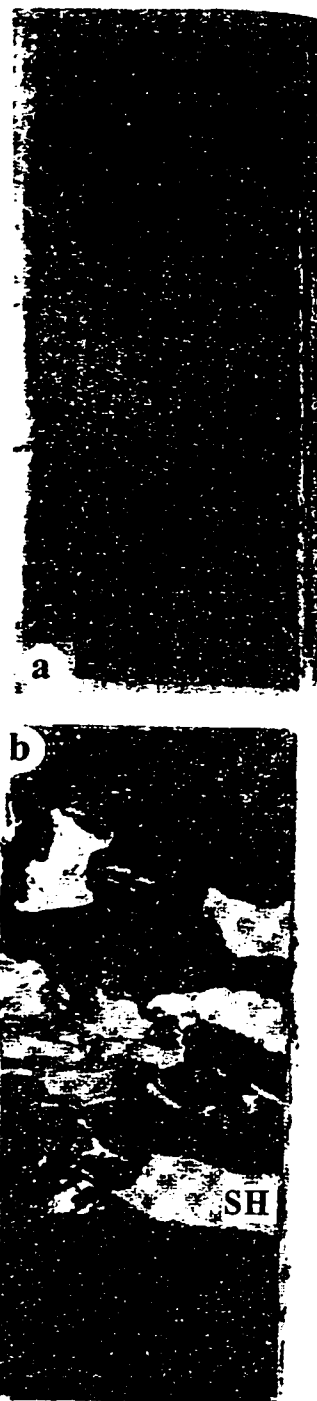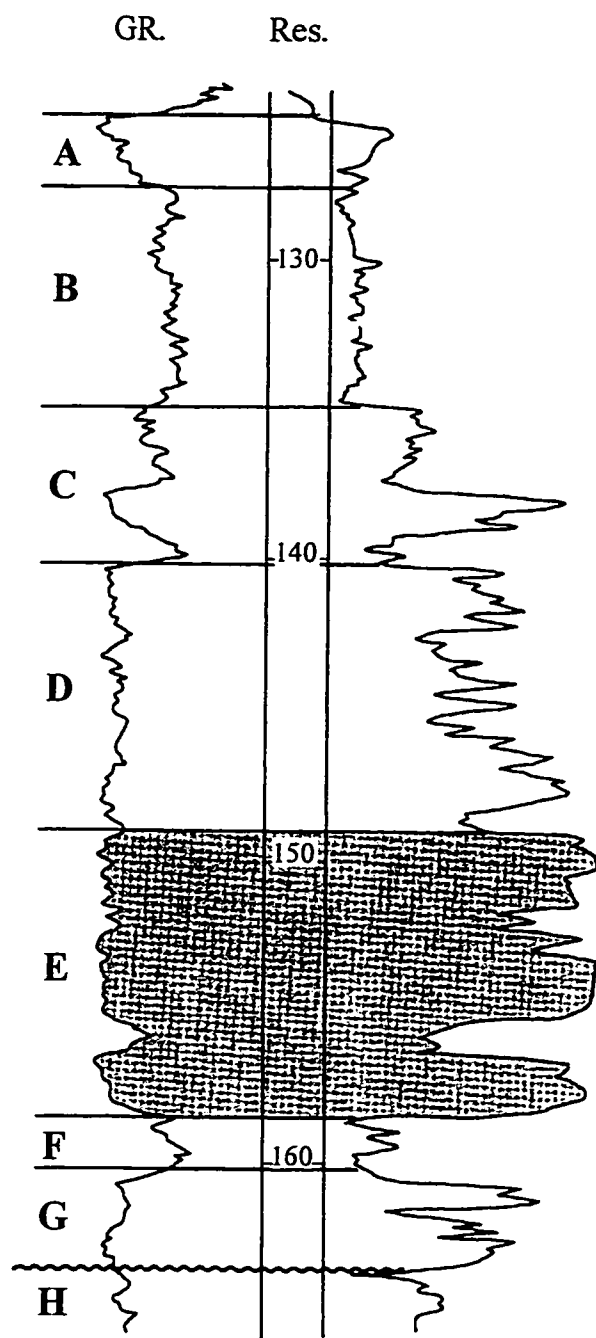
Figure 1.5 Unit E. (a) Rich oil sand with dip of cross-bedding shown by parting along the bedding planes; (b) Rich oil sand with shale rip-up breccia (SH), most of the breccia fragments are not in contact with each other (Modified from Rottenfusser et al. 1988)
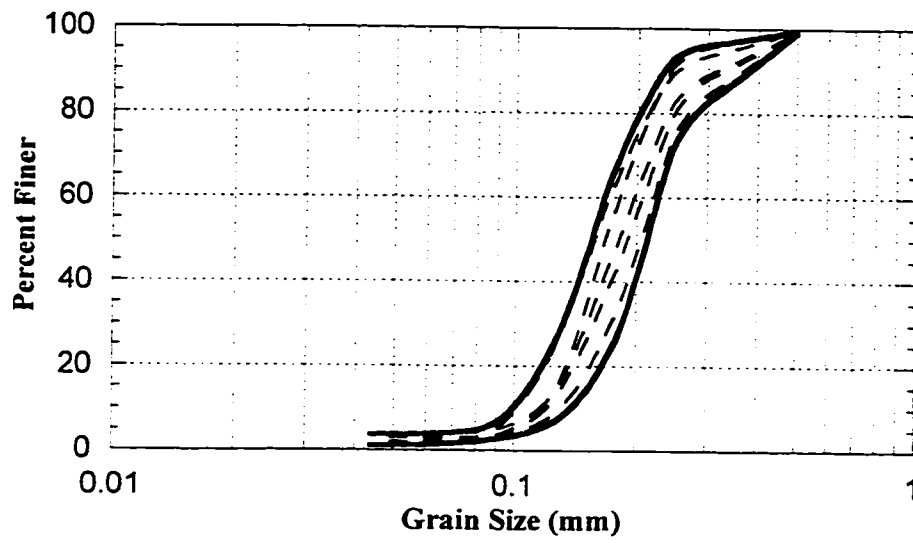
Figure 1.6 Domain of Unit E grain size distribution

Based on data from Rottenfusser et al. (1988)
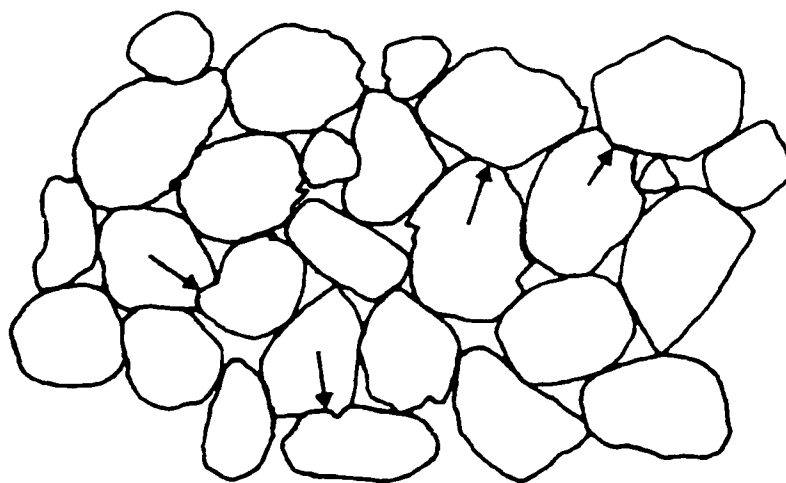
Figure 1.7 Fabric of Athabasca oil sands

Mostly tangential fabric, but many straight and interpenetrative contacts (arrows)
(Modified from Dusseault and Morgenstern 1978)
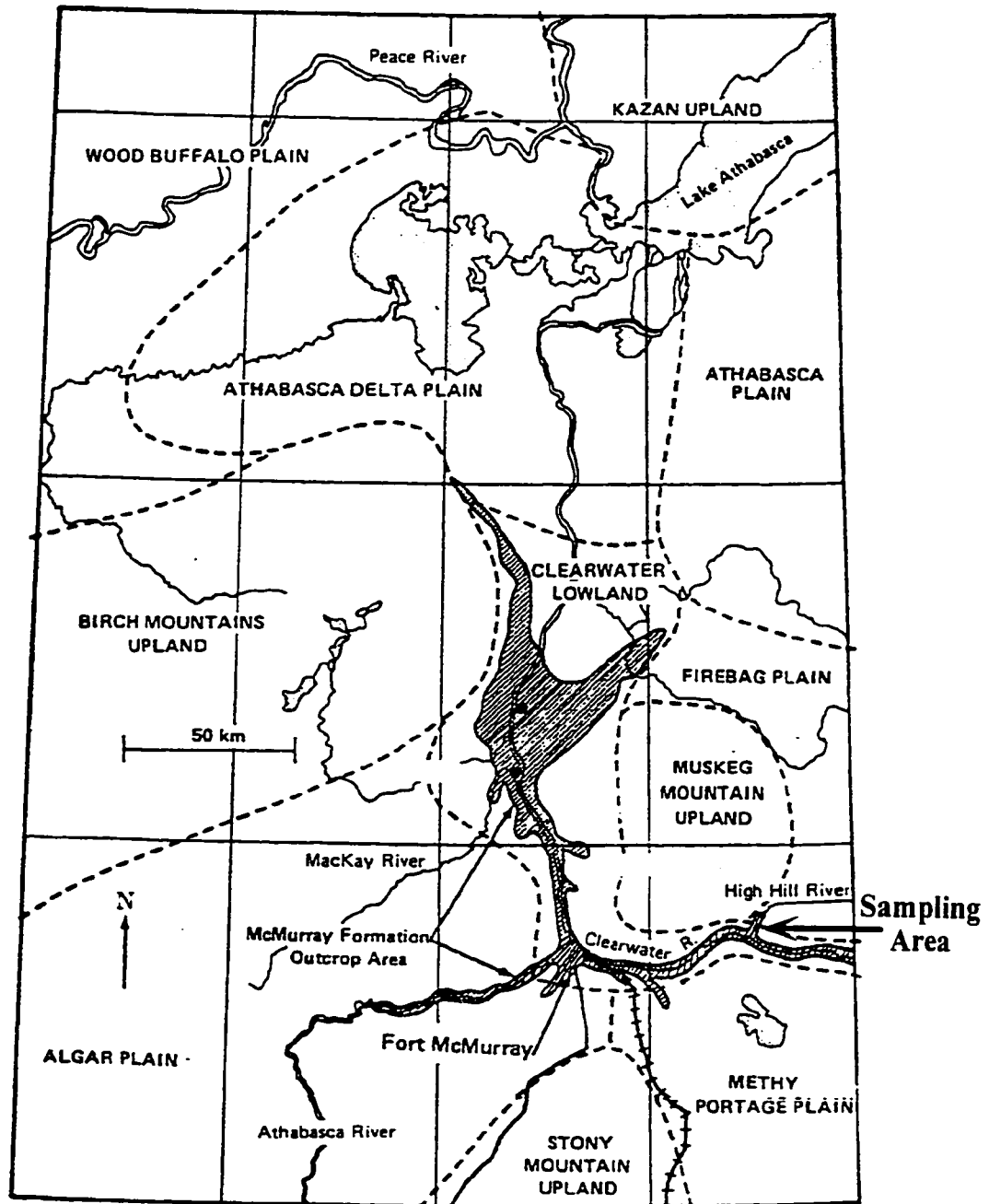
Figure 1.8 Physiography of the Athabasca oil sands and location of sampling area
(Modified from Dusseault 1977)
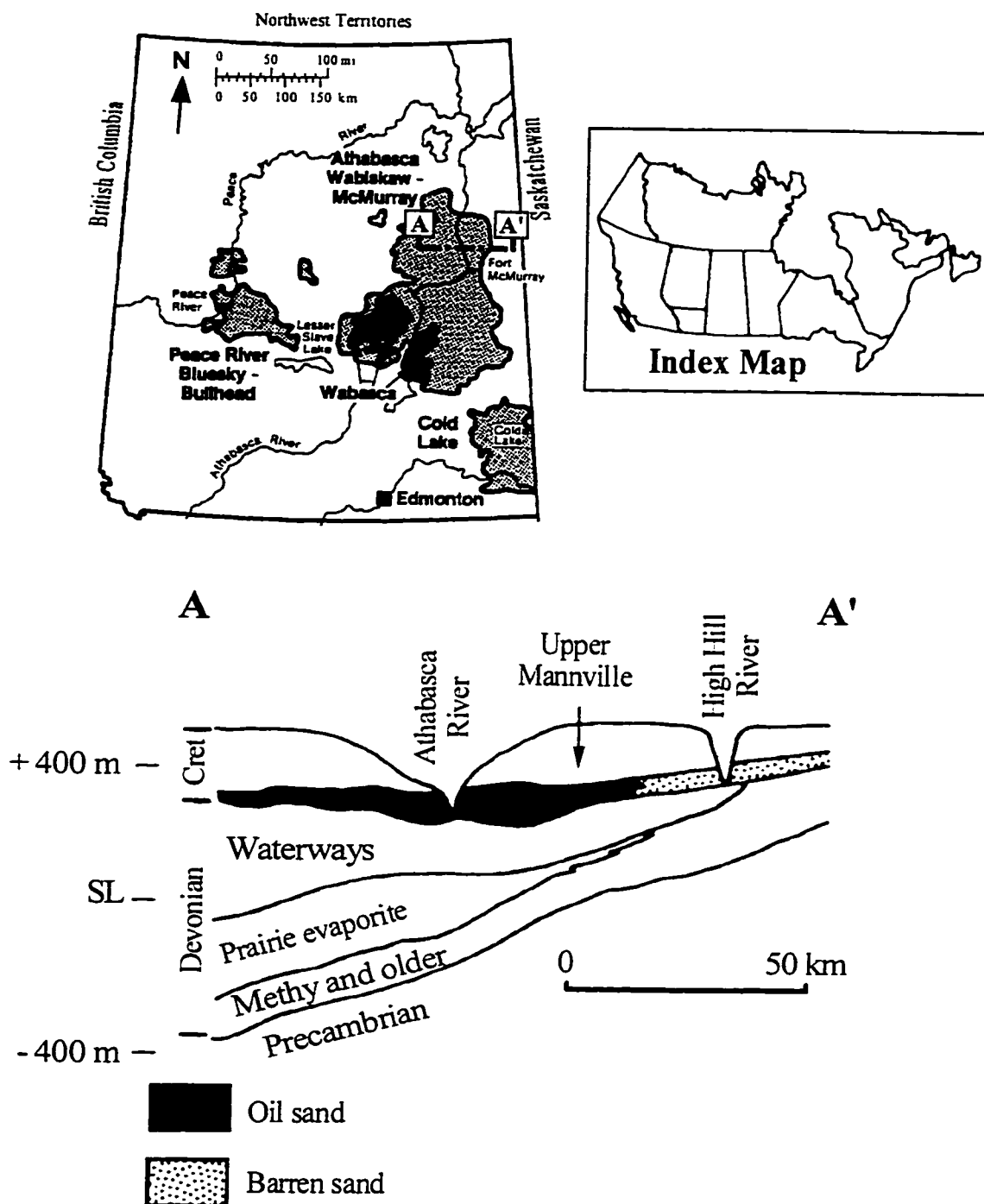
Figure 1.9 Map of the Alberta oil sands accumulations and schematic cross-section of the Athabasca Deposit

(Modified from Mossop 1980)
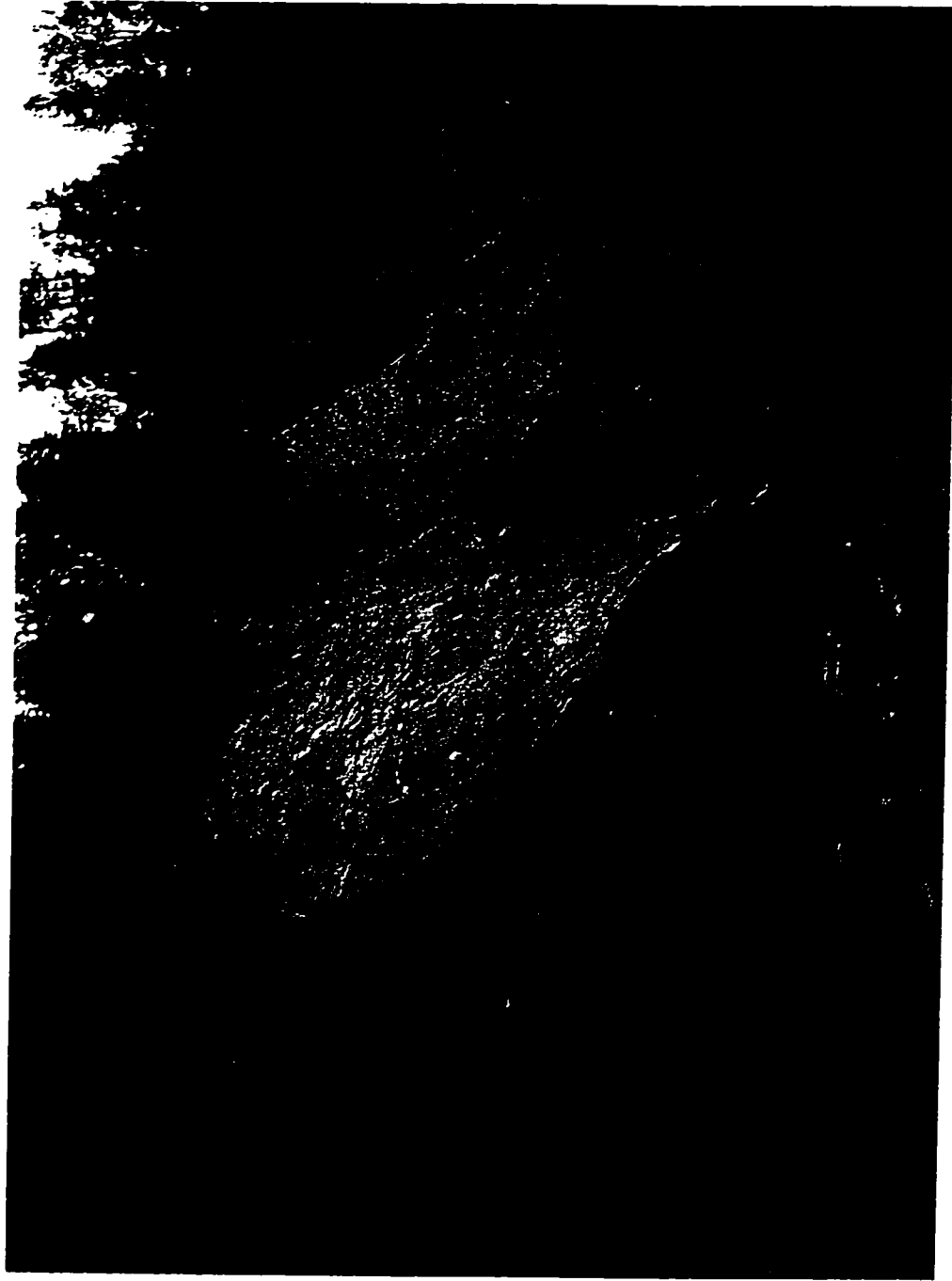
Plate 1 View of the sampling area from the river level
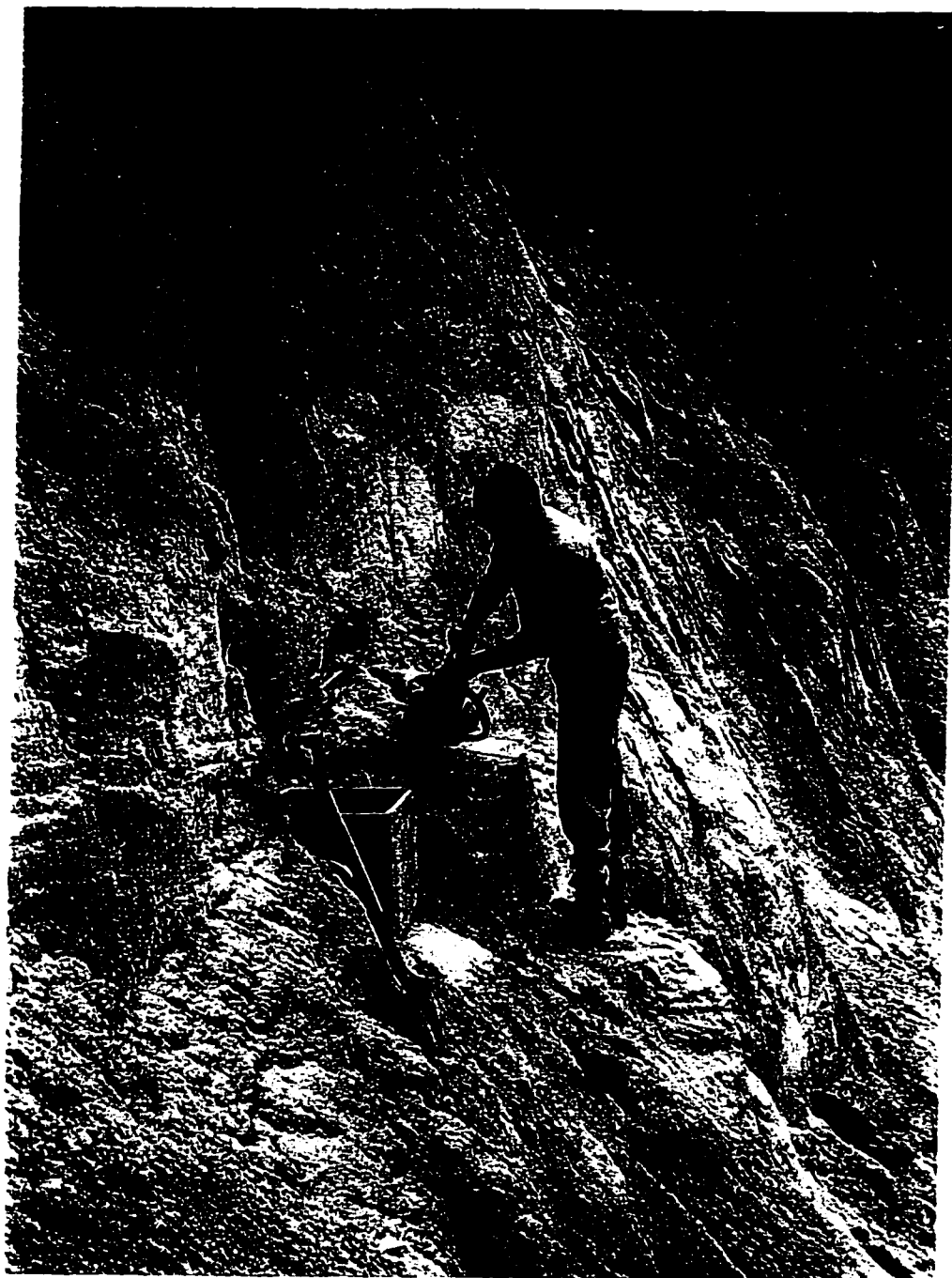
Plate 2 Cutting a block sample
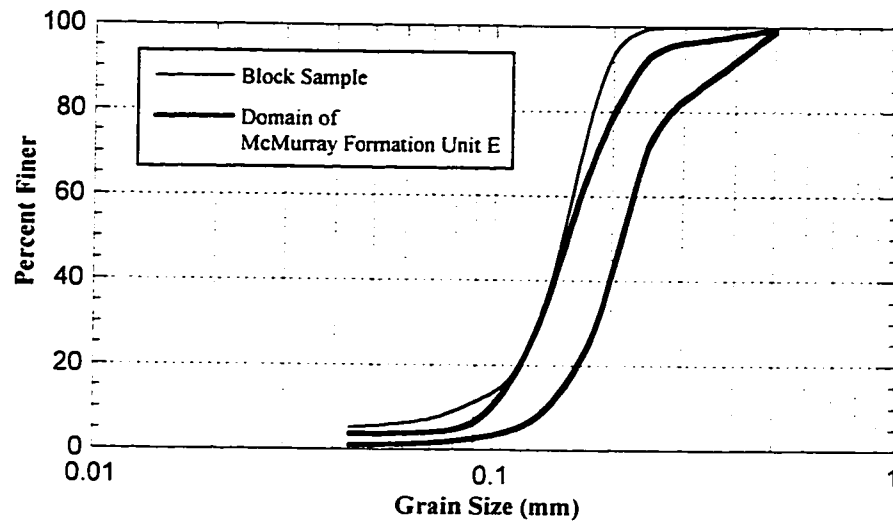
Figure 1.10 Grain size distribution of the block sample

CHAPTER 2   NEW STRESS PATH TRIAXIAL PERMEABILITY TESTING SYSTEM

2.1 Introduction

The triaxial test is the most common and versatile experiment used to determine the stress-strain properties of soil. It is a special version of the cylindrical compression test that is used to determine the mechanical properties of many materials, such as concrete. In this cylindrical compression test the principal planes are fixed in relation to the axis of the specimen.

Triaxial test is widely used for the laboratory measurement of shear strength under controlled conditions of drainage, and of deformation characteristics. Other soil parameters, for instance hydraulic conductivity, can also be measured in a triaxial test.

The main advantages of the triaxial test are:

(1) the control of drainage conditions and the measurement of pore pressure; as well
(2) the different stress paths that can be followed; and
(3) the ability to perform both stress-controlled and strain-controlled tests.

Most triaxial tests on soil specimens are done following one stress path, confining pressure constant and axial stress increasing. However other stress paths are of importance, in particular for drained tests, and where deformation characteristics are under consideration (Bishop and Wesley 1975). There is a need for a simple form of triaxial apparatus in which the stress paths can be implemented more readily than in the conventional equipment.

A new stress path triaxial testing system with the capability of continuous measurement of permeability was developed for this study. This chapter describes a form of hydraulically loaded triaxial cell, which satisfies both requirements of simplicity and versatility. Cylindrical specimens can be tested following a wide range of stress paths, subject only to the condition that the total and effective stresses remain positive (relative to atmospheric pressure) at the end caps. This apparatus is called the Bishop-Wesley stress path triaxial cell.

2.2 Bishop-Wesley stress path triaxial cell

Bishop and Wesley (1975) introduced a hydraulically loaded triaxial cell known as the Bishop-Wesley stress path triaxial cell. It is designed for a wide range of stress path tests on soil of low and medium strength, for use with either controlled rates of strain or controlled rates of application of stress (Bishop and Wesley 1975).

2.2.1 Description of the apparatus

The principal features of this cell are illustrated in simplified form in Figure 2.1. The upper part is similar to a conventional triaxial cell except that the vertical load in a compression test is applied by moving the specimen pedestal upwards from below and pushing the top cap against a stationary load cell, which records the load. It should be noted that the apparatus is self-contained, it requires no loading frame and is quite portable. It is equally well suited to both stress controlled and strain controlled loading.

The specimen pedestal is mounted at the top of a loading ram, the bottom end of which is a piston and pressure chamber. The axial load is applied to the specimen by increasing the pressure in the bottom pressure chamber. This arrangement with the load applied from below has several advantages. Setting up the specimen is very simple, as in a conventional apparatus, but no corrections are required for loading ram weight. The upper part of the cell, which is removed for mounting or dismantling the specimen, is light and easy to handle. Axial strain measurements can be made externally by means of the cross-arm arrangement attached to the ram between the Bellofram seals.

The ancillary equipment needed for use with the cell, such as pressure systems, depends on the type of test to be undertaken. Any type of pressure control systems suitable for the triaxial tests can be used. For controlled stress tests three controllable pressure sources are required while for axial strain controlled tests two controlled pressure source and a constant rate of flow source would be enough.

For the current testing program three independent controllable pressure systems are needed to operate the cell. One to provide the cell chamber pressure, the other to provide the loading pressure on the bottom of the ram. The third pressure system is necessary to apply a back pressure to the specimen.

2.3 Principle of operation of stress path triaxial cell

Tests are carried out by controlled application of three pressures:

(1) cell pressure
(2) lower chamber pressure acting on the ram
(3) back pressure.
The following section describes the stress/pressure relationships specific to the geometry of the Bishop-Wesley cell.

2.3.1 Stress relationships

The notation used here is substantially the same as that used in Bishop and Wesley's paper (1975). The pressures and forces acting on the loading ram are indicated in Figure 2.2 (Head 1986) and are:

- axial stress applied to the specimen, σ_a, in terms of total stress;
- radial stress (cell pressure), σ_r, in terms of total stress;
- lower chamber pressure acting on the ram, p;
- weight of loading ram piston (see Figure 2.3), W;
- effective area of Bellofram seals, a;
- area of cross-section of specimen at any time, A; and
- initial area of specimen, A_o.

The value of back pressure, U_{back}, at any time is controlling the actual state of effective stress on the specimen.

The upward force on the ram is equal to $p\,a$. The total downward force on the ram is the sum of the following:

- weight of ram, W,
- friction in the linear bearing and the rolling seals, f,
- cell pressure on exposed annular area, $\sigma_r\,(a - A)$,
- axial stress on specimen area, $\sigma_a\,A$.

For equilibrium, the upward and downward forces must balance, hence:

$$p\,a \;=\; W \;+\; f \;+\; \sigma_r\,(a-A) \;+\; \sigma_a\,A \qquad\qquad [2.1]$$

re-arranging Equation 2.1:

$$\sigma_a \;=\; p\,\frac{a}{A} \;-\; \sigma_r\!\left(\frac{a}{A}-1\right) \;-\; \left(\frac{W+f}{A}\right) \qquad\qquad [2.2]$$

the area A varies as the test proceeds in accordance with the following equation:

$$A \;=\; A_o\!\left(\frac{1-\varepsilon_v}{1-\varepsilon_a}\right) \qquad\qquad [2.3]$$

where ε_v and ε_a are volumetric and axial strain respectively.

For any particular test it is easy to determine from Equation 2.2 the way in which the pressures p, σ_r and back pressure are varied in relation to each other to produce a required stress path. Any stress path between the lines representing failure in axial compression and failure in axial extension can be followed, subject only to the limitation of the safe working pressures of the Bellofram seal and the triaxial cell.

Conventional types of triaxial tests, which require constant rate of strain, can be carried out by connecting the loading pressure chamber to a constant flow pump.

2.4 Range and performance of apparatus

The apparatus was primarily designed for tests on soils of low and medium strength in the low and medium stress range but can handle quite a wide range of values of σ_r, σ_a and U_{back}. The accuracy of the stress and stress observations depends mainly on the control and measurement system used.

The Bishop-Wesley stress path triaxial cell used in this study was a Wykeham Farrance model WF 12400 triaxial apparatus. Based on the parameters for this apparatus and considering the safe working pressures of the Bellofram seals and the triaxial Perspex cell wall, Figure 2.4 shows the operating limits of the apparatus (zone ABEF) for a 38 mm diameter specimen.

It will be seen from Equation 2.2 that the value of σ_a depends on p, the pressure in the lower pressure chamber, the area ratio a/A where a is the effective area of the Bellofram seal and A the cross-sectional area of the specimen, the value of σ_r and to a minor extent the weight of the loading ram and specimen, W, and friction in the linear bearing and the rolling seals, f. These parameters for the present apparatus have the values shown in Table 2.1. Figure 2.3 shows weight of different components of loading ram. Section 2.4.1 describes the method of obtaining the frictional force.

The values in Table 2.1 give an upper limit AB to σ_a in Figure 2.4 and a lower limit EF that lies in the tensile stress range for all values of σ_r. The apparatus can, in principle, fail a specimen with unconfined compression strengths of approximately 5200 kPa.

In extension, a maximum stress difference $(\sigma_r - \sigma_a)$ of 1000 kPa may be applied, if the maximum cell pressure is used and zero adhesion at the end caps is assumed. The apparatus can apply substantial negative values of σ_a if suitable end-grips are used, but these are associated with positive values of σ_r. The line EF represents the limit of the apparatus in extension. It should be noted that this diagram is in terms of total stress.

In terms of effective stress, the limiting state lines for friction angle values, ϕ', of 20°, 30°, 40° and 50° are also shown. Since the boundary line ABEF is in terms of total stress it is necessary to know the amount of back pressure, U_{back}, in order to find the capacity of the cell for a particular specimen and stress condition.

Figure 2.5 shows an example of a specimen with estimated maximum friction angle, ϕ', of 30° to be tested under effective confining pressure of 400 kPa with a back pressure, U_{back}, of 500 kPa. First, the effective stress state is found with the help of $\phi' = 30°$ state line (point ES). Then by adding the value of back pressure the corresponding point in total stress space is obtained (point TS). It is within the boundary line ABEF and thus the apparatus is capable of shearing this specimen under these stress conditions.

2.4.1 Frictional force

Frictional forces derive from moving the linear bearing and unrolling and rolling up the two Bellofram seals and amounted to 6.635 N for this particular cell. This is equivalent to an axial stress difference of 6 kPa for a 38 mm diameter specimen and must be taken into account, in planning the pressure path, if feed back from the load cell is not used.

The value of frictional force was obtained by performing a calibration test, the layout of which is shown in Figure 2.6. A conventional load frame was used for this test. The load cell had to be calibrated specifically for tensional forces beforehand. A hinge connection should be used for both load cell calibration and this test (Figure 2.6).

Frictional force in the cell was obtained from the difference in total force on the load cell when the load frame ram was moving down and when the ram was moving up. The following equations were used to derive the frictional force:

load cell reading when the load frame ram is moving down is:

$$(Load)_{Down} = W + f \tag{2.4}$$

load cell reading when the load frame ram is moving up is:

$$(Load)_{Up} = W - f \tag{2.5}$$

the difference between these two load measurements is equal to twice the frictional force:

$$(Load)_{Down} - (Load)_{Up} = (W + f) - (W - f) = 2f \tag{2.6}$$

the frictional force was thus calculated from Equation 2.6.

2.5 Pressure control system

The apparatus has been designed to suit any pressure control system, which can continuously vary pressure in a predetermined manner. As it was mentioned three independent controllable pressure systems are needed to operate this apparatus: loading pressure on the bottom of the ram, cell pressure and back pressure.

In this testing program compressed air-water systems were used for all three pressure systems, as shown in Figure 2.7. Stainless steel reservoirs were used for this purpose. In order to increase the volume of compressed air above water level, two reservoirs with capacity of 500 cc and 1000 cc, connected in series, were used in each pressure system.

Compressed air pressure was controlled by a series of solenoid valves. Electric solenoid valves controlled by a computer adjusted the desired pressure in the compressed air. For

each pressure system six solenoid valve were used: three for increasing the pressure and three for decreasing the pressure, as shown in Figure 2.7. Each solenoid valve in a set of three had one orifice. However the orifice sizes of these three solenoid valves were not the same. The diameters were 0.2, 0.33 and 0.51 mm (0.008, 0.013 and 0.020 inch) respectively. The following section provides specific information regarding the solenoid valves.

2.5.1 Solenoid valves

A solenoid valve is a combination of two basic functional units (Figure 2.8):

(1) a solenoid (electro-magnet) with its core, and
(2) a valve body containing one or more orifices.

Flow through an orifice is shut off or allowed by the movement of the core when solenoid is energized or de-energized (Figure 2.8). When the solenoid is energized in a direct acting valve, the core directly opens the orifice of a normally closed valve. Two way solenoid valves have one inlet and one outlet pipe connection. They are used to allow or shut off flow.

The solenoid valves used in this testing equipment were two way direct acting general service solenoid valves. They were ASCO 8262 solenoid valves and had a normally closed construction. They were closed when de-energized and opened when energized.

Response time from fully closed to fully open, depends on the valve size, operating mode, electrical service, fluids, temperature, inlet pressure and pressure drop. The response time for the direct acting valves on air service under average conditions was 5 to 10 milliseconds.

The maximum operating pressure differential of a solenoid valve refers to the maximum pressure difference between the inlet and outlet against which the solenoid can safely operate the valve. The maximum operating pressure differential of the valves used in this study, for air, was 1240 kPa (180 psi).

2.5.2 Computer controlled pressure system

Figure 2.7 shows the layout of the pressure system used for this equipment. For cell and back pressure systems a compressed air reservoir of 1100 kPa was used as the source for increasing pressure and venting to atmosphere for decreasing the pressure. This was adequate since the maximum pressure needed by either of these pressure systems was less than or equal to 1000 kPa. This was also within the maximum operating pressure differential of 1240 kPa for the solenoid valves.

Pressures up to 2070 kPa were anticipated to operate the bottom chamber pressure system. Since this was above the pressure usually provided by conventional compressors in a soil mechanics laboratory, a compressed nitrogen bottle was used in conjunction with

a gas pressure regulator valve to provide this pressure. However, this pressure was above the maximum operating pressure differential for the solenoid valves. To solve this problem a tubing system was used with the help of two three-port valves (Figure 2.7) which was operated in the following manner:

For the beginning of the test when the bottom chamber pressure was increasing, the same combination of pressure sources was used like the other pressure systems: 1100 kPa reservoir as higher pressure source and atmosphere for decreasing the pressure.

When the bottom chamber pressure approached the limit value in this situation, which was 1100 kPa, the operator would rotate both three-port valves at the same time toward the direction shown in Figure 2.7. This resulted in compressed Nitrogen bottle being the source for pressure increase and the compressed air reservoir of 1100 kPa as the source for decreasing the pressure. The pressure coming from Nitrogen bottle could be set at any desirable value however it should be kept under safe working pressure of bottom chamber Bellofram seal, i.e. 2070 kPa.

The reverse of this procedure was applied in the unloading part of the test. It should be noted that if in any circumstance the differential pressure on solenoid valves exceeds the maximum operating pressure for them, it would result in a constant leak of gas from the valves. This would cause the computer controlled system to constantly try to maintain the pressures. This is thus not catastrophic for a test in progress. if it is fixed as soon as possible.

A computer continuously monitored the three pressure systems and adjusted them to the set pressure values, if necessary, sending commands to the solenoid valves. The LabVIEW software (National Instruments 1993) was used to create the controlling computer program.

Since there were three valves with different orifice sizes, there were 7 possible combinations of some or all of these valves opening at the same time. There were three cases of only one of the valves being open and 3 cases of different combinations of two of them being open plus the case of all three of them opening at the same time. These combinations were numbered from 1 to 7 in the computer program according to the overall size of opened orifices. Therefore combination 1 was the smallest valve being open while 7 was the combination of all three valves open. Each valve remained open only for a fixed predetermined time. This was done for safety reasons. This time was chosen according to the size of the orifice and depending on the condition of pressure change (increasing or decreasing).

Once the computer detected a difference between the set pressure and the actual pressure it attempted to adjust it by opening the valve with the smallest orifice size or combination 1. If there was still a difference between the pressures, computer would open the next combination of valves, e.g. combination 2 and so on. This resulted in a slight offset around the set pressure of approximately ± 1 kPa.

Full control over these three pressure system made it possible to follow almost any desired stress path between any two points lying within the section of stress space bounded by failure in axial compression and failure in axial extension. The results of stress path tests with this equipment are presented in Chapter 6.

2.6 Triaxial permeability set up

Hydraulic conductivity or coefficient of permeability of soil and rock specimens can be determined by any controlled test in which the cross-sectional area, the hydraulic gradient, and the quantity of flow are known. The triaxial test equipment used in this testing program provided facilities for maintaining a flow of water through a specimen while it was subjected to a controlled effective stress path (Figure 2.9). This made it possible to measure and monitor the permeability of specimen when it was undergoing changes in stress and strain (Chapter 3).

The method of permeability testing which was used in this study is the flow-pump method. A multi-speed flow-pump was used to maintain a constant rate of water flow entering the specimen. The head difference induced by this flow was measured continuously with time with a differential pressure transducer.

Figure 2.9 presents the scheme of the experimental equipment wherein a flow-pump (syringe pump) and a differential pressure transducer were connected to the Bishop-Wesley stress path triaxial cell. The cell was modified to accommodate two drainage ports at each end of the specimen. This allowed the direct measurement of differential pressure across the specimen, avoiding errors due to loss of pressure head in tubing and connections.

The flow-pump used in this study was an Isco LC-5000 precision pump. This syringe pump has a 500 ml capacity, a flow rate range of 0.1 ml/hr to 400 ml/h, and a 25.5 MPa pressure rating. The pump was operated in a constant flow mode. The syringe barrel and piston were made of 304 stainless steel. The pump seals were graphite-filled Teflon. The pump was designed for applications requiring precise, pulse-free delivery of liquids. The flow rate accuracy was ± 1 %, of range ± 1.5 μl/min.

The differential pressure transducer was a Validyne variable reluctance model DP 103 with a Validyne power and signal conditioning unit model CD 23 Digital Transducer Indicator. With this system, differential pressures could be monitored over arbitrary ranges from a maximum range of 140 kPa (1427 mm H_2O) to 0.055 kPa (5.6 mm H_2O) with a resolution of about ± 0.5 %. A ± 10 volt DC output may be obtained for a pressure of ± 0.055 kPa.

Lubricated end platens were used in most of the triaxial permeability tests during this study. Lubricated end platens are described further in Section 2.9.1 and in more detail in Chapter 3.

The lubricated ends configuration consisted of enlarged end platens and a small central porous disc, for drainage (Figure 3.6). The end platens of 45 mm diameter were used for tests on 38 mm diameter specimens.

Since the diameter of the central porous disc was smaller than the specimen diameter, the flow path of water injected through this porous disk into the specimen was not a rectilinear flow. Chapter 3 describes the special equations that were developed for the analysis of this case. However it is preferable to have a porous disk as large as possible without compromising the lubricated end system. Porous disks of 19 mm diameter were used throughout the tests with lubricated end configuration on specimens of 38 mm diameter. Even though they were half of the specimen diameter they occupied only 25 % of the specimen's cross-sectional area. Since a triaxial specimen is a case of axisymmetry, the location of these porous disks on the center of the specimen lessened the problem of friction at end caps. There is much less lateral displacement near the axis of symmetry.

The flow passed through a flow reversing board, which provided the possibility of changing the direction of flow inside the specimen. Hence the flow inside the specimen could be either upward or downward.

From the start of the permeability test there was a continuous injection of water from the syringe pump through the specimen to the back pressure system. Therefore it was not possible to monitor the specimen's volume change through the back pressure line. For this reason a second volume change measurement device was installed on the cell pressure line in order to obtain the specimen's volume change (Figure 2.10). Several corrections had to be made to the measurements of the device on the cell pressure line. They are discussed in Section 2.10.

2.7 Computer controlled data-logging

Typical measurements made during a test included:

(1) bottom chamber pressure (using a pressure transducer)
(2) cell pressure (using a pressure transducer)
(3) back pressure (using a pressure transducer)
(4) axial load (using a submerged load cell)
(5) differential pressure across specimen (using a differential pressure transducer)
(6) pore water pressure (using a pressure transducer)
(7) axial displacement (using a LVDT)
(8) specimen volume change (through either back pressure or cell pressure line, using a volume change measurement device).

Figure 2.10 shows the layout of measurement devices. Outputs from the transducers monitoring the test were connected to a computer-controlled data-logging system (Figure 2.11). System permitted unattended tests to be conducted.

Figure 2.11 shows the schematic representation of data processing and control system. The NB-MIO-16 multifunction I/O board from National Instruments (1991) was used. The NB-MIO-16 is a high-performance multifunction analog, digital and timing I/O board. With this board, laboratory processes can be automatically monitored and controlled.

The LabVIEW software (G language) was employed to create the data processing and pressure control computer program. The computer took continuous readings from all transducers, displaying it on the screen every second. It recorded data automatically at prescribed intervals. The data were also processed for the presentation of results, which was displayed on the screen. Data fed back from test measuring devices were processed and proper commands were transmitted to the solenoid controller, which made the required adjustments to the applied pressures. The automatic stress path system is described in Section 2.12.

Measurements of axial load, axial displacement, volume change and differential pressure are explained further in the following sections.

2.8 Axial load

The initial intent was to measure the axial load in the specimen using a submerged load cell. The stress path triaxial cell, however, provided an alternative to using the submerged load cell as the axial load could be obtained from the bottom chamber pressure. By substituting the correct value for weight of loading ram, W (Figure 2.3), frictional force, f, current values of cell pressure, σ_r and A, cross-sectional area of the specimen into Equation 2.2, the axial load on the specimen could be computed.

Figure 2.12 illustrates a calibration test set up for the measurement of axial load through readings of bottom chamber pressure. A pressure regulator in series with a compressed air-water reservoir was used to apply the load. The actual load was obtained by readings from a proving ring. In this calibration test there was no cell pressure, thus Equation 2.2 could be rewritten as:

$$\sigma_a A = p a - (W - f) \tag{2.7}$$

The axial load obtained from this equation and bottom chamber pressure transducer readings are plotted against load cell and proving ring readings in Figure 2.13. It is seen that the axial load calculated by Equation 2.7 was more accurate than value obtained from the load cell readings. Therefore in this study the specimen axial load was obtained from the bottom chamber pressure transducer readings.

It is essential that a top cap with a fixed kinematic condition be used in the triaxial testing. Hence the load cell and the top cap of this apparatus were designed to provide a fixed end cap configuration. Figure 2.14 illustrates this design.

2.9 Axial displacement

Axial displacement of specimen was obtained by means of a LVDT as illustrated in Figure 2.10. The following small corrections had to be made to the readings of this LVDT:

(1) apparatus and load cell deformation under deviatoric load, $\sigma_a - \sigma_r$. Deformation of the load cell and the triaxial apparatus due to the applied deviatoric load on the specimen may lead to an error in strain readings. This however can be measured by loading a rigid metal cylinder fitted in place of the soil specimen inside the cell.

(2) apparatus deformation due to changes only in the cell pressure, σ_r. Deformation of the triaxial cell due to internal pressure change may cause a false strain reading, which can be determined by pressurizing the cell.

(3) bedding error due to the use of lubricated ends. This problem is discussed in Section 2.9.1.

Specific calibration tests for each of these errors were conducted and triaxial test results were corrected accordingly.

2.9.1 Lubricated end configuration and bedding error

Lubricated end configuration was used in most of the triaxial tests of this study. Lubricated end platens were essential since they produced a more uniform deformation of the specimen. This subject is discussed in detail in Chapter 3.

The lubricated ends system used consisted of polished metal platens and a disc of rubber membrane material, separated by a film of high vacuum silicone grease as a lubricant (Figure 3.6). In this study two alternate layers of membrane and grease was used in each end of the specimen.

Rowe and Barden (1964) developed lubricated enlarged end platens to minimize the effects of end restraint. They have determined that if the friction angle between the specimen and the end platen can be kept below 1°, the end restraint effects can be considered negligible and the end platens can be assumed to be frictionless.

A detailed study of the resistance to sliding of greased rubber on a smooth surface, related to the theoretical thickness of grease, was conducted by Duncan, Seed and Dunlop (1966) and reported by Head (1986). They showed that the angle of friction increases sharply as the thickness of grease is reduced below about 0.04 mm, but above that thickness the angle is 1° or less. In practice a smear of grease would normally be about 0.05 to 0.1 mm thick (Head 1986). An excessive thickness must be avoided because this can lead to squeezing out, erroneous strain measurements and possible blockage of porous discs. These investigators also found that sand grains may tend to penetrate the rubber with a resulting increase in friction. This may be overcome by using more than

one sheet of rubber when testing sands. Lubrication was found to remain effective in long-term compression tests on small specimens of up to 3 ½ days duration.

Lubricated ends are bound to introduce some errors into the measurement of strain and strength of sand specimens. Norris (1981) indicated that to obtain a value of strength indicative of the sand, an optimum end membrane thickness should be used, or alternatively, multiple greased thin membranes with a combined thickness greater than (or equal to) the optimum thickness. For tests on sands the effect of the size of particles may be significant. Investigations by Norris (1981) showed that several factors influence the optimum thickness, the most significant being the size of particles. He suggested using an end membrane thickness equal to at least 1.5 times the mean particle size.

In the triaxial tests with lubricated ends, conducted in this study, two layers of 0.4 mm thick membrane were used at each end of the specimen. Based on Norris (1981), this was satisfactory, since the mean grain size of the sand tested was 0.155 mm.

The compression of the lubricated ends which is termed the bedding error, is primarily due to two effects: initial lack of fit between the specimen surface and the lubricated platen, and penetration of the grease and membrane layer by the constituent particles of the specimen. Bedding errors were discussed by Sarsby, Kalteziotis and Haddad (1980). They showed that the magnitude of the bedding error is independent of the specimen height and must be expressed as a deformation and not a strain. They also found that bedding error is related to the axial effective stress.

Plewes (1987) applied a correction for axial deformation of lubricated ends to the triaxial test results. The correction used by Plewes was obtained by the following test:

Instead of soil specimen a steel disk was installed in the triaxial cell with lubricated ends. Axial load was incrementally applied and the deformation response recorded. The correction was simplified to a relationship between axial load and axial deformation.

Using similar procedure as Plewes (1987) a special calibration test was conducted and a relationship was obtained in which the bedding error was correlated to the deviatoric load. Figure 2.15 presents the result of this test and the corresponding relationship. In the course of this study, the triaxial test data of lubricated end configuration were corrected using this relationship.

2.10 Volume change

Volume change measuring device of the type shown diagrammatically in Figure 2.16 was used in this study. This device consisted of a hollow thick-walled cylinder containing a floating piston attached to a Bellofram rolling seal at either end. The units used were of 50 cm^3 capacity with the capability of reading to 0.01 cm^3. They can be used at pressures up to 1400 kPa, but a minimum pressure of about 30 kPa was needed to expand the Bellofram seals. These devices were calibrated against an accurate burette.

Since there was a continuous flow of water through the specimen to the back pressure line, it was desirable to monitor the specimen volume change on the cell pressure line. Measurements of volume change on the cell pressure line required several corrections and were consequently less accurate than volume change measurements made on the back pressure line in routine tests (Head 1986).

Factors, which affect the movement of water into or out of the cell chamber, must therefore be considered in the cell line volume change measurements. They are:

(1) Expansion of cell due to pressure increase

During an increase in cell pressure the cell itself expands, and this volume change must be deducted from the observed displacement of water. The volume change characteristics of the cell was measured with the cell filled with water only. Figure 2.17 shows the result of this calibration test. Variations in the torque used to tighten down the fixing nuts of the cell can introduce an error into this calibration (Bishop and Henkel 1962). Therefore in all tests the same amount of torque was used to tighten the nuts of the cell. In this study the volume change measurements were corrected for the cell expansion.

(2) Expansion of cell with time

Continued expansion of the Perspex cylinder of the triaxial cell (creep) with time under constant pressure might be a concern in tests of long duration. This was not the case in this thesis since duration of tests was only three hours (Chapter 4).

(3) Air trapped at top of cell

Variable amounts of air may be trapped inside the cell, and lead to deviations from the cell calibration curve. This error is minimized by allowing water to run from the air release valve as the cell is filled. Furthermore, the air could be forced into the solution under high cell pressures. This was done in this study by keeping a cell pressure of 1000 kPa overnight for the entire tests.

(4) Movement of ram

During the loading of the specimen water is displaced by movement of the ram into the cell. This correction amounts to the cross-sectional area of the ram multiplied by axial deformation. However, a calibration test was performed and the resulted correlation is displayed in Figure 2.18. This correction was performed in this study. As mentioned earlier, in a test analysis, the measurements of the specimen axial deformation should be corrected first.

2.11 Differential pressure

In a permeability test with the flow-pump method, a constant rate of water flow is maintained through the specimen. The induced pressure head difference is monitored continuously by a differential pressure transducer. The value of hydraulic conductivity can be computed from the differential pressure transducer readings. Correct set up and calibration of this transducer is critical for obtaining high quality results.

The differential pressure transducer used in this study was a variable reluctance pressure transducer (Section 2.6). A diaphragm of magnetically permeable stainless steel was clamped between two blocks of stainless steel. Embedded in each block was an inductance coil. When a pressure difference was applied through the pressure ports, the diaphragm deflected toward the lower pressure. This deflection changed the magnetic reluctance, which was converted to an electrical output signal. As the diaphragm displacement was linear with applied pressure, the output signal was also linear with pressure.

The following section describes issues on mounting, plumbing and calibration of the differential pressure transducer.

2.11.1 Mounting

It is preferred that the transducer is mounted in a way so that its diaphragm is in the vertical plane. This results in zero gravitational deflection of the diaphragm, which is noticeable in low pressure range and most particularly with liquid media. These were both the case in this study and thus the transducer was mounted vertically.

2.11.2 Plumbing

The transducer plumbing should allow transducer removal, if necessary, without shutting down the test in progress. A differential pressure transducer used for measuring pressure difference requires extensive valving not only to place it into operation but also to remove it without overpressure damage. In this case, a valve arrangement shown in Figure 2.19 was used. To safely pressurize the transducer, the drain valve was closed and the bypass valve opened. Then both shutoff valves were opened to apply line pressure to both sides of the transducer. Finally, the bypass valve was closed. To depressurize the transducer, the bypass valve was opened the shutoff valves closed, and the drain valve opened.

2.11.3 Calibration

The transducer should be calibrated with the actual cabling to be used. For calibration, a known source of pressure is required. The transducer is then calibrated for the expected range of pressures. There are several aspects involved in calibrating a differential pressure transducer for use in a triaxial permeability stress path test and are described in the following section.

2.11.3.1 Fast calibration

Depending on the sensitivity of diaphragm used, a limit exists for the maximum pressure difference that can be measured. In the event that the differential pressure has exceeded this limit the transducer must be calibrated again. Therefore, a simple setup was designed for fast calibration of the transducer and is illustrated diagrammatically in Figure 2.20.

Two pipettes were used to provide pressure on each side of the transducer. The bypass valve was opened and the water levels in both pipettes were equalized. This was the zero differential pressure reading. The bypass valve was then closed and the water level in each pipette was raised or lowered in order to create the desired pressure difference on the transducer. The pressure difference on the transducer was calculated from the difference in the height of water in each pipette. This calibration test procedure proved to be fast and accurate.

2.11.3.2 Calibration against back pressure

As shown in Figure 2.9 the differential pressure transducer was connected to the back pressure system. It had been observed that the zero reading of the differential pressure transducer (bypass valve opened) varied with changes in the amount of pressure present in the back pressure system. Thus another calibration test was required to capture this variation during the expected range of changes in the back pressure.

This calibration might not be necessary in a conventional drained compression test, where the back pressure is kept constant during the test. However in the case of stress path testing, in which the back pressure was varied during the test, it was essential that the differential pressure transducer readings be corrected for changes in the back pressure.

2.11.3.3 Pipeline pressure losses

When carrying out a permeability test in a triaxial cell, there are losses of pressure head due to friction and turbulence in the connecting tubing, porous discs and constrictions in valves, tube connectors and cell ports. These losses may be insignificant when the rate of flow is very small, but for higher rates of flow the head losses in the pipework and connections (referred to here as pipeline losses) may be as much as or greater than the pressure difference across the specimen itself (Head 1986).

Oldakowski (1994) performed triaxial permeability tests on oil sand specimens and reported a system pressure loss making up about 40 % of total pressure drop across specimens. These pressure losses must then be taken into account in the permeability calculations.

In order to minimize this problem, provisions were made to measure directly the differential pressure across the specimen. Figure 2.9 illustrates the modifications made to

the bottom pedestal and the top cap to accommodate two additional drainage ports permitting direct measurement of differential pressure. These modifications resulted in a substantial reduction in the pipeline losses. Since porous disks are responsible for a part of pipeline losses it was imperative that a very coarse porous disk be used in the permeability test.

The following procedure was used for determining the pipeline losses in the triaxial cell (Figure 2.21):

(1) top cap was placed on the pedestal with saturated porous discs in place. They were surrounded by a rubber membrane. Flow conditions then corresponded to those during a test without a specimen present.

(2) cell chamber was filled with de-aired water and a cell pressure exceeding the pressure applied to the porous disks was maintained.

(3) a constant flow rate corresponding to the flow rate to be used in the tests was maintained through the system and the differential pressure was recorded.

(4) with the use of flow reversing board, both upward and downward flows were tested.

If a very sensitive diaphragm with a very low pressure range is used in the differential pressure transducer, it will show a time dependent pipeline pressure loss. This is likely due to the accumulation of very small air bubbles in the system. If this proves to be the case, a calibration test for pipeline pressure losses should be conducted for the same duration as the intended triaxial permeability tests. However, it is better to choose an appropriate pressure range for the transducer and reduce the pressure loss by shortening the tubing and using coarse porous disks.

In this study the diaphragm No. 8-26 with a pressure range of up to 3.5 kPa was installed in the differential pressure transducer. The transducer used was a Validyne variable reluctance model DP 103 (Section 2.6).

With this modifications the calibration test was run as specified. The pipeline loss should be measured for both upward and downward flow directions through the system. Figure 2.22 shows the system pressure loss. Although the correction due to pipeline pressure losses were in fact negligible they were applied to the differential pressure transducer readings.

2.12 Automatic triaxial stress path system

Before the start of any test, the calibration relations were entered into LabVIEW program. Initial specimen dimensions, such as height and cross-sectional area were also entered. During the test, the computer continuously monitored all the transducers and using the previously entered calibrations equations, produced the stress-strain data. It calculated the axial and volumetric strain and modified the specimen cross-sectional area accordingly (Equation 2.3). The produced stress-strain data were displayed on the screen

every second and were incorporated in the stress path program. They included the effective axial stress σ'_a and the effective confining pressure σ'_r.

Deviatoric stress, q, and mean effective stress, p' were then calculated by the program using the following equations:

$$q = \sigma_a - \sigma_r \qquad\qquad [2.8]$$

$$p' = \left(\frac{\sigma'_a + 2\sigma'_r}{3}\right) \qquad\qquad [2.9]$$

In this study stress path was defined in the q and p' stress space. A stress path thus could be described as q being a function of variable p'.

As mentioned earlier any stress path could be achieved by controlled application of three pressures:

(1) cell pressure,
(2) lower chamber pressure acting on the ram and
(3) back pressure.

The materials tested in this study were dense sand, which had to be brought to saturation. Since back pressure was used as means of saturating the specimens, a back pressure of at least 500 kPa had to be applied during the test. On the other hand the maximum permissible pressure on the Perspex cylinder of the triaxial cell was 1000 kPa. This corresponded to a confining pressure of the same value in terms of total stress. Therefore it was decided that the maximum total confining stress of 1000 kPa was applied and kept constant during all tests. The desired stress path would then be achieved by manipulation of the back pressure.

Figure 2.23 illustrates the scheme of the automatic stress path testing used in this study. An equation representing the desired stress path, correlating deviatoric stress q to mean effective stress p' was entered into the program before the test. The specimen was then brought to the desired initial condition (point p'_o). The shearing started in the strain controlled mode by using the second syringe pump to provide a constant flow rate to the bottom pressure chamber (Figure 2.9).

If the computer did not change the back pressure, the test would be a conventional triaxial drained test, which has stress path of a straight line with the slope of 3 to 1 (Figure 2.23). However in the stress path testing the computer constantly monitored the values of q plus p' and calculated the required adjustment to the back pressure, Δu. This adjustment of back pressure was then automatically implemented instantly and the desired stress path was obtained. This automated stress path testing system worked very well and the results of stress path tests obtained with this system are presented in Chapter 6.

With the full control over these three pressure system, any other scheme of implementing stress paths was possible. In fact any desired stress path in the stress space lying within the section of space bounded by failure in axial compression and failure in axial extension could be followed.

2.13 Summary

- A versatile hydraulically operated triaxial apparatus was developed for stress path and permeability testing. The apparatus was described and its range and performance was discussed.

- The apparatus can be used with any pressure control system. Compressed air-water systems were used for the pressure systems. Electric solenoid valves controlled by a computer adjusted the desired pressure in the compressed air. LabVIEW software was used to create the data-logging and pressure control computer program.

- The triaxial permeability test set up used, was discussed and explained. Issues of calibration of equipment and necessary corrections for obtaining proper stress-strain values were explained.

- The scheme of automatic stress path testing system was presented. The computer took an almost continuous reading from all transducers. By continuous updating of the stress-strain values the program kept track of the actual stress path. In order to implement a desired stress path, the required pressures in the pressure systems were calculated. The computer monitored the pressure systems and adjusted them, if necessary, sending commands to the solenoid valves.

Table 2.1 Specifications of the stress path triaxial apparatus model WF 12400

Parameter	Value
Specimen diameter (mm)	38
Maximum cell pressure σ_r (kPa)	1000
Minimum cell pressure σ_r (kPa)	0
Maximum lower chamber pressure p (kPa)	2070
Minimum lower chamber pressure p (kPa)	0
Maximum axial load (kN)	6
Effective area of the Bellofram seal a (cm^2)	29.225
Cross sectional area of specimen A_o (cm^2)	11.341
Weight of loading ram W (g)	See Figure 2.3
Frictional force f (kN)	6.635 x 10^{-3}
Maximum ram travel (mm)	25

Axial screw adjustment

Displacement transducer

Dial gauge

Load cell

Perspex cylinder

Specimen

Rods to activate dial gauge and displacement transducer for axial strain measurements

Cell chamber

Cell pressure

Bellofram seal

Hollow ram linking Bellofram pistons

Linear motion bearing

Crosshead for displacement measurement

Drainage /
Pore pressure /
Back pressure

Bellofram seal

Bottom chamber

Loading pressure

Figure 2.1 Schematic layout of Bishop-Wesley Stress Path Triaxial Cell
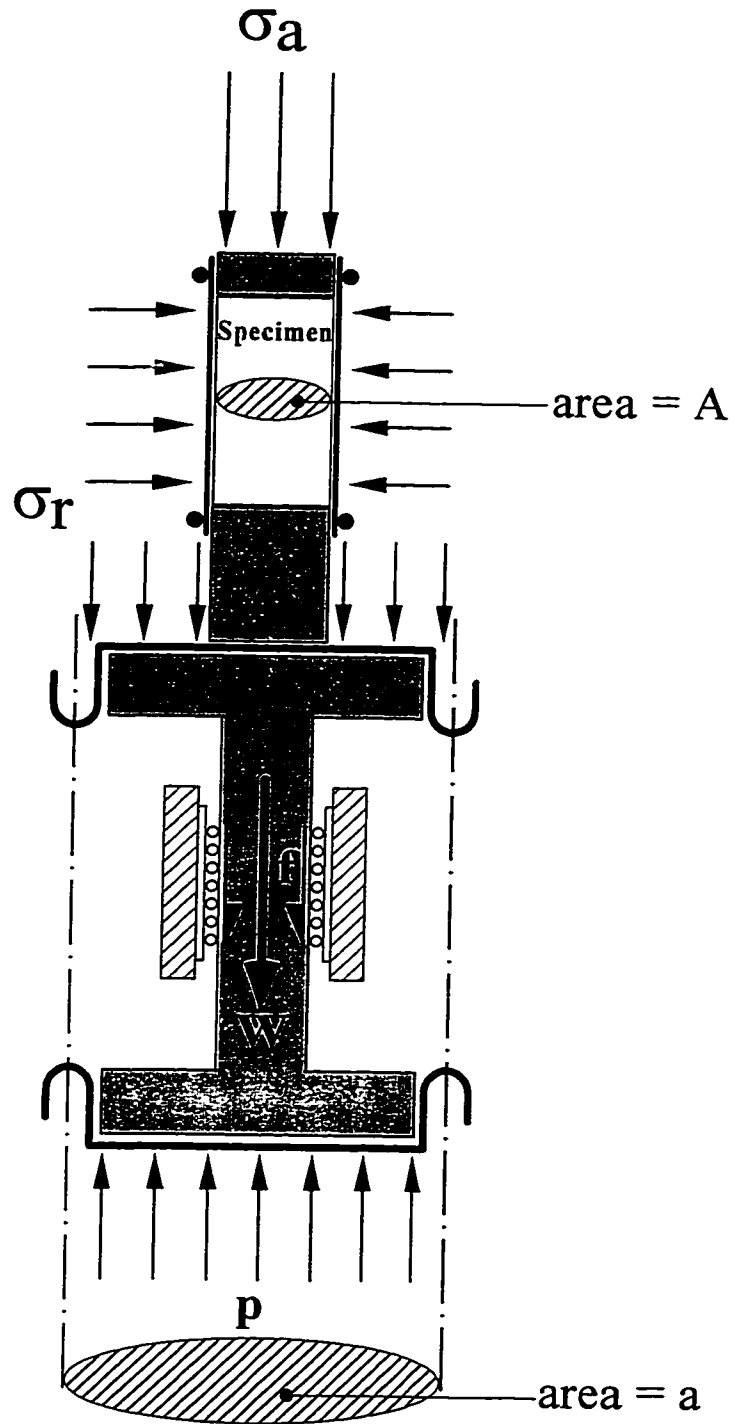
Figure 2.2 Pressures and forces on loading ram and specimen
(Bishop-Wesley triaxial cell)
(Modified from Head 1986)

Top cap (273.4 g)

Specimen (75 g)

Bottom pedestal (116 g)

Pedestal seat (661.3 g)

Displacement rods (623 g)

2 Bellofram seals (12 g)

Frictional force (6.635 N)

Loading ram (2547.3 g)
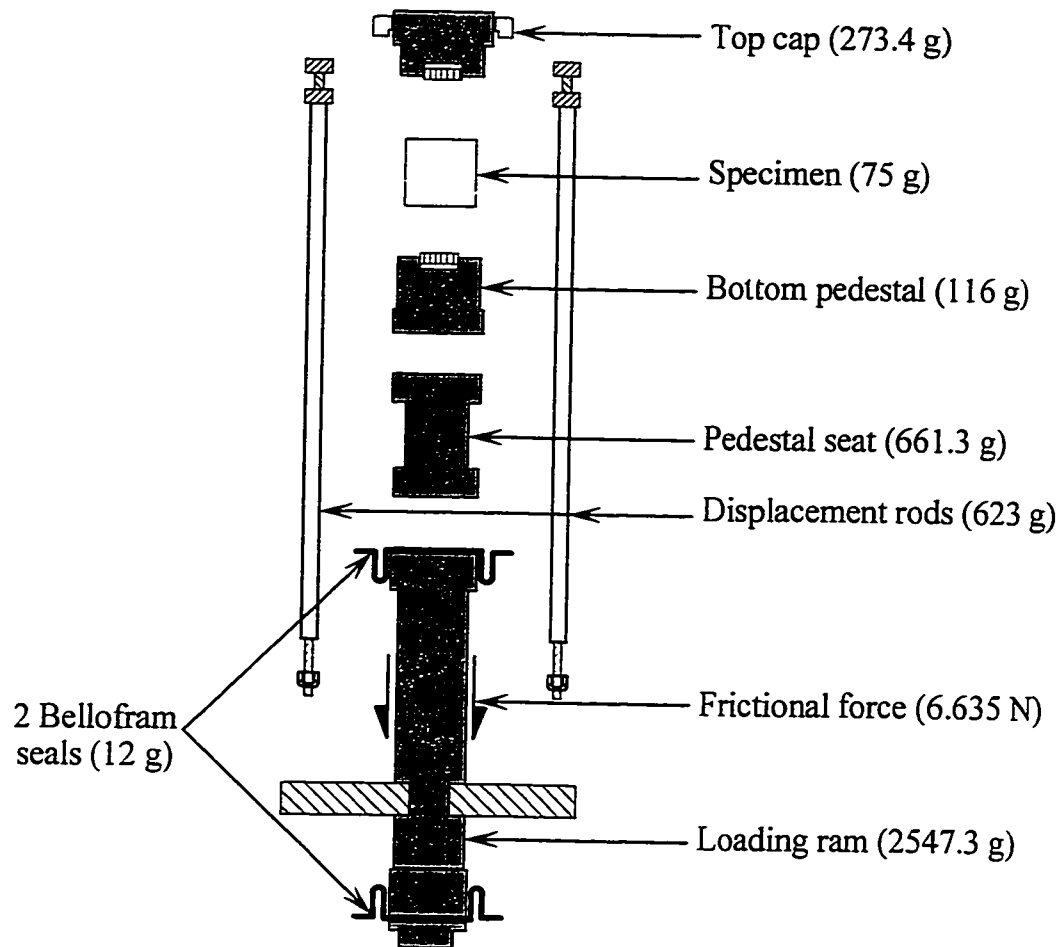
**Figure 2.3 Weight of different components of loading ram
in Bishop-Wesley stress path cell**
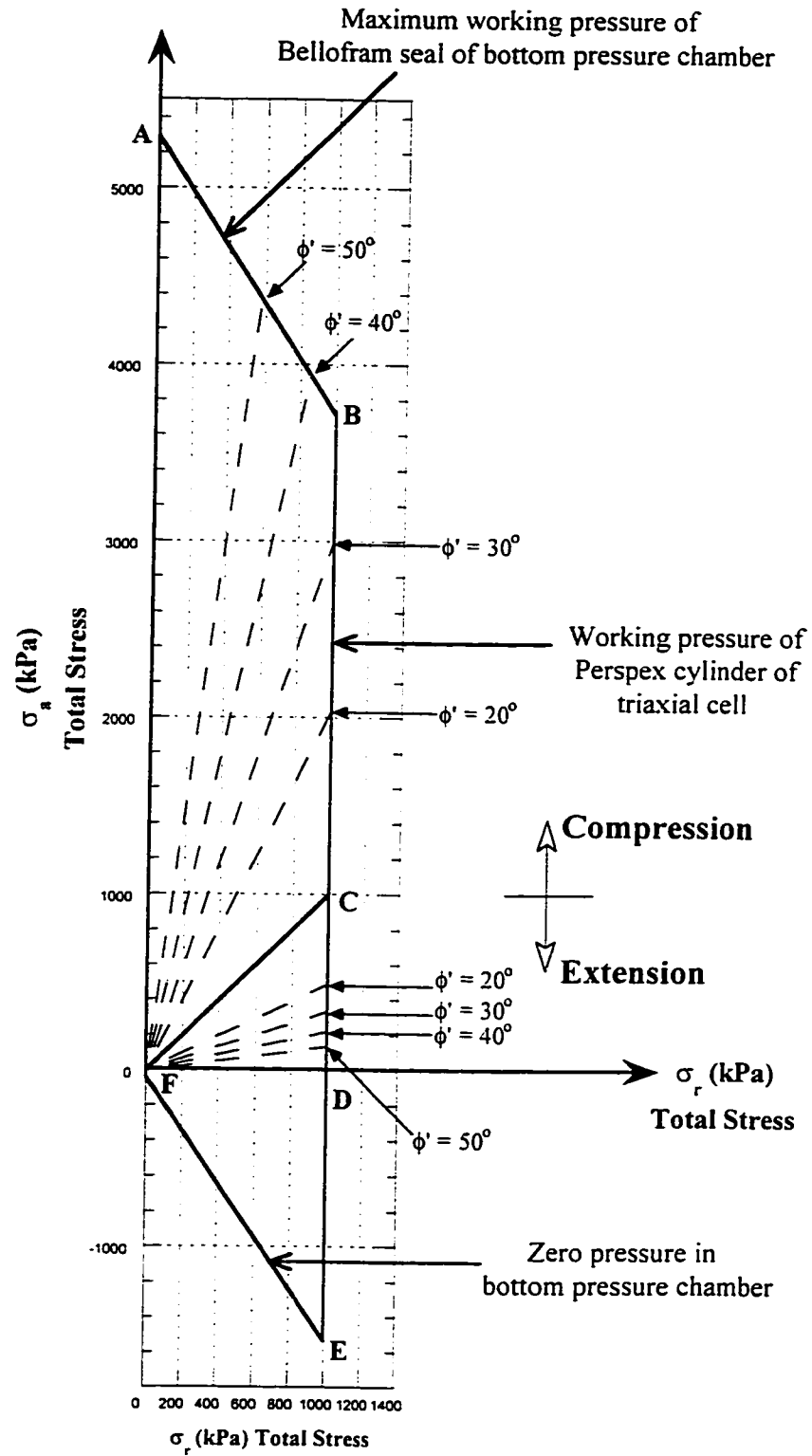
Figure 2.4 Stress limits for Bishop-Wesley stress path triaxial cell
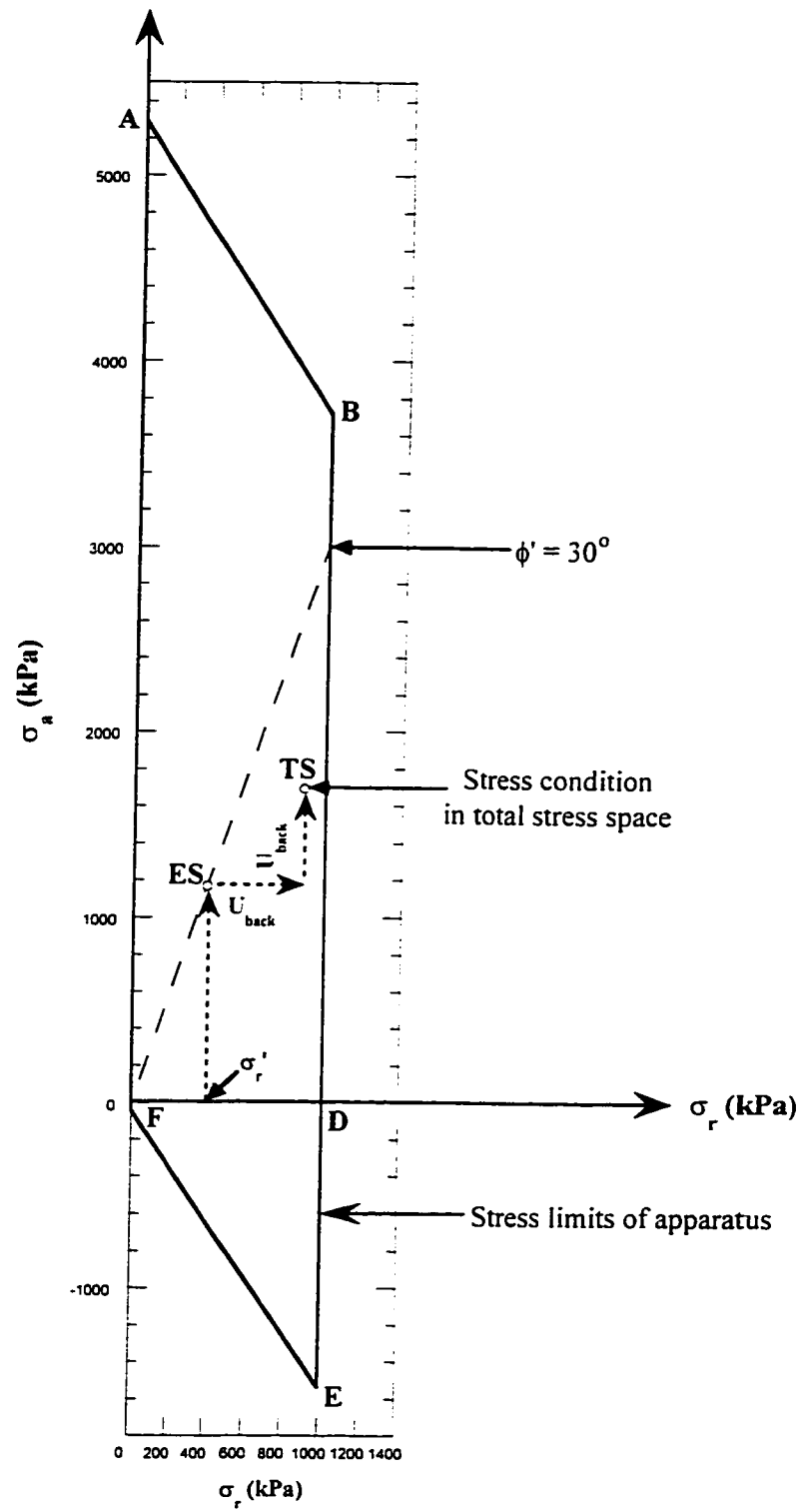
Figure 2.5 Effect of back pressure on stress condition in total stress space

Load cell

Hinge connection

Load frame

Bishop-Wesley
triaxial cell

Load frame ram going down

Load frame ram going up
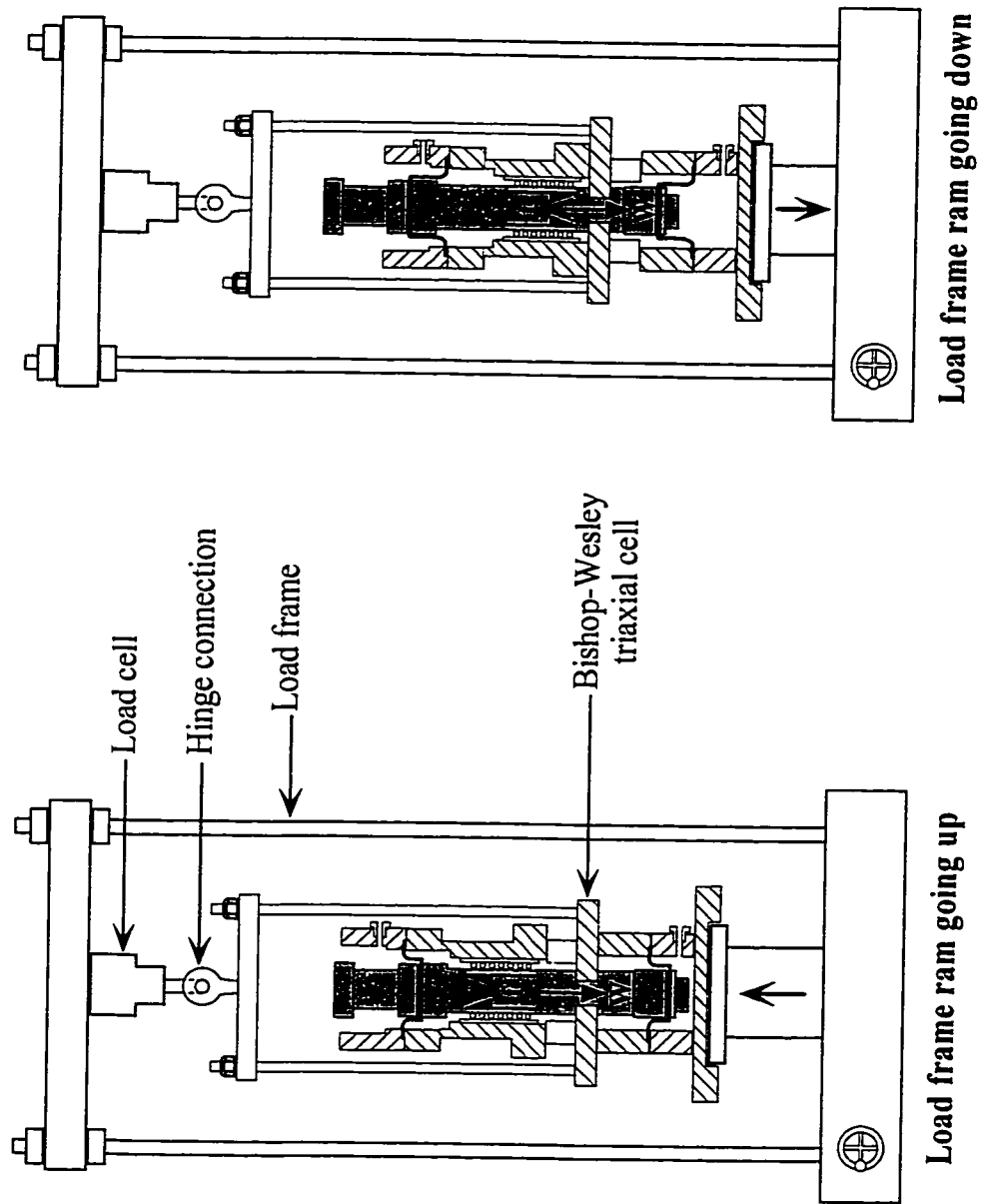
Figure 2.6 Layout of calibration test to obtain the frictional force in loading ram
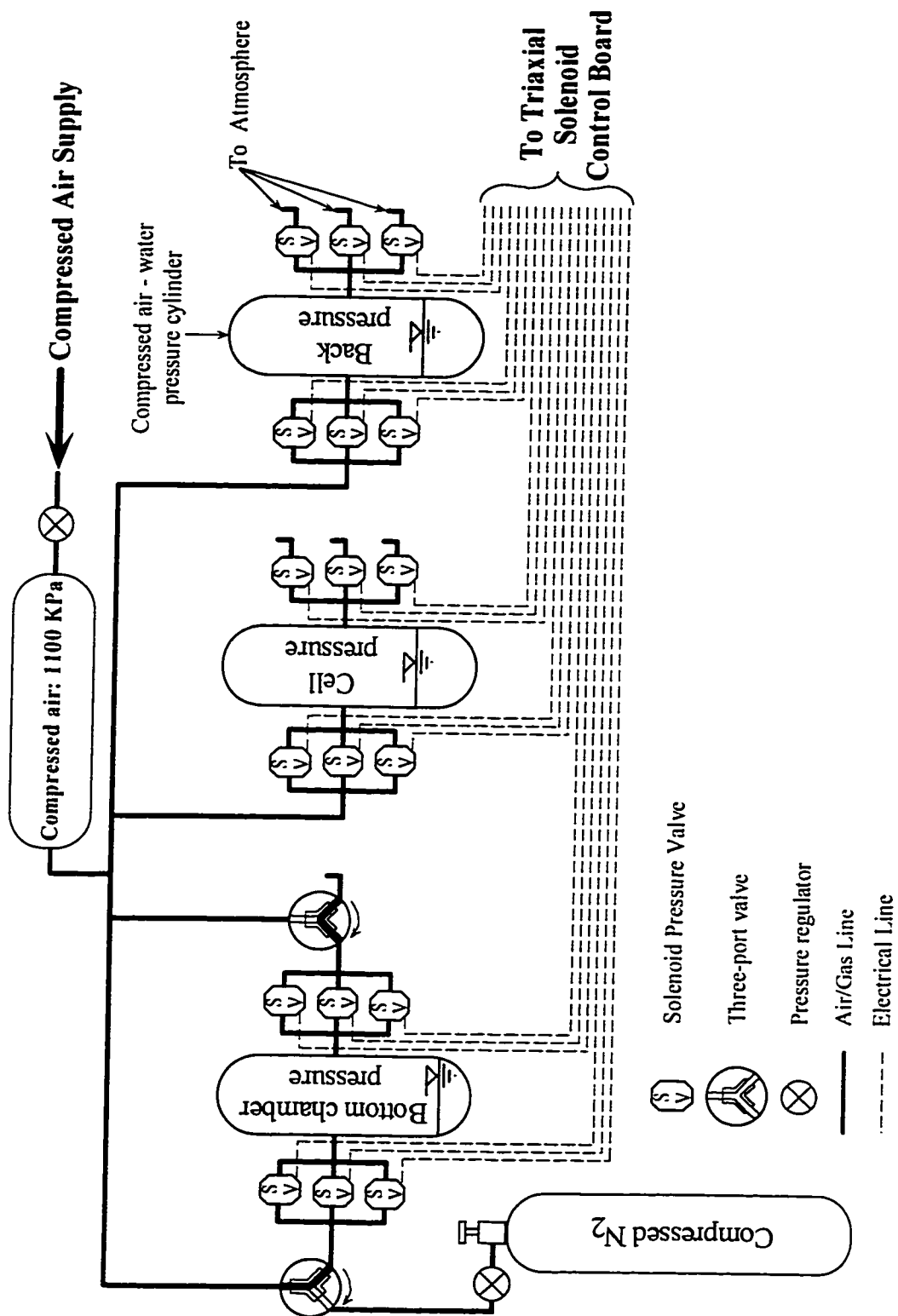
Figure 2.7 Scheme of the experimental equipment

Flow ⟶   Flow ⟶

De-energized   Energized
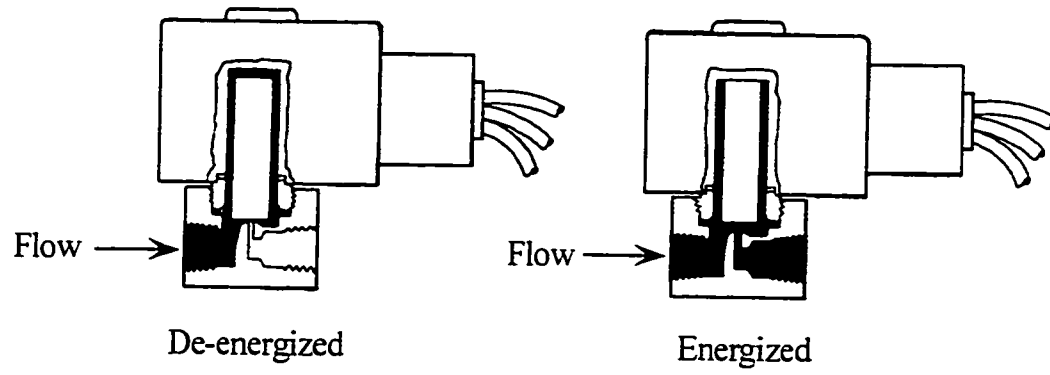
Figure 2.8 Two way direct acting solenoid valve
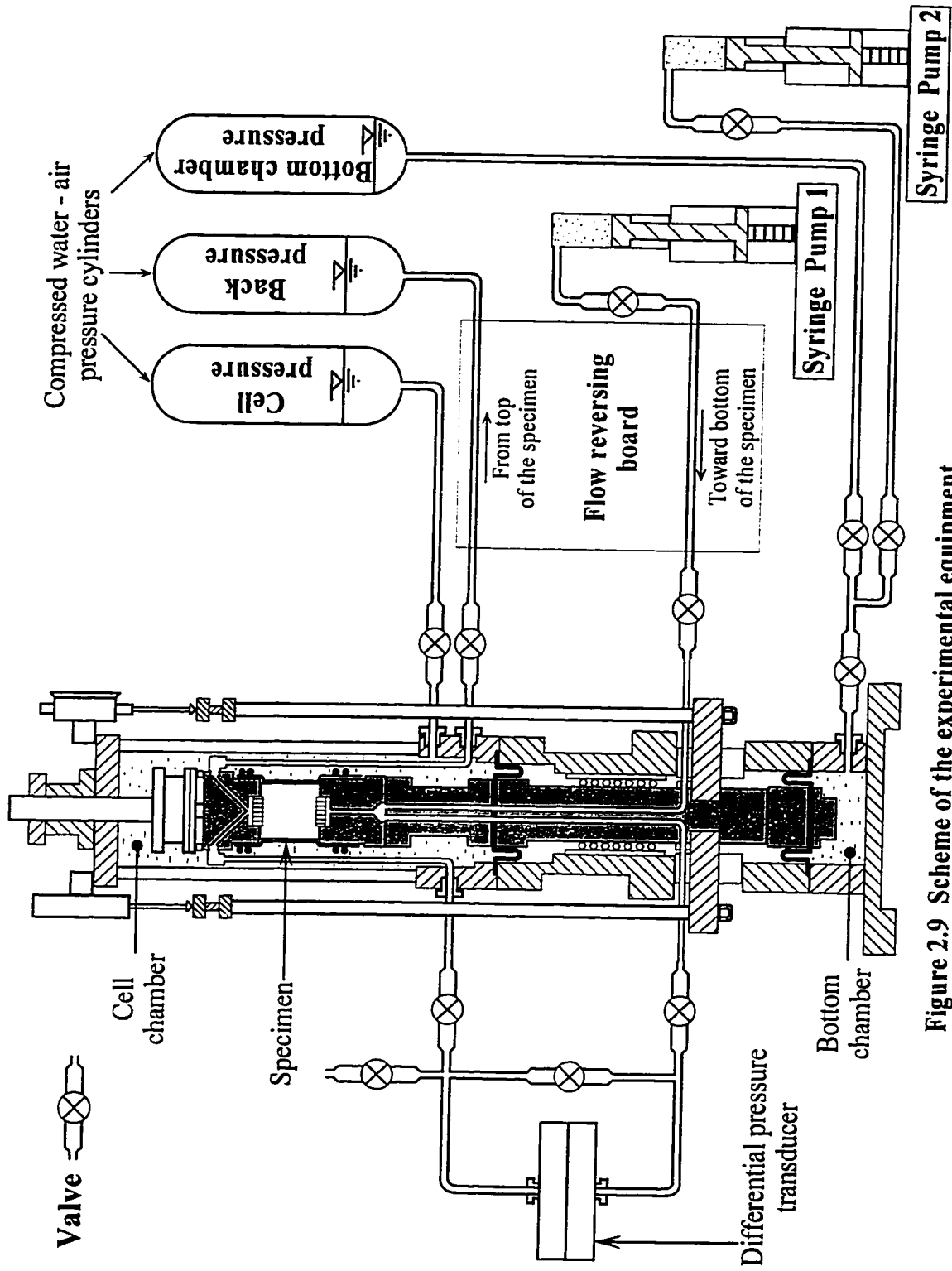
Figure 2.9 Scheme of the experimental equipment
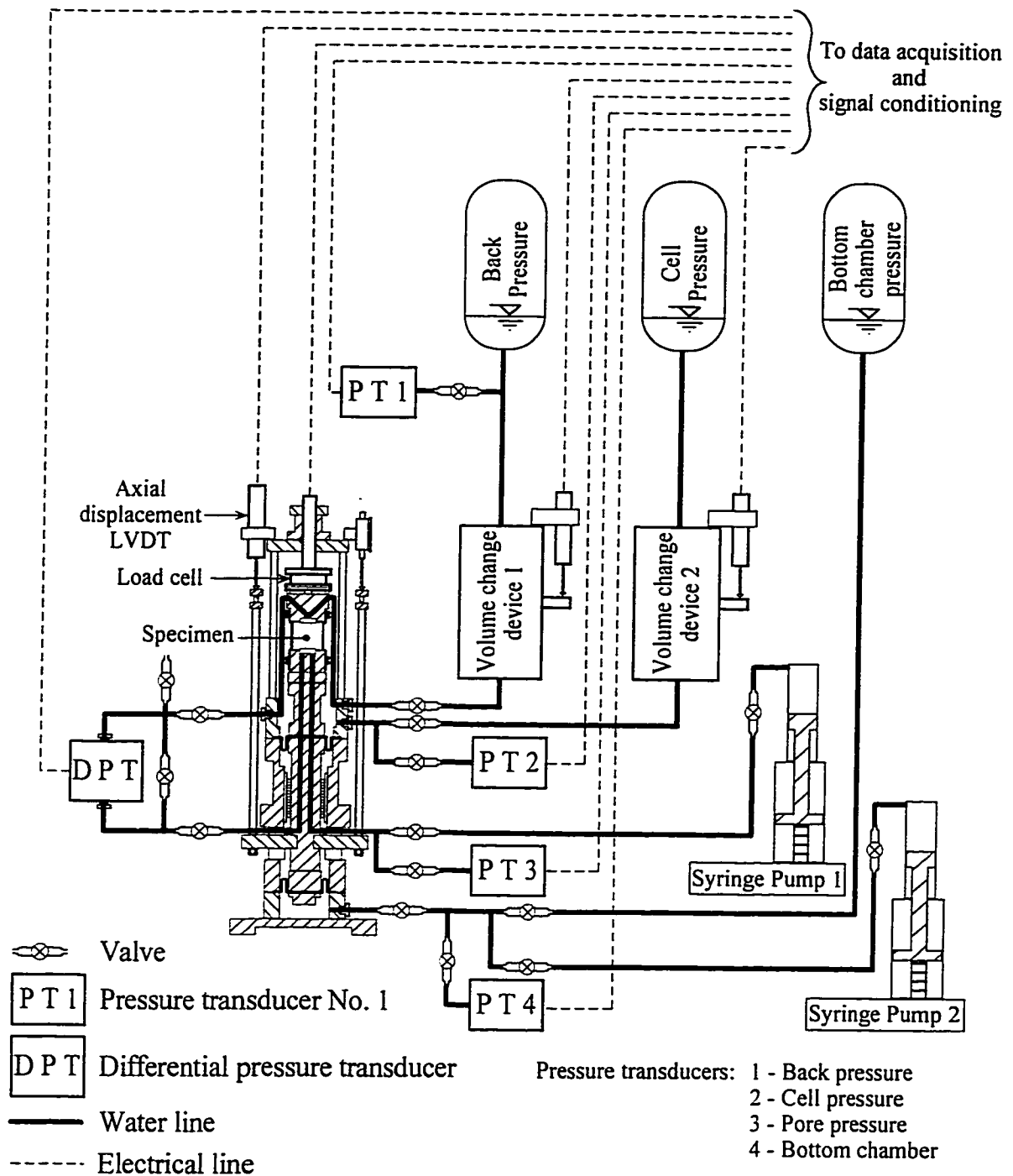
Figure 2.10 Lay out of measurement devices

49

Triaxial solenoid control board

Solenoid Controller

Signal Conditioner

Excitation
Balancing
Amplifying
Digital display

I / O

ANALOG

Computer

Macintosh IIsi

NB-MIO 16
(Multifunction analog, digital and timing I/O board)

To solenoid pressure valves

System's output signals:

- Bottom chamber pressure transducer
- Cell pressure transducer
- Back pressure transducer
- Load cell transducer
- Differential pressure transducer
- Pore pressure transducer
- Axial displacement LVDT
- Volume change device 1 (LVDT)
- Volume change device 2 (LVDT)

Figure 2.11 Schematic representation of data processing and control system
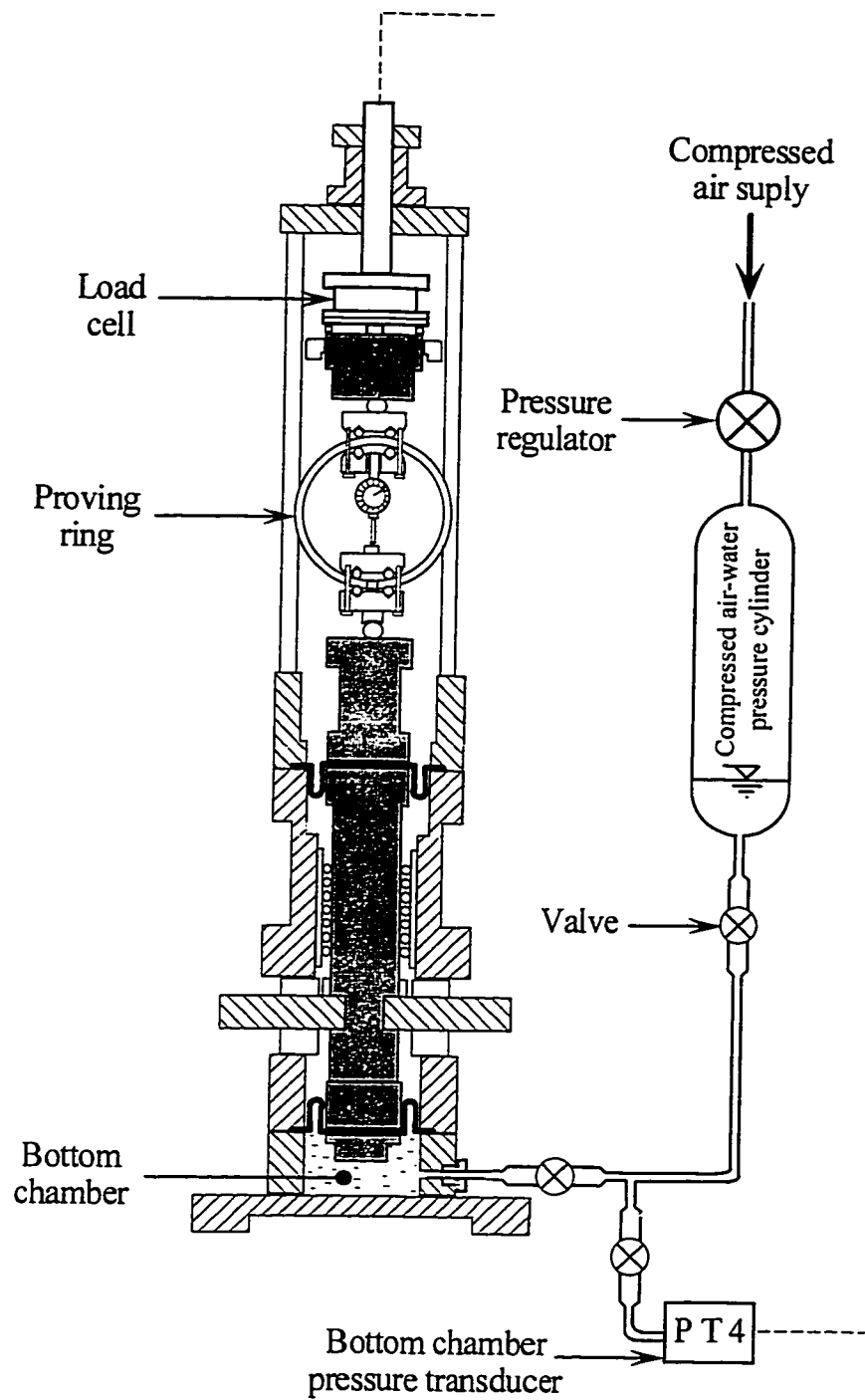
Figure 2.12 Measurement of axial load through bottom pressure chamber transducer
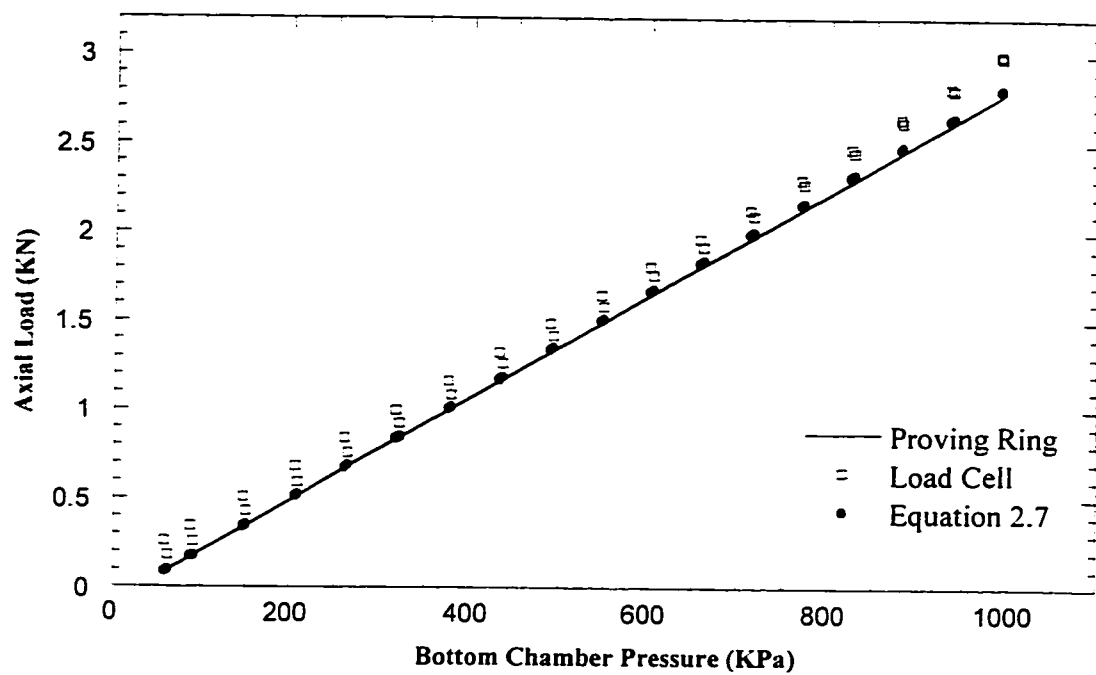
Figure 2.13 Axial load obtained from load cell and bottom chamber pressure transducer

Screw adjustment

Load cell
Metal screws
Guide rod

Guide shaft
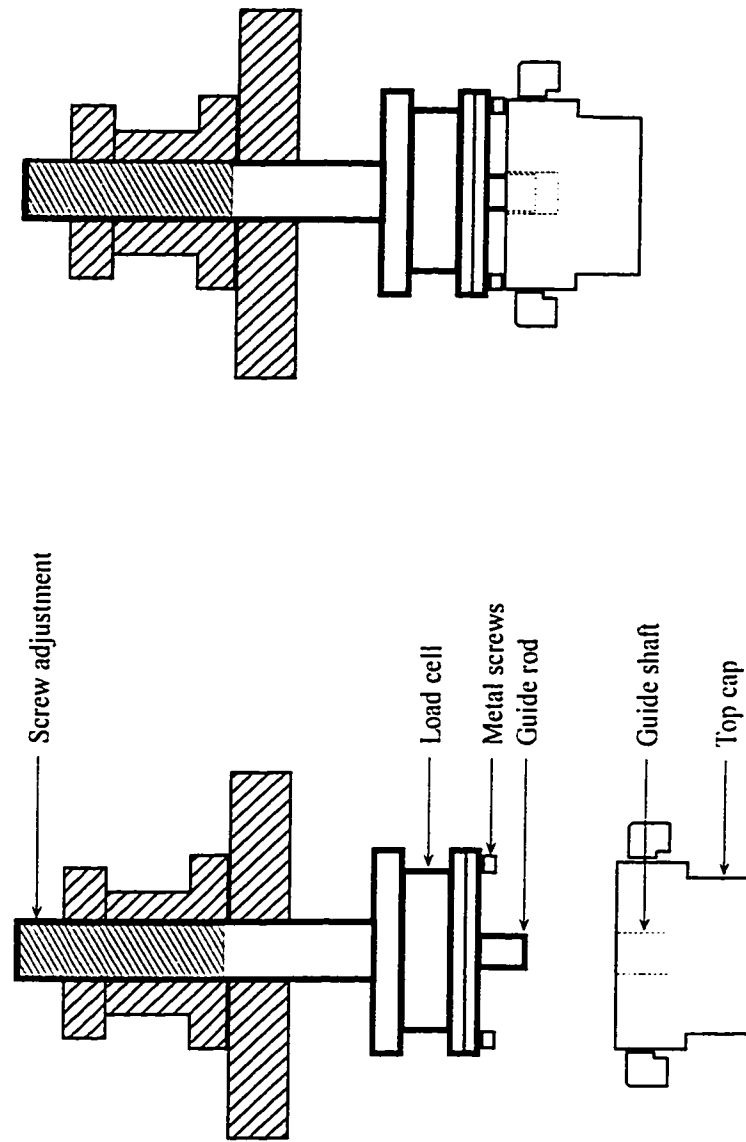
Top cap

Figure 2.14 Fixed top cap design used in the triaxial apparatus
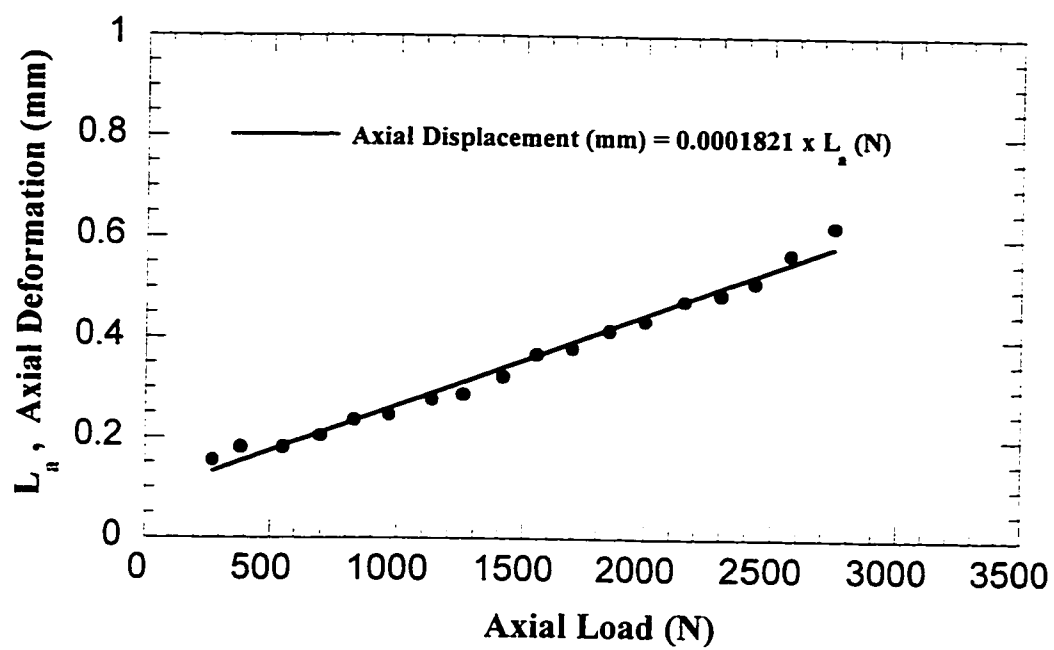
Figure 2.15 Correction for axial deformation of lubricated platens
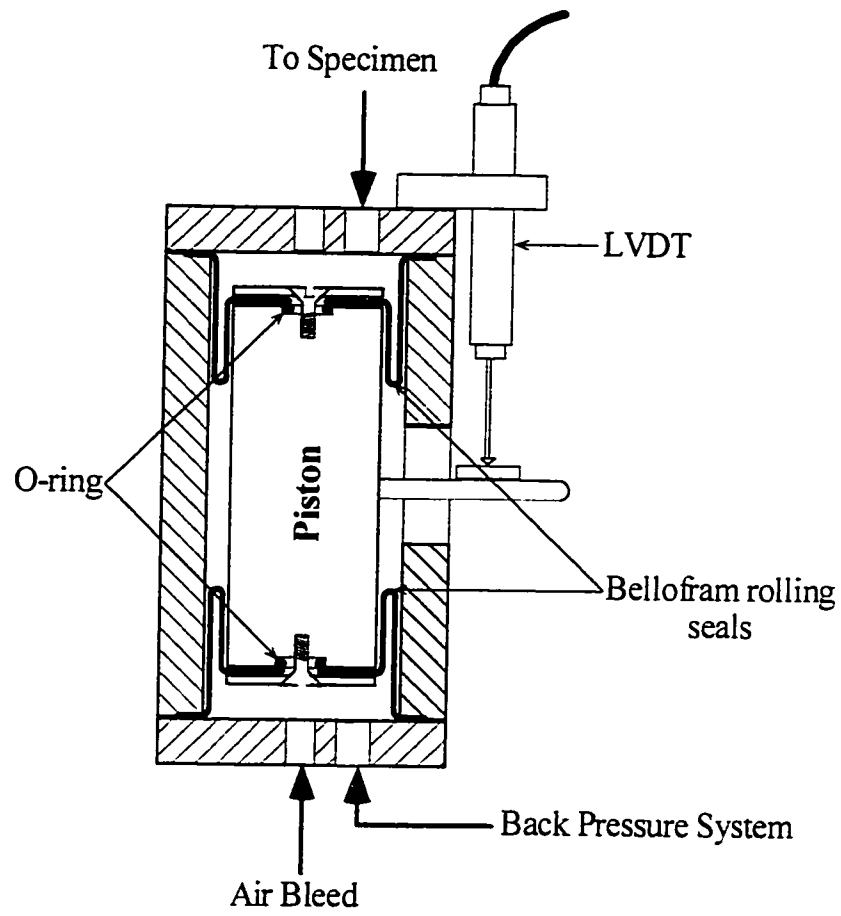
Figure 2.16 Volume change measurement device

(Modified from Head 1986)
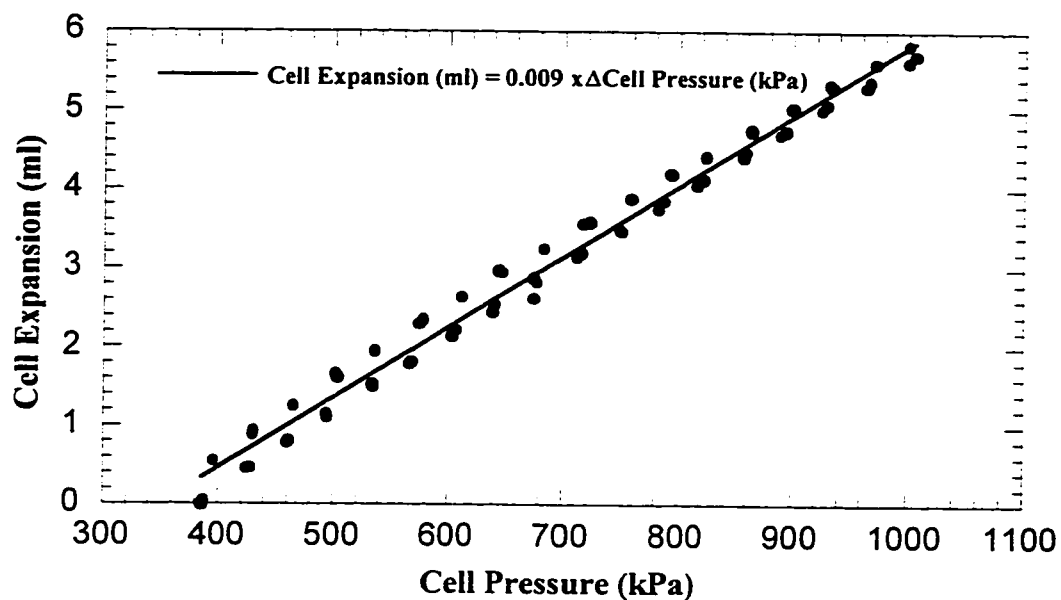
Figure 2.17 Expansion of cell due to pressure increase
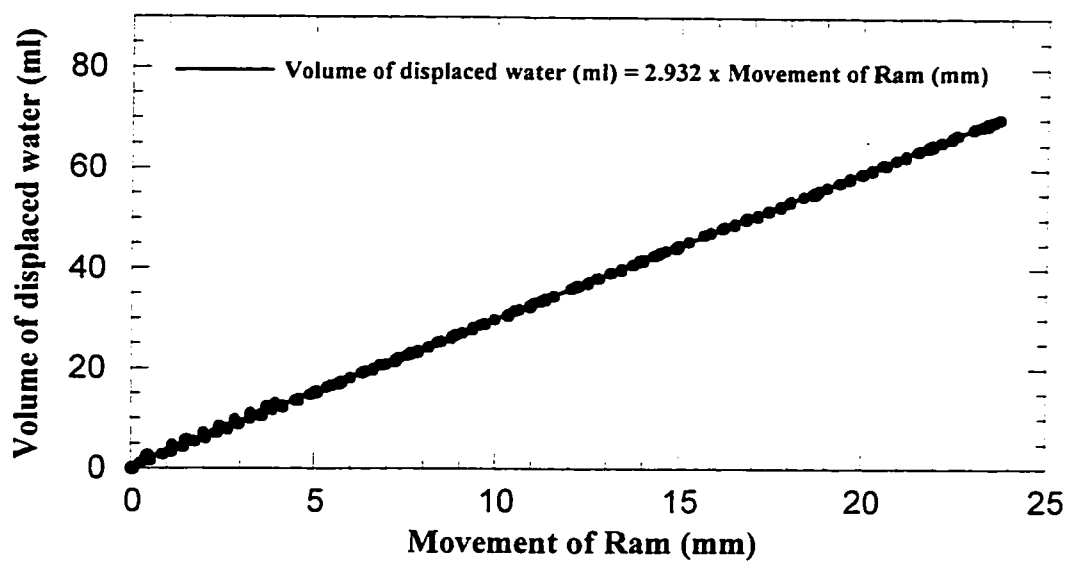
Figure 2.18 Displaced water due to the movement of the ram into the cell
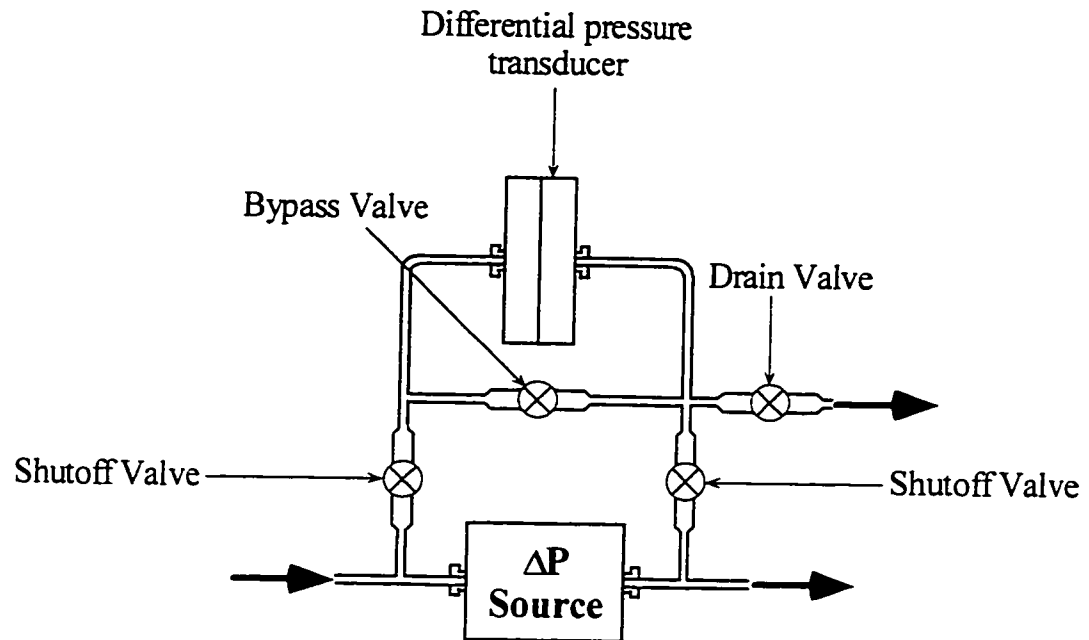
Figure 2.19 Typical valve arrangement of differential pressure transducer for measurement of pressure difference ΔP
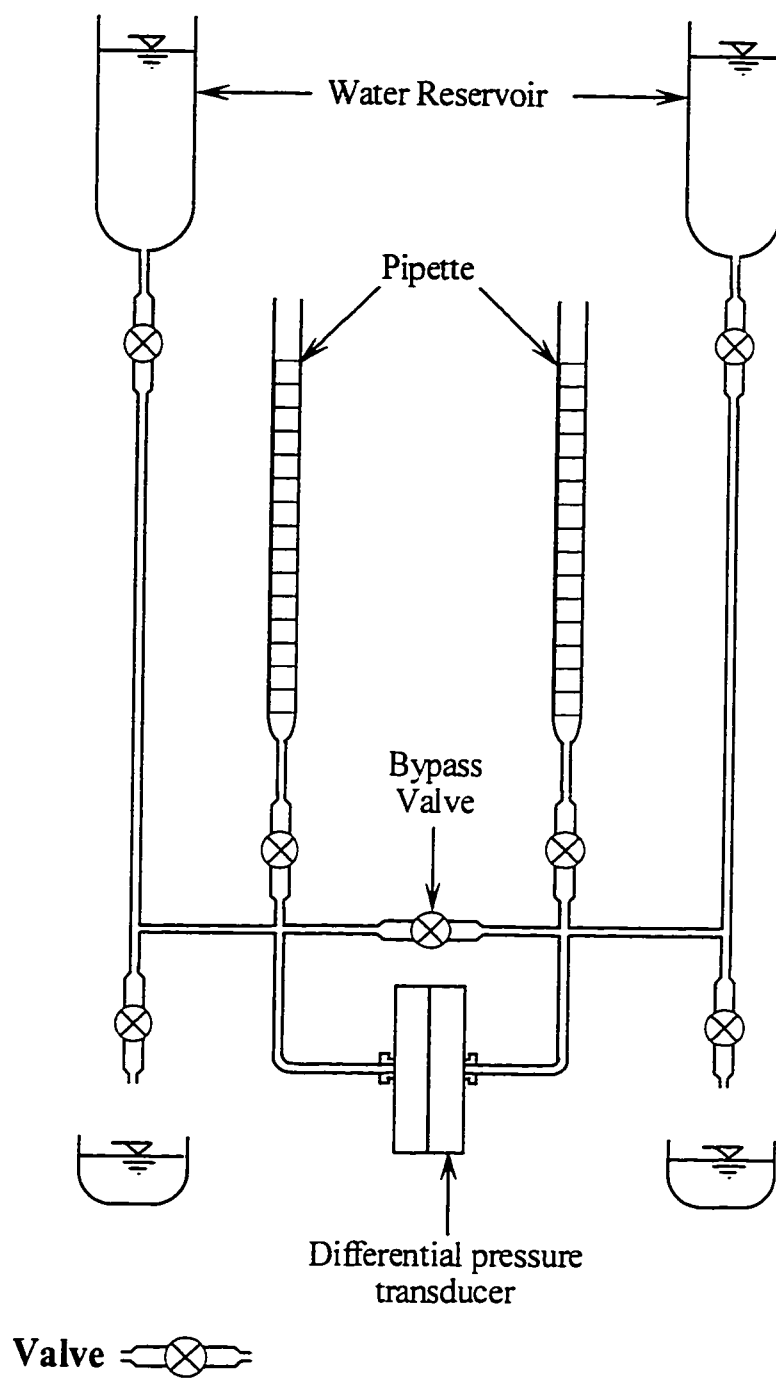
Figure 2.20 Calibration of differential pressure transducer

Porous Discs

Cell pressure

Back pressure

Flow reversing board

Differential pressure transducer

Valve

Syringe Pump
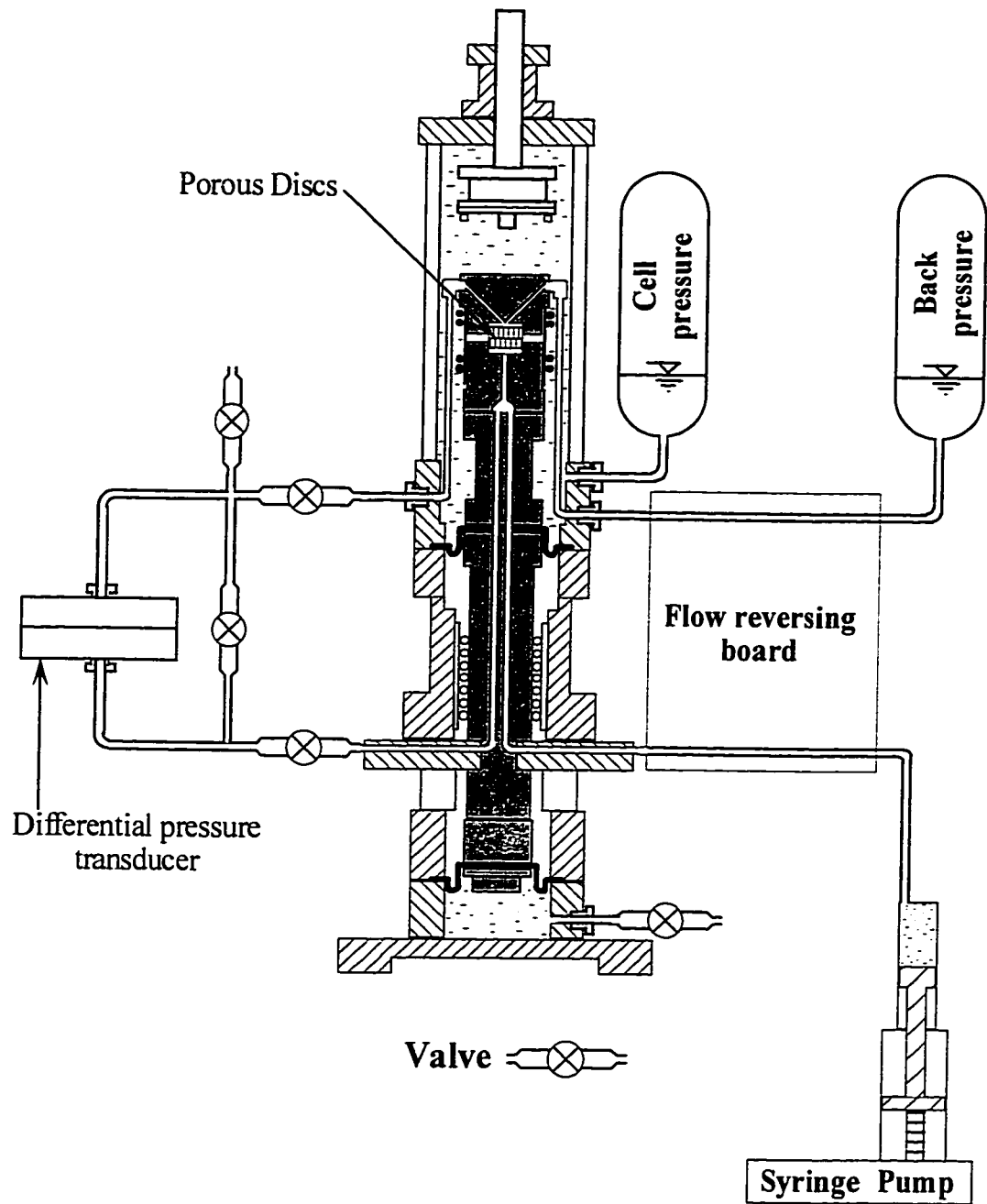
Figure 2.21 Measurement of pipeline loss in the triaxial cell
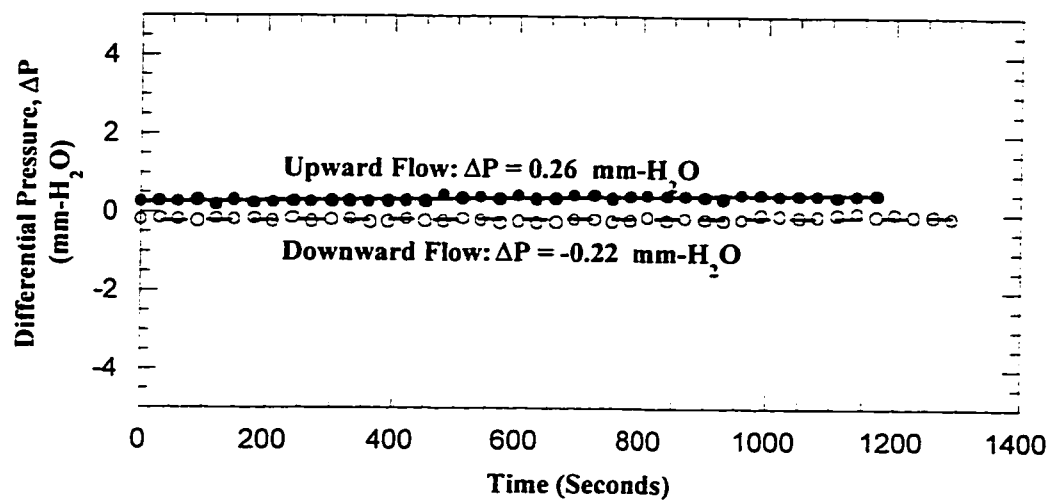
Figure 2.22 Pipeline pressure loss
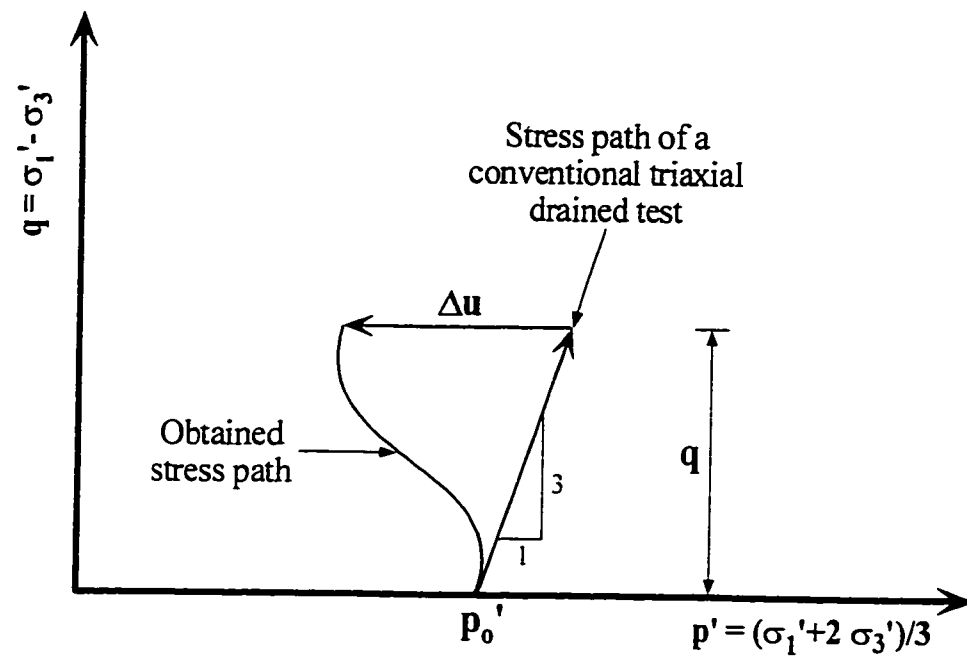
Figure 2.23 Implementation of stress path with changes in pore pressure

(p_o' is the initial effective confining pressure)

CHAPTER 3   PERMEABILITY TESTING OF SAND DURING A TRIAXIAL SHEAR TEST[1]

3.1 Introduction

Hydraulic conductivity or coefficient of permeability, k, is defined as the discharge velocity through an unit area under an unit hydraulic gradient. The hydraulic conductivity of soil and rock specimens can be determined by any controlled test in which the cross-sectional area, the hydraulic gradient, and the quantity of flow are known.

In this study the hydraulic conductivity of McMurray Formation oil sand, was measured and monitored when it was experiencing changes in stress and strain.

The most common type of equipment used in the study of stress-strain and other characteristics of soils is the triaxial test apparatus. The triaxial test equipment provides facilities for maintaining a flow of water through a specimen, while it is subjected to a known effective stress state. Repeat or continuous tests after achieving a number of effective stress conditions can be carried out on the same specimen without having to remove and re-set it. Some of the advantages of measuring permeability in a triaxial cell are (Head 1986):

(1) The specimen can be first saturated under the application of a back pressure, thus reducing or eliminating obstructions to flow due to bubbles of gas.

(2) Saturation by back pressure can be used, and is achieved much quicker than saturation by prolonged flooding or circulation only.

(3) The test can be carried out under effective stresses and at pore pressures, which relate to the field conditions.

(4) Undisturbed test specimens can be set up easily, and there are no cell wall effects which might give nonuniform flow conditions, and

(5) Changes in permeability of a specimen undergoing triaxial shear can be monitored.

3.2 Conventional technique

The conventional laboratory technique for determining the permeability of saturated soils consists essentially of (Olsen 1966):

(1) Placing a soil specimen in a triaxial cell connected in series with a volume measurement device.

(2) Producing flow through the soil with a known hydraulic head difference across the specimen, and

(3) Determining the induced flow rate from measurements of the volume measurement device.

The hydraulic conductivity, k, is calculated from the applied head difference, ΔH, the induced flow rate, q, the length, L, and cross-sectional area, A, of the specimen using Darcy's law:

$$q = k i A \qquad [3.1]$$

where, i, the hydraulic gradient, equals $\Delta H/L$.

The principal difficulties with this technique arise from the long times and/or high gradients required to obtain measurable flow rates. When permeability is determined using low applied gradients, longer periods of time are often required to measure the flow rate. Such measurement is not only time consuming, careful precautions must be taken to correct them for volume changes in the specimen. Furthermore the initial transient response of the specimen that precedes the steady state condition can not be detected. This introduces an error in permeability measurements.

3.3 Flow-pump method

Approaches for minimizing and avoiding these difficulties with conventional methods were developed in research studies about three decades ago (Olsen 1966). The flow-pump method was introduced with the use of a multispeed flow-pump to maintain a constant flow rate of water entering or leaving the specimen while the head difference induced thereby was measured with a sensitive differential pressure transducer (Olsen 1966 and Olsen et al. 1985).

Figure 3.1 illustrates this technique used in a triaxial apparatus. This approach provides three advantages over the constant head method. First, it avoids direct flow rate measurements and the experimental errors associated therewith. Second, it enables permeability measurements to be conducted much more rapidly and at substantially smaller gradients. Third, the process of steady state hydraulic flow through a specimen could be distinguished from the initial transient response. The second advantage arises because long time periods and/or high gradients are not needed to produce measurable flow rates, and also because transducers allow pressures to be measured with a high

degree of resolution and accuracy. A unique capability of the flow-pump method is that the head difference induced by an externally imposed constant flow rate can be monitored and recorded continuously with time in terms of the electrical output of the differential pressure transducer.

3.4 Importance of lubricated ends in triaxial permeability testing of dense sand

One objective of a triaxial permeability test is to investigate the changes in the permeability of a specimen while it is being sheared. Accordingly it is advantageous to monitor the changes in the specimen porosity, a major factor influencing the permeability. Porosity is calculated from measured volume changes of the specimen assuming it is undergoing uniform deformation. Thus it is highly desirable that the measurements of the specimen volume change represent the entire specimen rather than one specific zone. It is then critical to implement a test set up that will lead to a uniform stress and deformation condition on the triaxial specimen. It is accepted that use of lubricated end platens will achieve this.

3.4.1 Non-uniform deformation of the triaxial specimen

One of the main criticisms of the triaxial test with conventional end platens is the non-uniformity of stress and deformation at all but extremely small strains. At large strains, nonuniformity of deformation of the specimen is the source of numerous major errors. There are two main causes of this non-uniformity:

(1) Frictional restraint at the specimen ends which causes the formation of dead zones adjacent to the platens (Figure 3.2). This leads to both the barreling effects and the concentration of dilation in local zones, which in turn results in the premature development of a failure surface.

(2) The tendency to localized failure surfaces, particularly in dense, brittle or fissured material, associated with a nonuniform soil state.

In conventional drained tests (permeability tests), failure is localized either to a central zone or to a narrow failure surface and the measured volume change does not refer to the total volume of the specimen (Rowe and Barden 1964). Tests rarely can be continued sufficiently past the peak to reach the critical void ratio state, as the development of a predominant failure surface usually causes premature collapse. Errors due to end restraint are of greatest significance in specimens that tend to dilate, such as dense or stiff soils tested at low effective confining pressures (Head 1986). This is in fact the case with oil sand specimens.

An indication of the shear stress developed in a normal triaxial test specimen of a height/diameter ratio of 2 with conventional (fixed or restraint) end platens, is shown in Figure 3.3 (Lee 1978). The shearing stress contours pertain to an effective principal

stress ratio of $\sigma'_1 / \sigma'_3 = 4$, which might be associated with failure in many soils. Note that if the end platens of the specimen were truly frictionless, they would support no horizontal shear stress, and shear stress would be equal to zero throughout the entire specimen, as is the approximate case throughout the middle third. The existence of the nonzero shear stresses produces the observable effects of end restraint. In the absence of shear stresses at the end, the specimen deforms as a uniform cylinder with uniform stress conditions throughout the specimen (Raju et al. 1972).

The restraining effects at the end platens can be reduced considerably by a simple method described by Rowe and Barden (1964). The use of lubricated end platens appreciably reduces the above mentioned sources of error (Head 1986).

3.4.2 Modes of failure

Two basically different types of failure can occur in triaxial specimens of sand (Lade 1982):

(1) Under conditions of uniform stress and strain, zone failure occurs. In this type of failure multiple failure planes traverse the specimen at angles of $\pm (45 + \phi'/2)$ degrees to the σ'_3 direction, as shown in Figure 3.4.

(2) Under conditions of nonuniform strain, line failure can occur. In this type of failure two practically solid bodies slide past each other along a single failure plane, which is oriented at $(45 + \phi'/2)$ degrees to the σ'_3 direction (Figure 3.4).

Which type of failure will develop in a given case depends on three factors:

(1) Uniformity of density

Non-uniformity in the density of a test specimen promotes development of line failures. Loose zones constitute zones of weakness, and the sand in these zones will fail at smaller stresses than required to cause failure in the more dense parts of the specimen. After a failure plane has developed which completely transects the specimen, it can fail by line failure even though the strength of the sand in the more dense parts of the specimen is not fully mobilized.

(2) Tendency to dilate or compress

A tendency to dilate during shear aggravates initial nonuniformity of density and makes line failure more likely. This is so because, having dilated, the sand is less dense and therefore weaker than it was in the beginning. Thus once a line failure begins in a dilating sand, the sand in the failure plane becomes progressively looser and weaker than the rest of the specimen. The stronger the tendency to dilate the more pronounced is this effect. A tendency to compress during shear has the opposite effect.

(3) Boundary conditions

Regardless of the uniformity of density of the specimen and the changes in density resulting from dilation, zone failure will occur if the boundary conditions enforce uniform strains throughout the specimen.

The best boundaries for enforcing uniform strains are stiff, lubricated, flat surfaces. Such boundaries reduce friction greatly, with the result that the stresses are essentially uniform. They also prevent development of line failure provided the potential planes of sliding are oriented such that they would have to intersect the boundary. In triaxial compression tests with uniform stress conditions the failure plane is oriented at $(45 + \phi'/2)$ degrees to the planes of the cap and base, and transcends a length of $D \tan (45 + \phi'/2)$ as shown in Figure 3.5a. If the length of the specimen is equal to or greater than the length transcended by the failure plane, line failure can occur. If the specimen is short, with $L = D$, only zone failure can occur, as shown in Figure 3.5b.

3.4.3 Effects of end kinematic conditions

Goto and Tatsuoka (1988) considered the effects of two different end kinematic conditions:

(1) Rotation of cap

Because of the cap rotation, concentration of deformation occurs more easily, resulting in easier formation of single shear band. It is apparent that specimen deformation becomes less uniform as a result of cap rotation.

(2) Free horizontal movement of cap

Horizontal movement of the specimen end induces the non-uniform stress distribution because of the noncoaxiality between the loading piston and the specimen.

Goto and Tatsuoka (1988) suggested that for lubricated ends a fixed cap should be used.

3.5 Lubricated ends

Rowe and Barden (1964) developed lubricated enlarged end platens to minimize the effects of end restraint (Figure 3.6). The lubricated ends system now generally used consists of polished metal platens (aluminum or stainless steel) and a disc of rubber membrane material, separated by a film of high vacuum silicone grease as a lubricant. Several alternate layers of membrane and grease can be used. In a modified arrangement a small central porous disc, for drainage and/or pore pressure measurement, projects through a hole in the polished platen and penetrates slightly into the specimen (Figure 3.6).

Rowe and Barden (1964) have concluded that if the friction angle between the soil and the end platen can be kept below 1°, the end restraint effects can be considered negligible and the end platens can be assumed to be frictionless. They showed that the proposed configuration illustrated in Figure 3.6 could provide this condition.

Accordingly in this study the lubricated end configuration, with $L/D = 1$, and a fixed top cap were used.

3.5.1 Advantages and disadvantages

The modifications of a triaxial test on dense sand can be summarized into two subjects:

(1) Use of lubricated ends, and
(2) Use of $L/D = 1$.

It is beneficial to consider the advantages and disadvantages of each of them:

<u>(1) Advantages of lubricated ends</u>

In tests with lubricated end platens the stress and deformation conditions are uniform, the specimen deforms as a right cylinder and the results are more consistent (Raju et al. 1972). The more uniform development of dilation results in a tendency towards multiple failure surfaces and general plastic failure, rather than the premature development of a predominant failure surface. This means that measurements of volume change refer to the entire specimen rather than to one preferred zone and the critical void ratio state can often be attained (Rowe and Barden 1964).

The main application of lubricated ends appear to be in tests on dilating soils in certain research tests which require volumetric strain measurement of high accuracy (Head 1986). This is in fact the case with the permeability measurements of oil sand and reconstituted dense sand specimens in the triaxial test.

<u>(2) Disadvantages of lubricated ends</u>

The following limitations should be born in mind:

(1) More time and more care are needed for setting up,
(2) Lubricated membranes introduce errors in axial strain measurements which should be corrected for by suggested methods (Norris 1981 and Sarsby et al. 1980), and
(3) Due to smaller diameter of central porous disc relative to the specimen diameter, the flow path of pumped water during the permeability test is not a rectilinear flow and the simple form of Darcy's equation could not be used directly for permeability calculations. This problem will be discussed in more detail, subsequently.

<u>(3) Advantages of $L/D = 1$</u>

A better specimen economy for specimens taken from cores or block samples is one of the advantages of $L/D = 1$. Also in the case of reconstituted specimens, $L/D = 1$ is advantageous in the preparation of a more homogeneous specimen.

(4) Disadvantages of $L/D = 1$

The main disadvantage of this configuration will be in applying the results of such a test in practice, since current practice uses data from triaxial tests with conventional ends. However this is not the case in most research projects.

3.5.2 Zone failure versus line failure

As was mentioned, in a triaxial test with lubricated ends and if the specimen has a $L/D = 1$ or shorter, only zone failure can occur (Figure 3.5). It is appropriate to compare the two different modes of failure: line failure and zone failure.

A series of consolidated drained compression triaxial tests were performed on dense reconstituted oil sand specimens with both conventional and lubricated end platens. The result of these tests are presented in Chapter 6 (Figures 6.11 to 6.16).

The stress-strain curve of dense sand specimens with the conventional end platens (line failure) is steeper at small strains, as a result of the end restraint imposed by the rough cap and base. It may be noted that the stress-strain curve of the line failure specimen breaks over much more sharply and that the strain at failure is considerably smaller. These effects are due to the fact that most of the deformation of the specimen occurs within a narrow zone, as indicated in Figure 3.4. Thus triaxial tests with conventional end platens result in a nonuniform single slip stress-strain behavior.

The stress-strain curve for the zone failure specimen breaks over much more gradually, and the strain at failure is considerably larger, owing to the fact that the entire specimen is undergoing essentially uniform strain. It can be seen that the final values of volume change are not the same for the zone failure and line failure specimens. Once the sand in the narrow slip zone in the line failure specimen has expanded to its critical void ratio for the given confining pressure, no further volume change occurs in the sand mass outside the slip zone. However it is assumed that the volume change measured in a triaxial test represents the average volume change for the entire specimen. Therefore, the final calculated average void ratio for a line failure specimen with high dilation rate is much smaller than the actual critical void ratio for that sand at the given confining pressure (Lade 1982). Volume change occurs in the entire specimen with the zone failure. The obtained average porosity or void ratio at large strains in the dense zone failure sand specimen is much higher than that in the line failure specimen, and this void ratio is much closer to the critical void ratio. The average void ratios in line failure specimens do not approach a common value, thus reflecting the effect of nonuniform volumetric strains within the specimens (Figure 6.12 and 6.14). However the stress-strain behavior of specimens with lubricated end platens show a more uniform and consistent deformation (Figure 6.16).

Similarly Lade (1982) compared the results of tests with zone failure (lubricated ends with $L/D = 1$) and line failure (no lubrication with $L/D = 2.7$) on dense and loose Santa Monica Beach Sand. His results showed that the strength, the stress-strain behavior and the volume change characteristics are all affected by mode of failure.

Samieh and Wong (1997) investigated the effect of specimen slenderness ratio and platen end boundary conditions on the stress-strain responses of Athabasca oil sand at low effective confining stresses in triaxial compression. The results were consistent with those observed in tests on dense sands. A single shear band was developed when the conventional nonlubricated ends were used. The use of free lubricated ends and a short specimen resulted in a more stable and uniform deformation consisting of multiple shear bands.

Samieh and Wong (1997) performed magnetic resonance imaging on the sheared specimens. They observed that the internal homogeneity of shear deformation was much improved in tests with short specimens and lubricated ends.

3.6 Permeability calculations

Analyses of water flow in saturated soils are usually based on Darcy's law (Equation 3.1) which is an empirical relation. The original form of this law is applicable to rectilinear flow of a homogeneous liquid only. Thus in performing a permeability test, with the intention of using Darcy's original equation, it is important that the flow in the specimen is a rectilinear one.

In the case of lubricated end caps, the inflow/outflow drainage cross-sectional area is smaller than the specimen's. Thus the flow is neither rectilinear nor is its direction known (Figure 3.7). The simple form of Darcy's law is not suitable for analyzing this problem where flow paths are not parallel.

The class of problems characterized in that all boundaries of the flow domain are completely defined are said to be confined. Although closed-form solutions exist for special cases of confined flow, the resulting expressions are generally too complicated for engineering use (Harr 1962). The methods include analytical solutions using conformal mapping and complex variables. They are concerned with the determination of a function which will transform a problem from a geometrical domain, in this instance a rectangle, within which a solution is sought into one, also a rectangle, within which the solution is known.

In the case of two-dimensional seepage the Schwarz-Christoffel transformation should be used to conformably map the flow region in each of those planes onto the same half of an auxiliary plane, so that, the desired function can be established. Theoretically the solution exists for any configuration, however the use of Schwarz-Christoffel

transformation necessitates the evaluation of hyperelliptic integrals, complicating the solution.

An alternative, simple, although approximate approach for solving problems of confined flow is called the method of fragments. It will be showed in the following how this method could be used to solve the two-dimensional axisymmetric flow of water in the cylindrical triaxial specimen with lubricated ends configuration.

Numerical techniques could also be utilized. A finite element computer program was also used for the solution of this problem and is discussed later on.

3.6.1 Method of fragments

The method of fragments was first proposed by Pavlovsky in 1935 for the computation of seepage under hydraulic structures incorporating multiple piles (Figure 3.8a). The method was publicized by Harr (1962). Griffiths (1984) also followed the method for confined flow problems. He used a combination of published analytical solutions and numerical analyses to produce design charts for estimating seepage quantities. The fundamental assumption of the fragments method is that equipotential lines at various critical parts of the flow region can be approximated by straight vertical lines, the dotted lines in Figure 3.8a, that divide the region into sections or fragments.

In a permeability test of a cylindrical specimen in a triaxial test, flow is vertical through the specimen. The whole specimen is one fragment and equipotential lines confining it are horizontal. However the solution will be the same as seepage under hydraulic structures. It is also an axisymmetric flow. Because of the symmetry only a quarter of the cylindrical specimen needs to be considered.

Suppose that the discharge in a fragment is computed as:

$$q = \frac{k\,h}{\Phi} \qquad\qquad [3.2]$$

where q is the flow rate, k is the soil hydraulic conductivity, h is the head loss through this fragment and Φ is a dimensionless parameter called form factor.

Now considering the flow-net approach, the seepage quantity is calculated as:

$$q = k\,h\frac{n_f}{n_e} \qquad\qquad [3.3]$$

where n_f, is the number of flow channels and, n_e, is the number of equipotential drops. It is seen that the form factor Φ, in the method of fragments, could be compared with the ratio n_e/n_f in the flow-net solution.

Following Pavlovsky's procedure, the various form factors will be divided into types, and the characteristics of each type, here types I and IV will be studied. The fragment of type I is a region of parallel flow between impervious boundaries. Figure 3.8b shows such a region with a length of L and width of a. From Darcy's law:

$$q = k A \frac{h}{L}$$

[3.4]

And hence the form factor for a cylindrical specimen with the same boundary condition is:

$$\Phi = \frac{L}{A} = \frac{L}{\pi a^2}$$

[3.5]

For an elemental section of length dX and width y (Figure 3.8c):

$$d\Phi = \frac{dX}{\pi y^2}$$

[3.6]

Pavlovsky considered the sections shown in Figure 3.8d as his type IV fragments. Considering the symmetry this in fact is a 90° rotation of the case of vertical flow in a triaxial specimen with lubricated end configuration (Figure 3.7), assuming the axis of symmetry as an impervious boundary. To simplify the solution, Pavlovsky noted from his electrical analogues that the quantity of seepage above the streamline AB of Figure 3.8d was of small order and could be neglected. Hence he divided the flow region into two parts, labeled active and passive (Figure 3.8e) with the dividing line EF_o at an angle θ. On the basis of his analogue studies, Pavlovsky assumed $\theta = 45°$. With this assumption, depending on the ratio of b to s, two conditions need to be considered for a type IV fragment. Considering that $d = 2a$, and $L = 2b$ (Figure 3.7):

(1) $b \leq s$ or $L \leq 2s$

For this case (Figure 3.8f), the active zone could be considered to be composed of elements of type I fragments of length dX. Hence:

$$\Phi = \int_0^b \frac{dX}{\frac{1}{2}\pi y^2} = \int_0^b \frac{dX}{\frac{1}{2}\pi (a+X)^2} = \frac{2}{\pi} \frac{b}{a(a+b)}$$

[3.7]

Which is the same for the whole cylindrical specimen. Since; $d = 2a$, and $L = 2b$ (Figure 3.7):

$$\Phi \frac{D}{2} = \frac{2}{\pi} \frac{L D}{d(d+L)}$$

[3.8]

(2) $b \geq s$ or $L \geq 2s$

For this case (Figure 3.8g):

$$\Phi = \int_0^s \frac{dX}{\frac{1}{2}\pi(a+X)^2} + \int_s^b \frac{dX}{\frac{1}{2}\pi T^2}$$

[3.9]

And the form factor is:

$$\Phi = \frac{2}{\pi}\frac{s}{a(a+s)} + \frac{2}{\pi}\frac{(b-s)}{T^2} = \frac{2s}{\pi a T} + \frac{2(b-s)}{\pi T^2}$$

[3.10]

Substituting $d = 2a$, $L = 2b$ and $D/2 = T$ (Figure 3.7):

$$\Phi\frac{D}{2} = \frac{2}{\pi}\left[\frac{D}{d} + \frac{d}{D} + \frac{L}{D} - 2\right]$$

[3.11]

Dotted lines in Figure 3.9 represent Equation 3.8 and 3.11 for d/D values of 0.2 to 0.5 with various values of L/D. The performance of these equations was checked against a numerical solution.

3.6.2 Numerical solution

The numerical analysis was performed using the SEEP/W computer program (GEO-SLOPE, 1991). It is a finite element software product that can be used to model the seepage in porous materials such as soil and rock. SEEP/W has the capability of solving two-dimensional and axisymmetric flow problems. Four-noded quadrilateral elements with a typical mesh shown in Figure 3.10 were used in the analysis. Nine different configurations with d/D values ranging from 0.2 to 0.5 were analyzed. In all cases the starting ratio of L/D was 1 and then was gradually reduced to simulate an axial strain of at least 20%. More than 130 cases of different configuration were analyzed using the SEEP/W program. The total head at the bottom drainage of the specimen was set to zero while at top it was set to unity. Assuming that the soil is isotropic, with permeability and a total head loss of unity, the form factor for a particular configuration is given by the reciprocal of the total flow rate through the system. From Equation 3.2:

$$\Phi = \frac{1}{q}$$

[3.13]

where q is the total flow rate through the system. SEEP/W has the ability to compute the total seepage quantity that flows across the specimen cross section and thus the corresponding form factor was determined through Equation 3.13.

By varying the dimensions of the problem as described before, plots were developed relating the form factor to dimensionless groupings.

Solid lines in Figure 3.9 represent the finite element solution. It illustrates that the approximate solution has a very good accuracy for values of $d/D = 0.4$ and higher. Its results are within 20% of the numerical method's for $d/D = 0.2$. Based on the results from finite element solutions, a regression approach was followed and the following equations were obtained:

$$\Phi\frac{D}{2} = 4.23 - a_1\left(\frac{d}{D}\right) + a_2\left(\frac{d}{D}\right)^2 - a_3\left(\frac{d}{D}\right)^3 \qquad [3.14]$$

Where:

$$a_1 = 19.04 - \left(6.66\frac{L}{D}\right)$$

$$a_2 = 32.63 - \left(20.87\frac{L}{D}\right)$$

$$a_3 = 20.49\left(1-\frac{L}{D}\right)$$

Equation 3.14 is valid only for values of $L/D \leq 1$ and d/D of 0.2 to 0.5.

3.7 Anisotropic permeability

In both the method of fragments and the finite element analysis it was assumed that the specimen had an isotropic permeability. However if the ratio of vertical to horizontal permeability is known or could be assumed, any horizontal dimension in the equations of both methods should first be multiplied by the anisotropy factor. Factor R is defined as:

$$R = \sqrt{k_v/k_h} \qquad [3.15]$$

where k_v and k_h are vertical and horizontal permeability respectively.

3.8 Discussion and conclusions

- The triaxial test apparatus can be used to measure and monitor the permeability of soil specimens undergoing changes in stress and strain.

- Use of the flow-pump method in a permeability test offers several advantages including continuous monitoring of permeability at any time.

- Boundary conditions of the specimen in the triaxial test affect its deformations through the test. Lubricated end platens are required since they produce a more uniform deformation of the specimen.

- Flow inside a cylindrical specimen with lubricated end platens is not rectilinear (Figure 3.7). Thus the simple form of Darcy's law is not suitable for analyzing this problem. Although in theory a closed-form solution exists for any configuration, it involves the evaluation of hyperelliptic integrals. A simple approximate method for solving this problem is presented.

- The method of fragments solution has a good accuracy over a wide range of L/D and d/D values. It may, however, overestimate the permeability by up to 20% in very low values of d/D.

- The proposed equations (Equations 3.8 and 3.11) are valid for flow inside a cylindrical specimen where porous stones at both ends are of the same size (Figure 3.7). Following the presented procedure, similar approximate solutions could be derived for problems of different boundary conditions. One such case is a test specimen where bottom and top flow areas are of different sizes.

- The ratio of the form factor of a lubricated end set up to that of a rectilinear flow in a conventional end caps configuration is of significance. Figure 3.11 presents the ratio of lubricated end form factor to one of rectilinear flow for different values of d/D and L/D. This figure illustrates the importance of providing a rectilinear flow through the specimen, if the simple form of Darcy's law is to be used (Equation 3.1). In fact there would be an error in calculated permeability in a triaxial test with conventional end platens in which due to lack of necessary grooves in the end platens, a full cross-sectional area of injection/withdrawal of flow is not provided.

- The following equation clarifies this error. Equation 3.2 can be rewritten as:

$$k = \frac{q}{h} \Phi \qquad [3.16]$$

Figure 3.11 indicates that the amount of this error is significant and this could lead to an underestimation of permeability up to five times. Depending on the test set up used in a permeability test, this error may explain the higher values of permeability measured in the field relative to the ones obtained in the laboratory.
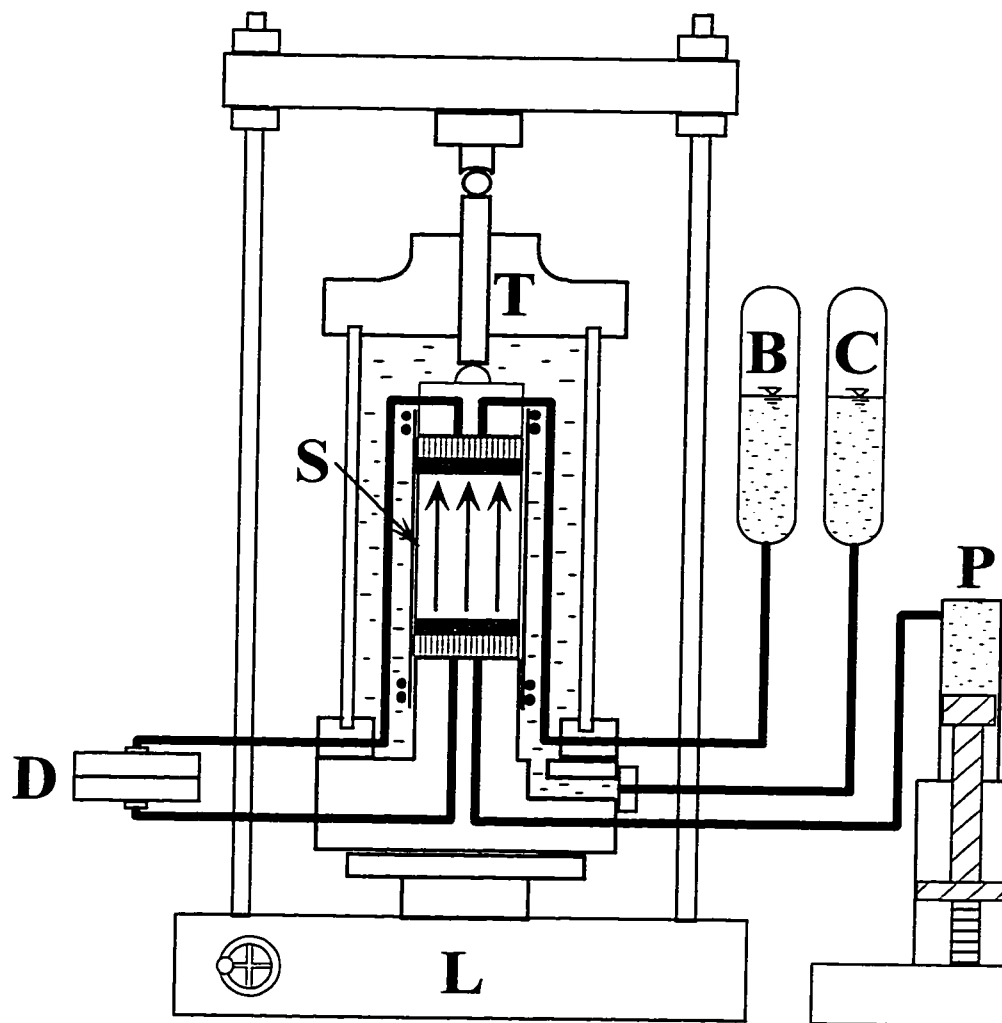
Figure 3.1 Scheme of triaxial permeability test

S specimen, T triaxial cell, L load frame, C cell pressure,
B back pressure, P flow pump, D differential pressure transducer
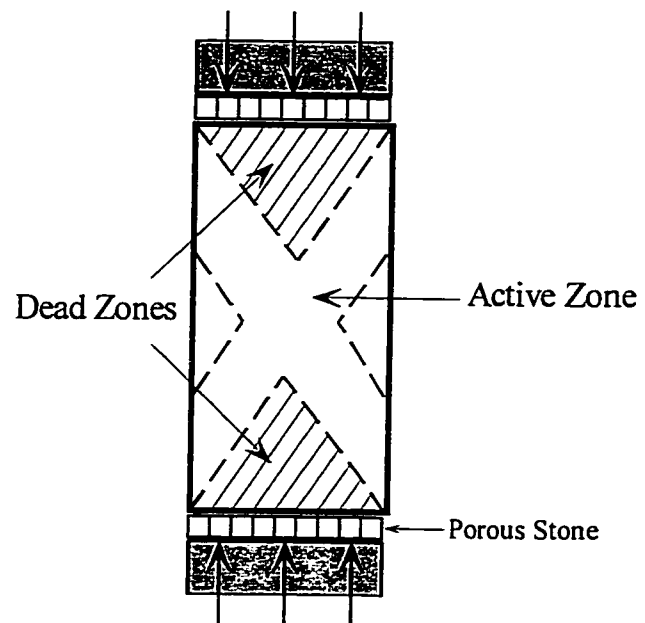
Figure 3.2 Dead zones in a triaxial specimen with conventional end platens
(Modified from Head 1986)
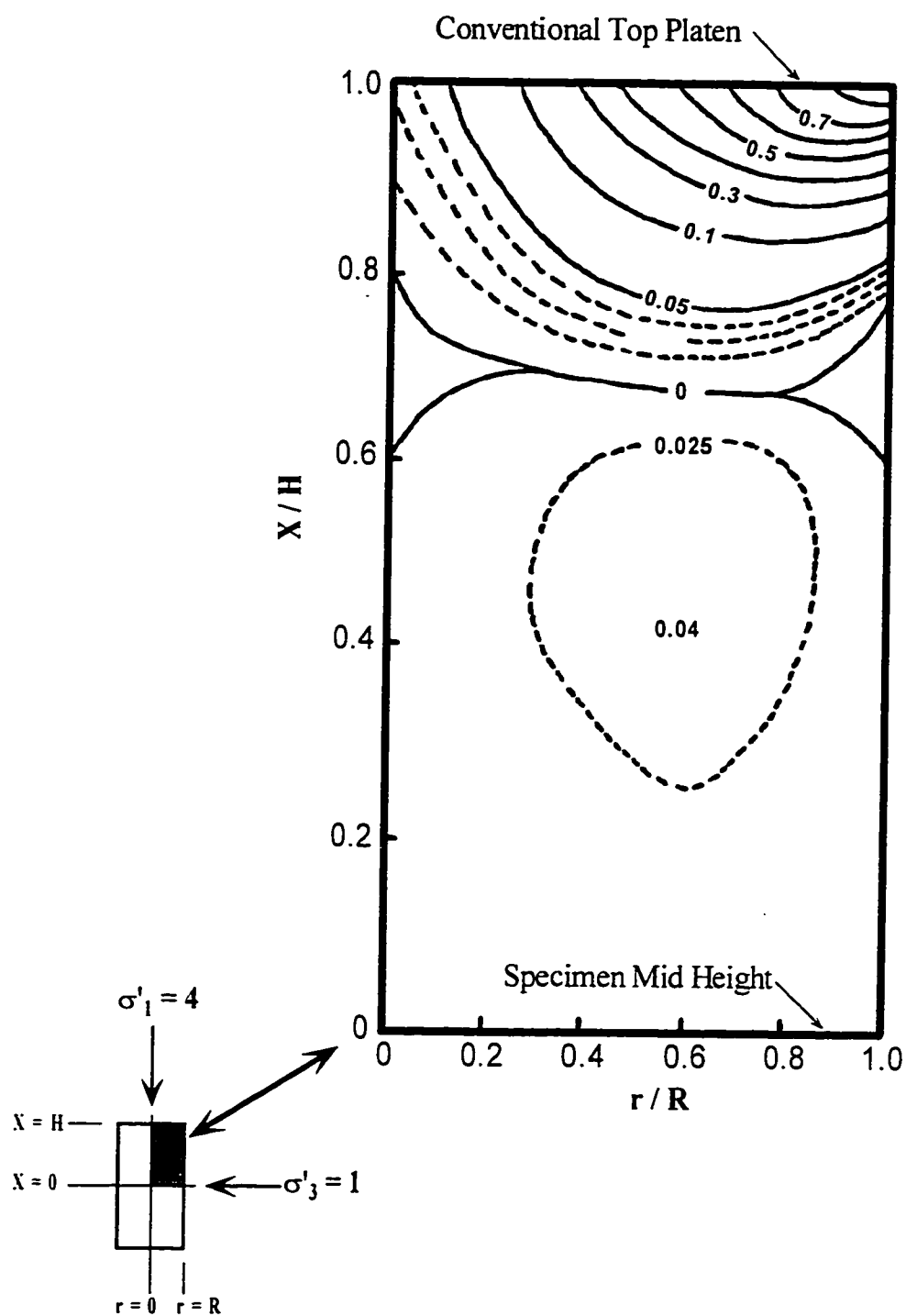
Figure 3.3 Distribution of shear stress throughout a triaxial specimen with end friction

(Modified from Lee 1978)
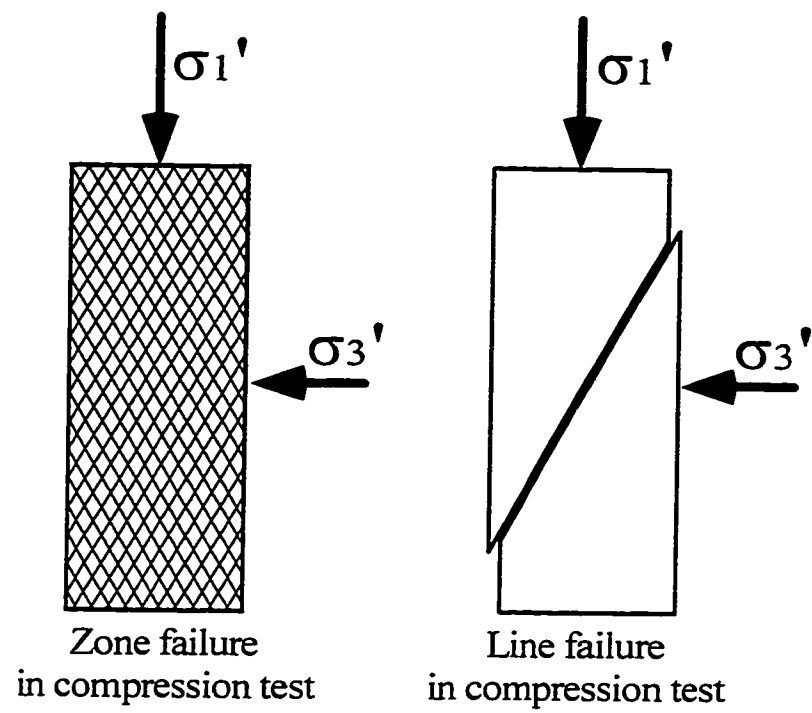
Figure 3.4 Zone failure and line failure in triaxial specimens
(Modified from Lade 1982)
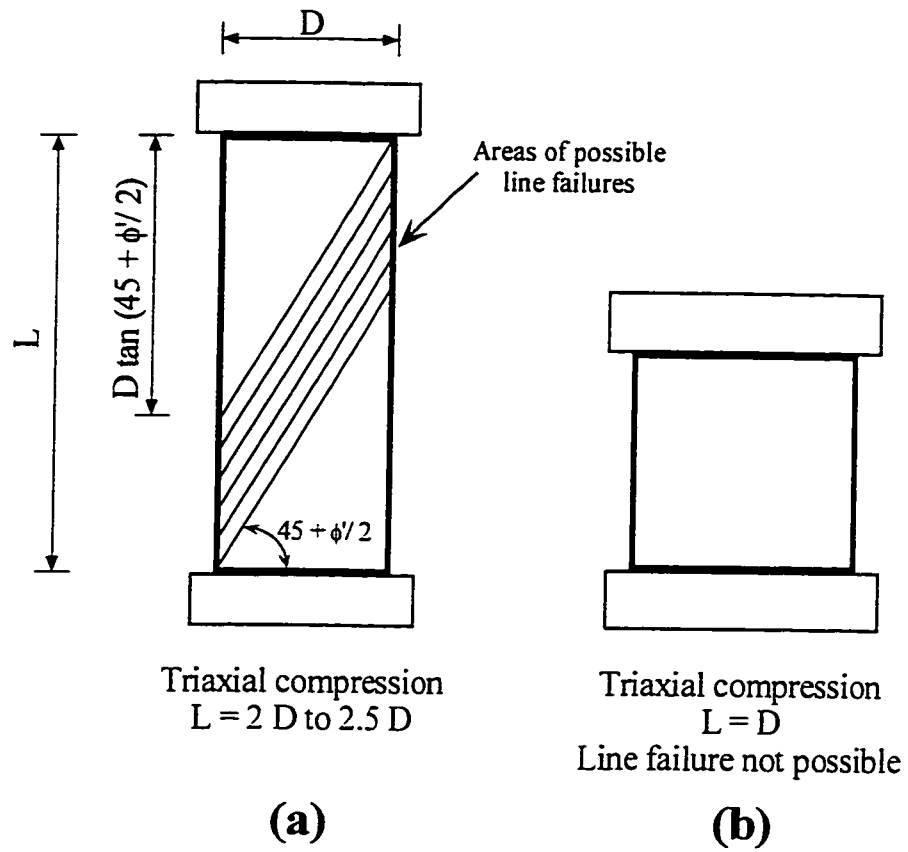
Figure 3.5 Boundary condition effects on failure type

(Modified from Lade 1982)

Specimen

Latex
Membrane

Silicone
Grease

O - Ring

End PLaten

Porous Stone
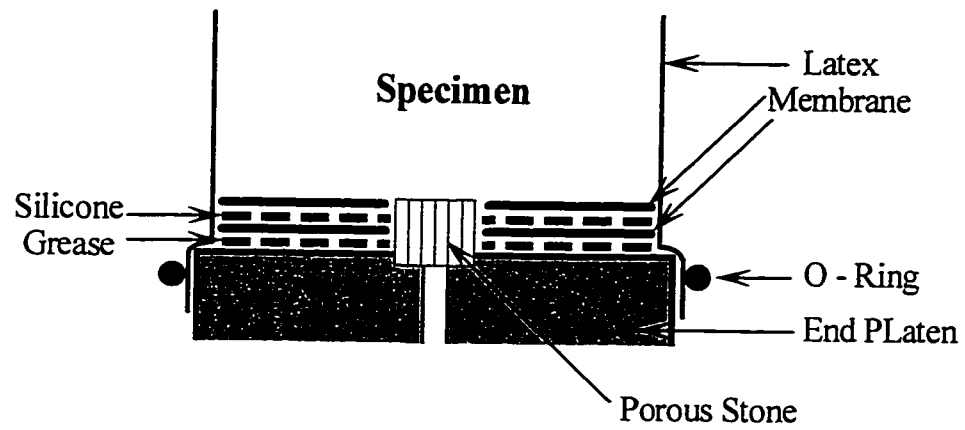
Figure 3.6 Lubricated end platen

Top Cap

O - Ring

Porous Stone

Specimen
Flow Vectors

Membrane

Silicone
Grease

L

Bottom Pedestal

d

D

Grooves
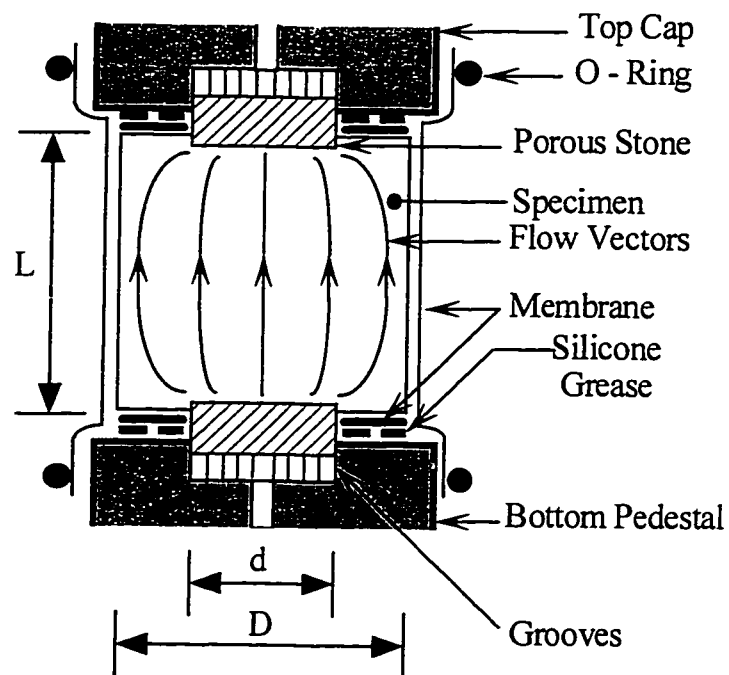
Figure 3.7 Flow in a lubricated end configuration
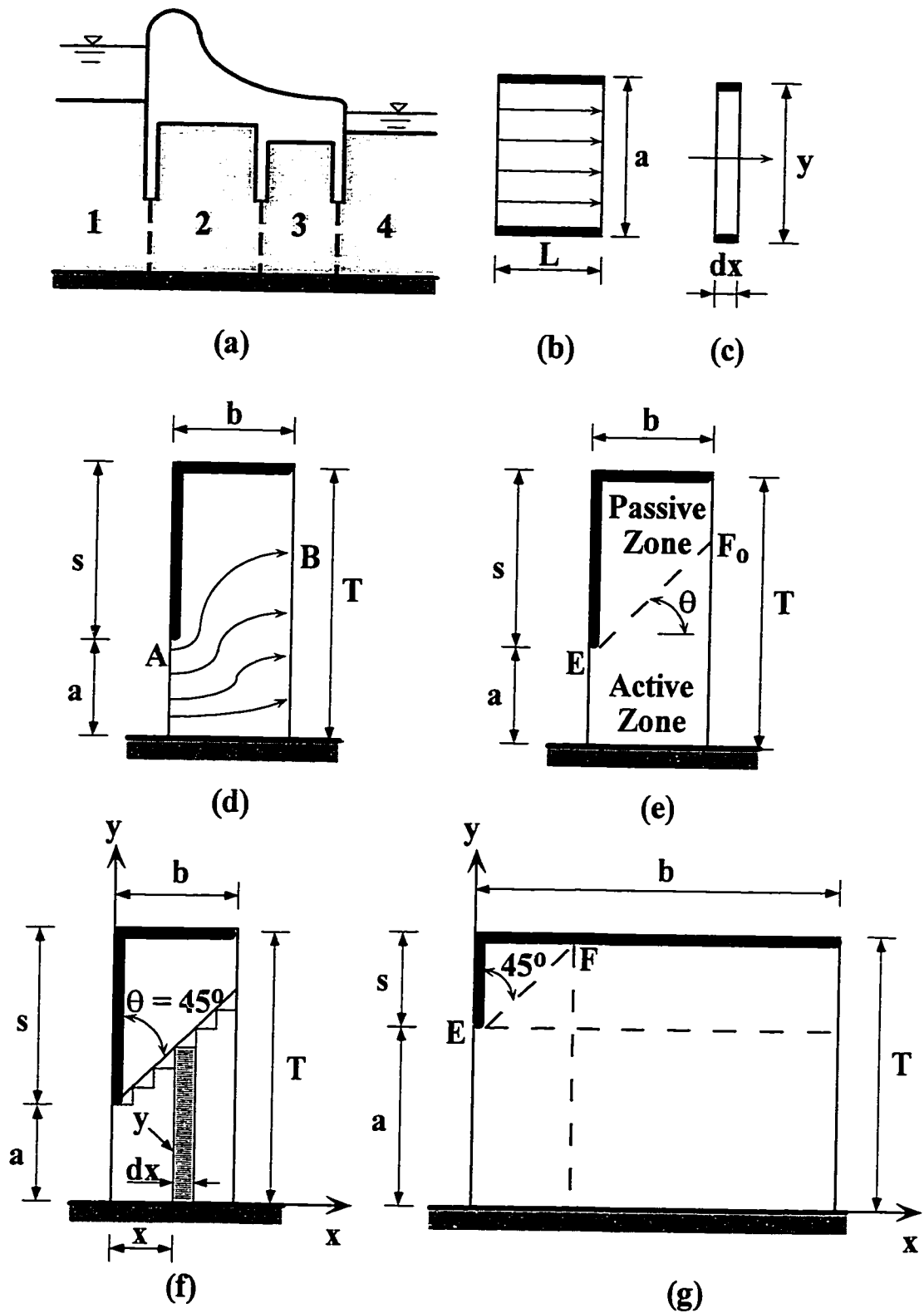
Figure 3.8 (a); Fragments in a flow region under a dam, (b) and (c); Pavlovsky's
fragment type I, (d), (e), (f) and (g); Pavlovsky's fragment type IV

(Modified from Harr 1962)
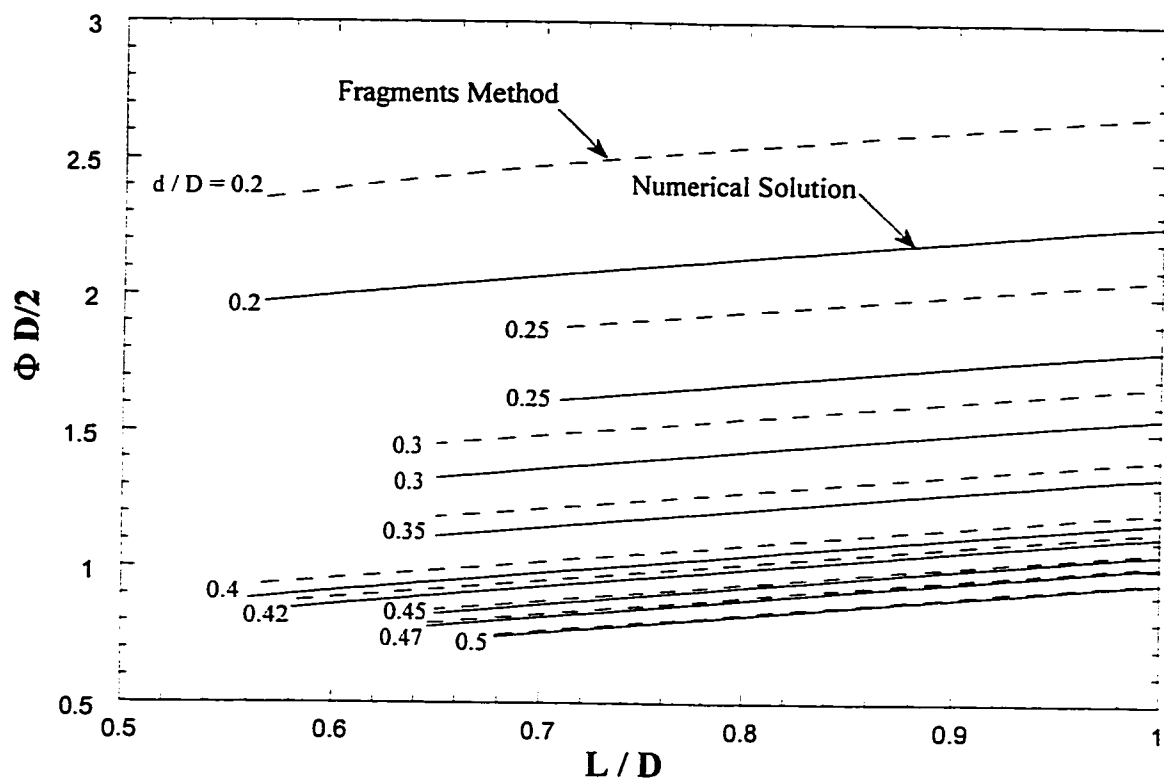
Figure 3.9 Variation of form factor Φ with different values of d/D and L/D
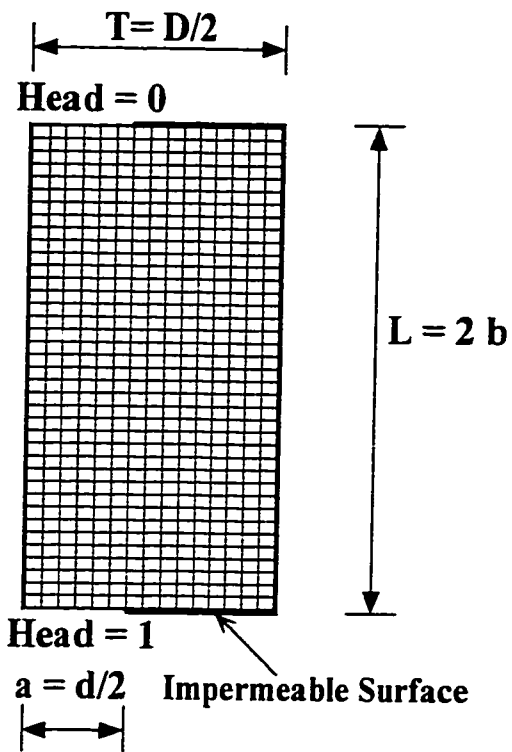
Figure 3.10 Typical mesh for finite element analyses
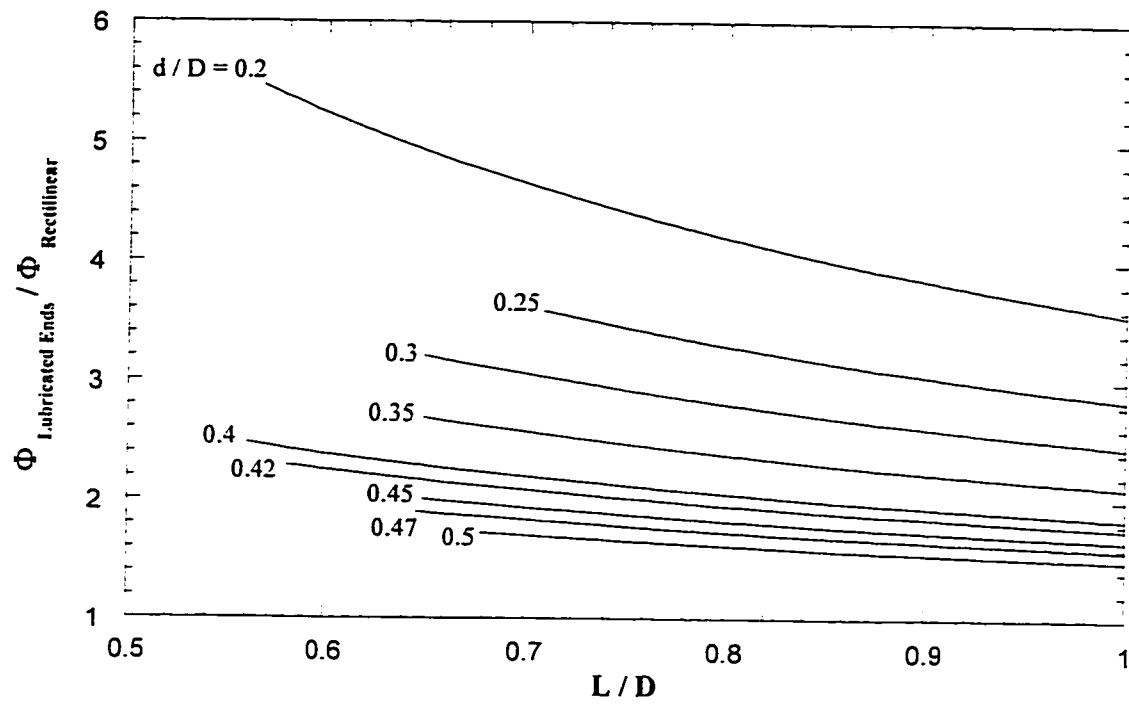
Figure 3.11 Ratio of lubricated end configuration form factor to that of rectilinear flow

CHAPTER 4 TESTING PROCEDURE FOR TRIAXIAL SHEAR AND PERMEABILITY TESTING OF SAND

4.1 Introduction

This chapter describes the test procedures adopted for triaxial shear tests and the permeability testing procedure during a triaxial test. Specimen preparation, saturation techniques, consolidation and data analysis procedures are also discussed. Procedures for obtaining grain size distribution and relative density of materials tested during this study are also defined.

4.2 Test materials

During the course of this study, reconstituted specimens made from three artificially mixed sands and undisturbed specimens obtained from the block sample were tested (Chapter 1). These four specimen types are described in detail in Chapter 6. Table 4.1 summarizes the properties of specimens tested in this study. The grain size distribution of these sands is plotted in Figure 6.6.

4.2.1 Grain size distribution

The ASTM standard method for particle-size analysis of soils, D 422-63, was followed in this study. The only difference was that the No. 325 sieve (45 μm) was used instead of the No. 200 sieve (75 μm).

4.2.2 Relative density

Relative density is derived from maximum and minimum dry density of sand. Although the official recommended name for this term is density index, I_D (Barsvary et al. 1980), the name relative density, D_r, was used in this thesis.

In this study the ASTM standard test methods of D4253 and D4254 were used in determination of maximum and minimum density of sand, respectively. Standard mold size of 2830 cm³ (0.1 ft³) and a vibratory table were used in the tests. The dry method was used in determining the maximum density. Table 4.2 displays the result of these density tests for the reconstituted sands.

4.3 Specimen preparation methods

Several techniques which are commonly used to produce reconstituted sand specimens with controlled uniformity and density will be discussed. Uniformity of a reconstituted

specimen is directly related to the repeatability of a test and is an important factor in a research program involving a series of tests on reconstituted specimens.

In order to improve the comparison of results between reconstituted and undisturbed specimens, a goal of this study was to prepare reconstituted sand specimens as dense as possible. To achieve this goal, the following preparation methods were evaluated:

(1) dry tamping
(2) moist tamping
(3) water pluviation
(4) slurry deposition
(5) wet vibration

the wet vibration method is a new technique which was developed during the course of this study.

Following the description of experimental equipment and test set up common to these procedures, each method is described.

4.3.1 Split former

Figure 4.1 provides a cross-section of split former. The split former serves as a mould into which sand can be compacted for the preparation of a reconstituted triaxial specimen on a triaxial pedestal. The split former consists of two segments for ease of disassembling and has a recessed extension to fit around the membrane O-ring seals. The former is lined with a latex membrane passed through the center of the former and stretched over the ends.

A port on the side of the former can be used to apply a vacuum to the rubber membrane so it is held in contact with the internal face while a specimen is being built up inside the split former. If a vacuum is applied, the mating faces of the two halves of the former are made airtight by coating them with silicone grease.

Depending on the preparation technique used, sand was placed in the split former in either dry (or moist) or saturated state. In each case the split former setup was different and is described in the following section.

4.3.1.1 Setup for saturated sand

The bottom pedestal drainage outlet on the triaxial cell was connected to a water reservoir (Figure 4.2). The reservoir was filled with de-aired water. By opening the drainage valve, the connection to the pedestal was also filled with de-aired water, displacing the air. The hole in the pedestal was covered by a porous stone, which had been saturated by boiling it in water. The water level was adjusted to the top edge of the porous stone and pedestal in the wet vibration and slurry deposition methods and the top of the split former in the water pluviation method.

A vacuum line was connected to the split former, holding the membrane in contact with its inner wall. After the specimen was formed inside the mould, the top of the specimen was carefully leveled and the loading cap was placed in position and the rubber membrane was sealed on to it with two O-rings.

Saturated sand possesses no cohesion. To enable the specimen to support itself a small negative pore pressure was applied by lowering the water reservoir so that the free water level was below the base of the specimen, with the valve on the cell pedestal opened (Figure 4.3).

At this point in the set up, the split former was removed and the height and diameter of the specimen were measured. The cell body was carefully fitted into place and tightened down, and the cell was filled with water and pressurized. The water reservoir was then placed alongside the cell eliminating the negative pore pressure. The specimen was then disconnected from the water reservoir and connected to the back pressure system, ensuring no air entrained in the flow lines.

4.3.1.2 Setup for dry or moist sand

A split former fitted with a vacuum connection, enclosing a rubber membrane, was clamped to the pedestal of the triaxial cell as described above, except that a dry porous stone was used. For this set up, two vacuum lines were required, one for connection to the split former, the other for connection to the pore pressure outlet on the triaxial cell (Figure 4.4). The latter was capable of applying a controlled suction to the specimen, which was monitored with a vacuum gauge.

After the specimen was formed, the top surface was carefully leveled, the top loading cap was placed in position and the membrane was sealed on to it using two O-rings. A small suction was applied to the base of the specimen to give it sufficient strength to stand while the split former was removed.

The specimen's dimensions were carefully measured and the cell body was fitted, filled with water, and pressurized as described above. The vacuum line was removed and pressure in the specimen was restored to atmospheric before proceeding with the saturation process.

4.3.2 Dry tamping

The oldest laboratory reconstitution technique is dry or moist tamping of soil in layers (Kuerbis and Vaid 1988). The technique consisted of pouring consecutive soil layers of specified thickness into a split former, and tamping each layer flat with a specified force and frequency of tamping before the next layer was placed. Figure 4.5 illustrates this method and shows the rammer used in this study. It had a 50 mm diameter face, a 475 g weight sliding freely on the central rod which controlled the height of the drop to 170 mm.

Specimens in tests No. 5 to 16 were made by dry tamping method. Dried sand was poured in five layers with each layer compacted by 20 blows of the rammer. Specimens made were of 50 mm by 100 mm dimension and the relative densities obtained by this method ranged from 70% to 106%.

Although high relative densities were obtained by the dry tamping method there were disadvantages associated with this method. Among them were the difficulty in saturating a dry sand specimen and the fact that tamping in thin layers can lead to holes in the rubber membrane. The issue of saturation is discussed subsequently.

4.3.3 Moist tamping

This method is similar to the dry tamping method. The specimen for test No. 17 was made by moist tamping. Sand was mixed with de-aired water to have 5% moisture content. The reconstituted specimen was made as described above. The resulting relative density was 65%. The moist tamping method can produce very loose to dense partially saturated specimens. Due to water tension forces between grains, specimens prepared by the moist tamping method could not be made sufficiently dense relative to the undisturbed specimens. This is not the case in a dry or saturated state of sand.

4.3.4 Water pluviation

Several researchers, including Vaid and Negussey (1984, 1988) have described the water pluviation specimen preparation technique. The procedure consists of depositing a known weight of dry sand that has been saturated by boiling with water in a flask and cooled to room temperature. Deposition is made directly into a membrane-lined, de-aired water filled, split former cavity (Figure 4.6). A rubber stopper with a glass nozzle is used to seal the flask after filling it with de-aired water to the brim. The glass nozzle is also filled with de-aired water. The flask is inverted into membrane cavity. Sand transfer from the flask to the cavity occurs under water by mutual displacement of sand and water under gravitational influence. The upward flow of de-aired water creates turbulence and suspends fine particles.

Following deposition and leveling, the top cap is put in place. The specimen was then densified by vibration while maintaining a small seating load on the top cap. During densification both top and bottom drainage lines were kept open. After densification was terminated, the membrane was pulled over top cap and sealed with an O-ring.

The fact that sand was pluviated through boiled de-aired water ensured the specimens' saturation. The water pluviation method was used in tests No. 18 and 19. The resulting relative densities were around 80%. Higher densities were not achieved possibly due to the arching action inside the split former. The height of the reconstituted specimens being twice the diameter in these two tests was a factor in the development of the arching action.

The water pluviation technique can produce uniform specimens of uniform sands (Vaid and Negussey 1984). However, segregation is a problem in water pluviation of sands with fines (Kuerbis and Vaid 1988). In both tests, No. 18 and 19, the fine particles were deposited last, mainly at the top of the specimen. The accumulation of fines at one end of the specimen did not provide a suitable condition for a permeability test.

However, the slurry deposition method introduced by Kuerbis and Vaid (1988) can produce homogeneous reconstituted specimens of sand containing considerable amount of fines as discussed below.

4.3.5 Slurry deposition

To overcome the inherent problem of particle segregation in water pluviation, a technique called the slurry deposition method was developed by Kuerbis and Vaid (1988). In this method sand is first water pluviated into a clear Plexiglas cylindrical tube instead of a former. The tube is sealed in order to mix the sand slurry. The details of this tube, its seals and the slurry deposition method are explained by Kuerbis and Vaid (1988).

The slurry within the tube was mixed by vigorously rotating the tube. The tube is then placed on the triaxial cell pedestal and a rubber membrane was installed around it. A split former was assembled around the pedestal and the tube. The specimen mixing tube was then carefully and steadily withdrawn to deposit the sand slurry within the specimen membrane in a homogeneous saturated state. The top of the specimen was leveled and top cap was installed. The densification process was similar to the water pluviation method.

Tests No. 20 and 21 were prepared using the slurry deposition method. The resulting relative densities were 76% and 87% respectively.

Although the slurry deposition method is capable of producing homogeneous saturated reconstituted specimens it is basically appropriate for materials with large amount of fines. A simpler method, the wet vibration method, proved more effective in producing dense sand specimens, and is described in the following section.

4.3.6 Wet vibration

The wet vibration method was used in producing dense reconstituted specimens for the triaxial tests with the lubricated end configuration. Specimens of 38 mm diameter by 38 mm height were made for these tests.

The split former used in this method had a removable piece, which worked as a guide sleeve. Figure 4.7 shows a cross-section of the split former. The split former and the triaxial apparatus were set up as described in Section 4.3.1.1 and shown in Figure 4.8. The difference was that before assembling the split former, a large diameter PVC tube was installed on to the triaxial base as illustrated in Figure 4.8. The triaxial apparatus with the split former setup on it was then placed on a vibrating table.

Dry sand was saturated by boiling for at least 10 minutes in distilled water and allowed to cool to room temperature. With the vibrating table turned on, the split former was slowly filled with wet soil using a scoop. After each increment of soil was added, it was inspected to see if a small amount of free water had accumulated on the soil surface. If not, the sufficient amount of water was let in through bottom pedestal drainage ports.

Sand was deposited into the former to a predetermined height. This height was determined to correspond to the volume of the specimen in the maximum void ratio state. During this process the frequency of vibration was adjusted to prevent excessive liquefaction and bulking of the sand.

A saturated porous disk was placed on the sand and a surcharge weight was put on top of the porous disk (Figure 4.9). The total mass of the surcharge base plate and surcharge weight was equivalent to a surcharge pressure of 13.8 kPa. This is similar to the surcharge used in the ASTM D4253 standard test method for determination of maximum density of sand. The vibrating table was then set on scale 6 (of maximum 10) and the triaxial cell was vibrated for 10 minutes. During this vibration period, the surcharge weight was held in a vertical position manually.

The surcharge weight and the porous disk were then withdrawn. The membrane was freed from the O-ring to allow for the guide sleeve to be removed from the split former. The membrane was rolled back again and held in position with two O-rings (Figure 4.10). The top of specimen was carefully leveled.

Top drainage tubing was connected to the top cap inside the PVC tube (Figure 4.10). Water was poured into the large diameter PVC tube to form a water bath above the split former. De-aired water was flushed through top cap tubing to displace the air. The hole in the top cap was then covered by a porous disk, which had been previously saturated by boiling water.

With the water level above the split former the top cap was slowly lowered in place. A small circular bubble level placed upon the top of the platen was used to keep the top cap level at all times during placement. The rubber membrane was then carefully sealed to the top cap with two O-rings. All this was done under water to ensure that there was no entrapped air at the top of the specimen and that the specimen remained saturated. The water in the PVC tube was then drained out.

The application of negative pore pressure and removal of the split former were the same as described in Section 4.3.1.1. After the split former had been removed, the PVC tube was taken off to allow for the assembly of the triaxial cell.

It should be mentioned that the split former used in the wet vibration method had an inside diameter equal to its depth, which was similar to the standard ASTM mold. This minimized the arching of sand grains during densification.

Reconstituted specimens in tests No. 23 to 26 and 30 to 34 were prepared with the wet vibration method. These specimens were made from the 3rd mixed sand (MS3). The resulting relative densities were from 96% to 148%.

The achievement of high values of relative density showed that the wet method can yield significantly higher values of maximum density. As mentioned, the value of maximum density of MS3 sand was obtained by performing the dry method of ASTM standard test D4253. It is apparent that this test had to be repeated using wet method so that the appropriate values of maximum dry density could be obtained. Unfortunately this observation was made when insufficient material remained to repeat the wet method of the standard test.

Unlike previous studies (Oldakowski 1994) that had used tailing sand, the MS3 sand used for the above mentioned tests was from the bitumen-free McMurray Formation block sample. The fact that these sand grains had not been through any cleaning process may be a factor in achieving densities close to the in situ densities of oil sand.

4.3.7 Undisturbed specimens

The undisturbed specimens were cored from a block sample of McMurray Formation oil sand (Chapter 1). Long cores were cut into smaller pieces. Each piece was then trimmed with sand paper to obtain a specimen with the dimensions of 38 mm diameter by 38 mm height. The specimen height and diameter were measured in eight different locations and the average diameter and height were calculated. The volume of the specimen was then computed. The specimen mass was measured and its dry density was obtained.

As illustrated in Figure 4.11 some portion of specimen in the center was then removed to accommodate the porous disks in the lubricated end set up. The specimen was weighed again and by knowing the dry density the new specimen volume was computed.

The apparatus setup for undisturbed specimen was similar to that of a dry reconstituted specimen. The specimen was mounted on the bottom pedestal and a membrane was installed around it. Two O-rings were installed on upper portion of the top cap. The excess membrane at top of the specimen was rolled down and the top cap was placed on the specimen. The membrane was rolled up to the top cap and the O-rings were pushed down to seal the membrane on to the top cap.

4.4 Test setup

Prior to conducting any test, all the tubing were flushed with de-aired water and the pressure in compressed air-water reservoirs were reduced to atmospheric pressure. A series of readings were performed for pressure transducers. Average values of these readings corresponded to the zero reading of pressure transducers.

The side surface of both the bottom pedestal and top cap were coated with a thin layer of silicone grease. In tests with lubricated end configuration, four pieces of membrane were cut so that they had the shape of a donut. The internal hole diameter corresponded to the diameter of the porous disk and had an external diameter of 38 mm. Two of these membrane pieces were placed on each end platen, separated from each other and the platen by a thin layer of silicone grease.

Split former / triaxial base set up and specimen preparation were performed as described previously. Using vernier calipers, specimen diameter and height were measured on at least six different locations. The measured diameters were corrected for the thickness of the membrane and the average diameter and height were then computed. In this study, latex membranes of 0.3 mm and 0.35 mm thickness and 38 mm and 50 mm diameter respectively, were used.

The cell body was carefully assembled into place and the cell chamber was filled with water and pressurized to 25 kPa. The negative pore pressure was eliminated by connecting the specimen drainage ports to the back pressure system. Back pressure was still zero at this moment.

In the case of the Bishop-Wesley stress path triaxial cell (Figure 2.1), the load cell was brought in contact with the top cap using the axial screw adjustment. For a conventional triaxial cell (Figure 3.1) the loading piston was brought in touch with the top cap using the load frame ram.

The cell pressure was increased to 50 kPa and subsequently the back pressure was increased to 25 kPa. By repeating these increments the desired confining pressure and back pressure were achieved while the effective confining pressure on the specimen was kept under 50 kPa at all times. The final values of confining pressure and back pressure depended on the chosen saturation process.

It was assumed that by maintaining a low effective confining pressure, the change in the volume of the specimen during this process was negligible.

4.4.1 Saturation procedure

In triaxial tests on saturated soils, saturation is normally carried out as a first step. The most usual method in practice is to apply a back pressure to the pore fluid incrementally, alternating with increments of confining pressure. As described previously, the back pressure is always a little less than the confining pressure to ensure that the effective stress remains positive. However for reconstituted specimens that were made dry and dry undisturbed specimens, water had to be introduced into specimen first. The following explains the technique used for the saturation of the dry specimens:

(1) Dry reconstituted specimens

These included specimens of tests No. 5 to 14. Specimens were first flushed with CO_2 under low pressure (30 kPa) for 30 minutes. This replaced the air inside specimen with more soluble gas, CO_2. Distilled water was de-aired by boiling and when it was still warm, 1200 cc of warm de-aired water was flushed through the specimen. This helped the gas inside the specimen to go into solution easier. The water flow through the specimen was induced by the application of a constant head. As described before, the back pressure was increased to 500 kPa and the specimen was left overnight to saturate.

(2) Undisturbed specimens

Specimens were flushed with 50 cc of de-aired water. The syringe pump rate of 15 ml/hour was used to induce an upward flow of water inside the specimen to minimize the possibility of fines migration during the saturation process. Cell and back pressure were increased gradually and the specimen was left to saturate under a back pressure of 900 kPa.

The method used for dry reconstituted specimens was very successful, but complicated. It was simpler to use higher values of back pressure for longer periods of time (undisturbed specimens method), since both methods yield the same result.

Tests No. 15 to 43 were saturated by being under a back pressure of 900 kPa for at least 16 hours.

4.4.2 Saturating specimens by back pressure

The advantages of using an elevated back pressure to obtain full saturation are summarized as follows:

(1) air in the void spaces within the specimen is forced into solution under the applied pressure when full saturation is reached;

(2) any air trapped between the membrane and the specimen is also dissolved;

(3) any air bubbles remaining in the drainage line and pore pressure connections, which could not be flushed out, are eliminated. This improves the response time of pore pressure and avoids the risk of air bubbles impeding drainage to back pressure;

(4) in a specimen that dilates during shear, water can be freely sucked in during a drained test without the movement being impeded by an air lock due to air bubbles; and

(5) reliable measurements of permeability can be made on soils in which saturation was achieved by applying a back pressure (Head 1986).

Lowe and Johnson (1960) had shown that the theoretical back pressure required to bring a specimen from an initial degree of saturation, S_i, to a final degree of saturation, S, by both compression and solution of the pore air is:

$$P = P_i \frac{(S - S_i)(1 - H)}{1 - S(1 - H)}$$ [4.1]

in which:

P is the change in pressure required to increase saturation from S_i to S,

P_i is the initial absolute pressure corresponding to S_i, and,

H is Henry's constant, which at normal room temperature is approximately equal to 0.02 cc of air per 1 cc of water.

For complete saturation, $S = 1$, Equation 4.1 reduces to:

$$P_{100} = 49 P_i (1 - S_i)$$ [4.2]

in which P_{100} represents the back pressure required to provide 100% saturation.

If the initial pressure, P_i, is atmospheric, substituting one standard atmosphere of 101.32 kPa and assuming that a degree of saturation of 90% is reached after the specimen is flushed, the required back pressure, P_{100}, is calculated to be 497 kPa.

During the course of this study a minimum back pressure of 500 kPa was maintained on the specimens at all times.

When pressurized deaired water is introduced into the void spaces in a specimen there is an immediate increase in the degree of saturation due to the compression of air in accordance with Boyle's law. Assuming that none of the free air goes into solution in the pore water, from Boyle's law it follows that the degree of saturation, S, resulting from an applied back pressure, P, is (Black and Lee 1973):

$$S = 1 - \frac{1}{49R + \frac{1}{1 - S_i}}$$ [4.3]

in which, $R = P / P_{100}$.

Application of P_{100} to any specimen will immediately produce a condition of 98% saturation or greater. However, to increase S to 99% requires twice the back pressure, and to increase S to 99.8% requires 10 times P_{100} unless the initial degree of saturation is already close or greater than these final amounts.

The time required for saturation under the appropriate back pressure ($P = P_{100}$) depends on the initial degree of saturation of the specimen, and whether a degree of saturation of

100% is to be obtained or whether a slightly lower value is acceptable. Theoretical times for final saturation values of 99, 99.5 and 100% are plotted graphically in Figure 4.12 (Block and Lee 1973). The time required appears to be greatest when the initial saturation lies in the range 75 to 85%. It decreases dramatically when the initial saturation exceeds 95%. There is substantial saving of time if 99.5% or 99% saturation can be accepted.

The commonly used procedure for evaluating degree of saturation of triaxial soil specimens is based on the determination of the B parameter as presented by Skempton (1954).

4.4.3 B value

Bishop (1973) developed the following expression for pore pressure response of a saturated porous material to an undrained isotropic stress increment:

$$B_{100} = \frac{\Delta u}{\Delta \sigma_3} = 1/[1 + n(C_w - C_g)/(C_s - C_g)]$$ [4.4]

where:

Δu is change in pore pressure due to $\Delta \sigma_3$, change in confining pressure,
B_{100} is pore pressure parameter for a fully saturated specimen,
n is the porosity,
C_s is the compressibility of soil structure,
C_w is the compressibility of pore water,
C_g is the compressibility of soil grains.

In this study the compressibility of water is assumed to be $C_w = 5 \times 10^{-7}$ kPa^{-1} (Head 1986).

For most sands, C_g is several magnitudes less than C_s and C_w, so:

$$B_{100} = \frac{1}{1 + n C_w/C_s}$$ [4.5]

The common criterion used to test compressible soil specimens for full saturation, i.e. a B value approaching unity, is clearly not valid for soils with low compressibility, like oil sand specimens (Agar 1984).

Since relatively high degrees of saturation can be achieved almost immediately following application of the specified back pressure, it becomes of interest to know what pore pressure response can be expected from specimens at these degrees of saturation. Black

and Lee (1973) developed the following expression for calculating the initial degree of saturation of a specimen based on the pore pressure parameter B:

$$S = \frac{1 - Z(1 - B)}{1 - ZQ}$$

[4.6]

where:

$$Q = B n_i \frac{C_w}{C_s}, \qquad Z = Y/D, \quad Y = C_s \frac{\Delta\sigma_3}{n_i}, \qquad D = 1 - \frac{P_i}{P_i + B \Delta\sigma_3}$$

in which:

n_i is the initial porosity and

$\Delta\sigma_3$ is the change in confining pressure.

For fully saturated specimen, $S_i = 1$, Equation 4.6 converts to Bishop equation for B_{100}, Equation 4.5. Table 4.3 illustrates the degree of saturation obtained through Equation 4.6 for tests No. 23 to 43.

Chaney et al. (1979) suggested a test method for determination of degree of saturation of soil specimens by B value measurement. Based on this method for the case of dense sands, the criterion for full saturation is that a plot of B versus back pressure becomes flat with increasing back pressure. In other words a measured B value that is constant and independent of the magnitude of the back pressure indicates full saturation.

Throughout this study, a series of B value measurement tests (B-test) was conducted on each specimen. Section 4.4.5 describes the procedure involved in a B test. According to the method suggested by Chaney et al. (1979), it was assumed that the specimen was saturated if the value of B was fairly constant in three consecutive B tests. In each B test the back pressure had been increased from its value in the preceding B test.

For tests No. 23 to 43 the above mentioned method was also used and the results are reflected in Table 4.3. It is evident that the value of soil structure compressibility, C_s, is important in evaluation of degree of saturation and thus should be measured.

4.4.4 Soil structure compressibility

The change in volume of a soil subjected only to isotropic stresses is governed by the change in effective stress, not total stress. The relationship between volume change (expressed as volumetric strain, $\Delta V/V$) and change in isotropic effective stress is given by the equation:

$$\frac{\Delta V}{V} = C_s \, \Delta\sigma'$$

<div align="right">[4.7]</div>

where ΔV is the change in volume, V the initial volume, C_s the volume compressibility of the soil skeleton, and $\Delta\sigma'$ the change in isotropic effective stress.

In this study the soil structure compressibility was determined from the volume change of specimen during the consolidation phase of the test (Table 4.3).

4.4.5 B-test procedure

The commonly used procedure for evaluating the B value of triaxial soil specimens was summarized by Bishop and Henkel (1962). The procedure involves closing pore fluid drainage valves, then applying increments of isotropic confining stress (cell pressure) and measuring undrained pore pressure increase with each increment of confining stress. The ratio of pore pressure increase to confining stress increment is the B value. The main disadvantage of using the standard B-test procedure is the fact that effective confining stress increases, thereby recompressing the oil sand micro-fabric prior to performing other strength or compression tests (Agar 1984).

Wissa (1969) described an alternate procedure for evaluating the B parameter. The method is based on the fact that pore pressure response in fully saturated soils is independent of the magnitude of the back pressure, whereas pore pressure response varies with back pressure in unsaturated soils. The following steps were followed in computing the B parameter:

(1) in the same way that cell and back pressure were increased in alternate steps of 25 kPa, they were reduced to a desired value. In this study, the back pressure was reduced to a value between 500 to 750 kPa. As mentioned earlier, a minimum back pressure of 500 kPa was kept on the specimen at all times. During the reduction of cell and back pressure, the effective confining stress on the specimen was kept below 50 kPa;

(2) with pore pressure fluid drainage prevented, a 50 kPa increment of isotropic confining stress was applied;

(3) the pore pressure response was measured and the B value was calculated as a ratio of resulting increase in pore pressure to the cell pressure increment;

(4) pressure in the back pressure system was increased the same amount as the increment in cell pressure (i.e. 50 kPa). Pore fluid drainage valves were opened to back pressure. This restored the initial effective stress; and

(5) with the new back pressure level, steps (2), (3) and (4) were repeated. These incremental B-tests were conducted for at least three pressure levels to ensure that the pore pressure response had stabilized.

4.4.6 Consolidation

The standard drained triaxial test is a compression test in which the specimen is first consolidated under an equal all-round pressure, and is then caused to fail by increasing the axial stress under condition of full drainage (Bishop and Henkel 1962).

The specimen's volume change was monitored as soon as a change in the effective confining pressure occurred. Consolidation was completed when no significant movement of the water occurred. The volumetric strain due to the consolidation process was calculated as: $\Delta V_c / V_o$ in which ΔV_c is the volume change due to consolidation and V_o is the initial volume before consolidation. As described earlier, this volumetric strain was used in Equation 4.7 to calculate the volume compressibility of the soil skeleton.

After obtaining the volumetric strain due to consolidation, the specimen's height and cross sectional area were corrected by following equations (Head 1986):

$$L_c = L_o \left(1 - \frac{1}{3} \frac{\Delta V_c}{V_o} \right)$$
[4.8]

$$A_c = A_o \left(1 - \frac{2}{3} \frac{\Delta V_c}{V_o} \right)$$
[4.9]

where:

L_o is the initial height of the specimen,

L_c is the corrected height of the specimen,

A_o is the initial cross-sectional area of the specimen,

A_c is the corrected area of cross-section of the specimen.

4.4.7 Rate of strain

In a drained triaxial compression test, the rate of loading or deformation is chosen so negligible excess pore pressure remain in the specimen at any time during the application of the axial load and particularly at failure (Bishop and Henkel 1962). The rate of strain is slow enough to ensure the dissipation of any excess pore pressure.

The rate of strain for cohesive soils is obtained from the consolidation results. For soils of higher permeability, the calculated test duration becomes small. Bishop and Henkel (1962) noted that as sands are free draining, the duration of the test is governed by the necessity of being able to take accurate readings of load and volume change. They suggested that a test time of about 1 hour is suitable. Head (1986) suggests that for soils of high permeability for which the calculated time for test is small, the test period should

not be less than about three hours so to allow enough time to take readings and to make the necessary adjustments.

To be consistent with the work of other researchers, a three hours duration was chosen for the tests in this study.

4.5 Permeability test procedure

The apparatus setup for triaxial permeability testing was described in Section 2.6. The differential pressure transducer is an important part of a permeability test. Issues regarding the correct set up and calibration of this transducer were discussed in Section 2.10.

Prior to the test the syringe pump was filled with 500 ml deaired water. Before mounting a test specimen, using the syringe pump, the entire tubing system was flushed and filled with deaired water.

4.5.1 Syringe pump

The syringe pump used in this study was operated in a constant flow mode. Although the pump was designed for precise, pulse-free delivery of liquids, its performance was tested against a volume change measuring device (Section 2.10). Figure 4.13 shows the syringe pump performance. Three constant flow rates of 40, 15 and 4 ml/hour were tested. While the syringe pump produced a constant pulse-free flow the actual flow rates were different from the set flow rates. The difference was higher in the smaller flow rates. In this study the computed flow rates (Figure 4.13) were used in the permeability calculations.

The flow rate to be used in a test and the direction of flow in a permeability test on an oil sand specimen is very much a function of the phenomenon called fines migration, which is described in the following section.

4.5.2 Fines migration

Fines migration has been recognized as a cause of permeability reduction in both consolidated and unconsolidated sandstone for many years (Kwan et al. 1988). Permeability damage due to fines migration can be caused by both chemical and mechanical effects. Mechanical flow forces can induce fine particles to migrate into pore throat constrictions resulting in decreased in absolute permeability. The movement of fines due to these flow forces has been associated with the flow velocity and is not restricted to fines composed solely of clay minerals (Kwan et al. 1988). Chemical interactions can also induce fines mobilization and clay swelling, often in concert with mechanically induced fines movement.

Since only one fluid, distilled water, was used in the permeability tests, the role of chemical effects was not examined during the course of this study.

The extent of fines movement and permeability reduction due to the flow forces was a function of the velocity of the flow and its duration. So it is preferred to conduct a permeability test with a low flow rate and for a short period of time. However as mentioned earlier the duration of tests in constant strain rate tests was predetermined. The following summarizes the permeability test procedure used in this study:

(1) if the specimen was dry, like the undisturbed specimen, an upward flow rate of 15 ml/h was used to flush the specimen with 50 cc of de-aired water. This water flooding took 200 minutes;

(2) before the start of the permeability test, the bypass valve of the differential pressure transducer (Figure 2.9) was closed and the transducer's zero reading was taken;

(3) by changing the configuration of valves on the flow reversing board the direction of flow in the specimen was changed to downward. A flow rate of 40 ml/hour was conducted through the specimen for at least 30 minutes and the differential pressure transducer readings were recorded;

(4) the measurements of the transducer were plotted against time. This was done to make sure that there was not a substantial fine migration phenomenon happening. Figure 4.14 shows the resulted plots for two tests. It is seen that the differential pressure transducer readings are stable;

(5) the downward flow rate of 40 ml/hour was resumed and the triaxial shear test was started;

(6) the plot described in step (4) was a linear line with a very gentle slope. This slope was measured and was used to correct the differential pressure transducer readings for the rest of the test; and

(7) by following these steps and procedures described in Sections 2.6 and 2.11 the hydraulic conductivity was computed for the tests.

Although this method showed to work for the start of the test, it was seen that after one hour or so the absolute permeability reduction due to fine migration started. This was evident by constant or slightly decreasing absolute permeability while specimens volume was still expanding (Chapter 8).

4.6 Analysis of data

After the end of the test the specimen was transferred into a container and oven dried over night. Care was taken to collect all particles of the specimen as the obtained dry

weight of the specimen was used in calculating the dry density and void ratio of reconstituted specimens.

After measuring the dry weight of the specimen, the material was washed over No. 325 sieve (45 μm) to remove the fine particles. The remaining sand was oven dried again and weighed. The difference between these dry weights was the portion of the fines in the specimen. This material was then dry sieved as explained in Section 4.2.1.

No change in the grain size distribution of the specimens before and after triaxial shear was observed. This was due to low confining stresses used in this study and the fact that oil sand is mainly from quartz.

After applying the correction for consolidation (Equations 4.8 and 4.9) the initial values for specimen's height, cross-sectional area and volume was obtained. Sections 2.8 to 2.11 explain the necessary corrections in order to obtain axial load, axial displacement and volume change. Thus axial and volumetric strains were calculated. The cross-sectional area of specimen at any time was obtained by Equation 2.3. With this value and the axial load the deviatoric stress was computed.

It should be mentioned that the zero reading for the axial strain was the moment that the specimen started taking the axial load. Therefore the axial load must be obtained first and then the axial strain calculated.

Cell and back pressure values were obtained through the readings of corresponding transducers. These readings were corrected for the zero readings explained in Section 4.4.

There were corrections for cell pressure and volumetric strain due to the use of latex rubber membranes in the triaxial tests. These corrections are discussed in the Section 4.6.2.

After necessary corrections to the readings of differential pressure transducer as described in Sections 2.11 and 4.5 the induced head loss was computed. The absolute permeability was then calculated by Equation 3.14 as described in Chapter 3.

4.6.1 Effect of temperature

It is shown in Chapter 8 (Equation 8.3) that the hydraulic conductivity, k, is not constant for a given soil but is related to the dynamic viscosity of the fluid (water), denoted by η_w. Viscosity varies with temperature and in the case of water increases by about 30% from 20° C to 10° C . Therefore the water temperature should always be taken into account when performing permeability tests (Head 1982). During this study the water temperature was monitored and recorded.

It is convenient to relate permeability data to a standard temperature of 20° C. The relationship between the dynamic viscosity of water and temperature is given in

appropriate references (Head 1980). If a permeability test carried out at T° C yields a coefficient of permeability, k_T, the corresponding value at 20° C, k_{20}, is calculated from equation:

$$k_{20} = k_T \left(\frac{\eta_T}{\eta_{20}} \right)$$

[4.10]

Where, η_T, and, η_{20}, are the dynamic viscosity of water at temperature T° C and 20° C respectively.

4.6.2 Membrane corrections

Membrane corrections are discussed under the following headings:

(1) membrane restraining effect
(2) membrane penetration effect on volume change

4.6.2.1 Membrane restraining effect

The restraining effect of the rubber membrane enclosing a triaxial specimen makes a small contribution to the confining pressure on the specimen. The influence of the rubber membrane on the measured strength of specimens in conventional triaxial compression tests at confining stresses greater than 100 kPa is considered to be negligible (Oldakowski 1994). However in the case of tests with different stress paths, which was carried out in this study, the effective confining stress at failure was as low as 15 kPa. Hence neglecting the restraining effect of the membrane may lead to significant errors in calculated stress ratios.

In the case of a sand specimen in a drained test under a very low confining stress, there is an increase in specimen diameter and the membrane stretches and exerts pressure on the specimen. This added confining pressure has to be added to cell pressure when the effective confining stress is calculated.

The confining pressure correction is derived as follows (Oldakowski 1994):

- The extension modulus of the rubber membrane material, which is required for calculating the membrane correction, is defined as:

Modulus M = tension per unit width / strain

Head (1982) described the extension modulus test on rubber membrane material. For data from an extension modulus test on a rubber membrane with 38 mm diameter and 0.3 mm thickness, Head (1982) suggested a value of 0.43 N/mm for the extension modulus. Oldakowski (1994) reported an extension modulus of 0.4 N/mm for a 0.28 mm thick

membrane. Due to the similarity in membrane thickness and diameter, the value of 0.43 N/mm was chosen for the extension modulus of the rubber membrane.

- The pressure exerted on a specimen by an extended membrane (Figure 4.15) is equal to:

$$p = (2FL)/(DL) = 2F/D$$ [4.11]

where:

p is the pressure exerted on the specimen,
F is the tension per unit width,
D is the membrane diameter,
L is the length of the membrane.

From the extension modulus definition:

$$F = M(D - D_o)/D_o$$ [4.12]

in which D_o is the initial diameter of the membrane.

Substituting Equation 4.12 in Equation 4.11 yields:

$$p = 2M(D - D_o)/(DD_o)$$ [4.13]

Equation 4.13 was used to determine the confining pressure correction due to membrane extension.

4.6.2.2 Membrane penetration effect on volume change

In a triaxial test on a granular soil a volume change measurement made as a result of an increase in confining pressure will be influenced by the penetration of the membrane enclosing the specimen into the voids between particles at the interface. This is known as the membrane penetration effect or the membrane compliance and is illustrated in Figure 4.16. It can affect volume change measurements on both the back pressure line and cell pressure line. The effect has been shown to depend mainly on particle size, and to a much lesser extent on state of packing and particle shape, as well as on membrane thickness and stiffness (Head 1986). It applies to materials of medium sand size and upward, and is of greatest significance with large diameter specimens. The effect is negligible for fine-grained soils, since even very thin membranes can not penetrate significantly into small voids.

The most dominant factors affecting membrane penetration effect are (Nicholson et al. 1993):

(1) grain size, including soil gradation,

(2) effective confining stress.

Historically researchers have always used the median grain size of a material, D_{50}, as the basis for compliance-volume relationships. Membrane compliance magnitudes are correlated with mean particle size, D_{50}.

Nicholson et al. (1993) noticed that virtually all materials examined by previous investigators had been uniformly graded. They found that for a wide range of non-uniformly graded sandy soils and gravelly soils, membrane compliance was much better correlated with smaller particle sizes, D_{20}, than with mean grain size. D_{20} is the particle size for which 20% of particles are finer. This is not surprising, as membrane penetration is a phenomenon associated primarily with the interstitial voids between soil grains, and studies of both flow and soil filter characteristics have long recognized that soil particles finer than the mean grain size control the characteristics of these inter-particle voids. Figure 4.17 schematically illustrates how the smaller particles in a soil gradation have a controlling influence on membrane compliance characteristics of more broadly graded soils. In Figure 4.17(a), a uniformly graded soil exhibits considerably more penetration than the more broadly graded soil of Figure 4.17(b), where finer particles partially fill the peripheral sample voids between the larger soil grains.

Nicholson et al. (1993) suggested the following empirical relationship between S, membrane compliance induced volume change per unit area of membrane per log-cycle change in effective confining stress, σ'_3 and D_{20} grain size (Figure 4.18):

$$S = 0.0019 + 0.0095 D_{20} - \left(0.0000157 D_{20}^2\right)$$ [4.14]

where S is in ml/cm^2 and D_{20} is in mm.

Sands used in this study had a D_{20} of 0.12 mm or less. As it can be seen in Figure 4.18 the membrane compliance obtained from Equation 4.14 is negligible for these materials. Therefore a membrane compliance correction was not performed in this research program.

4.7 Summary

- An objective of this study was to produce reconstituted oil sand specimens as dense as possible so that a better resemblance of results between reconstituted and undisturbed specimens could be achieved. To attain this goal different methods of preparing a reconstituted triaxial sand specimen were evaluated. Experimental equipment and test set up common to these procedures were described.

- A method developed during the course of this study, the wet vibration method, proved to be capable of producing dense uniform sand specimens. Steps involved in

setting up a triaxial test along with the wet vibration method were specified. Special attention was made to produce a saturated specimen.

- Procedures involved in preparing an undisturbed specimen, its test set up and saturation technique were described.

- Full saturation is vital in a permeability test. In the course of this study different techniques of specimen saturation were evaluated and specimen saturation by back pressure was chosen. A proper B-test, an integral part of the saturation procedure, was defined.

- In a flow-pump method of permeability testing a constant pulse-free flow is essential. The flow rates of the syringe pump used in this study were examined. The flow rate to be used in a permeability test on oil sand specimen is a function of the fines migration. In order to minimize the problem of fines migration a procedure specifying flow rate and direction of flow in different stages of a permeability test was devised.

- The required corrections and calculations in the analysis of the resulting data were described. They included the effects of temperature and the membrane corrections.

Table 4.1 Summary of specimen properties

Test No.	Test Configuration	Material Type	Preparation Method	Apparatus Type	ρ_{dmin} (g/cm³)	ρ_{dmax} (g/cm³)	ρ_d (g/cm³)	Dr (%)	Void Ratio	Porosity (%)	H (mm)	D (mm)
5	Conventional	1st Mixed Sand	Dry Tamping	Conventional	1.47	1.744	1.71	89.3	0.55	35.6	100.08	52.00
6	Conventional	1st Mixed Sand	Dry Tamping	Conventional	1.47	1.744	1.649	69.1	0.61	37.9	101.38	52.00
7	Conventional	1st Mixed Sand	Dry Tamping	Conventional	1.47	1.744	1.69	82.9	0.57	36.3	98.65	52.00
8	Conventional	1st Mixed Sand	Dry Tamping	Conventional	1.47	1.744	1.7	86.1	0.56	36.0	99.29	52.00
9	Conventional	1st Mixed Sand	Dry Tamping	Conventional	1.47	1.744	1.702	86.8	0.56	35.9	99.19	52.00
10	Conventional	1st Mixed Sand	Dry Tamping	Conventional	1.47	1.744	1.677	78.6	0.58	36.8	98.64	52.00
11	Conventional	1st Mixed Sand	Dry Tamping	Conventional	1.47	1.744	1.707	88.4	0.56	35.7	98.05	52.00
12	Conventional	1st Mixed Sand	Dry Tamping	Conventional	1.47	1.744	1.703	87.1	0.56	35.9	98.30	52.00
13	Conventional	1st Mixed Sand	Dry Tamping	Conventional	1.47	1.744	1.702	86.8	0.56	35.9	98.50	52.00
14	Conventional	1st Mixed Sand	Dry Tamping	Conventional	1.47	1.744	1.689	82.5	0.57	36.4	99.27	52.00
15	Conventional	1st Mixed Sand	Dry Tamping	Stress Path Cell	1.47	1.744	1.763	105.8	0.51	33.6	98.14	51.70
16	Conventional	1st Mixed Sand	Dry Tamping	Stress Path Cell	1.47	1.744	1.73	95.7	0.54	34.9	99.86	51.80
17	Conventional	1st Mixed Sand	Moist Tamping	Stress Path Cell	1.47	1.744	1.636	64.6	0.63	38.6	104.60	51.82
18	Conventional	2nd Mixed Sand	Water Pluviation	Stress Path Cell	1.417	1.664	1.605	78.9	0.65	39.4	106.30	51.57
19	Conventional	2nd Mixed Sand	Water Pluviation	Stress Path Cell	1.417	1.664	1.616	83.0	0.64	39.0	109.74	50.70
20	Conventional	2nd Mixed Sand	Slurry Deposition	Stress Path Cell	1.417	1.664	1.596	75.6	0.66	39.8	108.93	51.06
21	Conventional	2nd Mixed Sand	Slurry Deposition	Stress Path Cell	1.417	1.664	1.627	87.0	0.63	38.5	88.70	50.26
22	Conventional	2nd Mixed Sand	Wet Vibration	Stress Path Cell	1.417	1.664	1.561	62.2	0.69	41.0	99.45	50.63
23	Lubricated Ends	3rd Mixed Sand	Wet Vibration	Stress Path Cell	1.452	1.679	1.744	123.8	0.52	34.3	38.91	37.74
24	Lubricated Ends	3rd Mixed Sand	Wet Vibration	Stress Path Cell	1.452	1.679	1.784	137.6	0.49	32.8	41.79	37.77
25	Lubricated Ends	3rd Mixed Sand	Wet Vibration	Stress Path Cell	1.452	1.679	1.802	143.7	0.47	32.1	36.29	37.50
26	Lubricated Ends	3rd Mixed Sand	Wet Vibration	Stress Path Cell	1.452	1.679	1.814	147.6	0.46	31.7	36.39	37.52
27	Lubricated Ends	Block Sample	Vertical Core	Stress Path Cell	1.452	1.679	1.757	128.4	0.51	33.8	36.90	38.75
28	Lubricated Ends	Block Sample	Vertical Core	Stress Path Cell	1.452	1.679	1.734	120.3	0.53	34.7	39.68	38.63
29	Lubricated Ends	Block Sample	Vertical Core	Stress Path Cell	1.452	1.679	1.753	127.0	0.51	34.0	39.32	38.13
30	Lubricated Ends	3rd Mixed Sand	Wet Vibration	Stress Path Cell	1.452	1.679	1.693	105.3	0.57	36.2	38.44	37.75
31	Lubricated Ends	3rd Mixed Sand	Wet Vibration	Stress Path Cell	1.452	1.679	1.725	117.1	0.54	35.0	40.99	37.16
33	Lubricated Ends	3rd Mixed Sand	Wet Vibration	Stress Path Cell	1.452	1.679	1.702	108.6	0.56	35.9	39.46	37.73
34	Lubricated Ends	3rd Mixed Sand	Wet Vibration	Stress Path Cell	1.452	1.679	1.668	95.8	0.59	37.2	37.68	37.72
35	Lubricated Ends	Block Sample	Vertical Core	Stress Path Cell	1.452	1.679	1.751	126.3	0.49	32.9	38.88	36.52
36	Lubricated Ends	Block Sample	Vertical Core	Stress Path Cell	1.452	1.679	1.757	128.4	0.51	33.6	38.96	36.22
37	Lubricated Ends	Block Sample	Vertical Core	Stress Path Cell	1.452	1.679	1.747	124.9	0.52	34.0	36.11	38.15
38	Lubricated Ends	Block Sample	Vertical Core	Stress Path Cell	1.452	1.679	1.744	123.8	0.52	34.1	39.47	38.42
39	Lubricated Ends	Block Sample	Vertical Core	Stress Path Cell	1.452	1.679	1.75	126.0	0.51	33.9	38.80	38.48
40	Lubricated Ends	Block Sample	Horizontal Core	Stress Path Cell	1.452	1.679	1.783	137.3	0.49	32.7	40.22	38.44
41	Lubricated Ends	Block Sample	Horizontal Core	Stress Path Cell	1.452	1.679	1.754	127.4	0.51	33.8	40.47	38.41
42	Lubricated Ends	Block Sample	Horizontal Core	Stress Path Cell	1.452	1.679	1.729	118.5	0.53	34.7	36.75	38.53
43	Lubricated Ends	Block Sample	Horizontal Core	Stress Path Cell	1.452	1.679	1.758	128.7	0.51	33.6	38.92	38.73

Table 4.2 Summary of maximum / minimum density tests

Material Type	Test No. / Average	$\rho_{d\,max}$ (g/cm³)	e_{min}	$\rho_{d\,min}$ (g/cm³)	e_{max}
1st Mixed Sand (MS1)	1	1.733	0.529	1.452	0.825
	2	1.744	0.519	1.457	0.819
	3	1.75	0.514	1.478	0.793
	4	1.755	0.51	1.481	0.789
	5	1.74	0.523	1.486	0.783
	Average	1.744	0.519	1.47	0.802
2nd Mixed Sand (MS2)	1	1.666	0.59	1.419	0.867
	2	1.667	0.589	1.413	0.875
	3	1.656	0.6	1.414	0.874
	4	1.672	0.585	1.411	0.878
	5	1.662	0.594	1.421	0.865
	6	1.661	0.595	1.425	0.859
	Average	1.664	0.592	1.417	0.869
3rd Mixed Sand (MS3)	1	1.674	0.583	1.443	0.836
	2	1.675	0.582	1.453	0.824
	3	1.685	0.573	1.454	0.822
	4	1.681	0.576	1.456	0.82
	5	1.679	0.578	1.455	0.821
	6	1.68	0.577	1.451	0.826
	Average	1.679	0.578	1.452	0.825

Table 4.3 Specimens degree of saturation

Test No.	Back Pressure (kPa)	C_s (kPa^{-1})	Void Ratio	Porosity (%)	B_{100}	B	Saturation (%)
23	933.5	5.00E-05	0.519	34.19	0.997	0.626	90.67
24	794	5.00E-05	0.485	32.68	0.997	0.592	90.31
25	870	4.54E-05	0.471	32.00	0.996	0.746	95.19
26	840	5.03E-05	0.460	31.51	0.997	0.644	91.44
27	738	1.07E-05	0.534	34.81	0.984	0.560	97.95
28	732	8.82E-06	0.560	35.91	0.980	0.632	98.80
29	684	1.07E-05	0.514	33.96	0.984	0.654	98.68
30	698.8	1.67E-05	0.568	36.22	0.989	0.585	97.32
31	698.4	1.48E-05	0.543	35.19	0.988	0.574	97.46
32	698.1	9.48E-06	0.550	35.48	0.982	0.597	98.55
33	689.7	8.20E-06	0.560	35.90	0.979	0.495	98.14
34	695.1	5.48E-06	0.591	37.15	0.967	0.566	99.10
35	695.6	1.40E-05	0.513	33.92	0.988	0.667	98.32
36	698.88	2.59E-05	0.508	33.70	0.994	0.821	98.63
37	692	1.78E-05	0.520	34.20	0.990	0.685	98.07
38	691	1.73E-05	0.522	34.31	0.990	0.574	96.98
39	691.8	1.78E-05	0.517	34.07	0.991	0.619	97.40
40	695.8	1.55E-05	0.488	32.81	0.990	0.710	98.43
41	692	1.40E-05	0.513	33.92	0.988	0.690	98.52
42	690.3	1.39E-05	0.535	34.85	0.988	0.634	98.15
43	695.1	1.45E-05	0.510	33.77	0.988	0.734	98.75
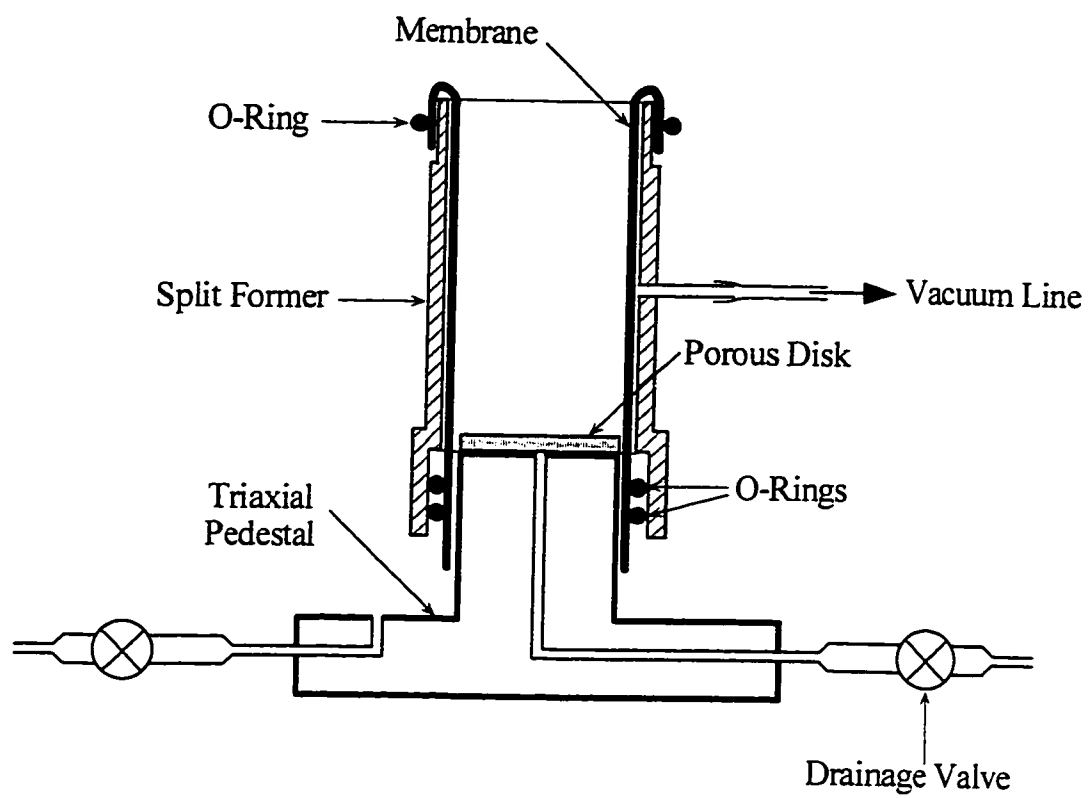
Figure 4.1 Split former set up
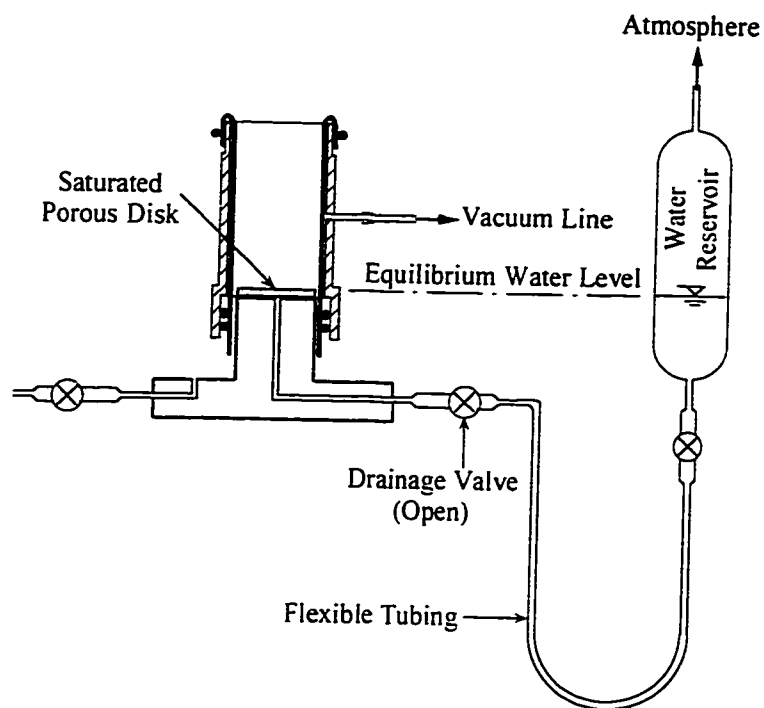
Figure 4.2 Set up for saturated sand
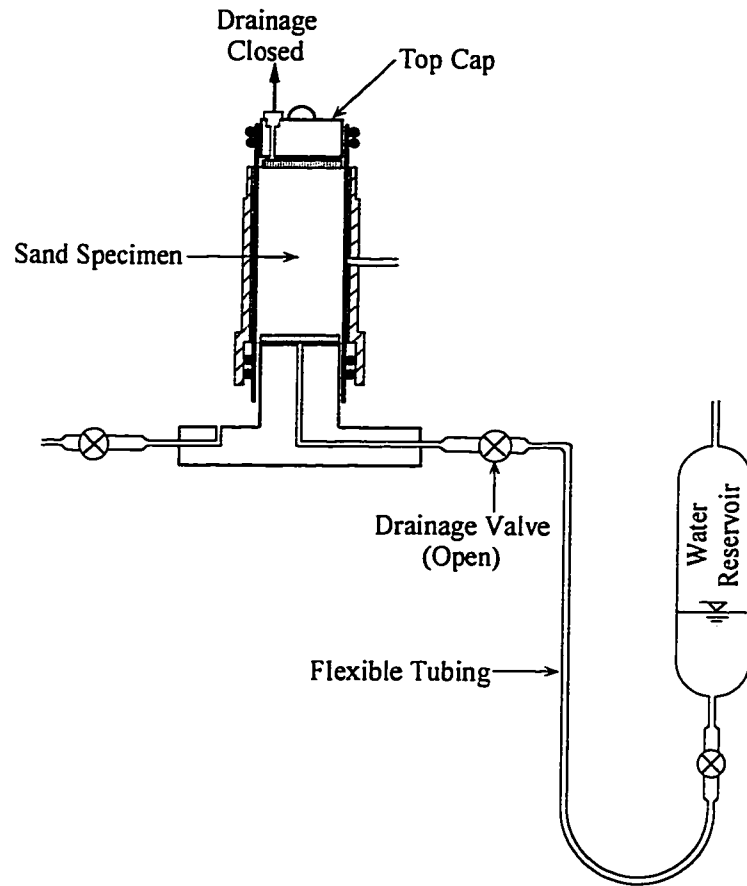
Figure 4.3 Application of suction to saturated sand specimen
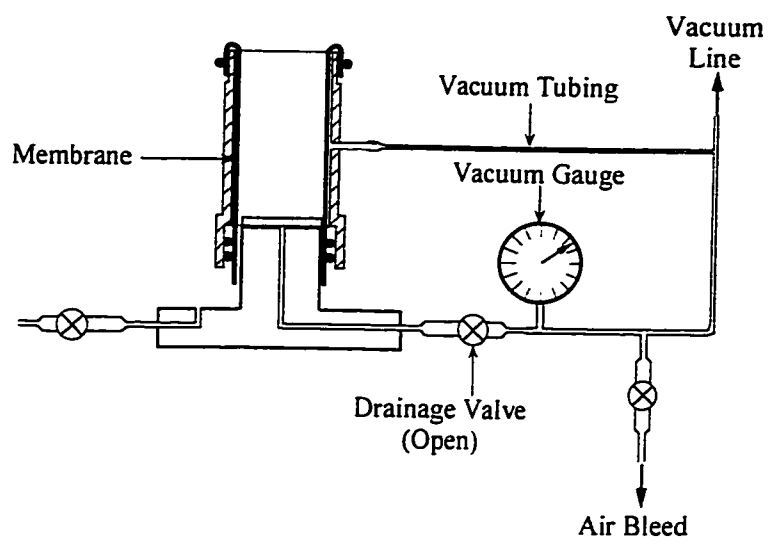
Figure 4.4 Set up for dry sand
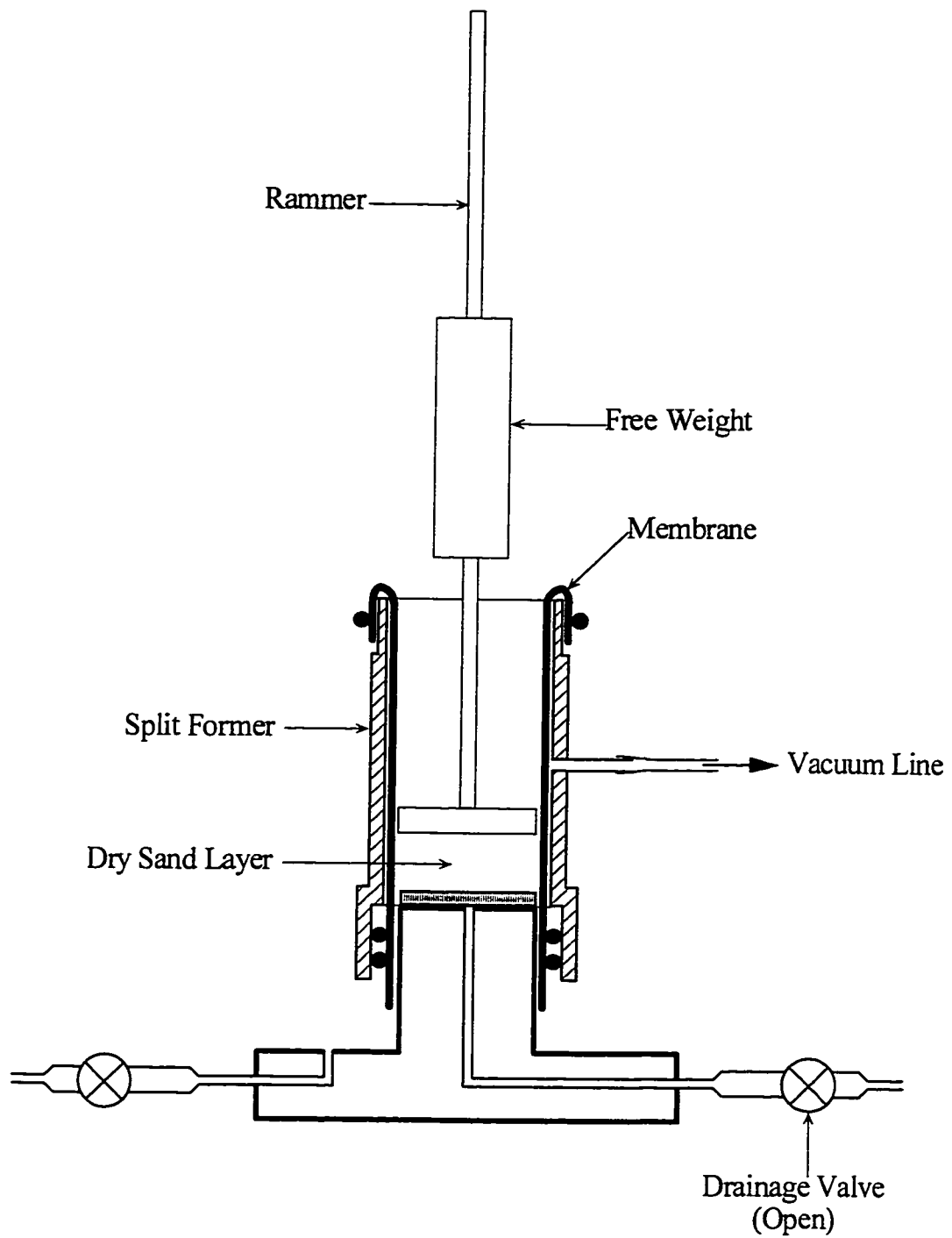
Figure 4.5 Dry tamping method
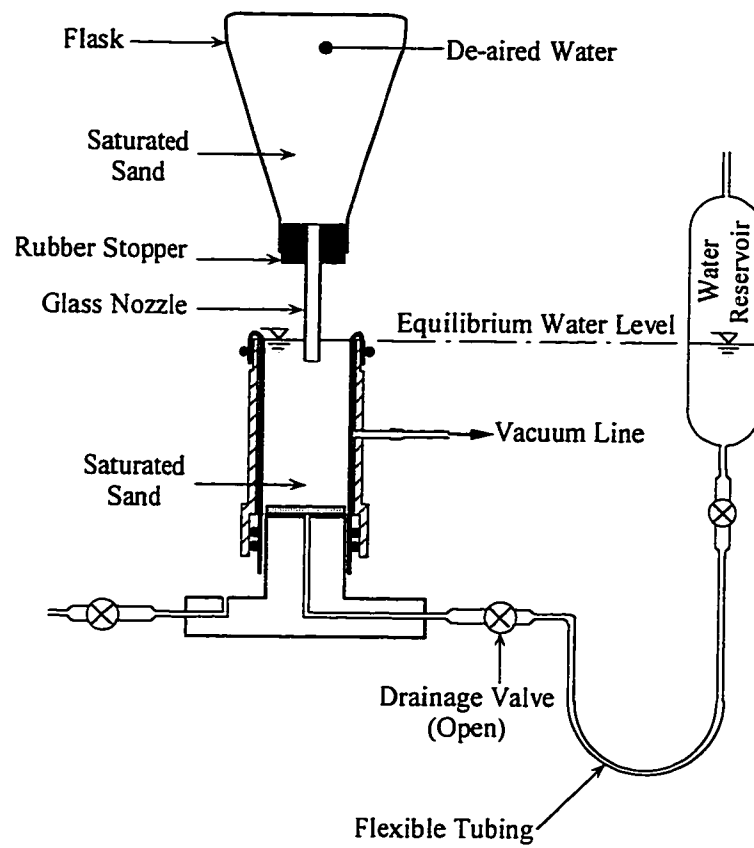
Figure 4.6 Water pluviation method
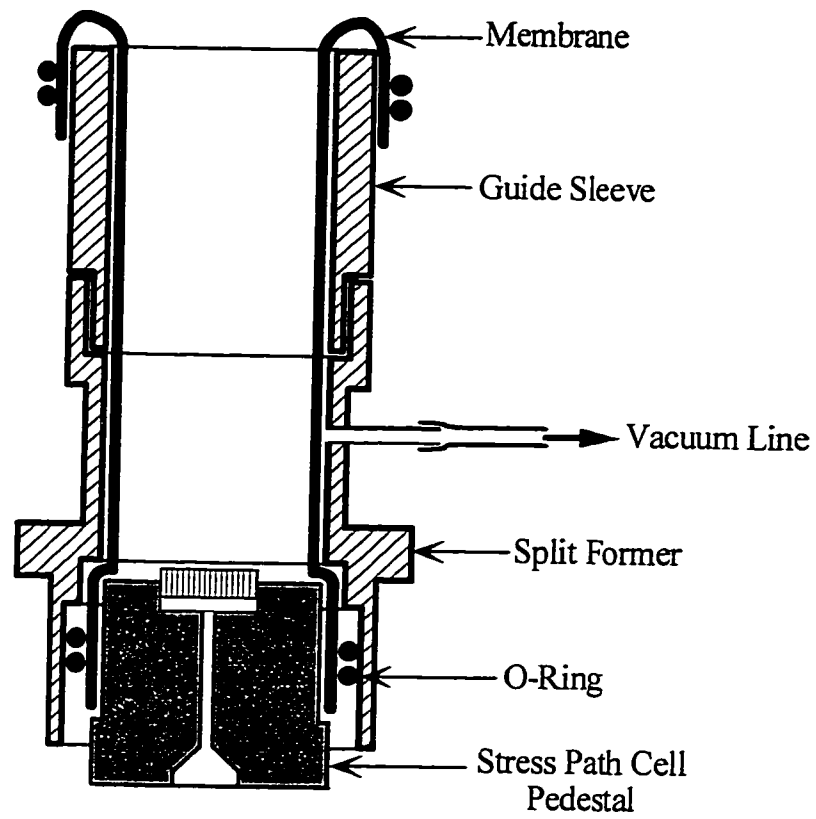
Figure 4.7 Split former for wet vibration method

PVC Tube

Split Former

Vacuum
Line

Equilibrium Water Level

Water Reservoir

Stress Path
Triaxial Cell

Flexible Tubing

Drainage Valve
(Open)
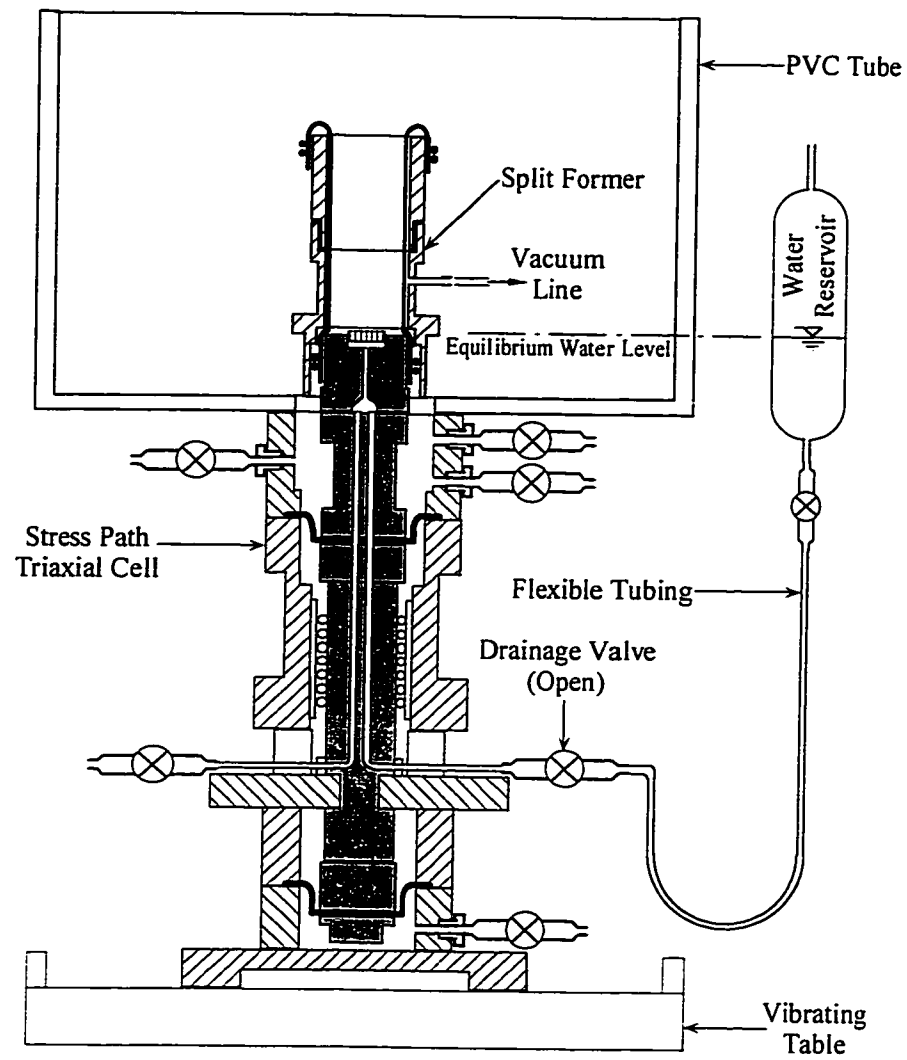
Vibrating
Table

Figure 4.8 Preparation set up for wet vibration method
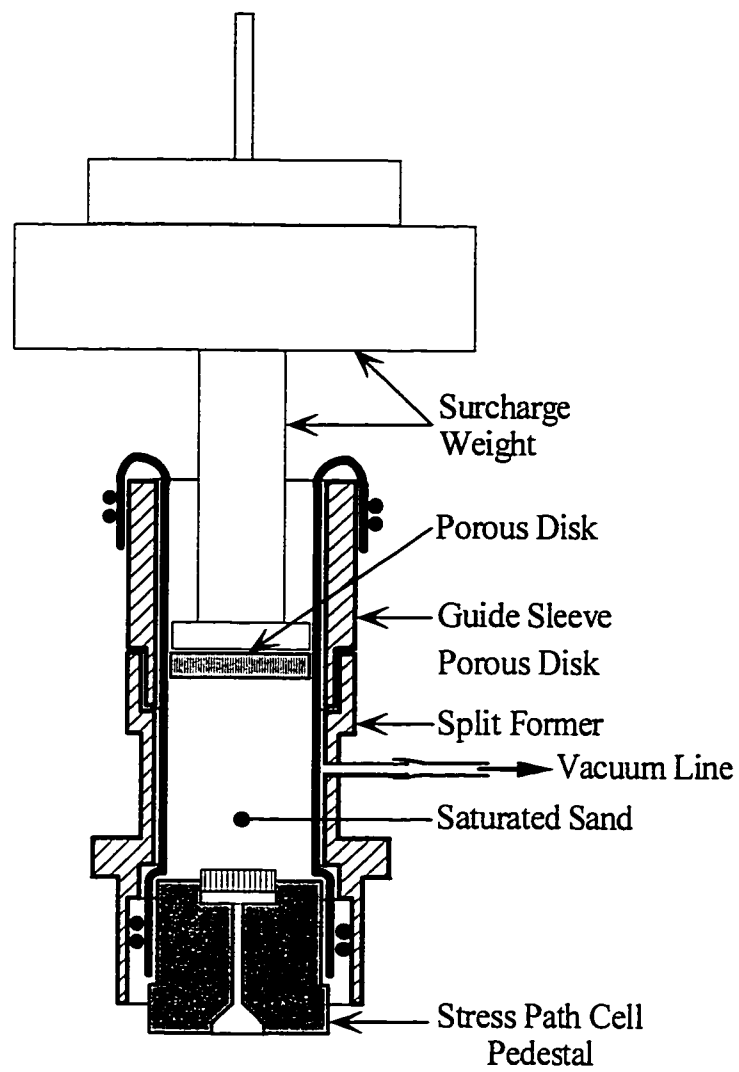
Figure 4.9 Wet vibration method
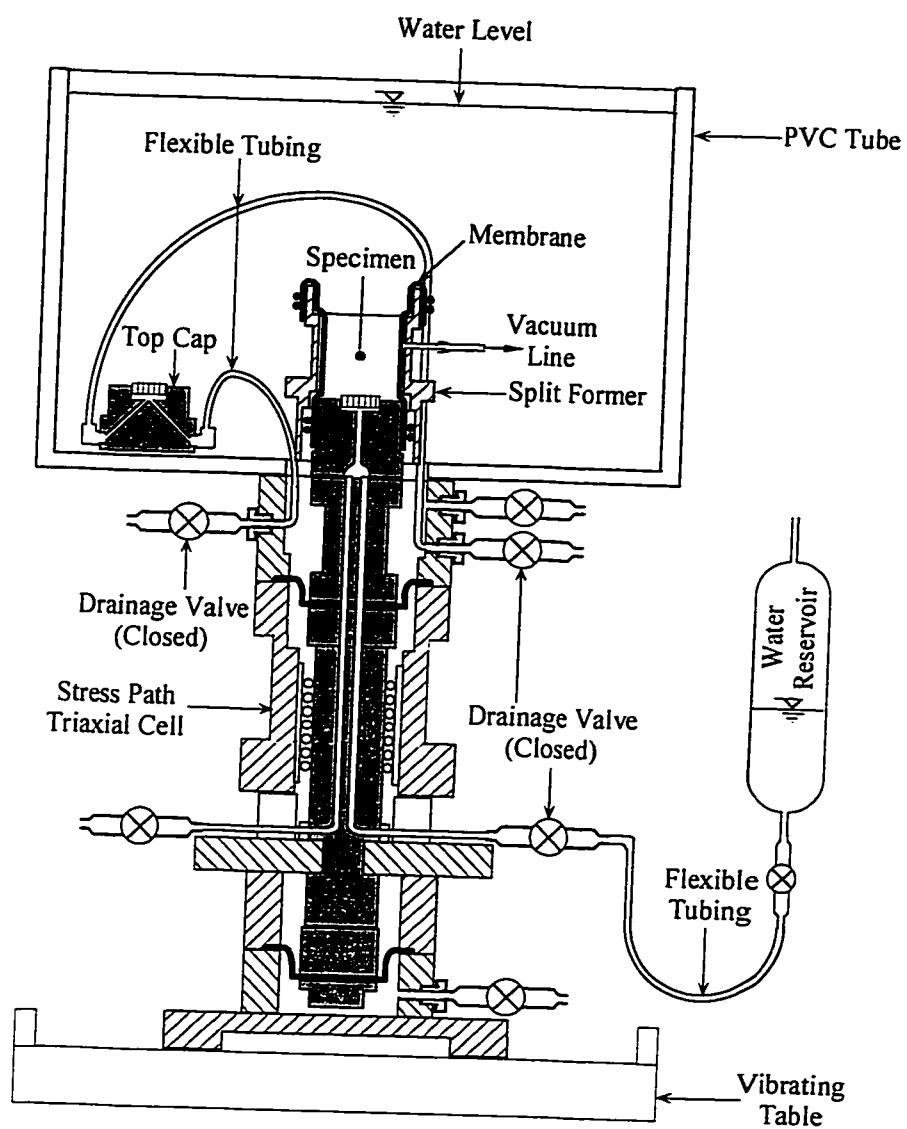
Figure 4.10 Installation of top cap in wet vibration method
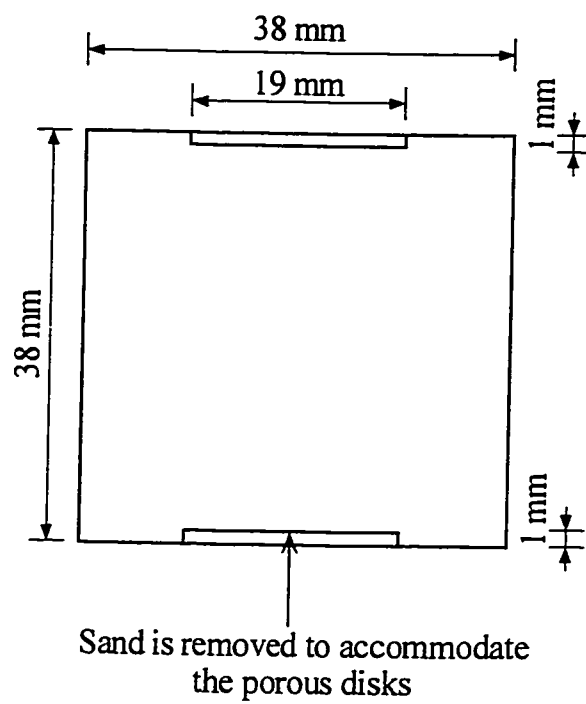
Figure 4.11 Dimensions of undisturbed specimens
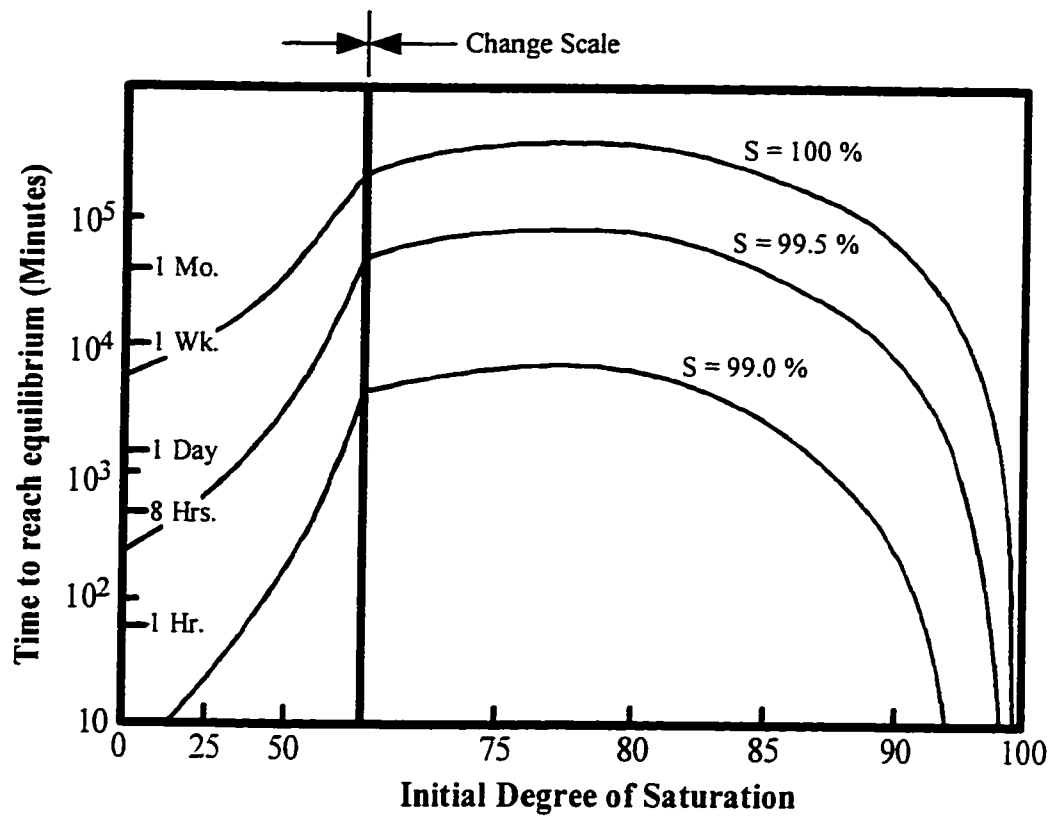
Figure 4.12 Time to reach a degree of saturation using back pressure
(Modified from Black and Lee 1973)
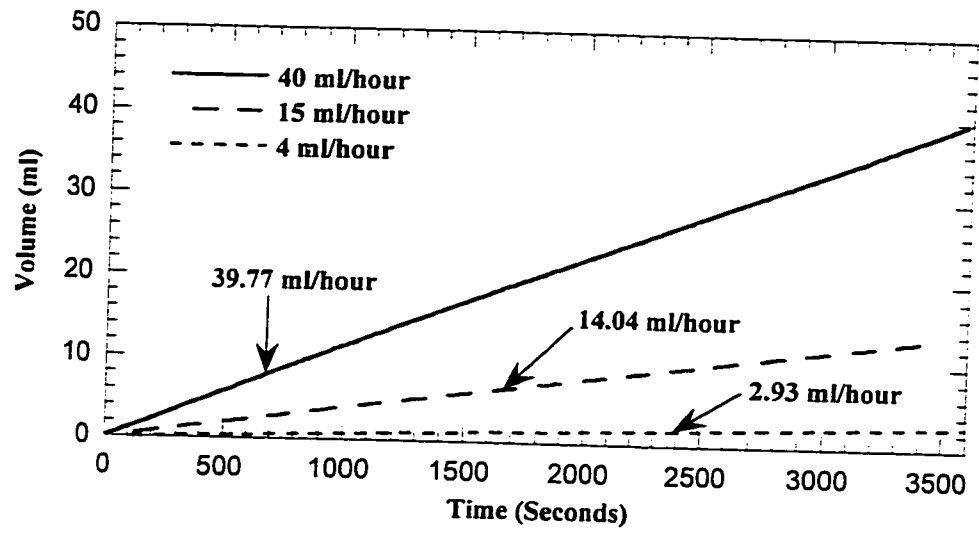
Figure 4.13 Syringe pump flow rates
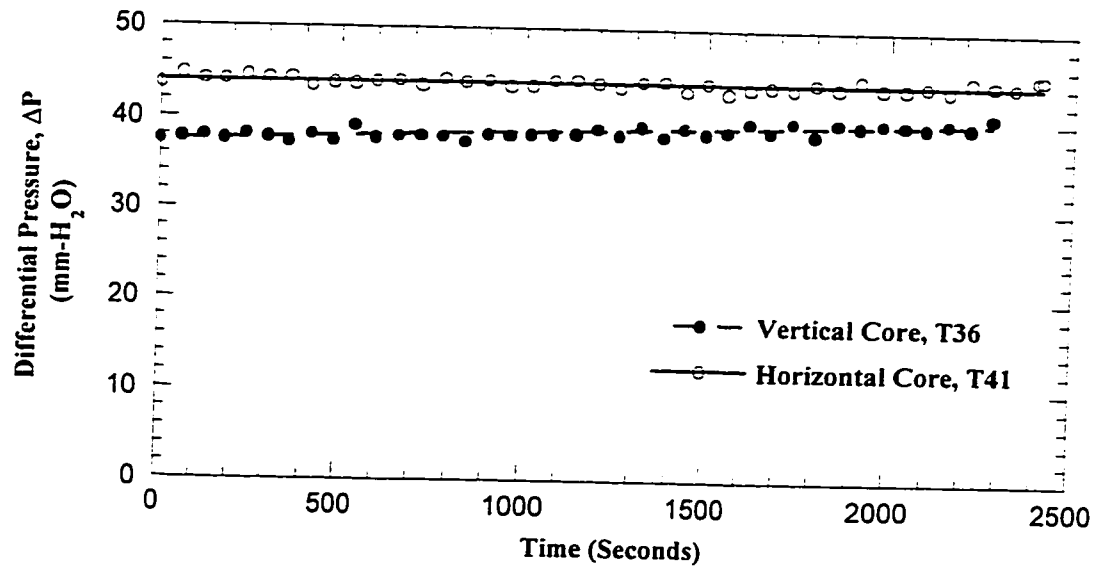
Figure 4.14 Fines migration test
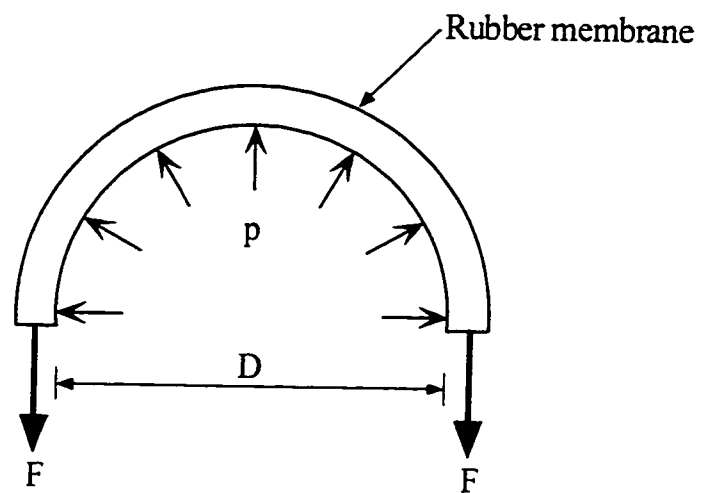
Figure 4.15 Confining pressure due to membrane extension
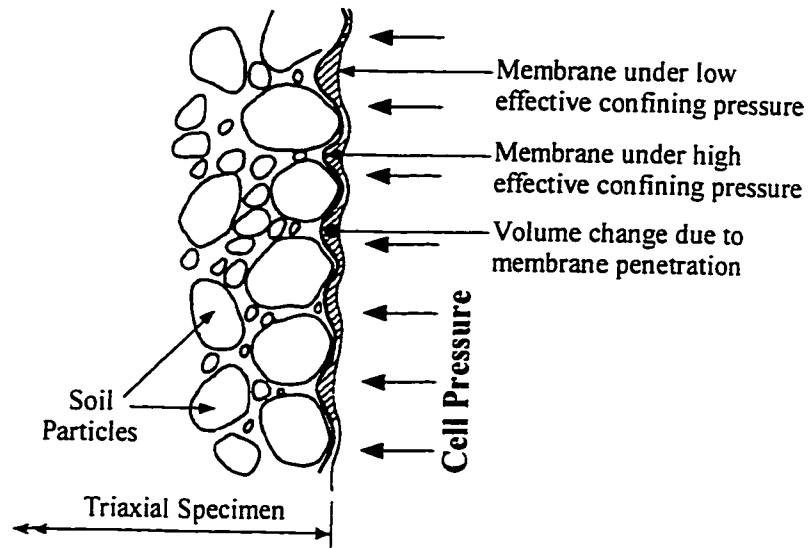
Figure 4.16 Membrane penetration effect in granular soils
(Modified from Head 1986)
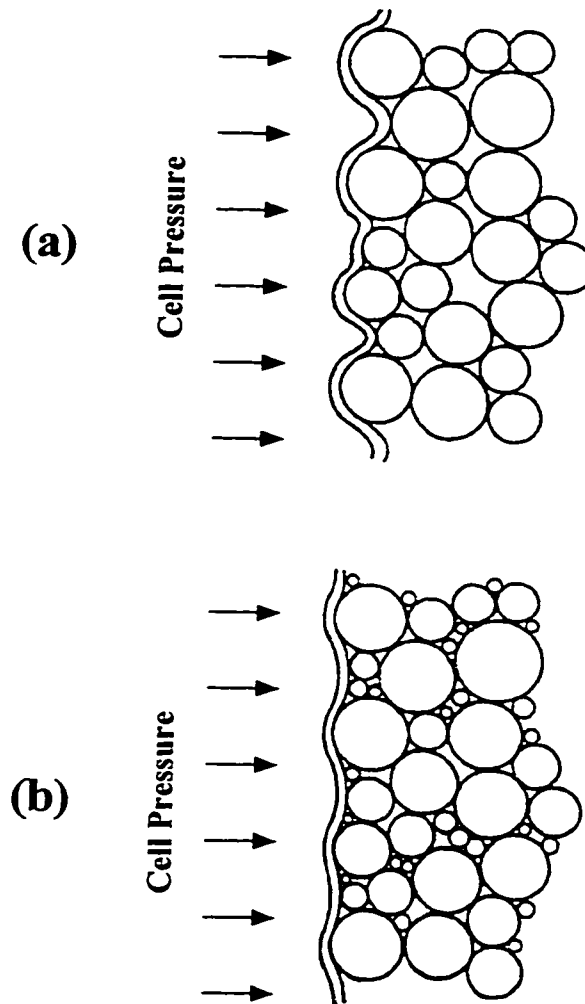
Figure 4.17 Schematic illustration of the controlling influence
of finer particles on the membrane compliance
(Modified from Nicholson et al. 1993)
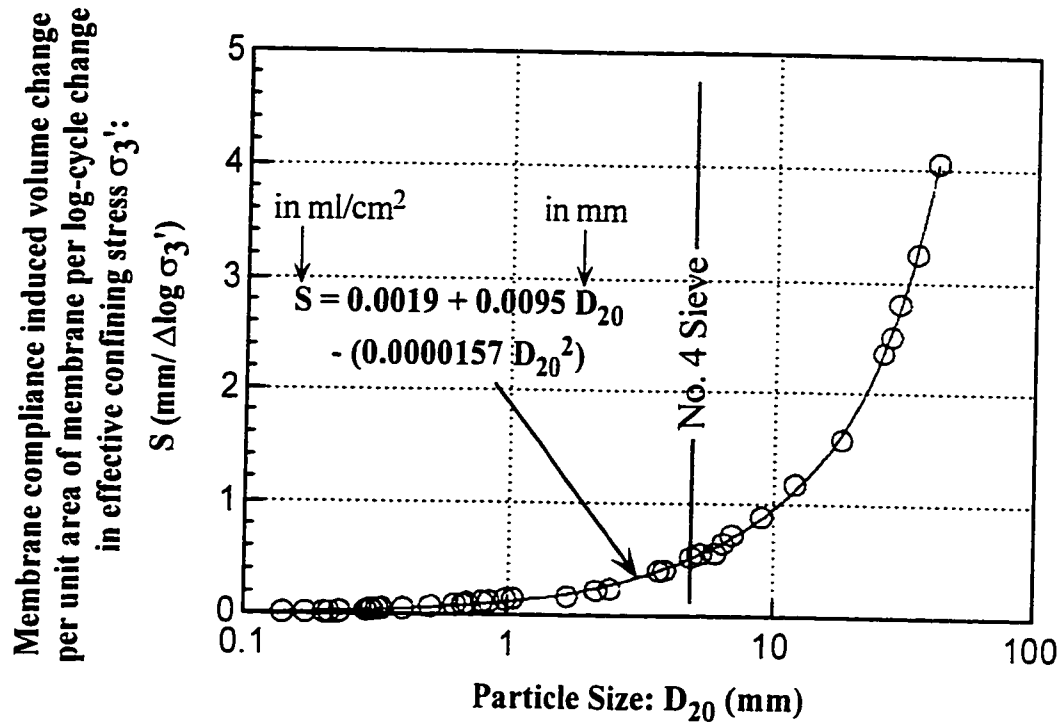
**Figure 4.18 Relationship between membrane compliance
and D20 particle size**
(Modified from Nicholson et al. 1993)

CHAPTER 5   THE FABRIC CHARACTERISTICS OF OIL SAND

5.1 Introduction

Many studies have shown that the mechanical properties of sands are not solely determined by density or void ratio. It has been pointed out that the structure or fabric of sands also can considerably affect their mechanical properties. Some of the important properties of sand are affected by the arrangement of the sand particles. Consequently, in order to understand the mechanical properties of sands, the properties and orientation of the particles must be studied.

5.2 Locked sands

Cohesionless sands are usually classified according to their relative density and a common distinction that is made is whether the sand is loose or dense. Dusseault (1977) suggested that another class of cohesionless sand exists in addition to loose and dense sands. They are called "locked sands". To differentiate locked sand from sandstone the following definitions were suggested by Dusseault (1977):

Locked sand: aggregate of dominantly sand-sized particles displaying little or no cohesion in a fully saturated, stress-free state. It is characterized by very high rates of dilation at failure and therefore a peak frictional strength considerably in excess of that displayed by dense sand.

Sandstone: an aggregate of sand-sized particles having either interparticle physical cementation, or a degree of interlock sufficient to give an appreciable stress-independent cohesion in a saturated state.

The geotechnical characteristics of locked sands were first identified as a result of research into the mechanical behavior of the Athabasca Oil Sands (Dusseault 1977, Dusseault and Morgenstern 1979), but the characteristics of locked sands are not peculiar to these sediments. It was shown (Dusseault and Morgenstern 1979) that locked sands exist elsewhere and are likely to be widespread. However the focus of this study is the McMurray Formation oil sands of the Athabasca Deposit.

Locked sands are commonly encountered in nature at relative densities greater than 100%. The high density is a function of the geological history of the material and gives the essentially cohesionless material a very low compressibility and high strength properties. This behavior may be understood in terms of particle shapes and textures that are characteristic of locked sands. A distinctive fabric develops as a result of diagenetic

processes which reduce porosity (Dusseault 1977). Geological age and quartzose mineralogy seem to be prerequisites for locked sand.

Dusseault (1977) used optical and scanning electron microscopy to observe the intergranular fabric of oil sand. They were used to identify those physical characteristics responsible for the behavior of locked sands, and to obtain an understanding of the geological history responsible for these materials. The resulting images display a subtle, interlocked texture characterized by a relatively high incidence of long and interpenetrative grain contacts and a sutured structure of low porosity. This is the logical consequence of the continuation of solution and recrystallization of quartz.

Figure 5.1 is a typical result of scanning electron microscopy in the current study and shows the fabric of undisturbed specimens of locked sand. Interpenetrative and long contacts are clearly visible.

An artificial or recently deposited assemblage of rigid particles displays only tangential intergranular contacts. Artificial densification, by any means other than grain rupture, does not significantly alter the characteristic tangential fabric. At the other end of geological spectrum, orthoquartzites of low porosity show a great intimacy of intergranular contact. Dusseault (1977) looked at the nature of the grain-to-grain contacts observed in locked sands. He identified four types of intergranular contacts:

(1) tangential;
(2) straight;
(3) concavo-convex (or interpenetrative);
(4) sutured (or micro-stylolitic).

Figure 5.2 shows these descriptive fabric classifications.

In the case of McMurray Formation oil sands (Figure 5.3), the incidence of tangential contacts is high, but straight and interpenetrative contacts are also relatively common (Dusseault and Morgenstern 1978).

The data generated in the scanning electron microscope studies by Dusseault (1977) constitute direct observational proof of the diagenetic model for "locked sands". Definite evidence of subtle diagenetic grain fabric was visible in all samples.

Grain solution, preferentially at grain contact points where stresses are highest, is an extremely effective porosity-reduction agent (Dusseault 1977). Recrystallization often occurs in the form of uniform overgrowth shortly after deposition because of an excess of silica in solution. Either solution or recrystallization alone could result in an interlocked structure.

Both crystal overgrowth and solution features can be observed in the McMurray Formation oil sands. Oil sands display grain roundness ranging from very angular to

very well rounded. The mixed nature of the McMurray Formation grains can be attributed to significant amounts of solution and overgrowth processes (Dusseault 1977).

Which particular process has been dominant is not important to engineering behavior, since both phenomena, or either phenomenon, can give rise to the cohesionless, highly dilative behavior exhibited by oil sands.

Dusseault (1977) concluded that the source of the unusually high strength of locked sands is a result of a characteristic diagenetic fabric identifiable by microscopic methods. Either solution or overgrowth may be responsible for the strength behavior, and evidence for both processes exists. Microscopic studies have proved invaluable in arriving at a rational explanation of the stress-strain-strength behavior of locked sands.

5.3 Structure of oil sand

The two dominant physical characteristics of oil sand are the quartzose mineralogy and the large quantities of interstitial bitumen (Dusseault and Morgenstern 1978). The quartz grains in oil sand are 99% water-wet, the sand is dense and consequently has a large number of contacts per grain (Figure 5.4). The majority of oil sands have small quantities of clay-sized material. These fines consist mainly of clay minerals, specifically, kaolinite and illite (Dusseault 1977).

Dusseault (1977) suggested that in the oil-rich oil sands, fine materials are hydrophilic and are concentrated in the water layer while bitumen and gas occupy the remainder of the pore space. The water-wet nature of oil sands means that bitumen occupies interstitial space and the water phase forms a continuous net around the sand grains (Dusseault and Morgenstern 1978). Figure 5.4 is considered at present to be representative of the in situ structure of oil sand (Dusseault and Morgenstern 1978).

Oil sands are usually saturated with bitumen and water in situ and contain varying amounts of dissolved gas. As discussed in Chapter 1, during coring and sampling the oil sand core experiences a decrease in effective stress and pore pressure. The drop in pore pressure causes gas evolution. Expansion of the oil sand specimen thus occurs as dissolved gases evolve and expand. This phenomenon disrupts the oil sand structure.

To avoid this problem, specimens obtained from a block of bitumen-free oil sand were used in this research program. This block sample of bitumen-free sand was taken along the banks of the High Hill River, approximately 60 kilometers east of Fort McMurray, Alberta (Figure 1.8).

Since this block of locked sand is bitumen-free, there was no disturbance to the fabric of the specimens cored out of the block sample.

5.4 Structure of dry bitumen-free oil sand

The bitumen-free block sample was completely dry in situ. This is probably due to the presence of a shale cap at top of this oil sand formation (Figure 1.4 and Plate 1). The block had dimensions of 22 cm by 22 cm by15 cm (Figure 5.10). It was a hard intact block sample with bright color. When rubbed, it was slightly friable with some dust coming off. Specimens cored out of the block possessed considerable cohesive strength in the dry state. However when left in water they merely kept their shape and had no strength. A slight load caused them to collapse. The reason for this behavior is explained further on.

In the course of this study a series of scanning electron microscope images were acquired from the specimens obtained from the bitumen-free undisturbed block sample. Figure 5.5 shows that the individual grains are welded into a coherent mass by an accumulation of fines at contact points. Figure 5.5 is a result of the enlargement of the upper left corner of Figure A43 (Appendix A). Figure A43 is the only image in the nine figures (Figures A38 to A46) that shows cracks in the areas of fines accumulation. Figure 5.5 was selected on purpose since due to the presence of the cracks the location of fines accumulation is easily distinguishable. Even though Figure 5.5 is not representative of the SEM specimens, it can be seen from the interlocked particles and the lack of relative movement between the grains that the interpenetrative structure of oil sand is intact. Therefore these cracks do not constitute disturbance.

Figure 5.6 illustrates that the fines are present in rings around the contact points between individual particles. Figure 5.7 is a closer look at this smooth paste of clay between two particles. A high magnification of the clay particles is shown in Figure 5.8. Large booklets of clay can be seen.

An energy dispersive X-ray analysis was performed on these clay particles. Figure 5.9a shows the resulting X-ray spectrum which is typical of kaolinite where the amount of silica and aluminum are equal. Figure 5.9b shows the quartzose minerology of the sand grains where silica dominates.

It is seen that the location of fine particles as indicated by Figure 5.4 and observed in these bitumen-free dry specimens are different. In Figure 5.4 it is suggested that fine particles are dispersed in water, which itself with or without bitumen occupies the interstitial space between particles. Figures 5.5 to 5.7 show that fine particles are present only at the contact points between particles where they form an adherent paste.

The question arises which one of these conceptions is correct. Therefore two hypotheses should be addressed:

(a) Figure 5.4 is a correct representation of a water saturated bitumen-free oil sand where the fines are suspended in the water in the pores.

(b) Figure 5.5 is correct. Fines are concentrated at particle contact points.

Even though it is not clear that which of the hypotheses is correct, there is an explanation of how Figure 5.4 could turn into Figure 5.5:

During drying of a water saturated oil sand (Figure 5.4) water retreats to the contact points accumulating the fines around these areas. When completely dry, as in the block sample, the fines form rings around the contact points. This explanation would indicate that hypothesis (a) is correct in oil sand that has not been desiccated.

In a dry bitumen-free oil sand specimen, deposition of these minor amounts of fines at grain contacts may indicate significant cohesive strength were in fact little exists. Specimens tested water saturated under low confining pressure showed negligible cohesive strength. Also in the case of saturated oil rich oil sands, Plewes (1987) reported that a short term tensile strength may be mobilized by the viscosity of the interstitial bitumen but no true cohesion exists.

5.5 Fabric of oil sand

In this study, the term "fabric" is that defined by Brewer (1964) to represent the spatial arrangement of solid particles and associated voids. Another fabric characteristic is the mutual relationship of individual particles to other ones (packing). In order to elucidate these two fabric characteristics, Oda (1972) suggested that four fabric elements must be quantitatively determined as summarized below:

(1) Preferred orientation of the long axes of nonspherical particles with respect to a fixed reference,
(2) Intensity of the preferred orientation,
(3) Three-dimensional distribution of normals to tangential planes at contact points between solid particles,
(4) Average number of contacts per particle, also called average co-ordination number, which is closely related to void ratio.

Oda (1972) named the first two elements as orientation fabric and the latter elements as packing.

5.6 Scanning electronic microscopy

The images of oil sand structure in this study were obtained with the use of a scanning electron microscope (SEM). Because the scanning electron microscope produces a photograph of a surface in three dimensions, it is particularly useful to study grain shapes and textures.

Oil-free McMurray oil sand specimens were relatively simple to prepare. Specimens were cut from block sample through careful use of a coarse-toothed hacksaw blade. In this study a total of 9 specimens were prepared for the scanning electron microscope (Figure 5.10). They were cut out from three locations on the oil sand block sample (a block of 22 cm by 22 cm by 15 cm dimension). On each location two horizontal specimens at perpendicular directions and one vertical specimen were prepared. Figure 5.11 shows the schematic of the specimen preparation. The reference axes, X, Y and Z are selected as shown. The axis Z is selected as the vertical direction and the axes X and Y as the horizontal directions, one of which corresponded to a plane parallel to the face of the slope from which the block sample was obtained.

The intact undisturbed specimens were trimmed down carefully to a square bar shaped specimen of an approximate 8 mm by 8 mm square shaped cross section and 20 mm in length. The specimens were then snapped off in the middle to give a clean, fresh face for observations. The base of the specimen was attached to a 12.5 mm metallic scanning electron microscope stub with low resistance contact glue, the fracture surface being at the top. After the special silver glue was cured (about 24 hours) the top fracture surface was blown gently with air to disperse any possible debris. Normally specimens have to be dried for the SEM process, however it was not necessary here since the oil sand specimens were already sufficiently dry.

Dried SEM specimens must be coated with a conducting film to prevent surface charging by the electron beam. The specimens used in this study were sputter coated with a thin layer of gold for this purpose. The specimens were then placed in the microscope chamber. Through the SEM process the specimens were kept under room temperature and were subjected to 4×10^{-7} torr of vacuum.

The SEM maintains high resolution under magnification and produces a depth field of the images. The shadows and perspective of the images provide abundant topographical information. Smaller particles can be discerned from distant particles on the image.

Images of different magnification were obtained from these 9 specimens. Appendix A contains all the SEM images obtained in this study. Figure 5.12 is an example of a typical SEM result. A measured white bar is put in each image to show the scale.

For the purpose of image analysis, images must be representative of the soil at a scale appropriate to the particles of interest. In this study a magnification was chosen so that there were between 600 to 900 particles on each image (Figure 5.12). This is a good sample from the statistical point of view (in similar studies by other researchers the total number of particles per image is usually below 250). The analyzed images were four vertical sections and two horizontal sections (Figures A3, A5, A7, A9, A11 and A13 in Appendix A). These images are from locations 2 and 3 only (Figure 5.10). On location 1 the orientation of obtained images relative to the reference axes was not known. Therefore images from location 1 were not used in the image analyses.

Some visible accumulation of fine particles was visible in some images from location 2. This is probably due to the fact that the corresponding specimens were snapped off along a seam of fines. Since a cluster of fine particles was seen as an individual sand particle by the image analyzer, these type of images were not used in the image analyses.

If the purpose of an investigation is to compare fabric characteristics qualitatively, then simple, visual comparison of images may be sufficient. However, as it will be discussed later, an anisotropic geomechanical behavior was observed in the oil sand specimen and a thorough study of its fabric was then necessary.

The images were analyzed quantitatively and qualitatively by utilizing a Macintosh Performa (Power PC) computer with NIH Image 1.6 digital image analysis software (NIH 1997).

5.7 Digital image analysis

As mentioned before the scanning electron microscope was used to obtain images of the oil sand fabric with high-resolution and proper magnification.

The algorithms described below have been incorporated into the image processing package Image developed by the U.S. National Institutes of Health (NIH). NIH Image is a public-domain program that supports a number of image processing features, such as particle shape analysis and editing, as well as a built-in macro programming language.

5.7.1 Segmentation

Digital image processing involves digitizing an image on the computer and filtering and processing the image in order to highlight the desired objects or calculate various quantities.

Several procedures are commonly used to create a binary image in which each particle is distinguished in the soil matrix. These procedures are collectively termed segmentation. In practice, the analyst employs these techniques sequentially to ensure that the final, segmented image is as close as possible to an accurate representation of the particles in the original image.

The elements of a digital image are called picture elements, or pixels. In an eight-bit gray-scale image (used by NIH Image), each pixel is assigned a gray level that varies from 0 (white) to 255 (black). The image analyzer measures the light intensity of every pixel on the image. For black and white SEM images, the measured light intensities range from 0 for white areas to 255 for black areas. Light intensities for varying shades of gray fall within this range. Images from SEM generally include several levels of gray. For image analysis, the solids and voids must be defined strictly as black and white, respectively.

Manual thresholding refers to choosing a single gray level above which all pixels are converted to black and below which all pixels are converted to white. Analytical results may be extremely sensitive to placement of the threshold gray level.

Many problems are encountered when trying to estimate fragmentation using SEM images. First, the individual particles in the image must be delineated, either by hand or using image processing techniques. Problems with nonuniform lighting, shadows, noise and range in particle sizes make delineation virtually impossible using standard edge-detection routines. Due to these difficulties, the standard digital image processing techniques such as thresholding or edge detection do an incomplete job of fragment delineation.

An alternative method is called "density slice" in which instead of a single gray level as a threshold a range of gray levels is chosen. All pixels within this range would be converted to black. Accordingly, the point is arranged to be either part of the solid or void spaces. Fortunately in the region where the sand particles touch, there usually will be relatively large gray-level differences due to the particle edges. In almost all cases there is at least some gray-level difference between touching sand particles.

For this study, an iterative technique was used to define the density slice that would best replicate the void and solid spaces on the original image. Using this method, the original image was transformed to a binary image. Figure 5.13 shows the binary image of Figure 5.12, produced by this delineating algorithm. The resulted binary images of all analyzed images are presented in Figures A4, A6, A8, A10, A12 and A14 of Appendix A.

After the particles have been delineated, shape and size information were calculated for each particle. The NIH Image program has built-in routines to calculate the following information for each delineated particle: area, best-fitting ellipse (major axis, minor axis, angle of major axis with the horizontal) and perimeter. This information is used in the statistical analyses described in the next section.

It should be noted that along the edges of an image, only parts of the particle will be visible and thus the size and shape parameters will be skewed for the edge particles. The NIH program allows the edge particles to be excluded from the data set for the statistical analyses.

Unfortunately there is no simple way to verify the accuracy of the binary image that is produced, except by careful visual checking of the print to be analyzed against the sample itself (Anderson et al. 1992). This was done here for each one of the final binary images.

5.7.2 Orientation of particles

The orientation of a nonspherical particle can be represented by the inclination of the longest or shortest axis of the grain to a fixed direction (Figure 5.14). In practice,

however, it is very difficult to find a true long or short axis of particles in a two dimensional image. An alternative method is used. That is, the state of three-dimensional orientation of grain particles is estimated on the basis of the degree of preferred orientation or parallelism of apparent longest axes observed in the vertical and horizontal sections, in the following manner (Oda 1972):

(1) Measure the angles θ_i, between apparent longest axis of all the grains and the reference axis (Figure 5.14) on each section.

(2) Make the frequency histograms of θ_i; thus obtained.

θ_i is an azimuth from $-90°$ to $+90°$. In the measurement of orientations of particles, no distinction is made of one end of the particle from the other. All measurements are therefore made in a range of $180°$.

Figure 5.15 shows the grain size distribution of one of the sands analyzed by Oda (1972). The grain size of this sand is similar to the oil sand block sample studied in this study (Chapter 1). Oda reported an axial ratio value of 0.605 for this sand. Axial ratio is defined later in section 5.7.3.

Figure 5.16 shows the frequency histograms of θ_i obtained by Oda. He observed that in the vertical section there is an almost unimodal frequency distribution with a distinct peak near $\theta_i = 0°$ while in the horizontal section, the distribution is polymodal. Oda concluded that the vertical section has a statistically significant preferred orientation of apparent long axis but the horizontal section does not have any preferred orientation.

The frequency histograms of θ_i of particles for the oil sand specimens analyzed here are shown in Figures 5.17 to 5.22. It may be seen that particles have strong preferred orientations in the vertical sections ($\theta_i = 0°$, i.e. there are more particles oriented along the horizontal direction) but almost completely random orientations in the horizontal sections.

A vector mean direction θ_m and a vector magnitude (V.M.) for each section was determined as an index for representing the intensity of fabric anisotropy by the following equations (Curray 1956):

$$\theta_m = \frac{1}{2} \arctan \frac{\sum Sin2\theta_i}{\sum Cos2\theta_i} \qquad (5.1)$$

and:

$$V.M. = \frac{100}{n} \left[\left(\sum Sin2\theta_i \right)^2 + \left(\sum Cos2\theta_i \right)^2 \right]^{1/2} \qquad (5.2)$$

Where n is the total number of measurements and θ_i is an inclination angle corresponding to i th particle.

Vector magnitude is an index measure to show the intensity of the preferred orientation of particles, which was first introduced by Curray (1956). Vector magnitude varies from 0% which means complete random orientation of apparent long axes to 100% which means their complete parallel alignment (Oda and Koishikawa 1977). The vector magnitude is, therefore, a rather sensitive measure of dispersion and is comparable to standard deviation or variance (Curray 1956).

As also observed by Oda (1972) in the case of frequency histograms of vertical sections, there could be found an almost unimodal frequency distribution having distinct peak near $\theta_i = 0°$. In the case of horizontal sections, however, the distribution was polymodal. These frequency distributions were also analyzed with a statistical examination, Rayleigh test of significance.

Curray (1956) realized that the distribution devised by Rayleigh for describing random phases in sound waves could be used for the analysis of geological orientation data. The problems are identical because each observation can be represented by a vector with direction and magnitude. The test is adapted to this application as:

$$p = e^{\left(- V.M.^2 \times n \times 10^{-4}\right)} \tag{5.3}$$

Where $V.M.$ is the vector magnitude, n is the number of observations and p represents the probability level of significance. Curray (1956) found that the level of significance of 0.05 to be appropriate for the study of sand grain orientation. No distribution is accepted as being significantly different from randomness unless there are less than 5 chances in 100 of its being due to chance. The calculated values of p are shown in Table 5.1. These values are much smaller than 0.05, indicating that there is an extremely low probability that the distribution could have arisen by chance sampling of a random population.

The value of θ_m for the vertical sections varied within a small range of 1° to 10°. It means that apparent long axes of grain in these specimens were preferably parallel to the horizontal plane, which was used as a reference axis.

The vector length was calculated to be from 18% to 25% for the vertical sections. Compared to values of vector length obtained in previous studies of natural sand deposits (Oda 1972, Oda and Koishikawa 1977, Oda et al. 1978), this value of vector length corresponds to a fair degree of preferred particle orientation. Corresponding values of vector length for the horizontal sections were 7.6% and 15.3%. Thus, an almost random orientation of particles in the horizontal plane was obtained. The specimen fabric is therefore of the cross-anisotropic type (Lade and Wasif 1988).

5.7.3 Axial ratio

The characteristics of fabric are closely related to the shape of particles, especially to the average flatness or slenderness. The following method was used by Oda (1972) to measure the shape factor of constituting grain particles:

(1) Measure the length of apparent shortest axis, L_2 and apparent longest axis, L_1 of each sand grain.
(2) Calculate the axial ratio:

$$Axial\ ratio = \frac{1}{n} \sum_{i=1}^{n} (L_2/L_1)_i \qquad (5.4)$$

where n, is the total number of measurements.

The value of axial ratio ranges from 0 to 1. When axial ratio approaches unity, the average of the projected image of the sand grain becomes close to a circle. Therefore, axial ratio can be considered as an index indicating the characteristic of particle shape. According to previous studies of several natural sands (Oda and Koishikawa 1977 and Oda et al. 1978), typical value of axial ratio ranges from 0.5 to 0.7. Table 5.1 shows the obtained values of axial ratio for the analyzed images of oil sand. They are fairly consistent and are between 0.68 to 0.71. This falls in the typical range for natural sands mentioned by other researchers. Thus it could be concluded that the diagenetic processes have not significantly changed the overall grain shape of oil sand.

Oda and Koishikawa (1977) examined different types of sand and concluded that statistically significant preference of particle orientation can be found in sands having their axial ratios around 0.65. They also observed that in a vertical sections, the preferred direction becomes closer to the horizontal when its particles become more slender or more platey, and no preferred direction can be observed on horizontal sections irrespective of their particle shape characteristics.

By the results obtained here and by other researchers (e.g. Oda 1972, Oda and Koishikawa 1977, Oda et al. 1978), it has become clear that when sand grains are deposited in a gravity field, irrespective of their shape character, they tend to rest in a stable position relative to the forces acting upon them. An anisotropic fabric assembly must be due to this tendency. Experimental evidence also showed that the nature and degree of fabric anisotropy of sand are determined by the shape characters of sand grains and by the way in which they were deposited.

5.8 Inherent anisotropy of oil sand

The structure of sand and strain or stress histories can considerably affect the mechanical properties of sands. Therefore anisotropy is one of the fundamental aspects to be taken into account for a better understanding of sand properties.

Geotechnical properties of sand depend primarily on the arrangement of particles, i.e. the "fabric". As such, any anisotropy in the fabric gives rise to directional dependence of geotechnical properties. Of particular importance is the influence of fabric anisotropy on the constitutive behavior of sands. Natural soils always possess some degree of anisotropy. Virtually all natural in situ sand deposits display fabric anisotropy due to parallel alignment of particles (Arthur and Phillips 1975).

Casagrande and Carillo (1944) were probably the first to model strength anisotropy in soils. They distinguished between inherent anisotropy and induced anisotropy, suggesting that anisotropy may be present before the soil is strained or may be induced by the straining process. Inherent anisotropy was therefore produced through the sedimentation of particles and defined as "a physical characteristic inherent in the material and entirely independent of the applied strains". Induced anisotropy was defined as a physical characteristic "due exclusively to the strain associated with an applied stress". Although these definitions were intended for strength they are equally useful for packing descriptions and stress-strain relationships (Arthur and Menzies 1972).

Strength anisotropy in naturally occurring clays is a matter of record, but less similar work has been done on sands owing to the difficulties of sampling cohesionless material. Observations of strength or stress-strain anisotropy in sands have therefore been limited mostly to a few laboratory prepared specimens.

Since sand consist of solid particles and associated voids, the general description of the anisotropy of sand must account for the relative arrangement of solid particles and voids. The direct measurement of granular fabric as discussed before includes the process of obtaining images and the image analysis methods. They are difficult and time consuming.

5.8.1 Summary of previous experimental results

Oda and Nakayama (1989) suggested that in order to discuss the anisotropy of soils in general, the following three sources of anisotropy should be considered:

(1) The anisotropic distribution of contact normals which is indicative of the mutual relation among particles;
(2) the preferred orientation of nonspherical voids; and
(3) the preferred orientation of nonspherical particles.

In biaxial compression tests on two-dimensional assemblies of rods, Oda et al. (1985) have observed that the inherent anisotropy by (1) and (2) tends to be completely altered during the relatively early stage of nonelastic deformation. The inherent anisotropy by

(3), on the other hand, still remains at the later stage of deformation. This is the reason why the strength is seriously affected by the direction of compression with respect to the axis of sedimentation (strength anisotropy).

Anisotropy due to preferred particle orientation is an important factor controlling the directional nature of shear strength, stress-strain behavior and other geotechnical properties of all types of soils (Oda 1972, Arthur and Menzies 1972). Therefore the anisotropy resulting from the orientation of particles was chosen as the focus of this study.

The influence of particle orientation on the constitutive behavior of soils has long been recognized. The stress-strain relationship and strength have been found to depend on the direction of loading with respect to the direction of particle orientation (Arthur and Menzies 1972, Oda 1972, Arthur and Phillips 1975, Oda 1981, Lade and Wasif 1988, Ochiai and Lade 1983, Ishibashi et al. 1991).

Several studies (Arthur and Menzies 1972, Oda 1972, Arthur and Phillips 1975, Oda et al. 1978, Oda 1981, Lade and Wasif 1988, Ochiai and Lade 1983) have been performed in drained triaxial compression tests on specimens prepared by pouring sand vertically into a tilted mold. By using different tilt angles, specimens were produced with anisotropic fabric whose symmetry axis formed different angles with the specimen axis. Thus these investigations have been performed on specimens with an inherent anisotropy grain structure, whose initial axis of symmetry was inclined at various angles with the direction of the major principal stress. Specimens made by the pouring procedure are characterized by the uniform anisotropic fabric irrespective of the shape of particles (Oda 1981).

The prefailure stress-strain behavior and strength observed in these tests clearly reflected the inherent anisotropic fabric in the sand specimens. The results of these studies have indicated that the maximum strength of homogenous specimens was mobilized in the drained triaxial compression tests when the major principal stress was applied perpendicular to the bedding planes and the minimum strength was obtained when the major principal stress was applied parallel to the bedding plane. The anisotropic behavior of the sand was clearly caused by the deposition alone (Arthur and Menzies 1972). Oda (1972), Oda and Koishikawa (1977) and Arthur and Menzies (1972) have mentioned that sand deposited under the action of gravity force shows anisotropic shear strength in a triaxial compression test. This is due to the preferred alignment of long axes of particles nearly parallel to a bedding plane.

Oda et al. (1978) tested undisturbed sand specimens, which were sampled from different rivers, beaches and dunes. The results of their observations are briefly summarized as follows:

Anisotropic parallel alignment of particles is universally observed, not only in river beach and coastal dune sands but also in artificially deposited sands. Although the anisotropic

orientation of particles in naturally deposited sands may be simulated by adopting a suitable method in a laboratory, naturally deposited sands must be distinguished from artificially deposited ones in the following two points as pointed out by Oda and Koishikawa (1977):

(1) The preferred direction of particle alignment in naturally deposited sands incline at an acute angle less than 30° to the horizontal (this tendency is due to the effect of water flow at the time of sedimentation) while the preferred orientation of particles in artificially deposited sands is practically parallel to the horizontal.

(2) While there is no significant parallel alignment of particles in horizontal sections of any artificially deposited sands, a marked alignment can be seen in horizontal sections of naturally deposited sands.

Oda and Koishikawa (1977) also concluded that the anisotropic shear strength of sand must be most remarkable when the following three conditions are satisfied:

(1) sand is composed of slender or platey particles,
(2) sand is densely compacted under the action of gravity, and
(3) sand is failed at low confining pressures.

Comparison of results from different sands suggests that the form of inherent strength anisotropy may differ considerably from one granular material to another (Arthur and Phillips 1975).

Regarding the effect of the initial fabric on the characteristics of deformation behavior, Oda (1972) noted the following observation:

The ratio of the secant deformation modulus at 50% strength (E50) between a specimen in which the bedding plane is perpendicular to the major principal stress and a specimen in which the bedding plane is parallel to the major principal stress is about two to three in densely compacted sands. Ochiai and Lade (1983) mentioned that the results of both isotropic compression tests and shear tests indicate that the compressibility is smallest in the direction perpendicular to the long axes of the sand grains.

In summary, the effects of the initial anisotropic fabric were mainly observed in the prefailure stress-strain and volume change behavior of the sand, whereas sufficient changes in the fabric had occurred at large strains to produce failure conditions which resembled those observed for isotropic sands.

5.8.2 Oil sand inherent anisotropy

The mechanical properties of sand such as deformation-failure behavior and permeability are very much influenced by its fabric. The results of image analyses performed on the SEM images obtained from undisturbed oil sand specimens showed a clear preferred

particle orientation parallel to the horizontal plane. The oil sand fabric is therefore anisotropic.

To represent results of tests on anisotropic materials, it is important to indicate clearly the directions of bedding planes relative to the longitudinal axis of the specimen. Two orientations of specimens were tested (Chapter 6). These undisturbed oil sand specimens were obtained by coring the block sample both vertically and horizontally (Figure 5.23). The obtained vertical specimens had a longitudinal axis perpendicular to the preferred orientation of particles while the horizontal specimens were parallel to these bedding planes.

In order to evaluate the effects of anisotropic fabric on the shear strength and deformation behavior of the oil sand a series of drained triaxial compression tests were performed on these specimens. The results of these tests are reported in detail in Chapter 6. Permeability measurements were also performed on these specimens, the results of which are discussed in Chapter 8.

Figures 5.24 and 5.25 show the stress-strain characteristics of oil sand at an effective confining pressure of 250 kPa. As was observed by other researchers, the shear strength of the material is much higher in the vertical specimens. However the strengths become closer with more shearing. It appears that the effects of the initial anisotropic fabric are substantially diminished at strains over 6%. Figure 5.26 illustrates the variation of peak friction angle with effective confining pressure. Again peak friction angle is much higher when the major principal stress was applied perpendicular to the bedding plane than parallel to it. Dusseault and Morgenstern (1978) also reported a higher strength of oil sand across bedding than along bedding.

Figure 5.25 shows the corresponding volume change curves. In both cases contraction is followed by a strong dilation that starts at the maximum shear strength. The volumetric strain pattern also reflects fabric. After 6% axial strain, the volumetric strains become similar.

Figure 5.26 shows that the peak friction angle reduces with an increase in confining pressure. This in part is due to the dilation angle of the material being smaller at higher effective confining pressures. Figure 5.27 shows the variation of dilation angle with confining stress. The preferred orientation of particles and resulting inherent anisotropy are more pronounced at low confining pressures.

The variation of tangent modulus of elasticity with confining pressure is plotted in Figure 5.28. The tangent modulus of elasticity of vertical specimens is higher than horizontal specimens. This is in agreement with the observation of Oda (1972) and Ochiai and Lade (1983) that compressibility is lower in the direction perpendicular to the bedding plane of particles.

Figure 5.29 illustrates the initial absolute permeability of the specimens. It can be seen that the absolute permeability is higher in the direction parallel to the bedding plane. This could be explained by the fact that the flow paths were much shorter in the direction parallel to the long axis of nonspherical particles than in the perpendicular direction, as schematically illustrated in Figure 5.30.

5.9 Summary

- It is shown that the shape and the orientation of granular particles is important in understanding the mechanical properties of granular materials.

- Images of bitumen-free oil sand specimens of the McMurrray Formation were obtained with the use of a scanning electron microscope (SEM). The images were analyzed with NIH Image 1.6 digital image analysis software (NIH 1997). The analyzed images were four vertical sections and two horizontal sections.

- The resulting frequency distributions were analyzed with a statistical examination, Rayleigh test of significance. It was seen in vertical sections that particles have strong preferred orientation. There are more particles oriented along the horizontal direction. Particles showed random orientations in the horizontal sections.

- It was concluded that when nonspherical sand grains were deposited, irrespective of their shape, they tend to rest in a stable position relative to the forces acting upon them. An anisotropic fabric assembly must be due to this tendency.

- The obtained values of particle axial ratio for the analyzed images fall in the typical range for natural sands, leading to the conclusion that the diagenetic processes have not changed significantly the overall grain shape of the oil sand particles.

- Anisotropy due to preferred particle orientation is an important factor controlling the geotechnical properties of sands. The oil sand anisotropy resulting from the orientation of particles was studied here.

- Undisturbed oil sand specimens with their longitudinal axis perpendicular to the preferred orientation of particles (vertical specimens) and parallel to the bedding planes (horizontal specimens) were tested (Chapters 6 and 8). The stress-strain behavior shows that the shear strength of oil sand was much higher in the direction perpendicular to the bedding plane and compressibility was lower.

- Permeability measurements showed that the horizontal absolute permeability was higher than the vertical permeability (Chapter 8). This is explained by the fact that the flow paths are much shorter in the direction parallel to the bedding plane.

Table 5.1 Index properties of images

Section	Plane	n	*Axial ratio*	θ_m (°)	*V.M. (%)*	p
Vertical	Z - X	742	0.693	1	18.8	4×10^{-12}
Vertical	Z - X	815	0.698	2	17.7	8×10^{-12}
Vertical	Z - Y	872	0.686	-10.2	20.1	5×10^{-16}
Vertical	Z - Y	914	0.679	6.6	24.7	7×10^{-25}
Horizontal	Y - X	756	0.706	39	7.6	10^{-2}
Horizontal	Y - X	616	0.694	-15.5	15.3	5×10^{-7}

n = total number of particles,
θ_m = vector mean direction (Degrees),
$V.M.$ = vector magnitude (%),
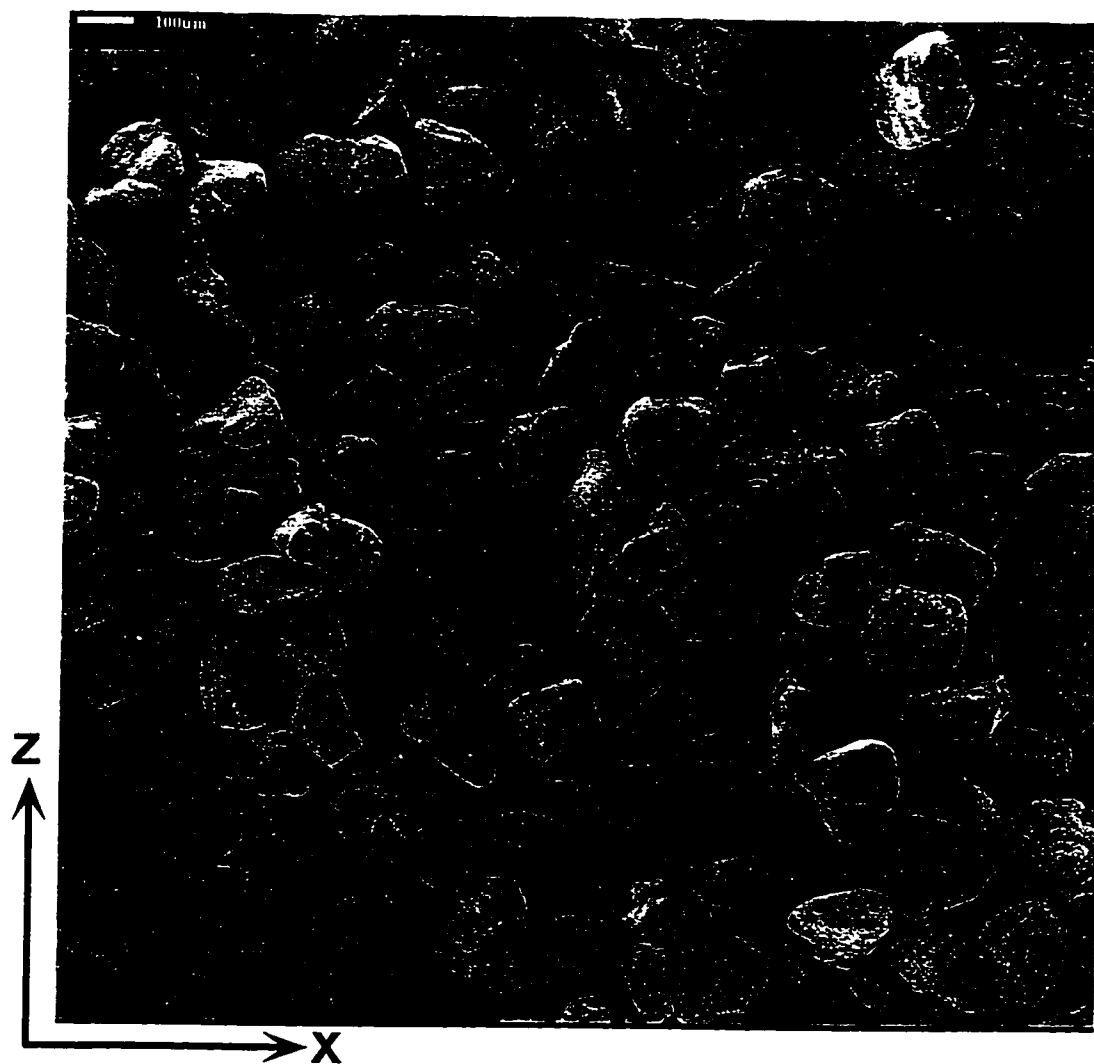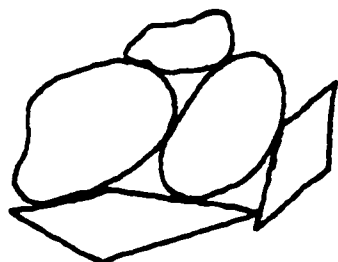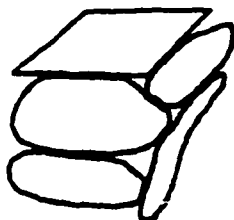p = probability level of significance.

Figure 5.1 Scanning electron microscope of a vertical section of bitumen-free McMurray Formation oil sand (Z-X plane)
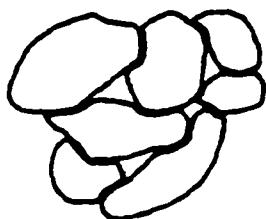**Location 3**
(White bar is 100 μm)

Tangential contacts
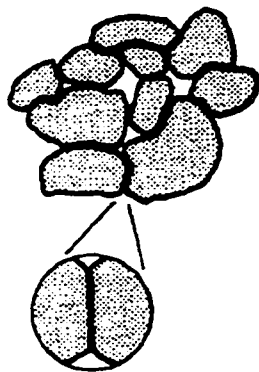Low contact area
High porosity

Straight contacts
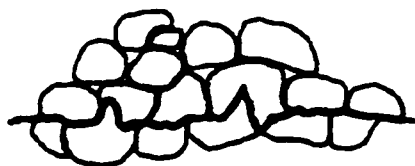Low to medium contact area
Medium to high porosity

Interpenetrative contacts
Medium contact area
Medium porosity

Sutured contacts (quartzose sand)
Medium to high contact area
Medium to low porosity

Carbonate type stylolite
Orthotropic (one-dimensional)

Figure 5.2 Intergranular fabric classification
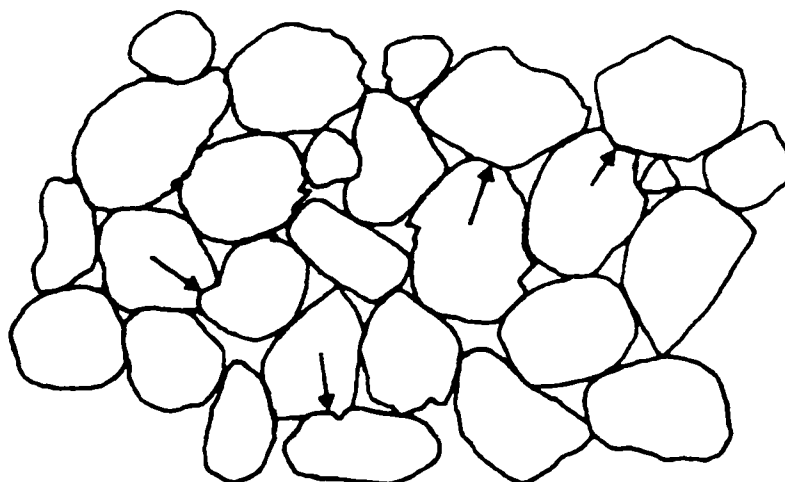(Modified from Dusseault 1977)

Figure 5.3 Fabric of Athabasca oil sands
Mostly tangential fabric, but many straight and interpenetrative contacts (arrows)
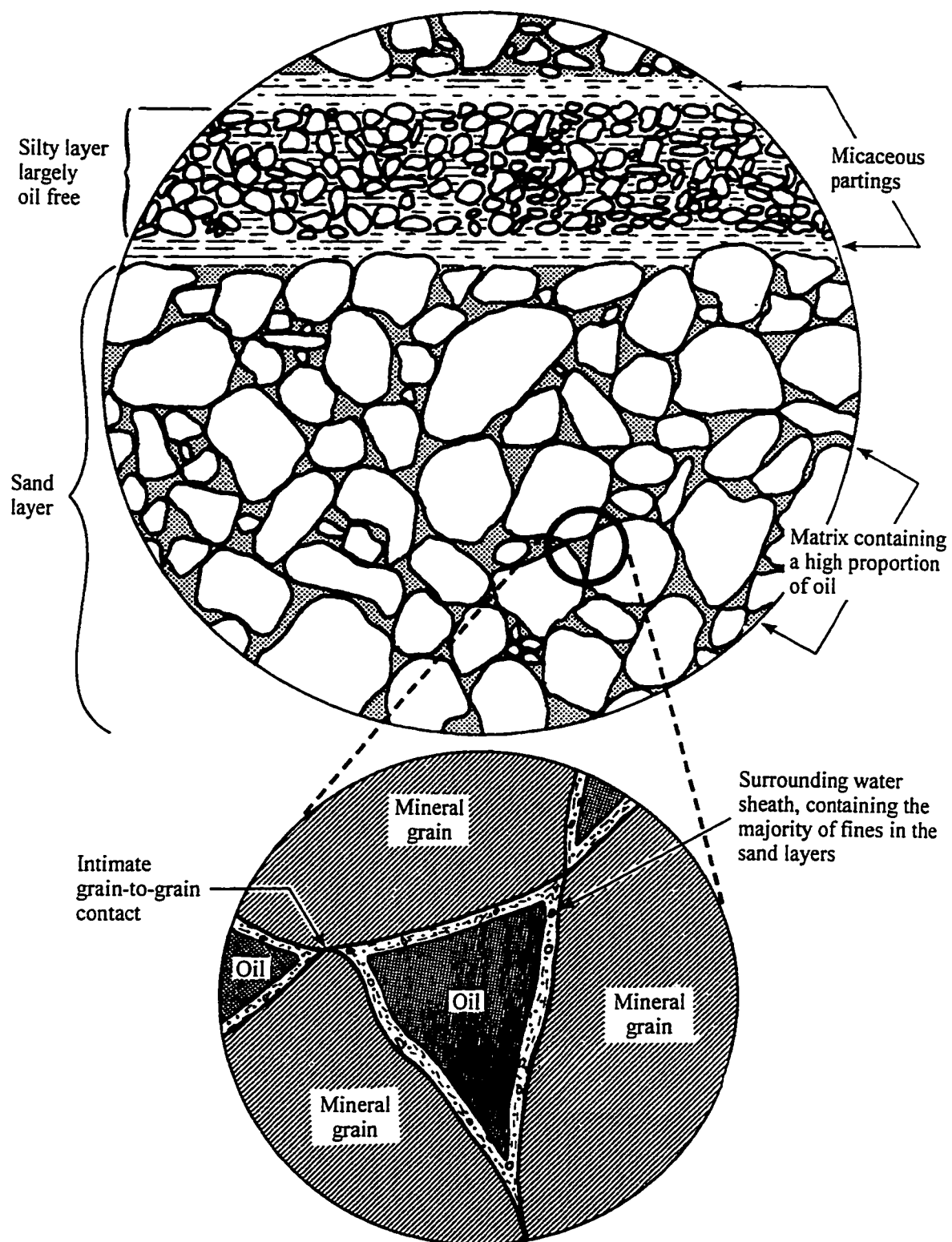(Modified from Dusseault and Morgenstern 1978)

Figure 5.4 In situ structure of oil sand
(Modified from Dusseault 1977)

**Figure 5.5 Scanning electron microscope of a vertical section of bitumen-free McMurray Formation oil sand (Z-X plane)
(orientation of this image is not known)
Location 1**
(White bar is 10 μm)

**Figure 5.6 Scanning electron microscope of a horizontal section of bitumen-free
McMurray Formation oil sand (Y-X plane)
(orientation of this image is not known)
Location 1**
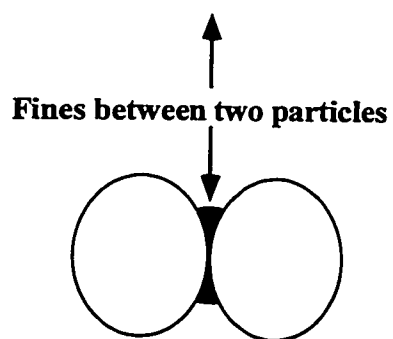(White bar is 10 μm)

Figure 5.7 Scanning electron microscope of a horizontal section of bitumen-free
McMurray Formation oil sand
Location 3
(White bar is 10 μm)

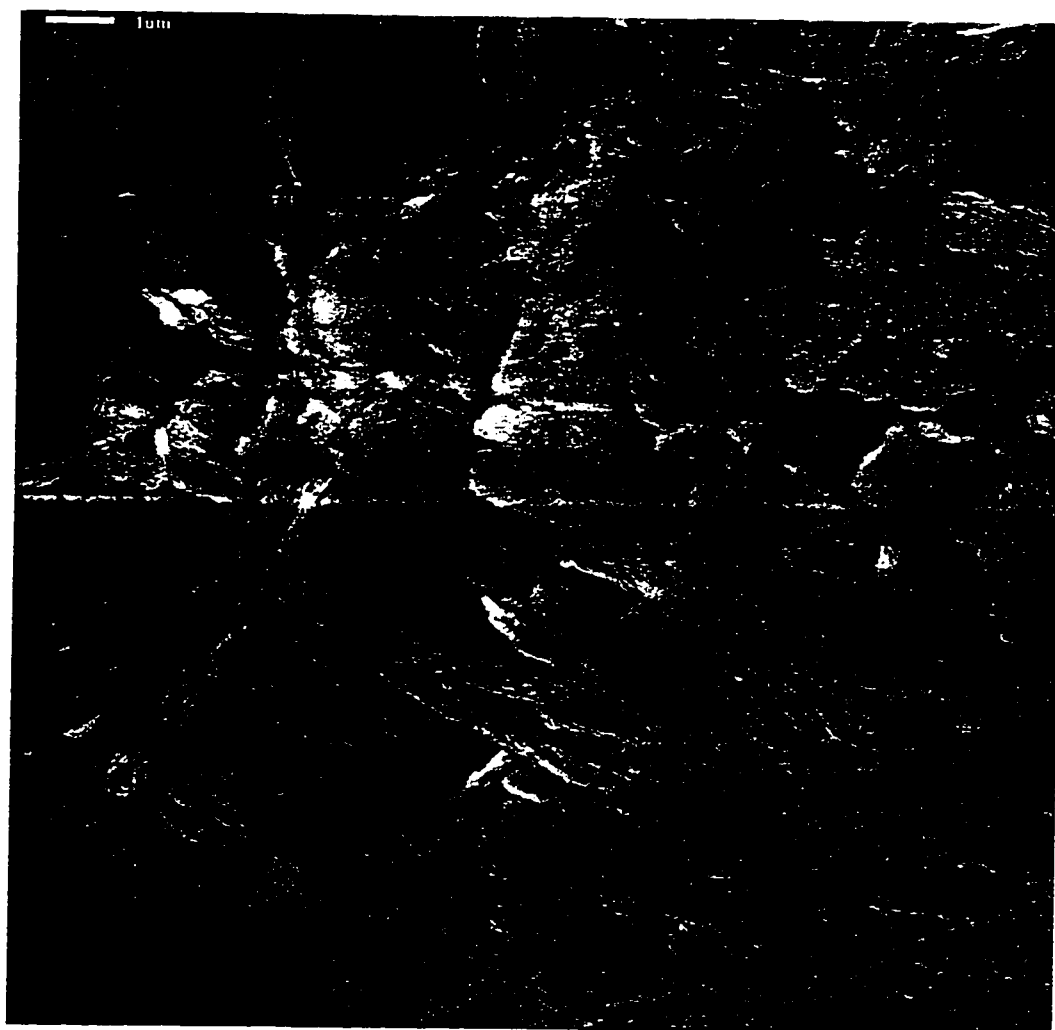Figure 5.8 Scanning electron microscope of a horizontal section of bitumen-free
McMurray Formation oil sand
(clay particles)
Location 1
(White bar is 1 μm)

Figure 5.9 X-ray spectrum of; (a) clay particles and (b) surface of sand grain
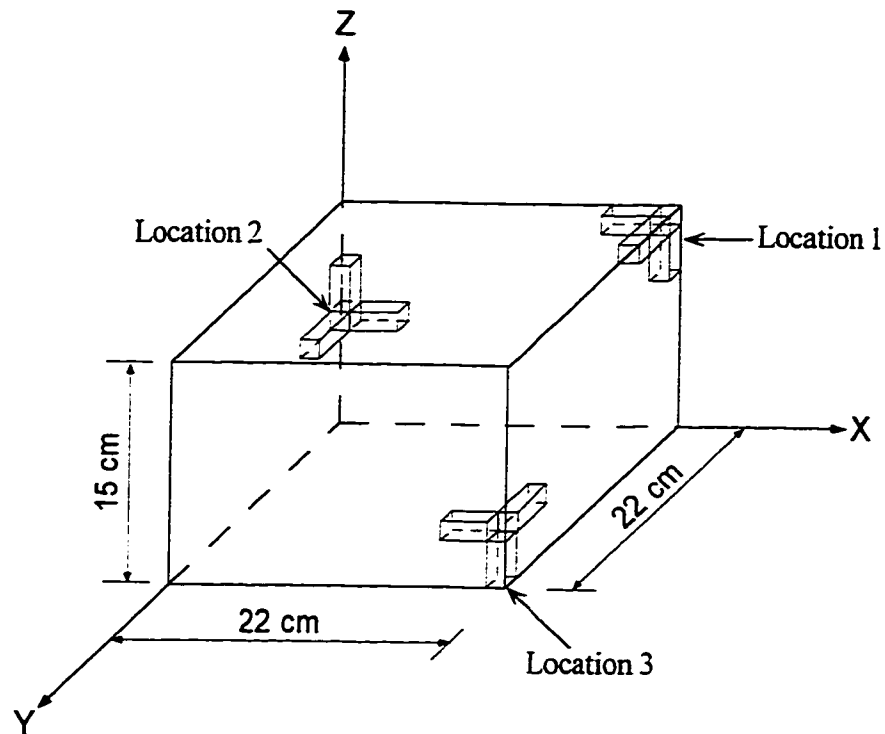
Figure 5.10 Schematic of block sample and locations where specimens were obtained
(X-Y is the horizontal plane)
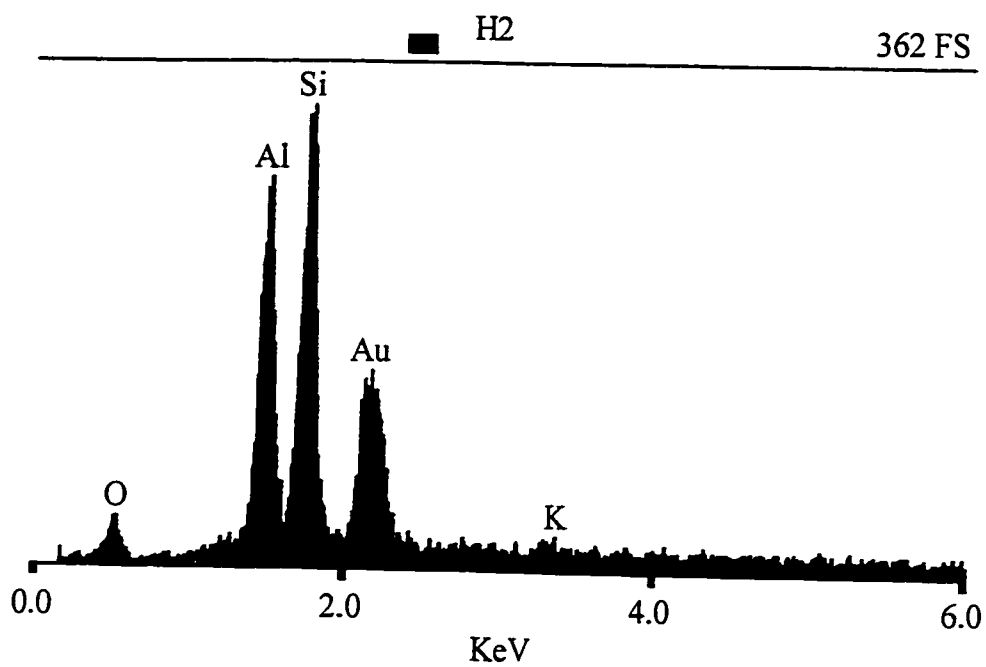

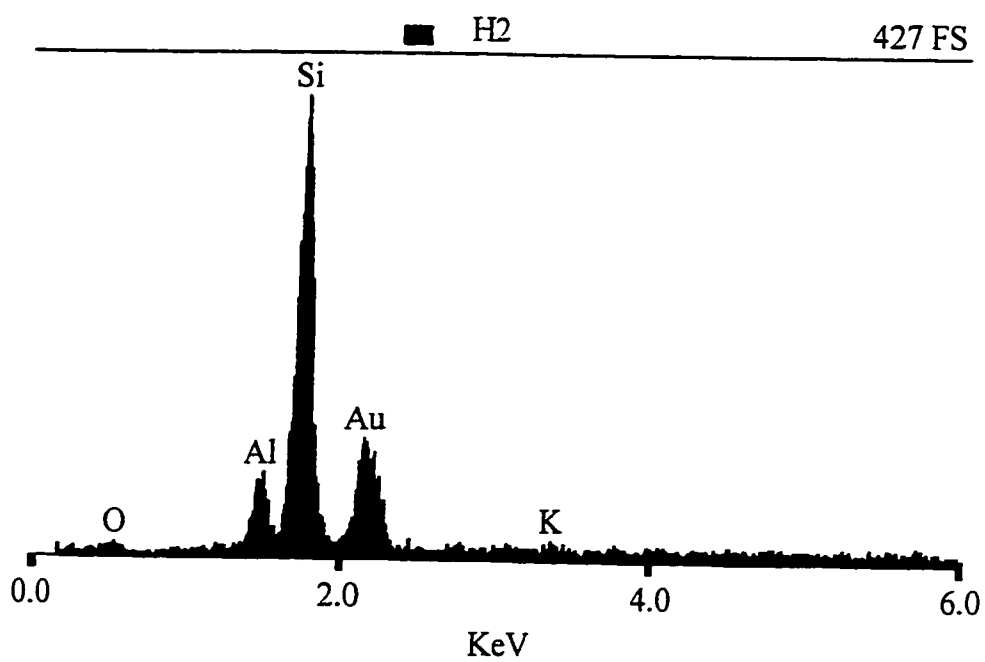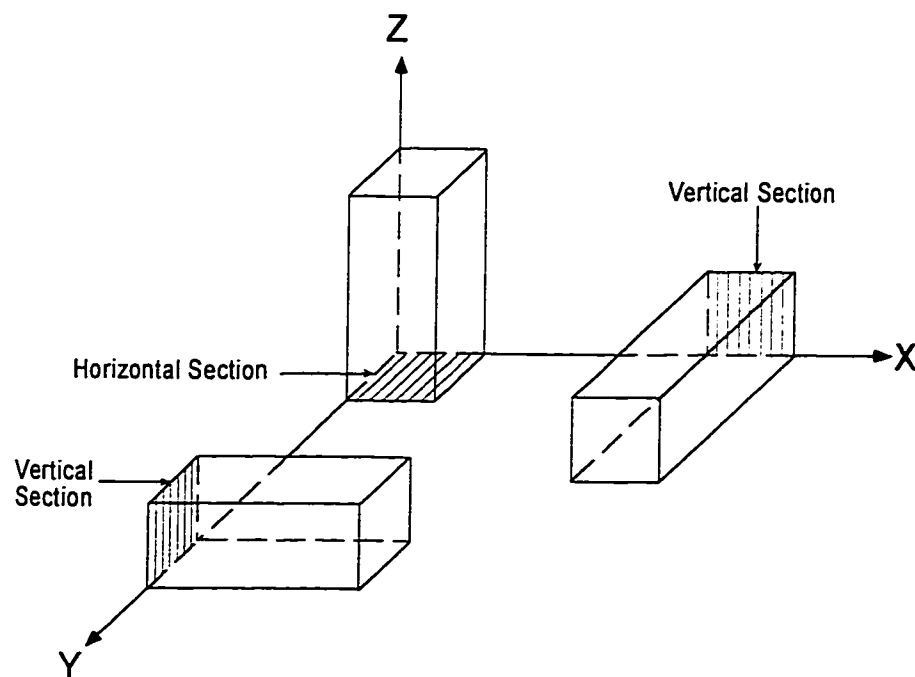**Figure 5.11 Schematic of specimen preparation**
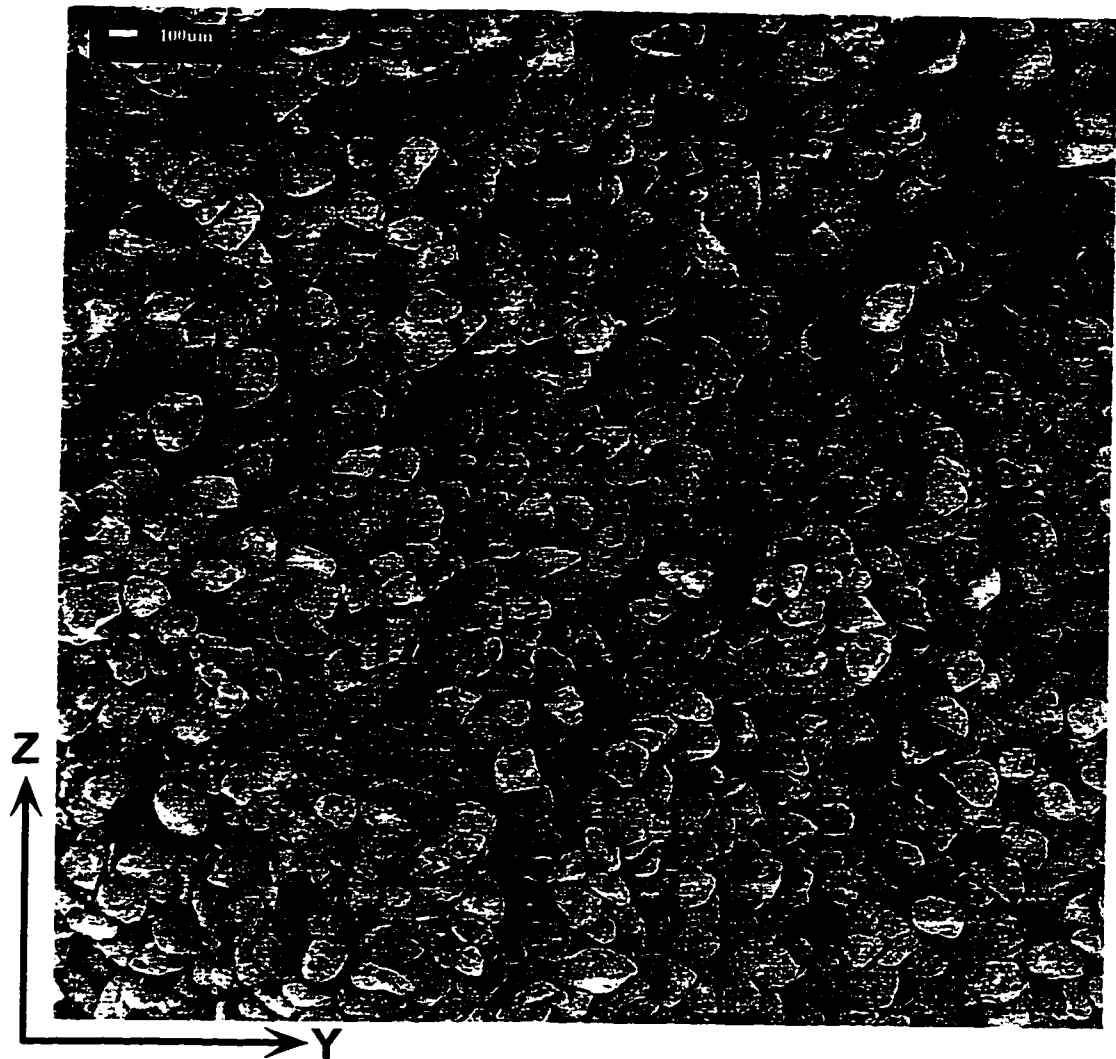
Figure 5.12 Scanning electron microscope of a vertical section of bitumen-free McMurray Formation oil sand (Z-Y plane)
Location 2
(White bar is 100 µm)
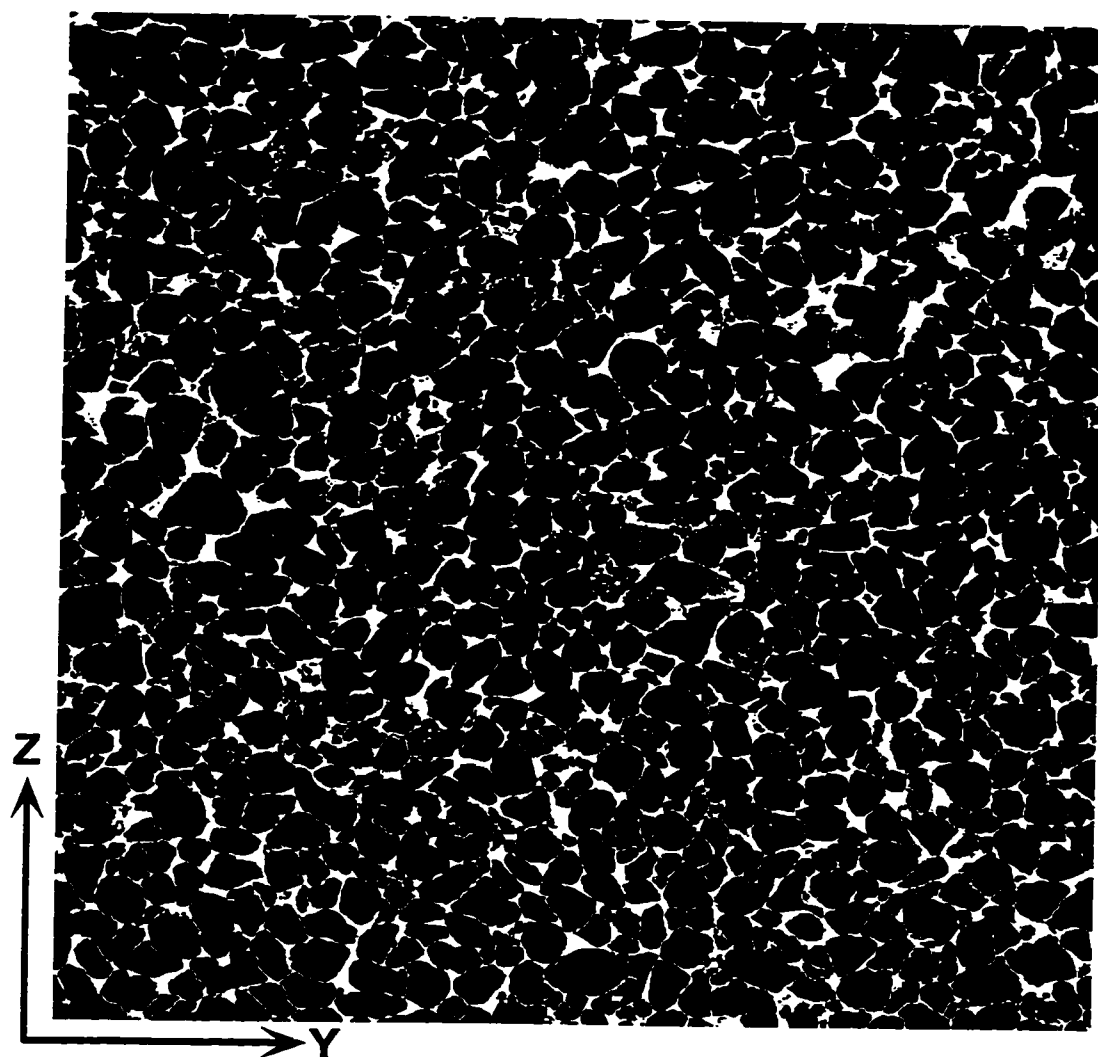
Figure 5.13 Binary image produced by delineating particles in Figure 5.12
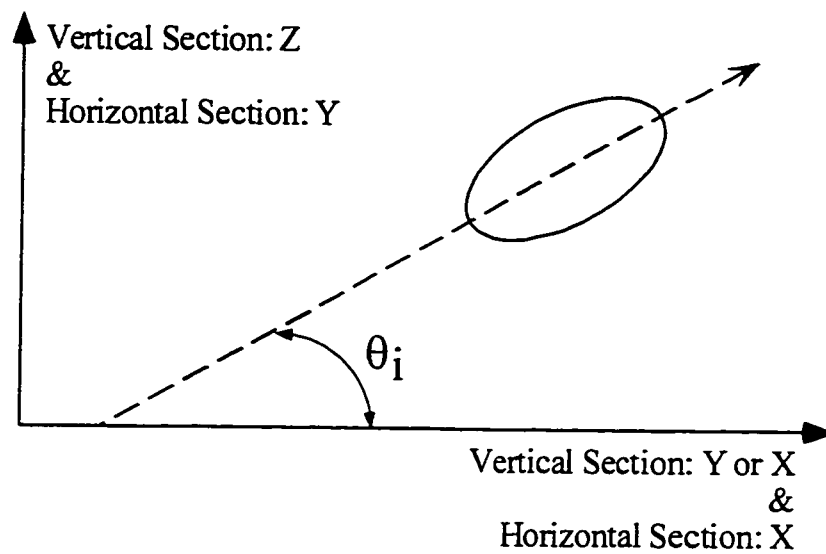
Figure 5.14 Orientation of apparent long axis of a particle on a vertical or horizontal section
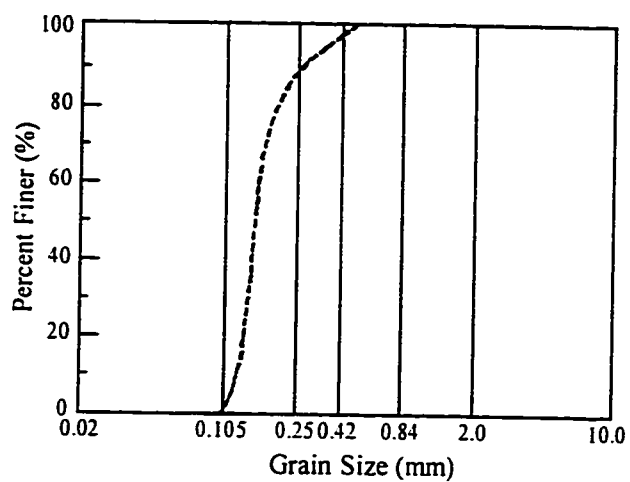
Figure 5.15 Grain size distribution of sand tested by Oda
(Modified from Oda 1972)
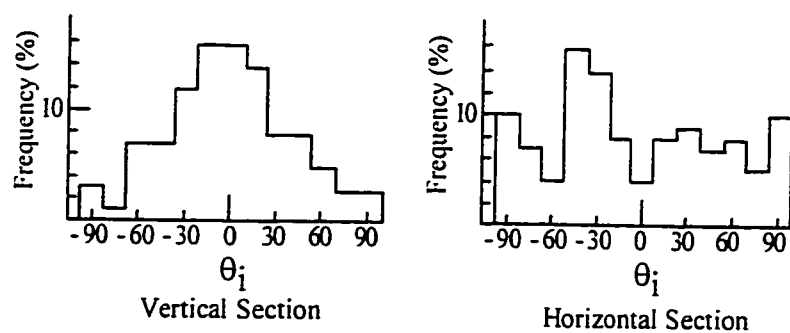
Figure 5.16 Frequency histograms of θ_i in a vertical and horizontal section
(Modified from Oda 1972)
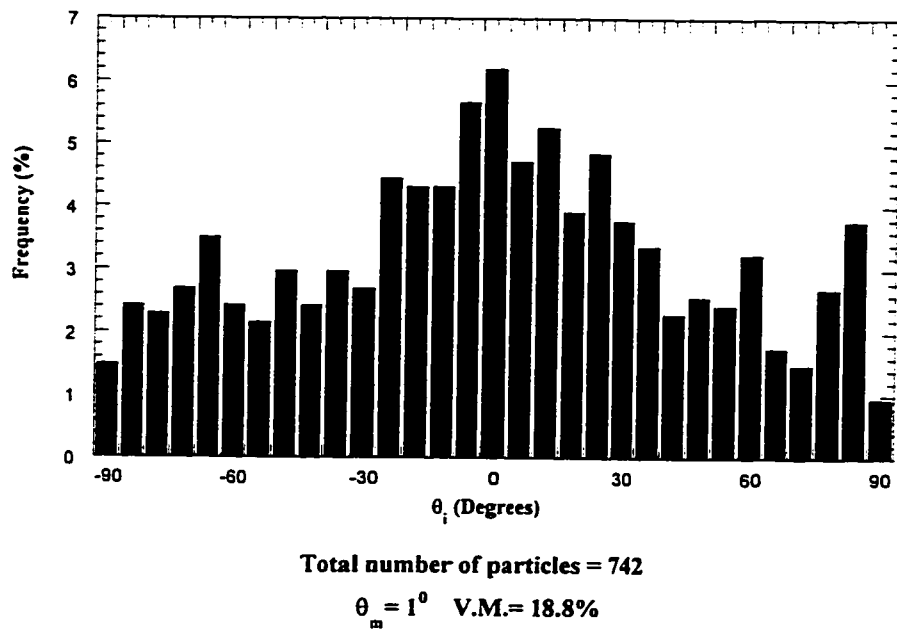
Figure 5.17 Frequency histograms of θ_i (measured from Axis X)
in a vertical section (Z-X plane)
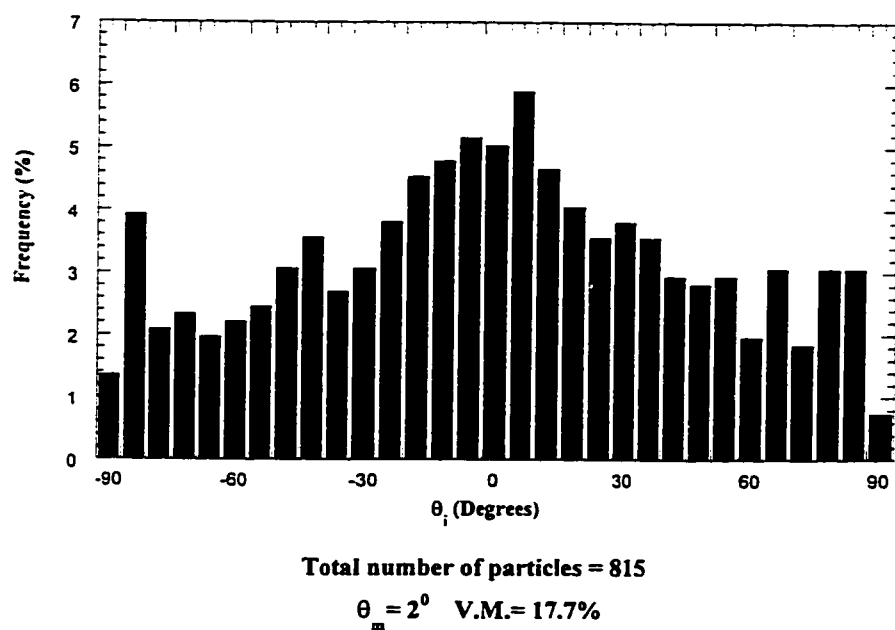
Figure 5.18 Frequency histograms of θ_i (Measured from Axis X)
in a vertical section (Z-X plane)
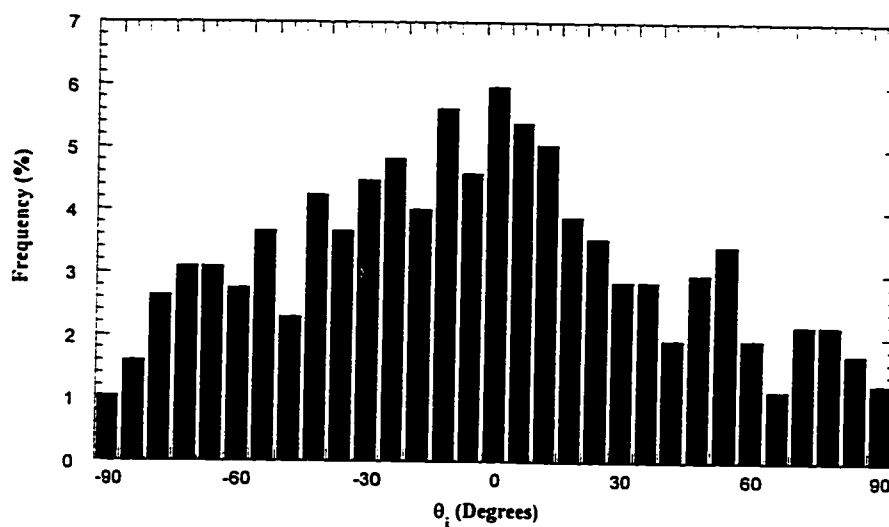
Total number of particles = 872

$\theta_m = -10.22^0$ V.M.= 20.1%

Figure 5.19 Frequency histograms of θ_i (measured from Axis Y) in a vertical section (Z-Y plane)
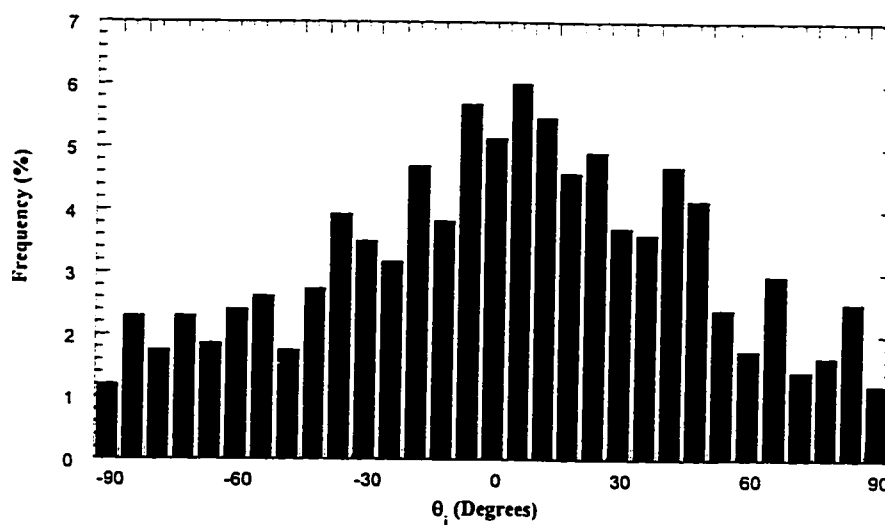
Total number of particles = 914

$\theta_m = 6.6^0$ V.M.= 24.67%

Figure 5.20 Frequency histograms of θ_i (Measured from Axis Y) in a vertical section (Z-Y plane)

Total number of particles = 756

$\theta_m = 39^0$ V.M.= 7.6%
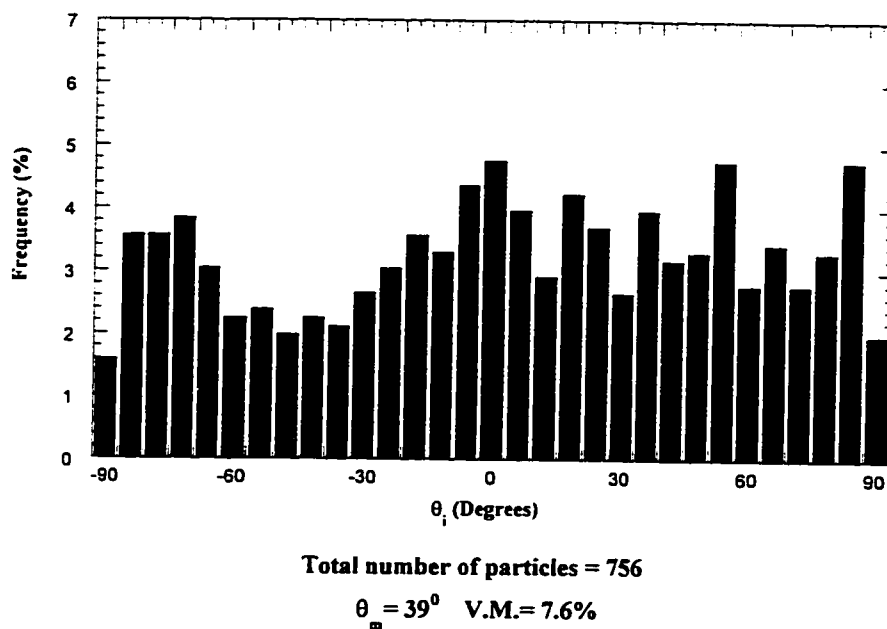
Figure 5.21 Frequency histograms of θ_i (measured from Axis X) in a horizontal section (Y-X plane)

Total number of particles = 616

$\theta_m = -15.5^0$ V.M.= 15.3%
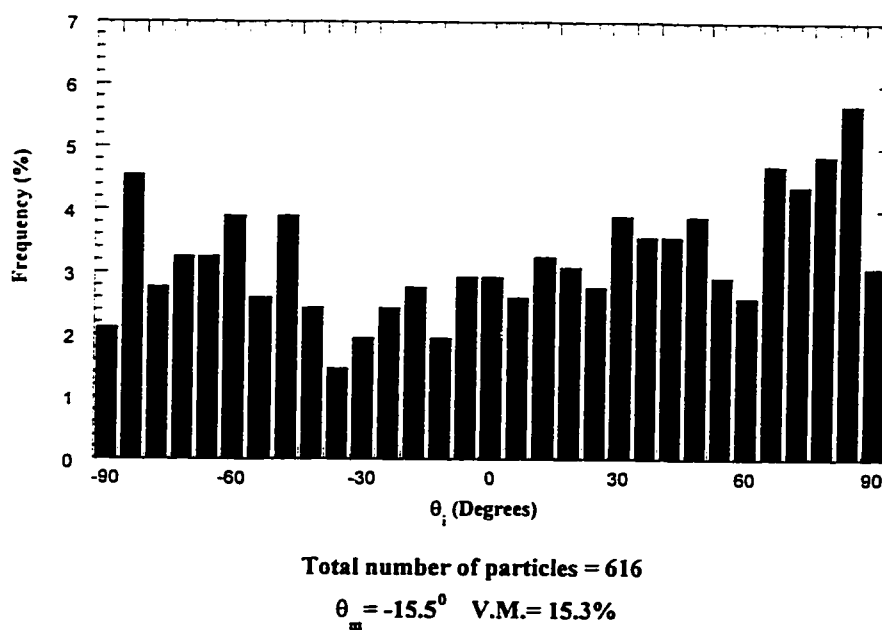
Figure 5.22 Frequency histograms of θ_i (Measured from Axis X) in a horizontal section (Y-X plane)
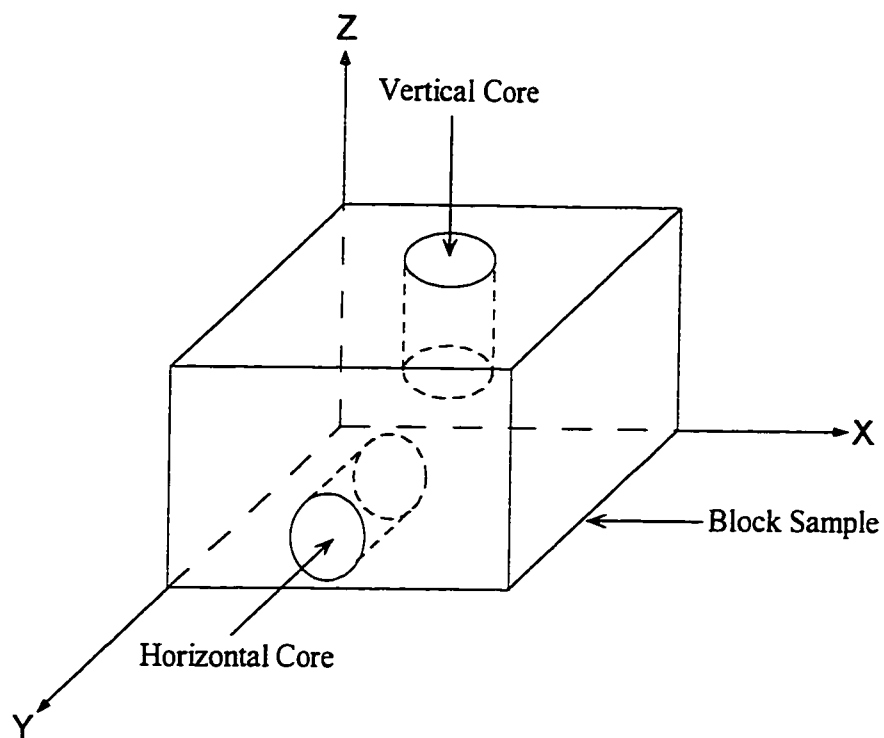
Figure 5.23 Schematic of vertical and horizontal core specimens in the block sample
(X-Y is the horizontal plane)
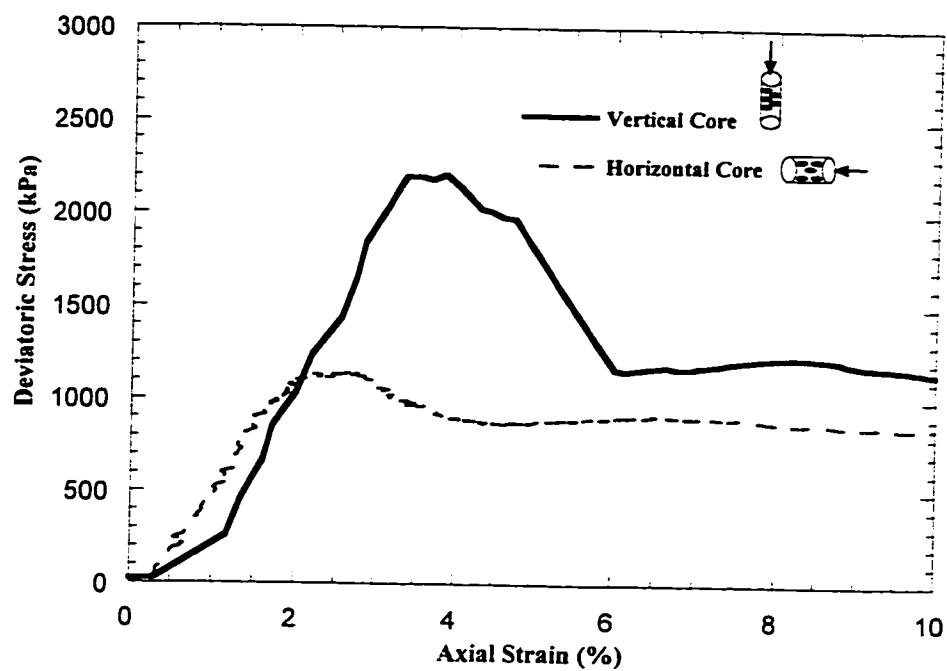
Figure 5.24 Stress - strain characteristics of oil sand ($\sigma'_3 = 250$ kPa)
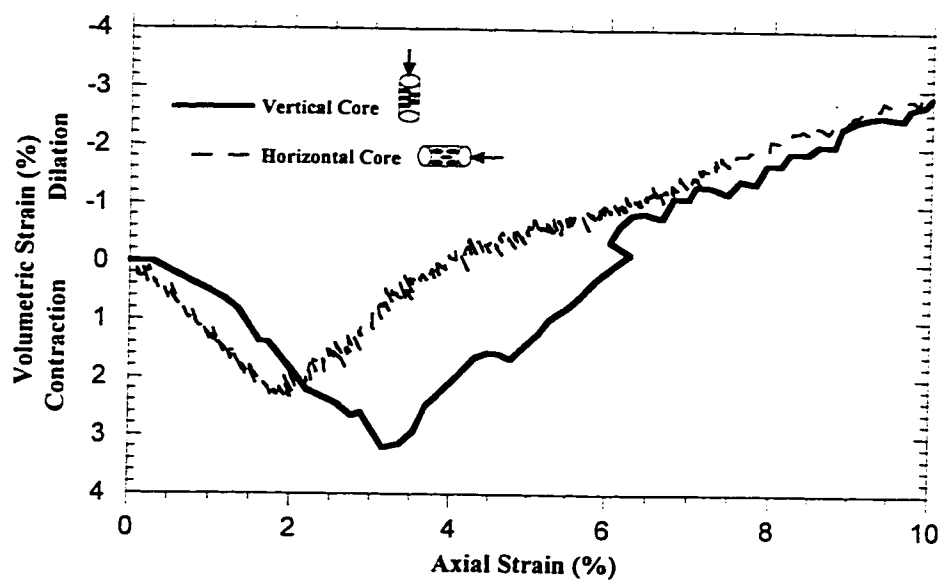
Figure 5.25 Volume change characteristic of oil sand ($\sigma'_3 = 250$ kPa)
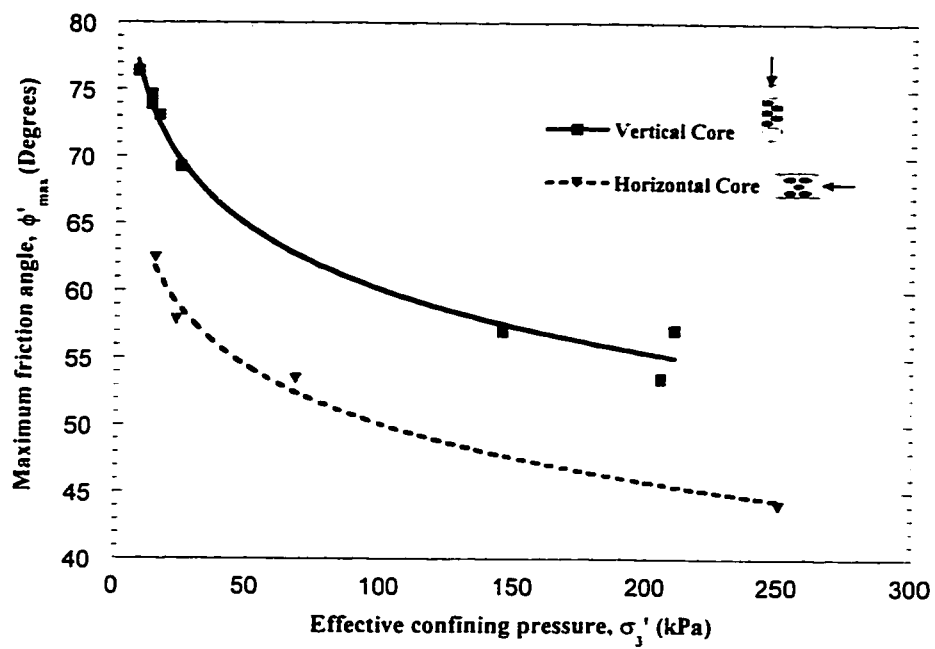
Figure 5.26 Variation of the maximum friction angle with effective confining
pressure
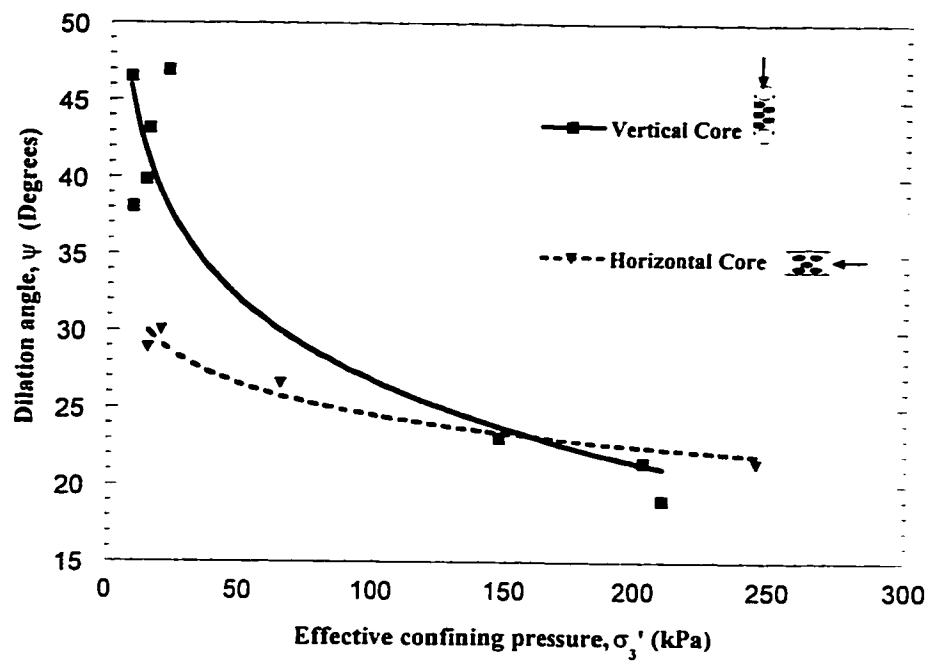
Figure 5.27 Variation of the dilation angle with effective confining pressure
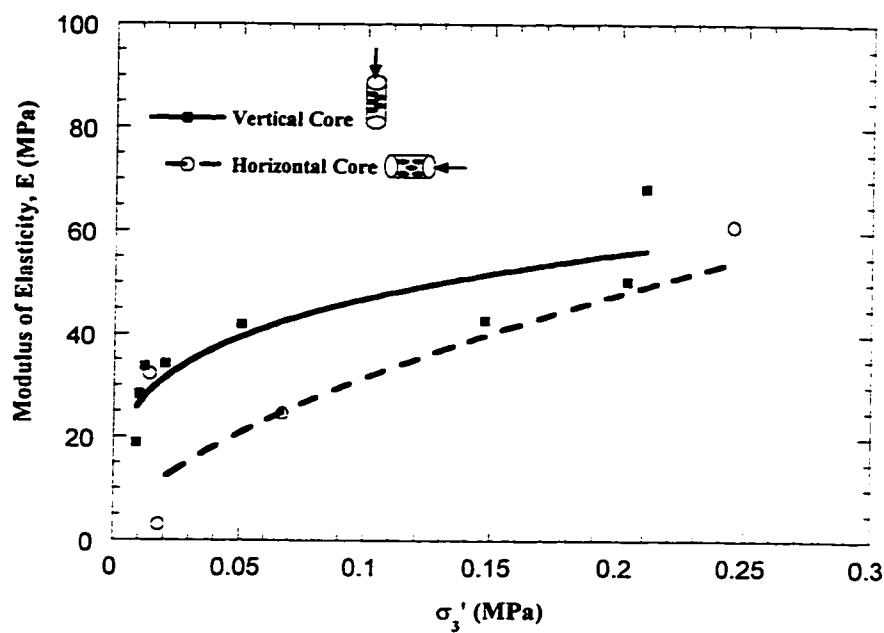
Figure 5.28 Variation of oil sand tangent modulus of elasticity with effective confining stress

Figure 5.29 Anisotropic permeability of oil sand

Flow perpendicular to long axes
(Vertical specimens)

Flow parallel to long axes
(Horizontal specimens)
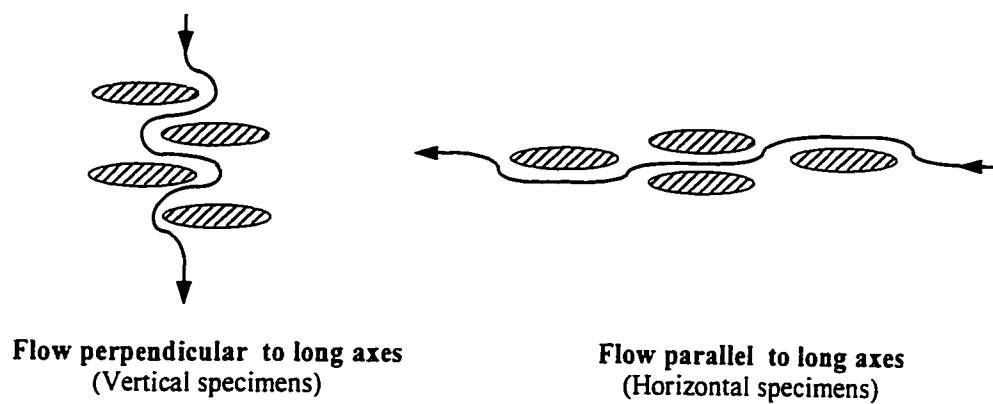
Figure 5.30 Flow paths perpendicular and parallel to grain axes

CHAPTER 6   OIL SAND GEOMECHANICAL BEHAVIOR

6.1 Introduction

A special form of steam flooding, known as steam assisted gravity drainage (SAGD), has been developed to recover oil from McMurray Formation oil sands. In the steam assisted gravity drainage process, the movement of oil to the production well is caused by gravity forces and the geometry is such that the oil moves approximately parallel to the interface which forms the boundary of a growing, steam-saturated zone known as the steam chamber. Injection of fluids at elevated temperatures and pressures results in stress and pore pressure changes not only in the heated portion of the reservoir but also in the formation in front of the advancing hot fluids. Thus the SAGD process results in a complex interaction of geomechanics and multiphase thermal flow in this cohesionless porous media. The geomechanical response of an oil sands reservoir to fluid pressure changes or to temperature changes results in stress and deformations that affect formation shearing and hydraulic properties (Chalaturnyk 1996).

During the course of this study an extensive laboratory testing program was conducted to examine the geomechanical properties of oil sands under conditions simulating SAGD. A series of triaxial tests were performed to replicate the stress and pore pressure conditions associated with steam stimulation. The test specimens included both undisturbed McMurray Formation oil sands and reconstituted sands. Table 6.1 shows a summary of tests and specimen properties.

The testing program was comprised of stress-strain, strength and permeability tests. Stress-strain and strength results of this testing program are presented and discussed here. Permeability test results are discussed in Chapter 8.

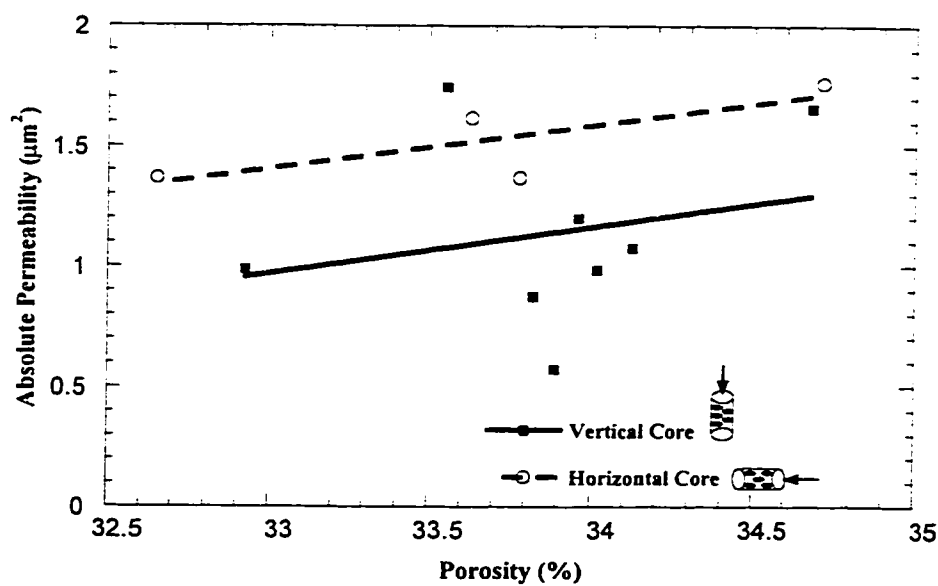The stress-strain behavior of McMurray Formation oil sands have been studied extensively in the past (Dusseault 1977, Agar 1984, Plewes 1987, Kosar 1989, Oldakowski 1994 and Chalaturnyk 1996). Dusseault (1977) showed that Athabasca oil sands have peak frictional strengths considerably in excess of those displayed by a dense sand. Agar et al. (1987) compared the peak friction angle of oil sand with that of quartzose Ottawa sand (Figure 6.1). The friction angle for oil sand is greater than that of dense Ottawa sand. However, the data presented in Figure 6.1 indicate that the strength of the two materials converge at very high confining stress levels. Dusseault and Morgenstern (1979) reported that a disruption of the initial fabric of oil sand returns the shear-strength behavior of the material to that of an ordinary sand. This behavior indicates that the fabric of the oil sand is responsible for the high strengths, and when this fabric is destroyed, the specimens behave as normal sands. Agar et al. (1987) observed that the shear strength of oil sand measured in triaxial compression tests was very sensitive to the degree of specimen disturbance. These experimental results indicate that a relatively small increase in the initial specimen porosity may result in a significant reduction in the measured shear strength.

Using data from shear box tests for both oil sand and Ottawa sand (Dusseault and Morgenstern 1978) the rate of dilation at failure was plotted as a function of the normal stress (Figure 6.2). It shows that energy required for dilation is responsible for the high frictional strengths of oil sand. Dilatancy is more pronounced at low effective confining stresses than at high confining stress levels. Despite the coarse-grained and quartzose nature of the Ottawa sand used and the relatively high densities attained (the more quartzose and coarse grained the material, the greater the shear strength), its dilative rates at failure are a fraction of those exhibited by locked sand material. Also Dusseault and Morgenstern (1978) reported large amounts of dilation at low stresses, despite the fine-grained character of the sands. Oldakowski (1994) showed that the magnitude of dilation caused by deviatoric stress is specially pronounced when stress conditions are approaching their state at failure and in post-failure region. He noted that the magnitude of dilation depends on the effective confining stress and specimen density (porosity).

Agar et al. (1987) concluded that the stress-strain behavior of Athabasca oil sand may be approximated reasonably accurately using the hyperbolic model up to about 80% of the peak deviatoric stress level. In Chapter 7 it is shown that in fact a nonlinear elastic behavior simulates fairly well the behavior of oil sand before peak strength.

Chalaturnyk (1996) combined the results of his study with experimental results of Oldakowski (1994). Kosar (1989), Plewes (1987), Agar (1984) and Dusseault (1977) to produce the most suitable peak failure envelope for McMurray Formation oil sand (Figure 6.3). All of these results were obtained from rich oil sands. The results of this study for core materials are also added to this plot.

As it can be seen from Figure 6.3, most of the previous experiments have been conducted under high confining pressures. A linear failure envelope of $\phi' = 60°$ and $c' = 0$ kPa defines reasonably well the envelope over the stress range of $(\sigma'_1 + \sigma'_3)/2 < 10$ MPa (Chalaturnyk 1996). A nonlinear curve fit through experimental data is also presented.

Scott et al. (1994) concluded that it is necessary that the behavior of locked sand should be studied under lower confining effective stresses. However most of previous triaxial tests on oil sands have been conducted at relatively high confining stresses (Figure 6.3). This is one of the reasons for this study to investigate the geomechanical behavior of McMurray Formation oil sand at low effective confining pressures.

6.1.1 Role of temperature and pore pressure

To model, in laboratory experiments, the changes in stress and pore pressure occurring in oil sand formation during hot fluid injection, it is useful to examine these changes in a stress path diagram. In geotechnical practice, it is accepted that the stress-strain response of sands are stress path dependent and the testing by Dusseault (1977), Agar (1984), Plewes (1987), Kosar (1989) and Oldakowski (1994) have confirmed this to be true for McMurray Formation oil sands.

A temperature increase causes thermal expansion of the sand grains and sand structure. A pore pressure increase during steam injection decreases the effective confining stress (Figure 6.4a). For the SAGD process, two predominant stress paths are followed within the reservoir, as shown in Figure 6.4b.

(1) first, under initially anisotropic stress conditions, pore pressure increases result in equal reductions in σ'_1 and σ'_3. In p'-q space, the stress path is horizontal because $\sigma'_1 - \sigma'_3$ is unchanged along this path. The stress ratio σ'_1/σ'_3, however, increases due to a reduction in σ'_3; and

(2) following the pore pressure injection stage, increasing horizontal stresses due to thermal expansion of the reservoir within the developing steam chamber initiate a stress path where the deviatoric stress and mean effective stress increase together. These stress increases are due primarily to an increase in horizontal total stress while vertical total stress remains relatively constant due to the shallow depth of the reservoir. At increasing depths, the vertical stress may also increase due to increased confinement.

Within a reservoir, the actual stress path will be a combination of these two stress paths (Chalaturnyk 1996). Due to practical restriction of the SAGD process there is a limit on the maximum pressure of injected steam. The pore pressure increase due to the SAGD process relative to the in situ pore pressures are thus a function of reservoir's depth. In shallow reservoirs with low in situ pore pressure this effect is considerable while in deeper reservoirs it may not be significant. Figure 6.4b demonstrates this effect on the resulted stress path.

6.1.2 Triaxial tests stress path

To simulate these stress paths, an experimental program was conducted which superimposed the effects of both stress changes and pore pressure changes. Figure 6.5 shows the stress paths implemented in this study. The stress path due to only thermal expansion could be compared to a conventional drained compression triaxial test in which the confining pressure remains unchanged while the major principal stress increases (path 1). A pore pressure increase will have a stress path of a horizontal straight line to the left (along the horizontal axis). Thus any stress path resulting from a combination of thermal and pore pressure effects will lie in the region between these two lines.

Consequently, in addition to path 1, testing was conducted along paths 2, 3 and 4 in order to examine oil sands behavior within this region. These stress paths illustrate the influence of pore pressure increase and as discussed above thus reflect the reservoir's depth. Path 2 is classically referred to as a constant mean effective stress path and paths 3 and 4 capture the effects of decreasing effective confining stress.

6.2 Test program

Table 6.1 shows the triaxial tests performed. Stress paths of Figure 6.5 were followed. Both test conditions of conventional end caps and lubricated end configuration were used. The merits of use of each of these test conditions and the importance of use of lubricated end configuration in permeability tests were discussed in detail in Chapter 3.

6.2.1 Test materials

Material tested in the course of this study included both undisturbed McMurray Formation oil sands and reconstituted sands.

6.2.1.1 Reconstituted specimens

During the course of this study reconstituted specimens made of three types of artificially mixed sand were tested. Figure 6.6 illustrates the grain size distribution of these sands. These mixed sands were reconstituted in the following order:

Different particle sizes of the original sand were separated first by dry sieving. The remaining particles on each sieve were then washed over that sieve and dried. The desired mixed sand is then made by mixing selected portions of different particle size. 1st and 2nd mixed sands (MS1and MS2 respectively) were made of the tailings stream from Syncrude's site in Fort McMurray while the 3rd mixed sand (MS3) was made of trimmings of undisturbed block samples (Chapter 1).

A series of conventional consolidated drained compression triaxial tests (Figure 6.5, path 1) were performed on these sands. The main objective in the preparation of reconstituted specimens was to create a sand specimen as dense as possible while maintaining specimen uniformity. These specimen preparation procedures were described in detail in Chapter 4. For completeness, the specimen preparation method and test condition for MS1, MS2 and MS3 are repeated below.

1st mixed sand (MS1)

MS1 represents a typical grain size distribution of Unit E of McMurray Formation. MS1 specimens were made using dry tamping method with resulted in relative densities ranging from 70 to 90 percent (Table 6.1). Specimens had a dimension of 50 mm by 100 mm (height/diameter = 2). The conventional end caps were used and the effective confining pressure ranged from 100 kPa to 500 kPa.

2nd mixed sand (MS2)

MS2 has a grain size distribution similar to that of the undisturbed block sample used in this study. MS2 specimens were made by two methods: water pluviation (confining pressures 100 and 200 kPa) and slurry deposition (confining pressure of 300 kPa). The

relative densities were 75 to 83 percent (Table 6.1) and specimens size were 50 mm by 100 mm (height/diameter = 2). Here also the conventional end caps were used.

3rd mixed sand (MS3)

MS3 was reconstituted to have a grain size distribution identical to that of the block sample. Specimens were made by the wet vibration method, described earlier (Chapter 4). High relative densities of 96 to 147 percent were obtained (Table 6.1). Lubricated end configuration with specimen size of 38 mm by 38 mm were used (height/diameter = 1). Effective confining pressures of 100 kPa to 250 kPa were applied.

6.2.1.2 Undisturbed specimens

All undisturbed specimens have grain size distributions similar to the block sample, out of which they are obtained (Figure 6.6). These specimens were obtained by coring the block sample both vertically and horizontally (Figure 6.7). Therefore two types of undisturbed specimen are tested in this study: vertical and horizontal core specimens.

The initial effective confining pressure of 250 kPa was chosen for most of the tests. For vertical specimens, confining pressures of 150, 200 and 210 kPa were also used for testing along stress path 1. Tests with similar stress paths were also conducted on reconstituted specimens made from MS3. For comparison these test results have also been included in this section.

All tests on undisturbed specimens and MS3 reconstituted specimens were performed with a lubricated end configuration and specimen dimensions of 38 mm by 38 mm. Specimens details are provided in Table 6.1.

6.2.2 Test procedure

As described in Section 2.12 the desired stress path was achieved by manipulation of the back pressure. The adjustment of back pressure was automatically implemented by the computer and the desired stress path was obtained. At the start of the test as the deviatoric stress was increasing the back pressure was increased as well, however, this stress path implementation could not be continued for the rest of the test. The following two cases describe the reason:

(1) Once the peak strength is realized the specimen will start to soften. In order to retain the same stress path, the back pressure has to be reduced. This does not correspond with the SAGD process. Therefore in the post peak region of the triaxial compression test the back pressure was kept constant.

(2) A positive effective confining stress is essential in performing a triaxial compression test. Thus when in some tests the effective confining stress was reduced to 15 kPa it was not allowed to reduce further. A minimum of 15 kPa effective confining stress was maintained in the rest of the test.

Either of these conditions whichever appropriate for the testing condition was implemented. Both these conditions mean that in the post peak region of the stress-strain plot, the actual stress path is one of a conventional drained stress path, like path 1. Figures 6.8 to 6.10 show the implemented stress paths. It could be seen that the computer controlled stress path testing equipment performed well in implementing the desired stress paths.

6.3 Test results

6.3.1 Reconstituted specimens

<u>1st mixed sand (MS1)</u>

Figures 6.11 and 6.12 show the stress-strain response of this material under stress path 1.

<u>2nd mixed sand (MS2)</u>

Figures 6.13 and 6.14 show the results of triaxial tests with stress path 1 on MS2 specimens. Both MS1 and MS2 specimens were tested with conventional end caps. From these figures it can be seen that, as it was discussed earlier in Chapter 3, triaxial tests with conventional end caps configuration result in a non-uniform single slip stress-strain behavior.

<u>3rd mixed sand (MS3)</u>

Figures 6.15 and 6.16 show the result of triaxial test on the MS3 specimens under stress path 1. Compared to the specimens tested with conventional end caps the stress-strain behavior of MS3 specimens sheared with lubricated end platens show a more uniform deformation. The results of triaxial tests with other stress paths on MS3 specimens are included with the undisturbed specimens results.

6.3.2 Undisturbed specimens

Figures 6.17 to 6.28 show the plots of the deviatoric stress versus axial strain and the volumetric strain versus axial strain of all the stress paths for horizontal core, vertical core and MS3 specimens. In all these tests the lubricated end configuration were used.

The stress-strain behavior of undisturbed specimens show that, at the confining stresses that these specimens were tested ($\leq$ 250 kPa), post-peak stress reduction is abrupt and residual strength is reached after a total axial strain of about twice the value of the failure strain. This extreme decrease in strength is an indication of a sudden disruption in the specimen's structure. The jagged shape of stress-strain curves of undisturbed specimens is also indicative of the interlocking structure of oil sand (Chapter 5).

6.4 Discussion

In this study it is assumed that when a triaxial specimen passes its peak frictional strength it has failed. Considering the results of tests at different effective confining stresses, a failure envelope describing the generalized stress conditions under which sand will "fail" can be determined. This failure envelope thus represents the peak frictional strength of the material over the effective stress ranges tested.

6.4.1 Reconstituted specimens

Peak failure envelopes was developed for each of these sands (Figure 6.29). Friction angles of 37°, 41° and 42.6° is computed for MS1, MS2 and MS3 specimens respectively. As expected the peak friction angle have a direct relationship with relative density (Figure 6.30).

6.4.2 Undisturbed specimens

Undisturbed core specimens show much higher peak frictional strength than reconstituted specimens. This is despite high relative densities attained by MS3 specimens. This behavior indicates that, as discussed in Chapter 5, the fabric of oil sand provides additional strength to oil sand. The stress-strain curves of undisturbed specimens shows that when this fabric is destroyed, specimens behave as normal sand.

A strength anisotropy is obvious in the undisturbed specimens. Vertical core specimens show higher strength and dilation rates than horizontal core specimens. As was discussed in Chapter 5, this is due to the fact that particles of oil sand block sample, which are non-spherical, have a preferred orientation parallel to the horizontal plane. Vertical core specimens had a longitudinal axis perpendicular to this preferred orientation of particles while longitudinal axis of horizontal core specimens were parallel to it.

A marked contraction is observed for the core specimens undergoing stress path 1 with constant effective confining stress. In the other stress paths in which the effective confining pressure decreases through the test the contraction diminishes. In fact for stress path 4, there is almost no contraction and dilation starts immediately after the start of shearing. This is due to a sudden increase in pore pressure and lower effective confining pressure associated with this stress path.

The dilative behavior is expected from these dense sands. Higher dilation rates are indeed associated with higher strength of undisturbed specimens compared to the reconstituted ones.

Figure 6.31 illustrates the peak failure envelopes of these materials for the effective stress ranges tested. Vertical core specimens show a high friction angle of 51°, with horizontal cores having a friction angle of 41°.

This geomechanical data is used in Chapter 7 to demonstrate a methodology in which the laboratory results could be incorporated in numerical simulation of oil sands at low confining pressures. This will show one of the potential applications of this study's experimental results. Related geomechanical parameters like dilation and stiffness are discussed in detail in Chapter 7.

6.4.3 Comparison with previous experimental studies

In this section the results of experiments by previous researchers are described and compared with the results of the current study.

Figure 6.32 shows the lower range, $(\sigma'_1 + \sigma'_3)/2 < 2\,\text{MPa}$, for the data in Figure 6.3. Although the undisturbed cores showed a lower friction angle than the one suggested by Chalaturnyk (1996) it should be noted that the data in Figures 6.3 and 6.32 are from a variety of specimens and the proposed failure envelopes should be looked at as a general guideline. In this context, the results are fairly consistent.

Although most of the tests by previous researchers have been conducted under high confining pressures, the following two tests are at a low effective confining stress and are used here for comparison (Figure 6.33). Both of these tests are conventional drained compression tests (stress path 1). Figure 6.33 also includes the result of the triaxial test on specimen T29, a vertical core specimen with initial porosity of 34%, tested under 210 kPa effective confining pressure.

Dusseault (1977) tested Athabasca oil sand specimens obtained from cored bore holes located 50 km north of Fort McMurray. Borehole refrigeration techniques were employed. The specimens were transported in chilled insulated boxes and stored in a refrigerated room until testing. Specimens were trimmed to a diameter of 76 mm. The specimen discussed here, specimen 117, was a fine-grained rich oil sand, with an initial porosity of 34.5%, which was located at depth of 117 m. Its height to diameter ratio was 2.09. The specimen was consolidated under 1000 kPa effective confining pressure and had an effective confining pressure of 400 kPa during the test. Results of the test on this specimen are presented in Figure 6.33.

Oldakowski (1994) conducted triaxial compression tests on oil sand cores obtained from wells drilled at the Underground Test Facility site (Chapter 1). Specimen preparation was conducted in a cold room. Cores were machined to a diameter of 38.1 mm and specimens of 38.1 mm length were cut out. Specimens were chosen from two stratigraphic units, E and D, which are composed of the richest oil sands at the UTF site. An isotropic compression with confining pressure of 7 MPa was applied to recompress the specimens. Figure 6.33 shows the results of test specimen S7. This specimen was chosen from stratigraphic Unit D (depth of 149.5 m) and had a porosity of 38%. The specimen was tested at an effective confining pressure of 240 kPa.

Figure 6.34 shows that the grain size distributions of these specimens are similar. It should be noted that all of these specimens were vertically cored specimens.

Specimens 117 and S7 were tested with conventional end caps. Specimen 117 had a height/diameter ratio of 2.09. As discussed in Chapter 3 this testing condition has a characteristic of a steeper stress-strain curve which peaks at smaller strain. As illustrated in Figure 3.4 these effects are due to the fact that most of deformation of the specimen occurs within a narrow shear zone. Figure 6.33a illustrates that the axial strain at peak strength for specimen 117 is much lower than that of the specimen T29. Core specimens in this study were tested with lubricated end caps and a height/diameter ratio of 1. Their stress-strain curves broke over more gradually and the strain at failure was considerably larger, owing to the fact that the entire specimen was undergoing uniform deformation (Chapter 3). Even though specimen S7 was tested with conventional end platens it shows a more ductile behavior. This is due to the fact that its height/diameter ratio was also 1 and therefore a single shear zone was not allowed to develop (Figure 3.4).

Specimen S7 had a high porosity which is an indication of disturbance. This is visible in its lower shear strength compared to the vertical core specimen, both tested under almost the same confining pressure (Figure 6.33a).

As discussed earlier specimen T29, like other core specimens tested under stress path 1 (Figure 6.17 to 6.22), experienced considerable contraction during shearing before the peak strength. This could be due to the use of lubricated end platens which result in the participation of the whole volume of the specimen in shear deformation as opposed to conventional platens which result in dead zones within a specimen's volume (Figure 3.2).

Specimen 117 acted somewhat similar to core specimens and contracted till peak strength. This shows the similarity of their fabric. Specimens tested by Oldakowski were disturbed and then recompressed under high confining pressures before the shear test. This could explain the relatively small amount of contraction at the beginning of shear.

All specimens showed the peak dilation rate to be at the peak shear strength (Figure 6.33b). Specimen 117 had a peak dilation angle (Chapter 7) of 24° which is close to the peak dilation angle of 25° for the T29 specimen. However with further shearing dilation reduces substantially in specimen 117 and ceases when the critical void ratio is reached on the failure plane. This is due to the fact that in tests with conventional end caps and a height to diameter ratio of 2 or more, single line failure takes place (Chapter 3). Therefore dilation occurs largely within a narrow plane, lessening the effect of dilation when compared with the entire specimen volume.

Specimen S7 had a dilation angle of only 11°, again showing the larger porosity and the disturbance of this specimen. Also it could be concluded that the formation of dead zones within the specimen due to the use of conventional ends had reduced the overall volumetric deformation of the specimen during shear.

Considering the testing condition of the specimens, it could be concluded that specimen T29 and specimen 117 tested by Dusseault (1977) display similar behavior. As they had

the same initial porosity and the same grain size distribution, their initial fabrics must have been similar.

6.5 Summary

- Undisturbed specimens of McMurray Formation oil sand, obtained from a block sample, were tested along with reconstituted specimens. The undisturbed specimens were obtained by coring the block sample both vertically and horizontally. A series of triaxial tests were performed to replicate the stress path conditions associated with SAGD.

- The computer controlled stress path testing equipment performed well in implementing the chosen stress paths.

- High density reconstituted specimens were obtained and showed similar but gentler trend in stress-strain behavior to that of undisturbed specimens.

- Strength anisotropy was observed in the undisturbed specimens as vertical core specimens showed higher strengths than horizontal core specimens.

- A noticeable contraction during initial shear deformation was observed for the core specimens which decreased with a reduction in effective confining pressure. This was attributed to the participation of the whole volume of the specimen in shear deformation due to the use of the lubricated end platens.

- Undisturbed specimens demonstrated high dilation rates. They were associated with higher strengths for the undisturbed specimens compared to the reconstituted ones.

- Vertical core specimens showed a peak friction angle of 51°. Horizontal cores have a peak friction angle of 41°.

- Undisturbed core specimens show a lower friction angle than the one suggested by Chalaturnyk (1996) however the results are consistent.

- Although most of triaxial tests on oil sands by previous researchers have been conducted at relatively high confining stresses, two tests with similar confining pressures were compared with a vertical core specimen. The difference in behavior of triaxial specimens with conventional end caps and lubricated end caps was captured. It was concluded that the vertical core specimen and specimen tested by Dusseault (1977) displayed similar behavior.

Table 6.1 Summary of tests and specimen properties

| Test No.	Test Configuration	Material Type	Preparation Method	Stress Path	σ'_3 (Kpa)	Permeability Test	ρ_d (g/cm3)	Dr (%)	Void Ratio	Porosity (%)	H (mm)	D (mm)
5	Conventional	1st Mixed Sand	Dry Tamping	1	300	No	1.71	89.3	0.55	35.6	100.08	52.00
6	Conventional	1st Mixed Sand	Dry Tamping	1	500	No	1.649	69.1	0.61	37.9	101.38	52.00
7	Conventional	1st Mixed Sand	Dry Tamping	1	100	No	1.69	82.9	0.57	36.3	98.65	52.00
8	Conventional	1st Mixed Sand	Dry Tamping	1	400	No	1.7	86.1	0.56	36.0	99.29	52.00
9	Conventional	1st Mixed Sand	Dry Tamping	1	100	No	1.702	86.8	0.56	35.9	99.19	52.00
10	Conventional	1st Mixed Sand	Dry Tamping	1	200	No	1.677	78.6	0.58	36.8	98.64	52.00
11	Conventional	1st Mixed Sand	Dry Tamping	1	500	No	1.707	88.4	0.56	35.7	98.05	52.00
12	Conventional	1st Mixed Sand	Dry Tamping	1	400	No	1.703	87.1	0.56	35.9	98.30	52.00
13	Conventional	1st Mixed Sand	Dry Tamping	1	300	No	1.702	86.8	0.56	35.9	98.50	52.00
14	Conventional	1st Mixed Sand	Dry Tamping	1	200	No	1.689	82.5	0.57	36.4	99.27	52.00
15	Conventional	1st Mixed Sand	Dry Tamping	1	100	Yes	1.763	105.8	0.51	33.6	98.14	51.70
16	Conventional	1st Mixed Sand	Dry Tamping	1	100	Yes	1.73	95.7	0.54	34.9	99.86	51.80
17	Conventional	1st Mixed Sand	Moist Tamping	1	100	Yes	1.636	64.6	0.63	38.6	104.60	51.82
18	Conventional	2nd Mixed Sand	Water Pluviation	1	100	Yes	1.605	78.9	0.65	39.4	106.30	51.57
19	Conventional	2nd Mixed Sand	Water Pluviation	1	200	Yes	1.616	83.0	0.64	39.0	109.74	50.70
20	Conventional	2nd Mixed Sand	Slurry Deposition	1	300	Yes	1.596	75.6	0.66	39.8	108.93	51.06
22	Conventional	2nd Mixed Sand	Wet Vibration	1	100	Yes	1.561	62.2	0.69	41.0	99.45	50.63
23	Lubricated Ends	3rd Mixed Sand	Wet Vibration	1	100	Yes	1.744	123.8	0.52	34.3	38.91	37.74
24	Lubricated Ends	3rd Mixed Sand	Wet Vibration	1	150	Yes	1.784	137.6	0.49	32.8	41.79	37.77
25	Lubricated Ends	3rd Mixed Sand	Wet Vibration	1	200	Yes	1.802	143.7	0.47	32.1	36.29	37.50
26	Lubricated Ends	3rd Mixed Sand	Wet Vibration	1	250	Yes	1.814	147.6	0.46	31.7	36.39	37.52
27	Lubricated Ends	Block Sample	Vertical Core	1	150	Yes	1.757	128.4	0.51	33.8	36.90	38.75
28	Lubricated Ends	Block Sample	Vertical Core	1	200	Yes	1.734	120.3	0.53	34.7	39.68	38.63
29	Lubricated Ends	Block Sample	Vertical Core	1	210	Yes	1.753	127.0	0.51	34.0	39.32	38.13
30	Lubricated Ends	3rd Mixed Sand	Wet Vibration	2	250	Yes	1.693	105.3	0.57	36.2	38.44	37.75
31	Lubricated Ends	3rd Mixed Sand	Wet Vibration	3	250	No	1.725	117.1	0.54	35.0	40.99	37.16
33	Lubricated Ends	3rd Mixed Sand	Wet Vibration	3	250	Yes	1.702	108.6	0.56	35.9	39.46	37.73
34	Lubricated Ends	3rd Mixed Sand	Wet Vibration	4	250	Yes	1.668	95.8	0.59	37.2	37.68	37.72
35	Lubricated Ends	Block Sample	Vertical Core	2	250	No	1.751	126.3	0.49	32.9	38.88	36.52
36	Lubricated Ends	Block Sample	Vertical Core	3	250	Yes	1.757	128.4	0.51	33.6	38.96	36.22
37	Lubricated Ends	Block Sample	Vertical Core	4	250	No	1.747	124.9	0.52	34.0	36.11	38.15
38	Lubricated Ends	Block Sample	Vertical Core	2	250	Yes	1.744	123.8	0.52	34.1	39.47	38.42
39	Lubricated Ends	Block Sample	Vertical Core	4	250	Yes	1.75	126.0	0.51	33.9	38.80	38.48
40	Lubricated Ends	Block Sample	Horizontal Core	1	250	Yes	1.783	137.3	0.49	32.7	40.22	38.44
41	Lubricated Ends	Block Sample	Horizontal Core	2	250	Yes	1.754	127.4	0.51	33.8	40.47	38.41
42	Lubricated Ends	Block Sample	Horizontal Core	3	250	Yes	1.729	118.5	0.53	34.7	36.75	38.53
43	Lubricated Ends	Block Sample	Horizontal Core	4	250	Yes	1.758	128.7	0.51	33.6	38.92	38.73
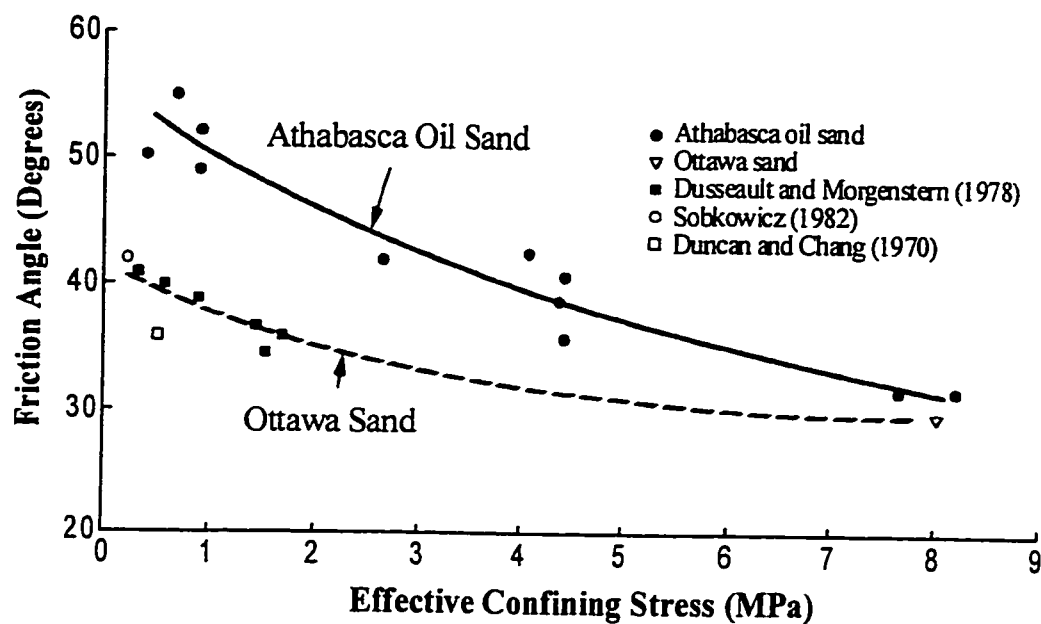
Figure 6.1 Comparison of the shear strength of Athabasca oil sand and dense Ottawa sand

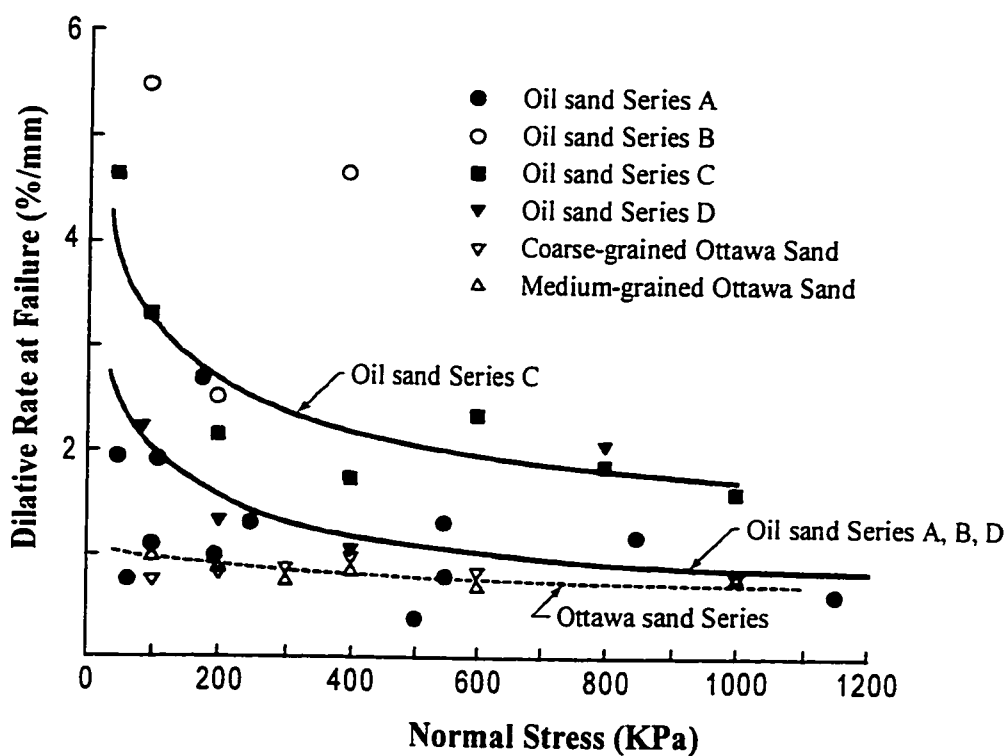(Modified from Agar et al. 1987)

Figure 6.2 Comparison of dilative rate of Athabasca oil sands with Ottawa sand

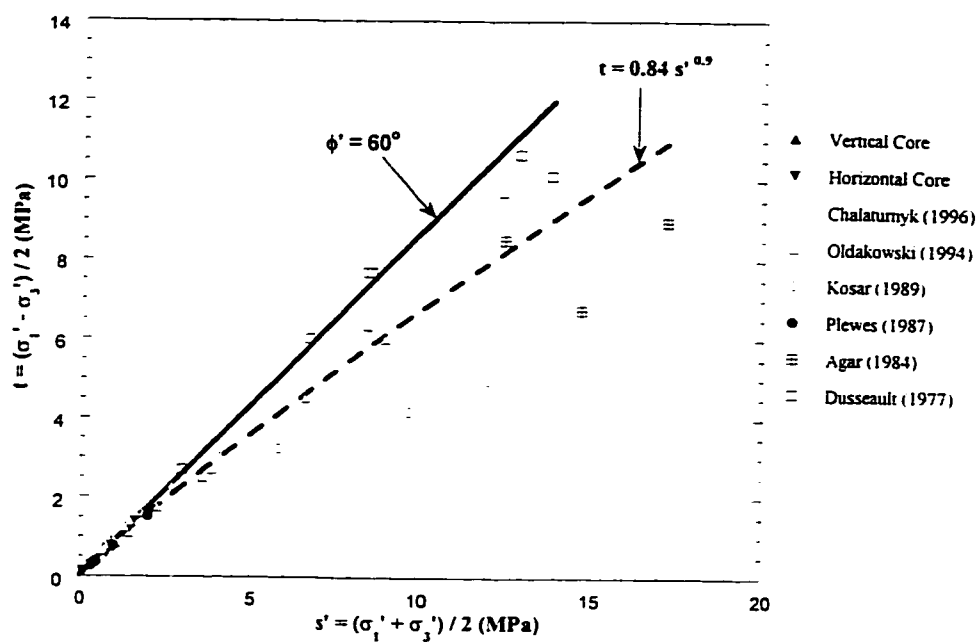(Modified from Dusseault and Morgenstern 1978)

Figure 6.3 Peak failure envelope for McMurray Formation oil sands
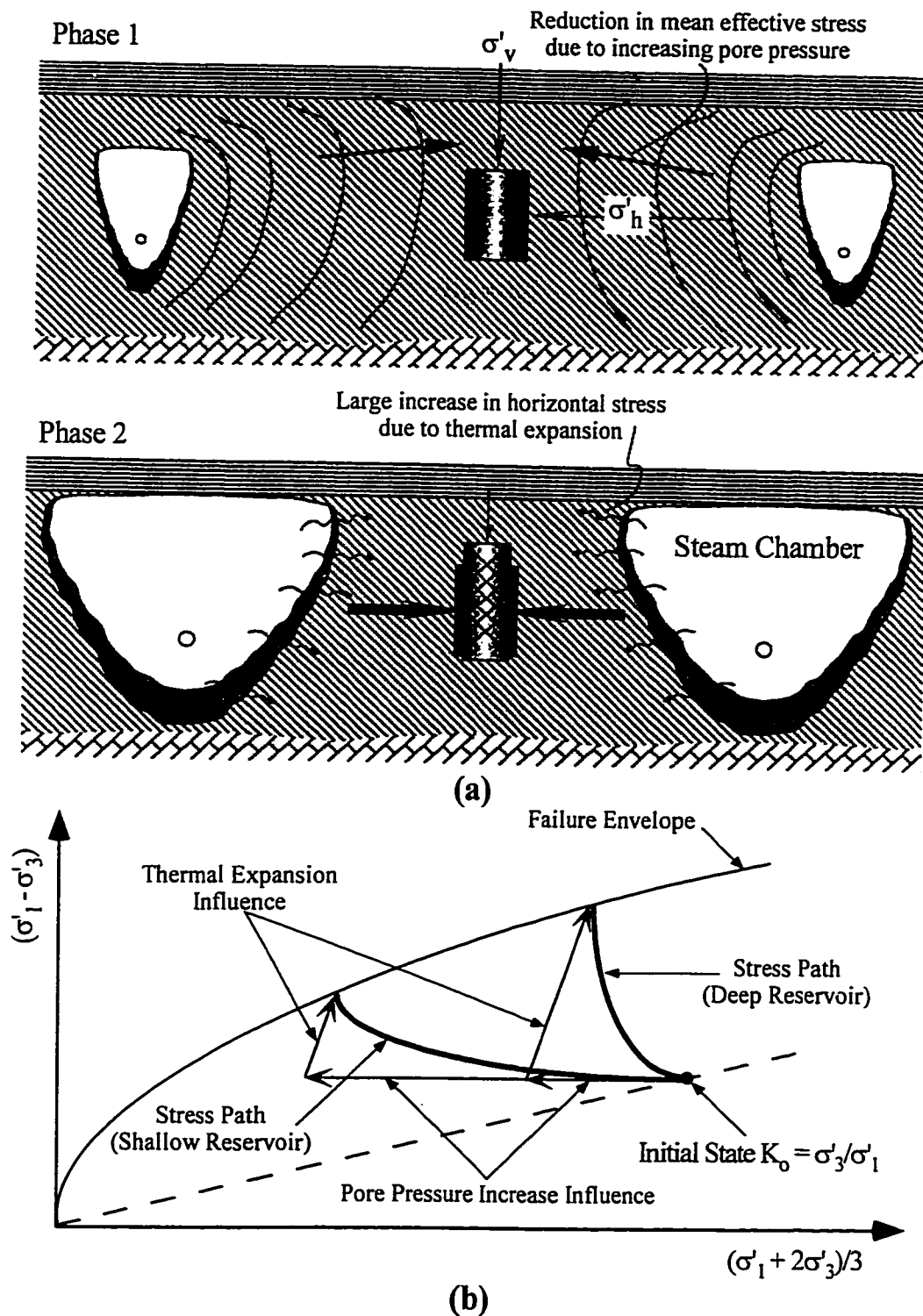(Modified from Chalaturnyk 1996)

Phase 1

Reduction in mean effective stress
due to increasing pore pressure

σ'_v

σ'_h

Large increase in horizontal stress
due to thermal expansion

Phase 2

Steam Chamber

(a)

$(\sigma'_1 - \sigma'_3)$

Failure Envelope

Thermal Expansion
Influence

Stress Path
(Deep Reservoir)

Stress Path
(Shallow Reservoir)

Initial State $K_0 = \sigma'_3/\sigma'_1$

Pore Pressure Increase Influence

$(\sigma'_1 + 2\sigma'_3)/3$

(b)

**Figure 6.4 Major stress path followed within reservoir during
SAGD process**
(Modified from Chalaturnyk 1996)
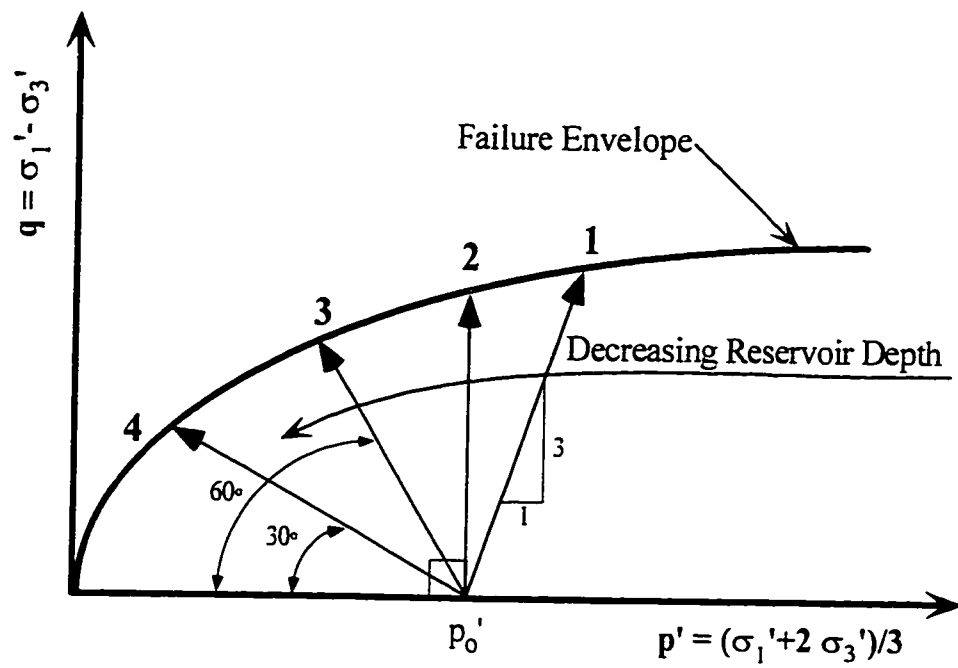
Figure 6.5 Schematic illustration of stress paths investigated
(p_o' is initial effective confining pressure)
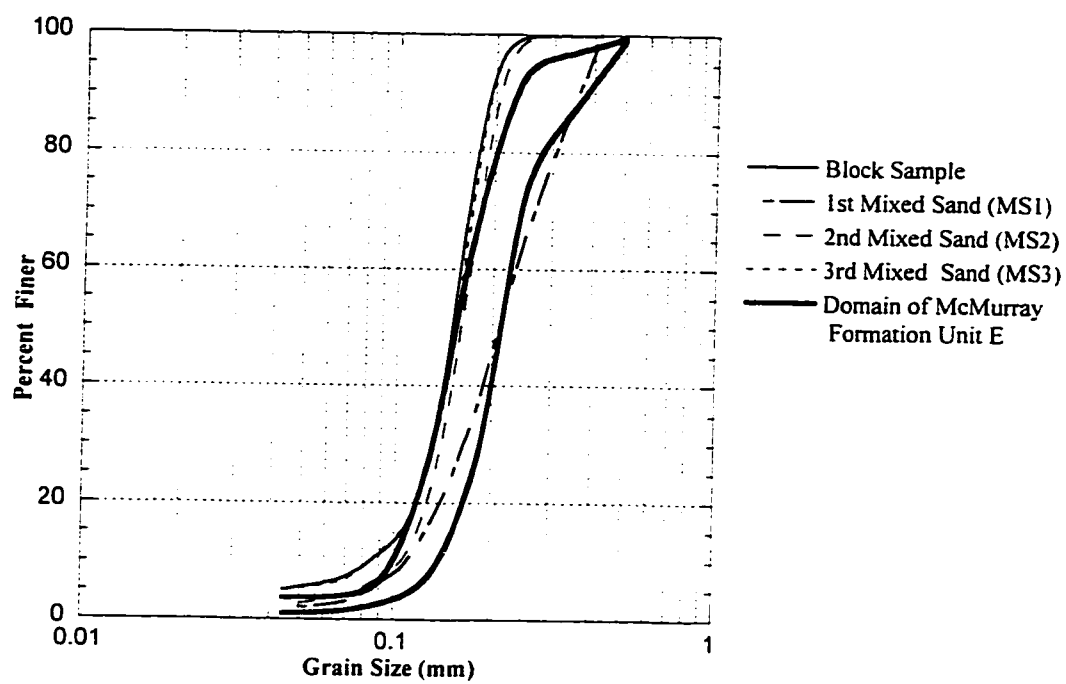
Figure 6.6 Grain size distribution of specimens tested
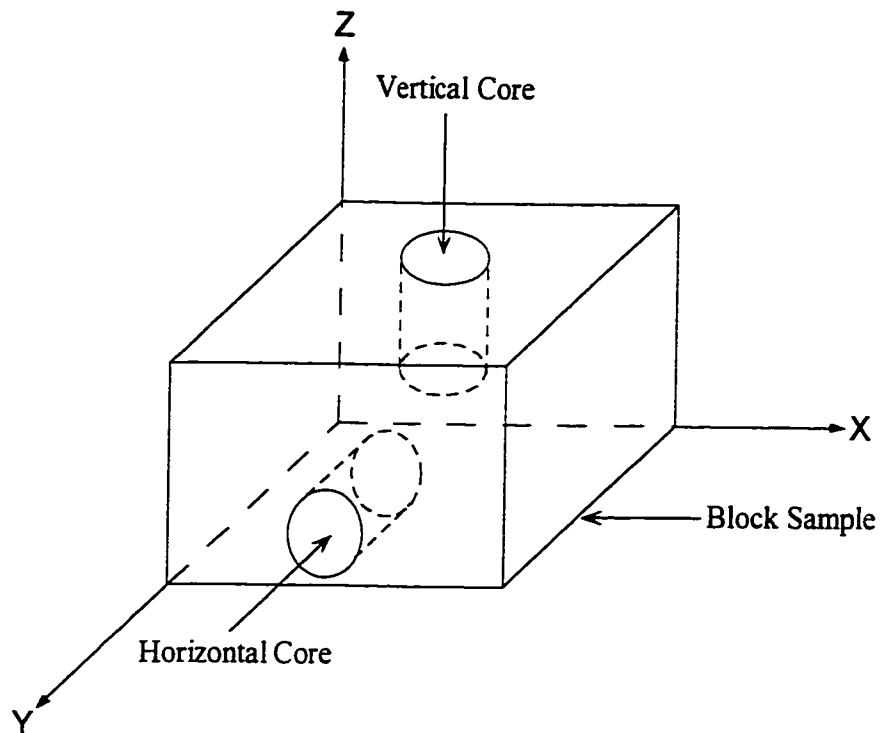
Figure 6.7 Schematic of vertical and horizontal core specimens in the block sample (X-Y is the horizontal plane)
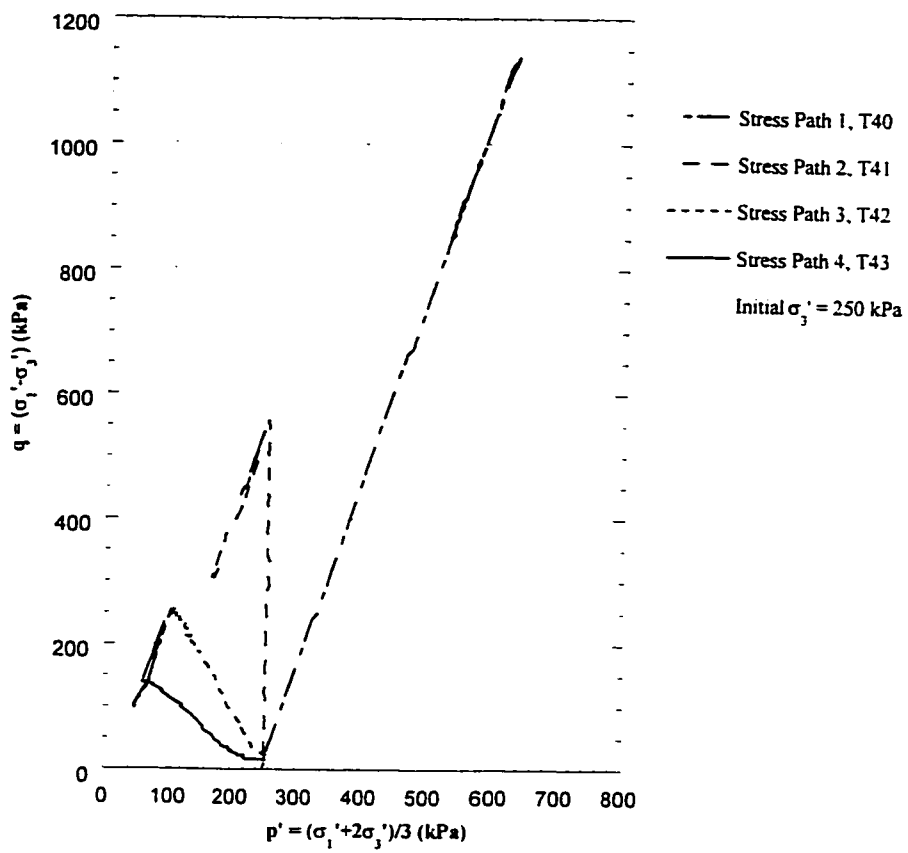
Figure 6.8 Implemented stress paths for horizontal cores
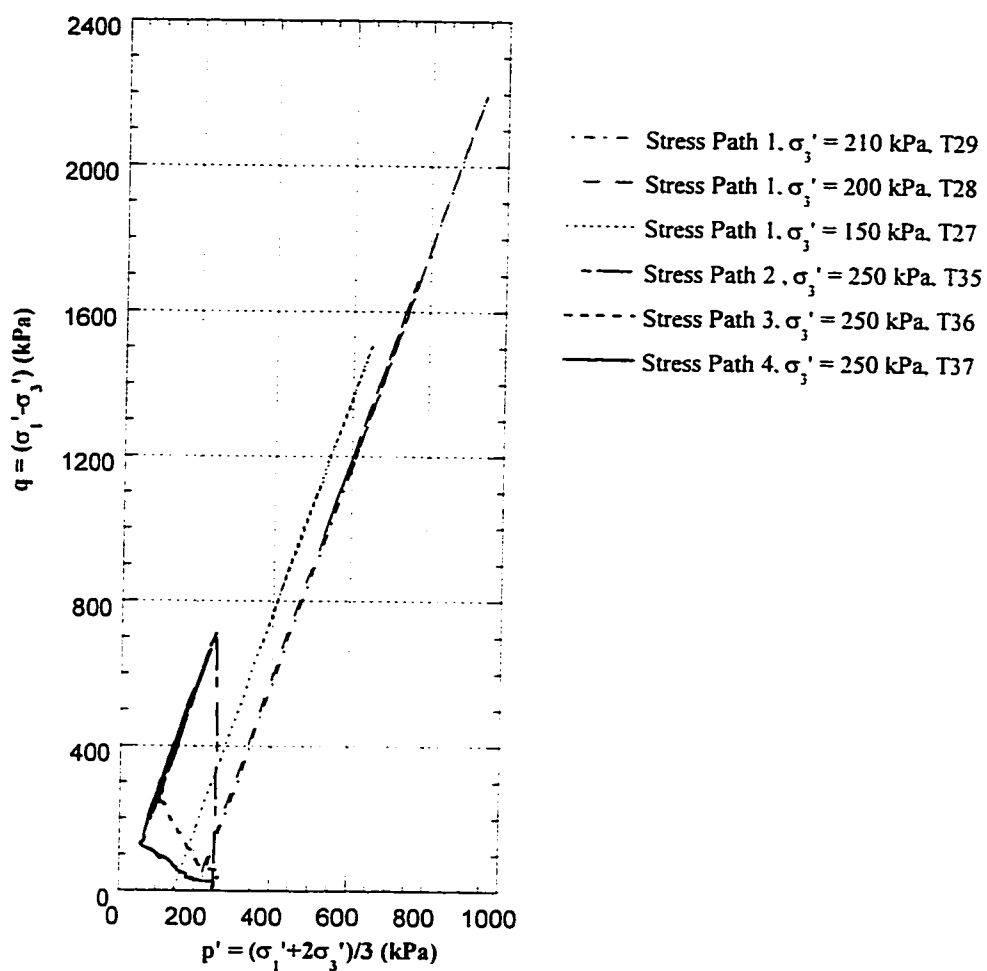
Figure 6.9 Implemented stress paths for vertical cores
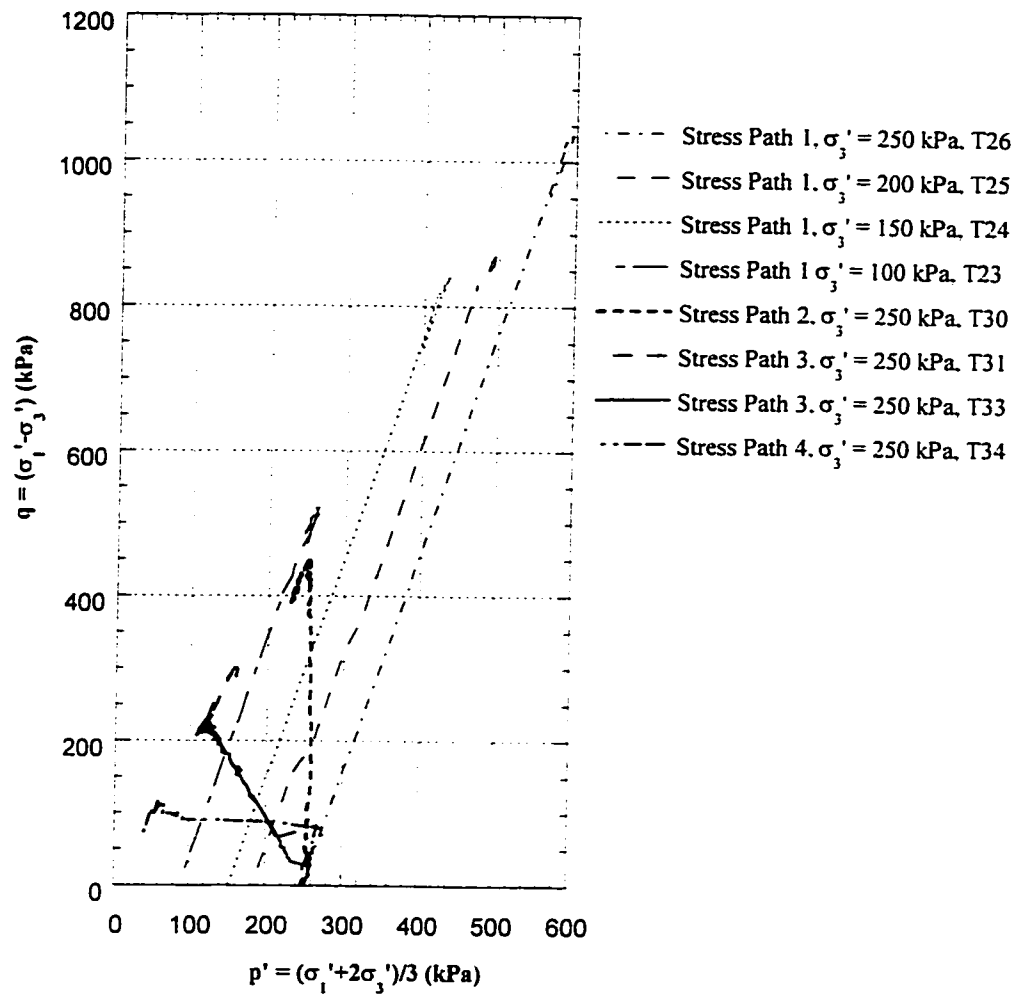
Figure 6.10 Implemented stress paths for reconstituted specimens (MS3)
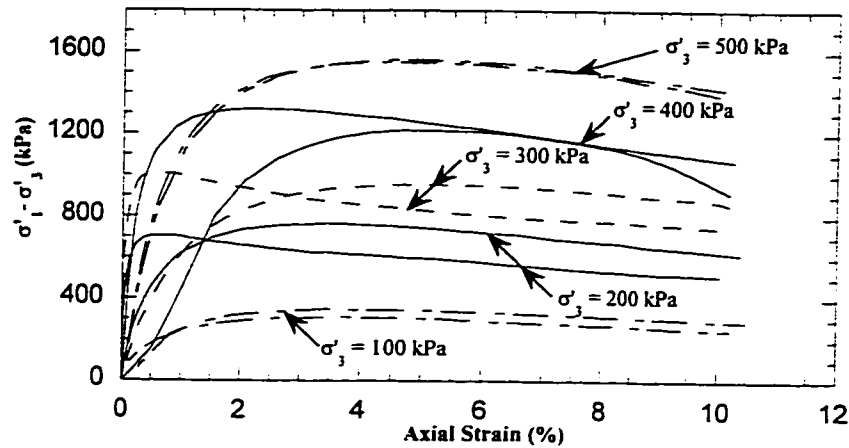
**Figure 6.11 Deviatoric stress versus axial strain,
Reconstituted specimens (MS1)
with conventional end platens**
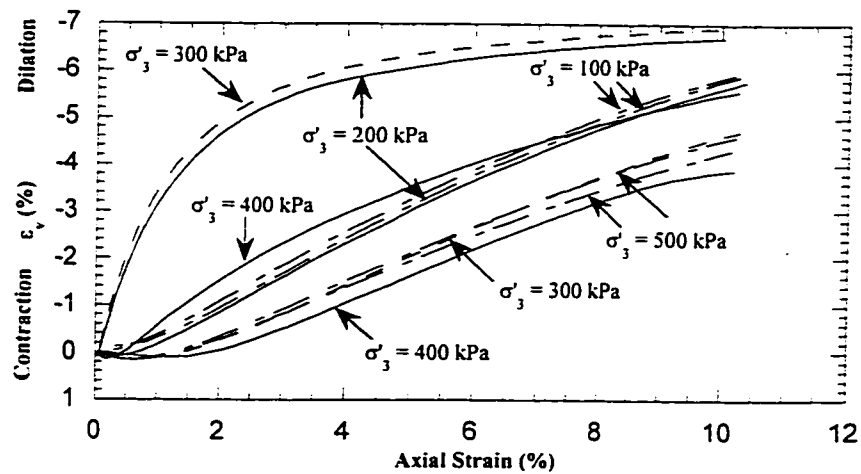
**Figure 6.12 Volumetric strain versus axial strain, Reconstituted specimens (MS1)
with conventional end platens**
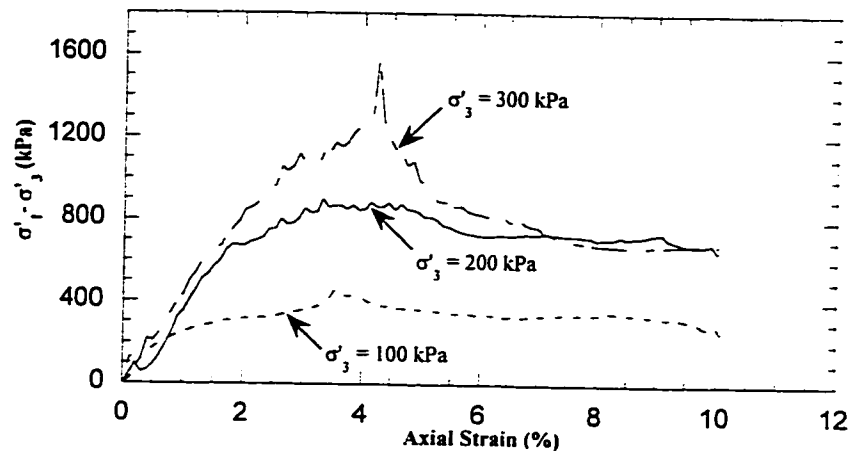
Figure 6.13 Deviatoric stress versus axial strain, Reconstituted specimens (MS2) with conventional end platens
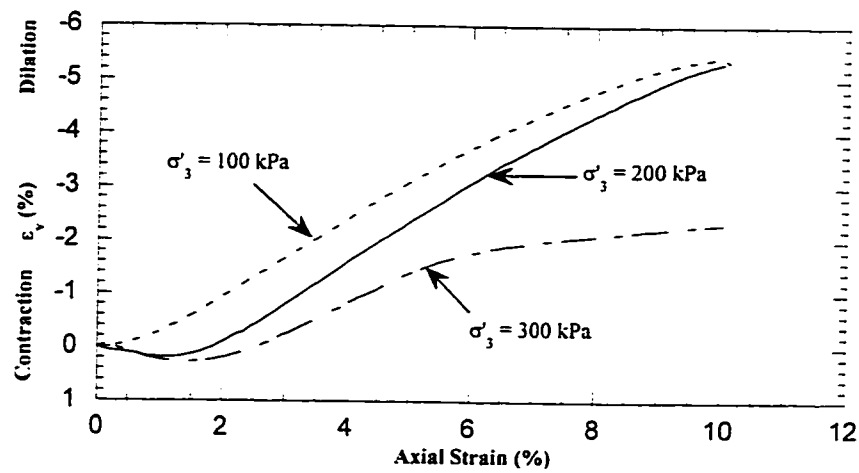
Figure 6.14 Volumetric strain versus axial strain, Reconstituted specimens (MS2) with conventional end platens
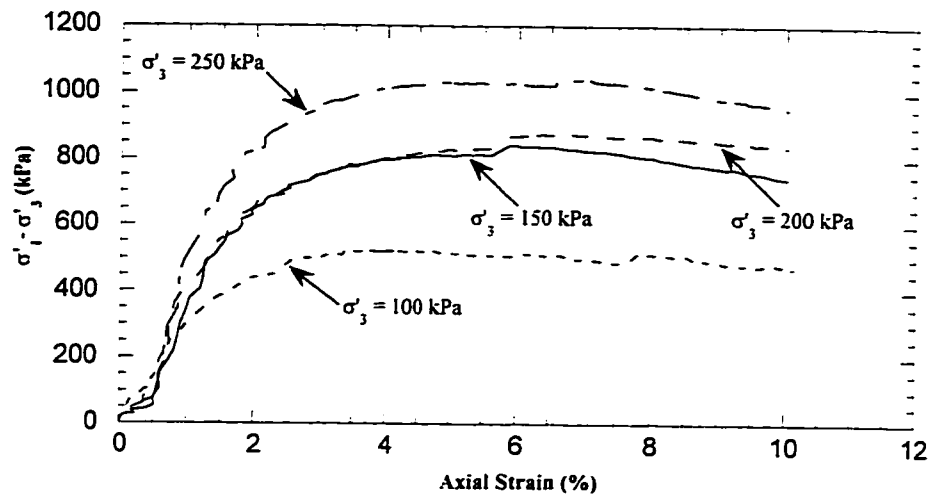
Figure 6.15 Deviatoric stress versus axial strain, Reconstituted specimens (MS3) with lubricated end platens
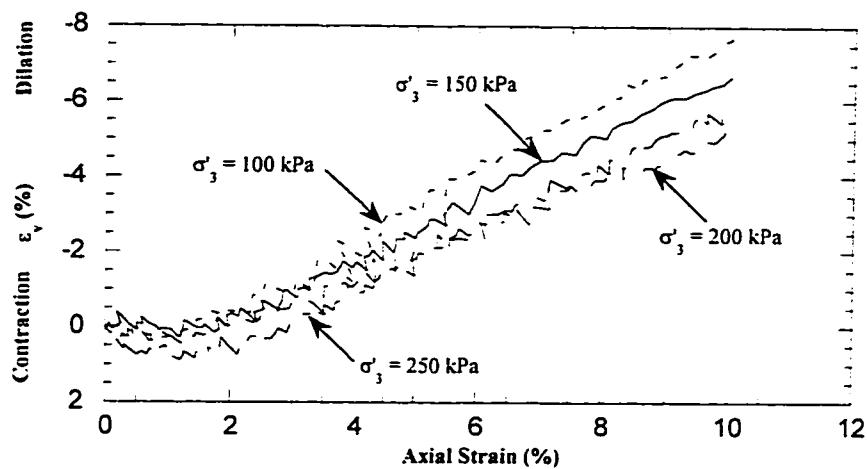
Figure 6.16 Volumetric strain versus axial strain, Reconstituted specimens (MS3) with lubricated end platens
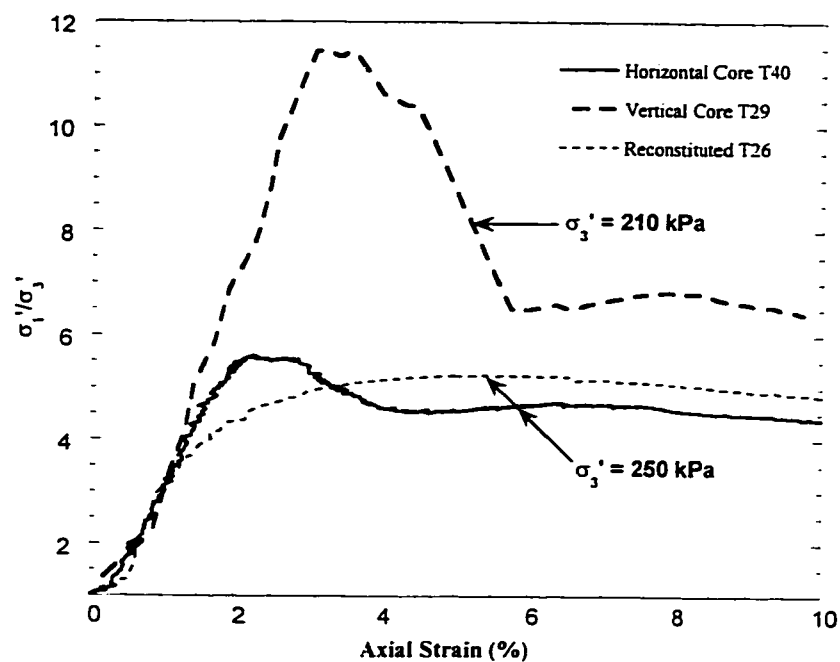
**Figure 6.17 Stress ratio versus axial strain
Stress Path 1**
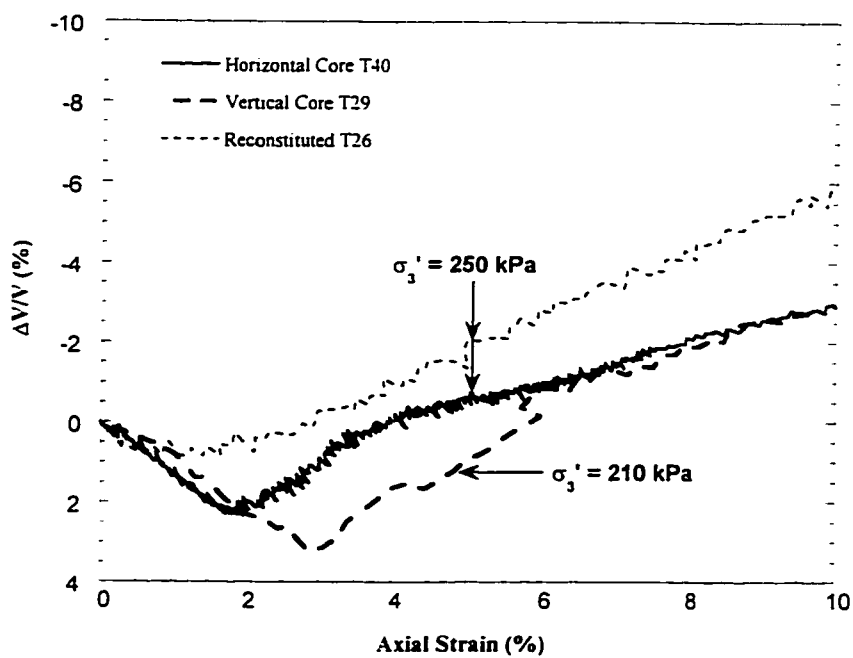
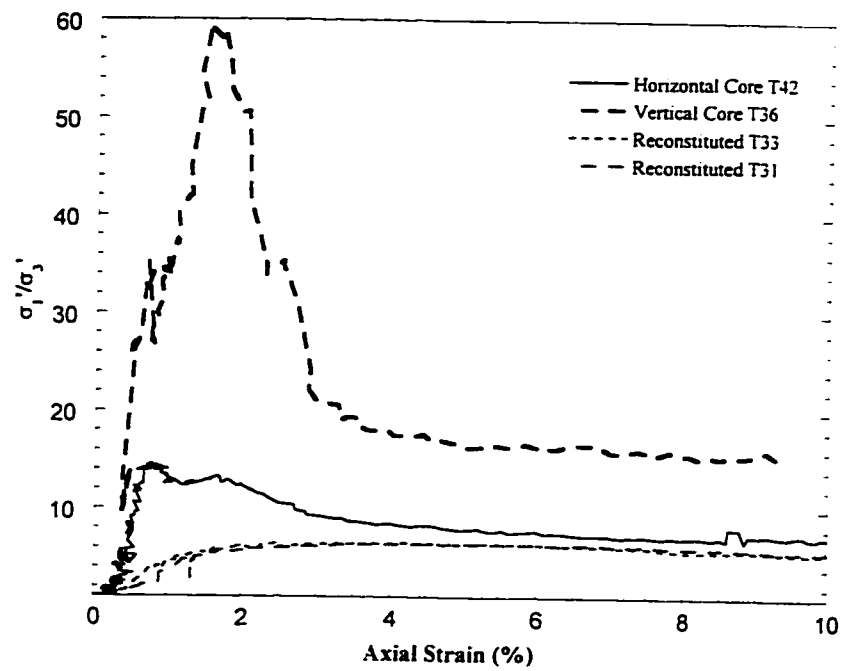**Figure 6.18 Volumetric strain versus axial strain
Stress Path 1**
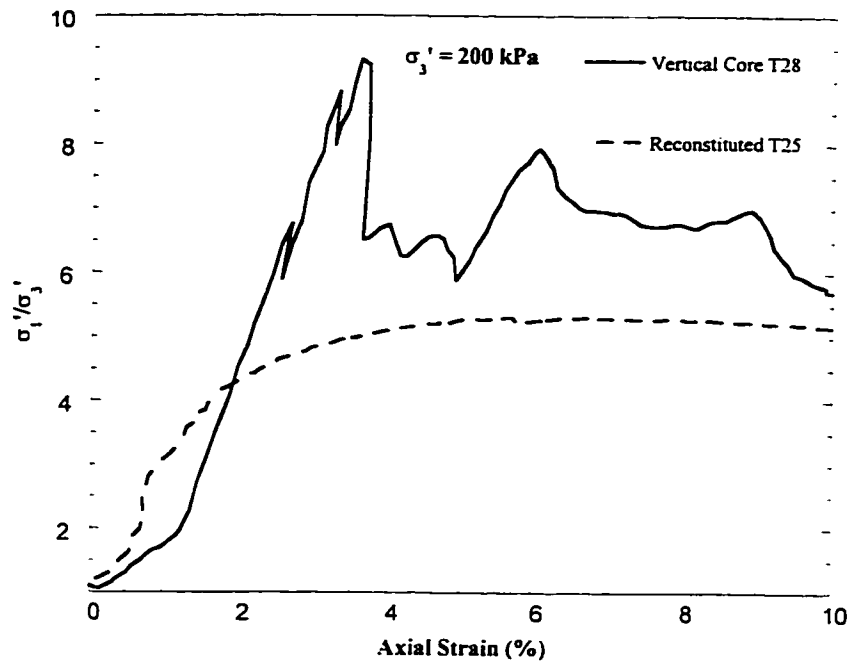
Figure 6.19 Stress ratio versus axial strain
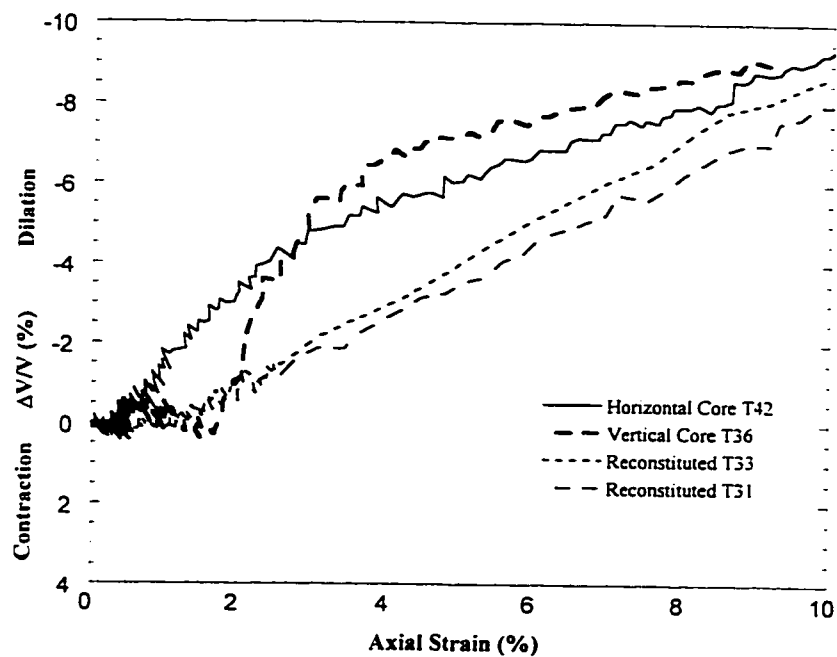**Stress Path 1 (σ'_3= 200 kPa)**
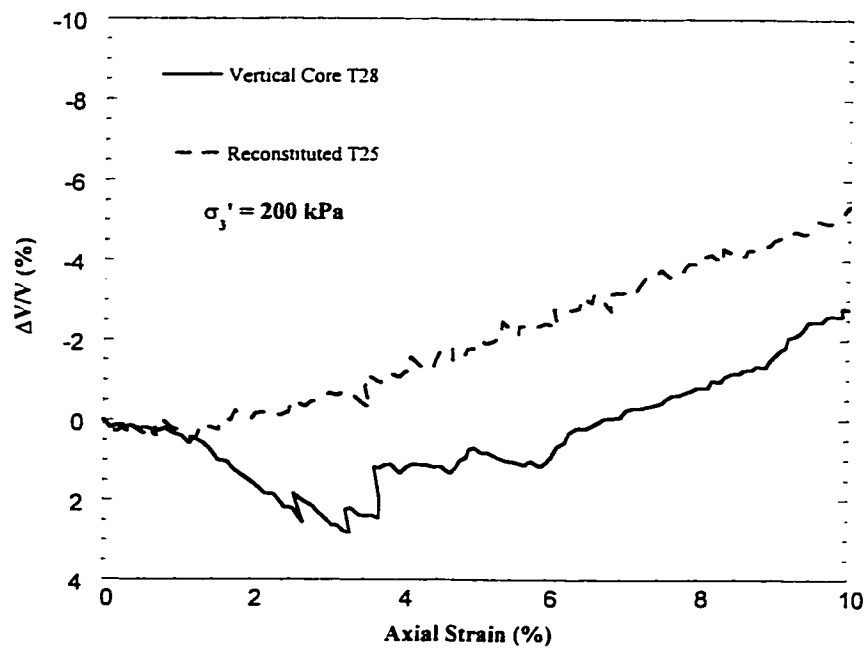
Figure 6.20 Volumetric strain versus axial strain
Stress Path 1 (σ'_3= 200 kPa)
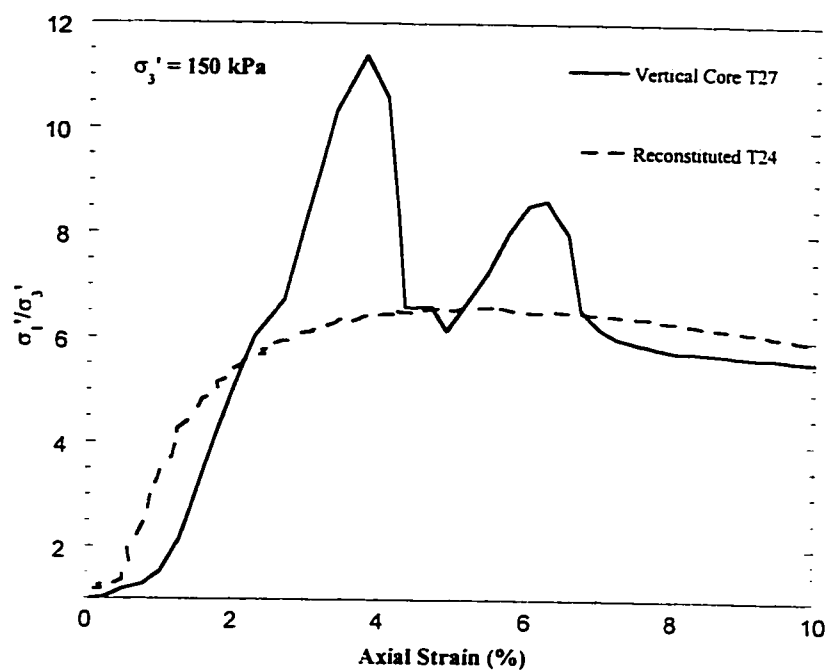
Figure 6.21 Stress ratio versus axial strain
Stress Path 1 (σ'_3=150 kPa)
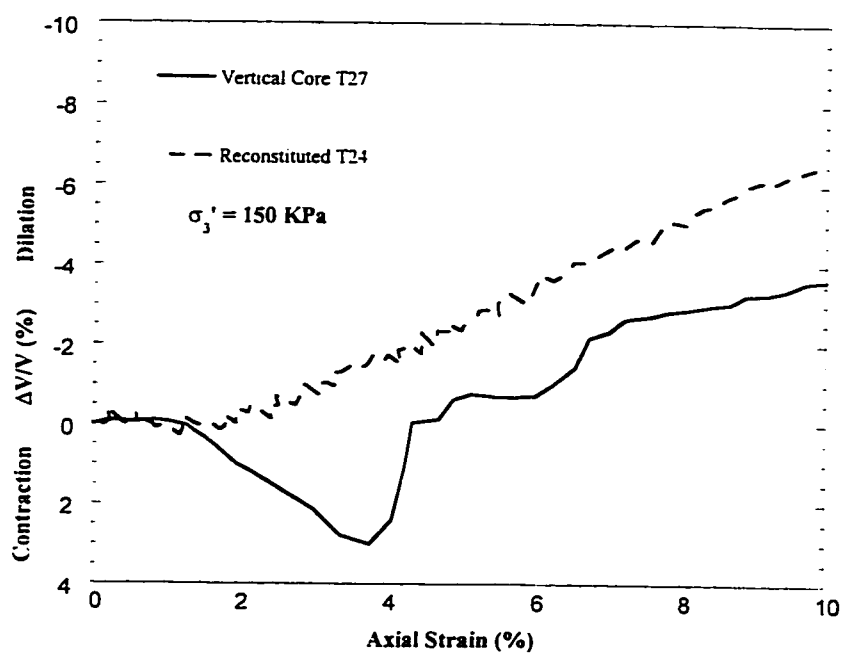
Figure 6.22 Volumetric strain versus axial strain
Stress Path 1 (σ'_3= 150 kPa)
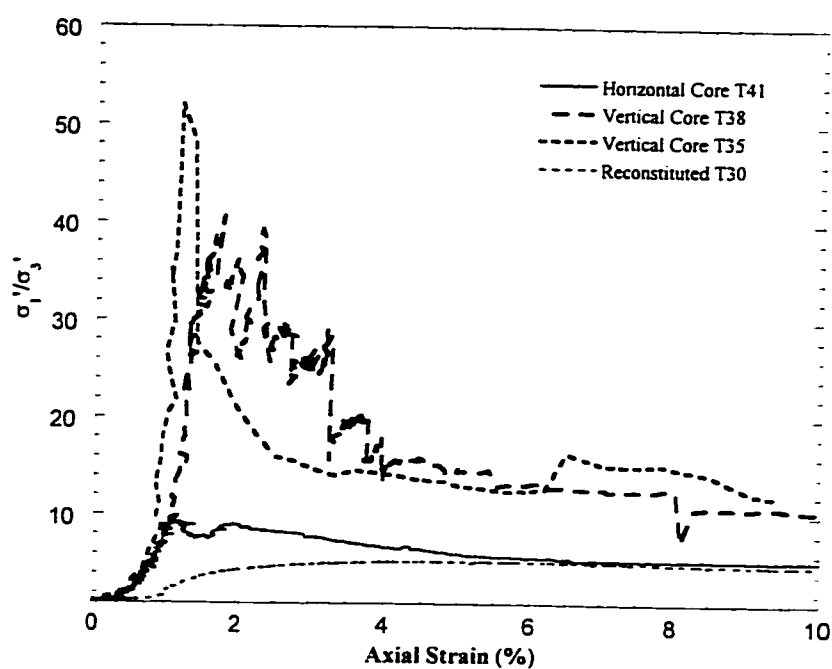
Figure 6.23 Stress ratio versus axial strain
Stress Path 2 (Initial σ'_3= 250 kPa)
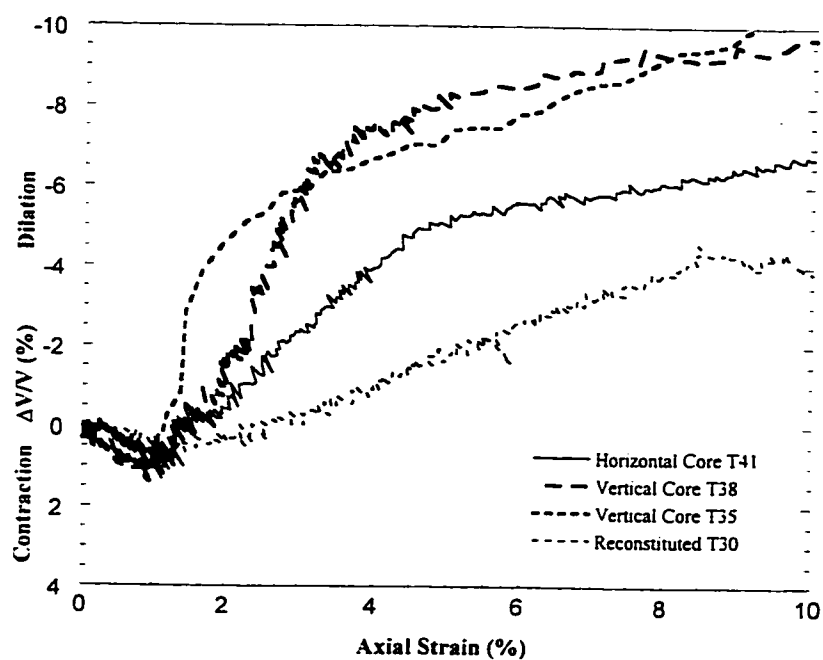
Figure 6.24 Volumetric strain versus axial strain
Stress Path 2 (Initial σ'_3= 250 kPa)

Figure 6.25 Stress ratio versus axial strain
Stress Path 3 (Initial $\sigma'_3 = 250$ kPa)

Figure 6.26 Volumetric strain versus axial strain
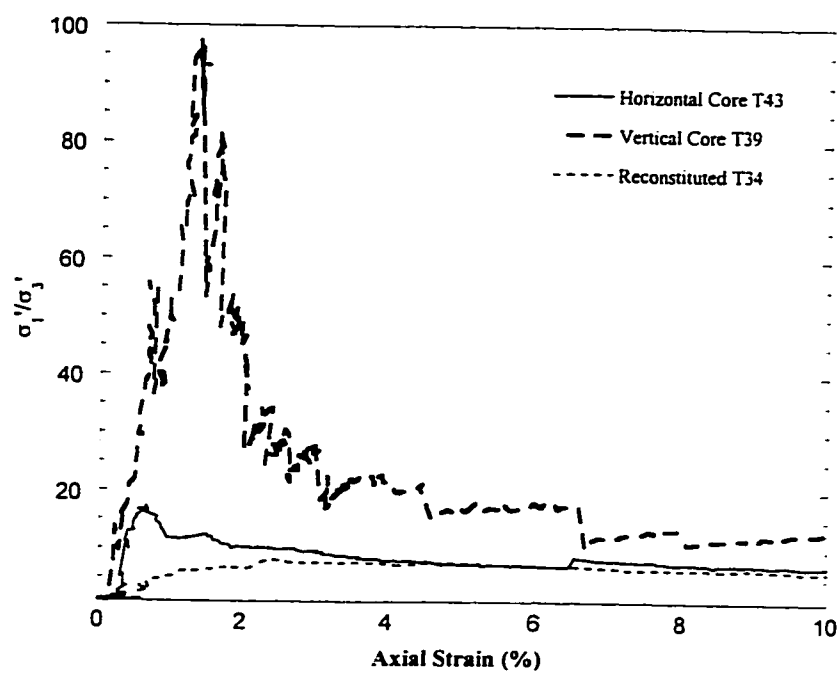**Stress Path 3 (Initial $\sigma'_3 = 250$ kPa)**

Figure 6.27 Stress ratio versus axial strain
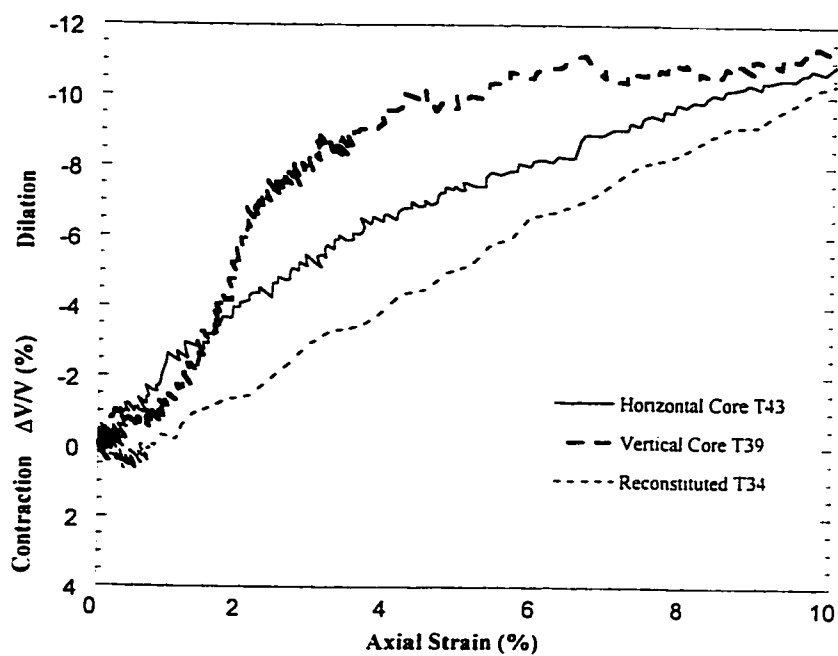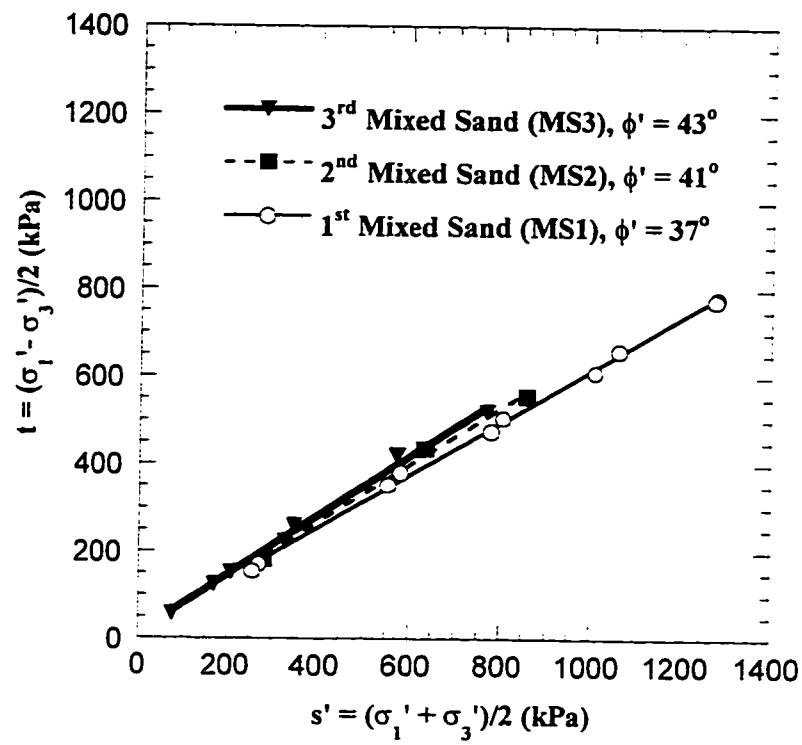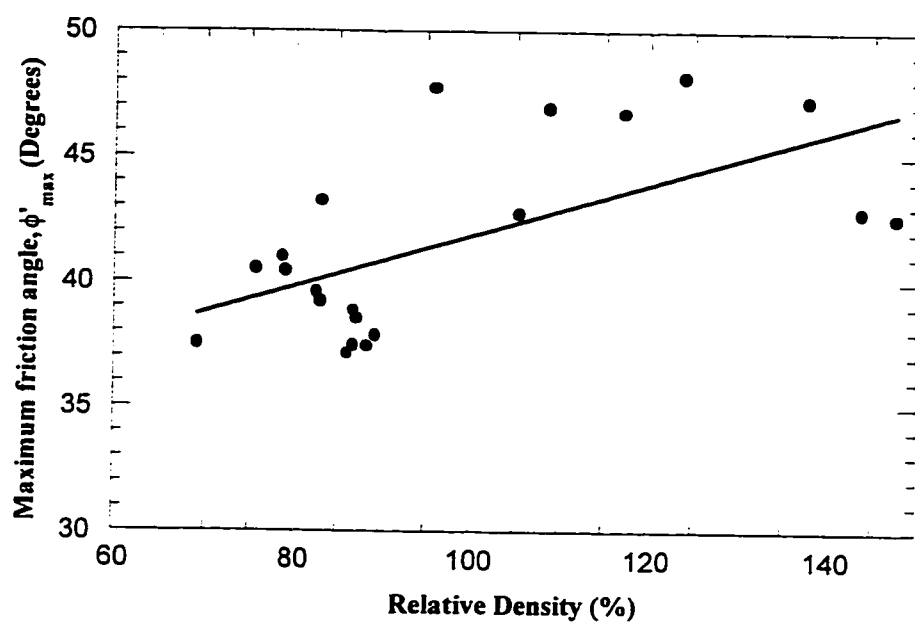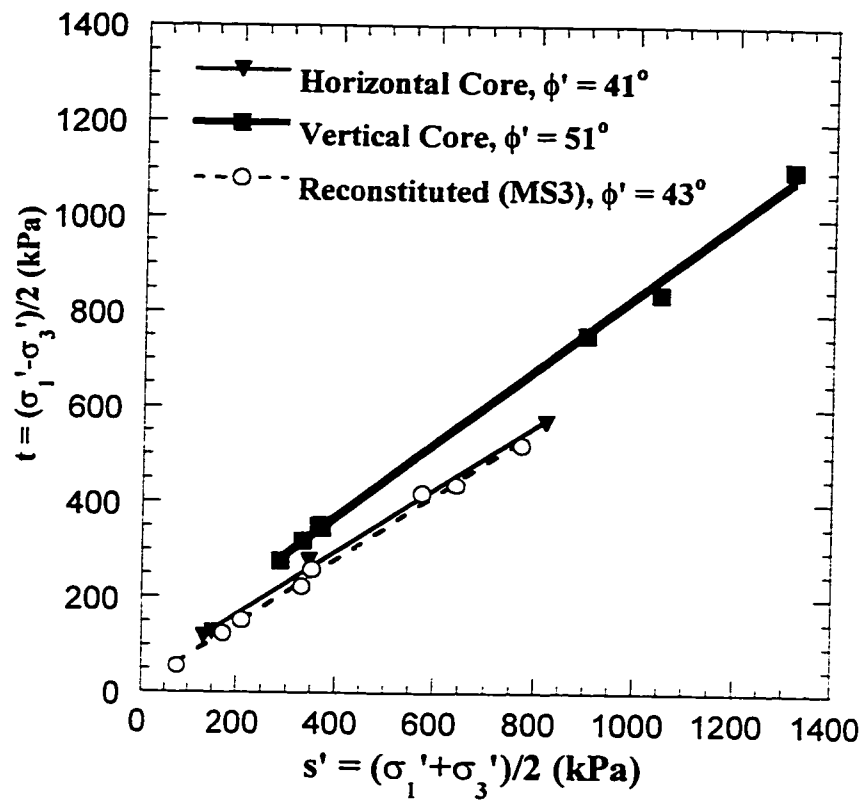Stress Path 4 (Initial σ'_3= 250 kPa)

Figure 6.28 Volumetric strain versus axial strain
Stress Path 4 (Initial σ'_3= 250 kPa)

**Figure 6.29 Failure envelope in s' - t space
Reconstituted specimens**

**Figure 6.30 Variation of maximum friction angle with relative density
Reconstituted specimens**

**Figure 6.31 Failure envelope in s' - t space
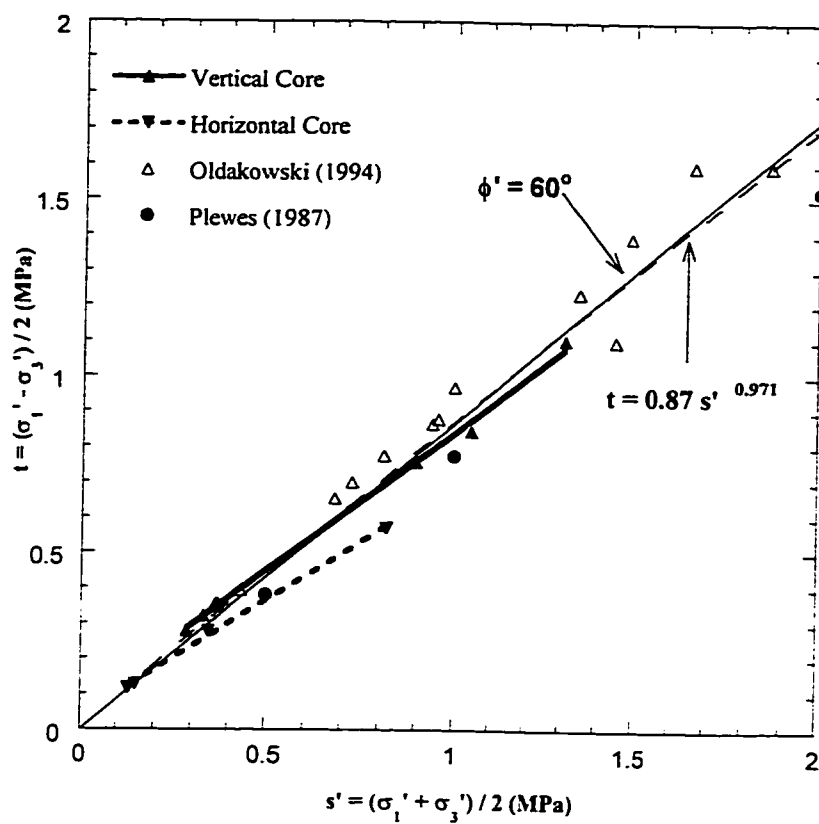Specimens with lubricated end configuration**

Figure 6.32 Peak failure envelope for values of $s' = (\sigma'_1 + \sigma'_3)/2 < 2$ MPa
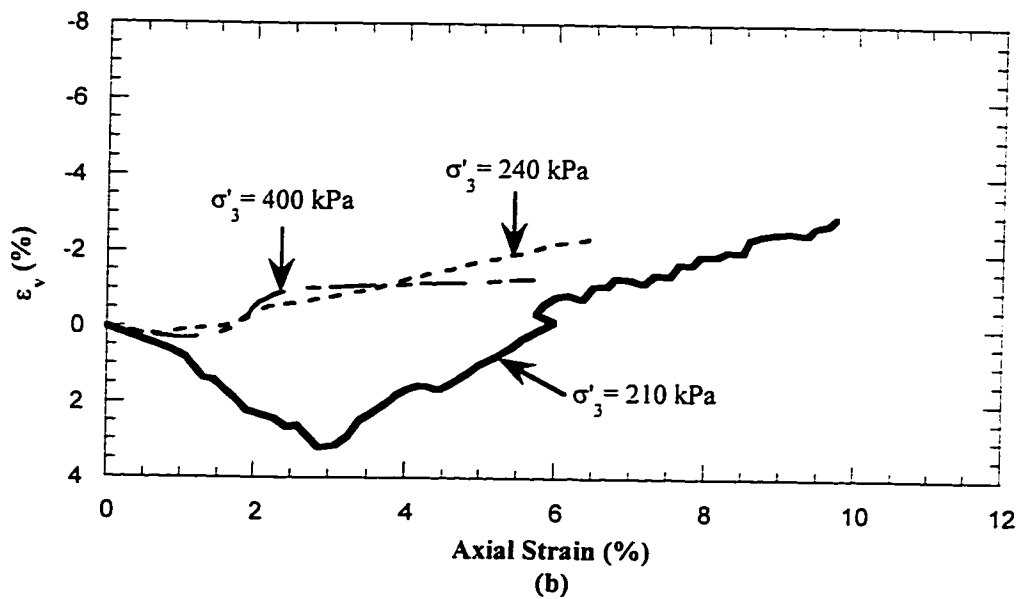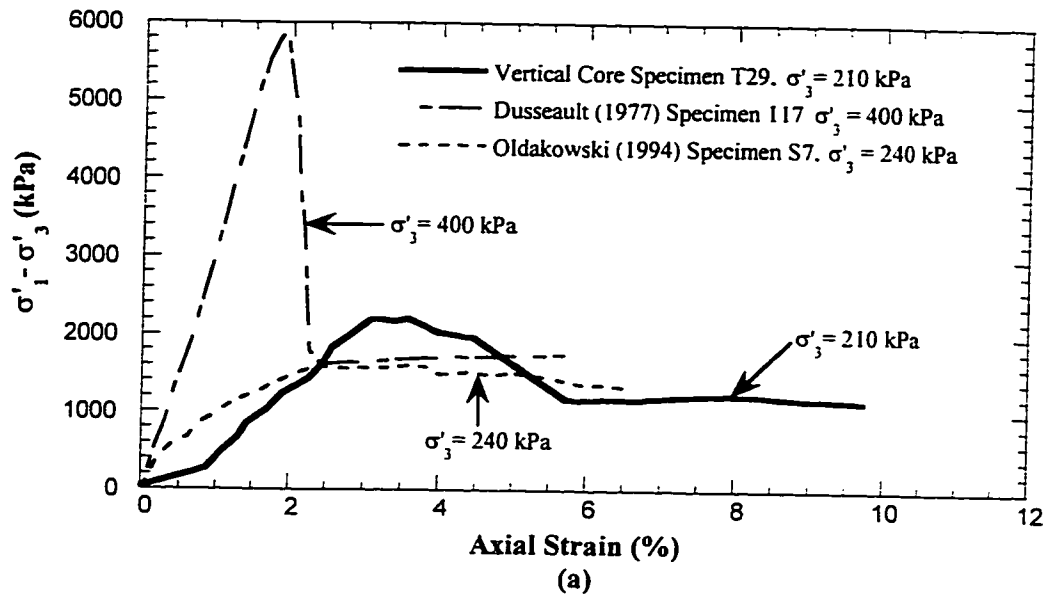(McMurray Formation oil sands)

Figure 6.33 Comparison of stress-strain results with previous experimental studies
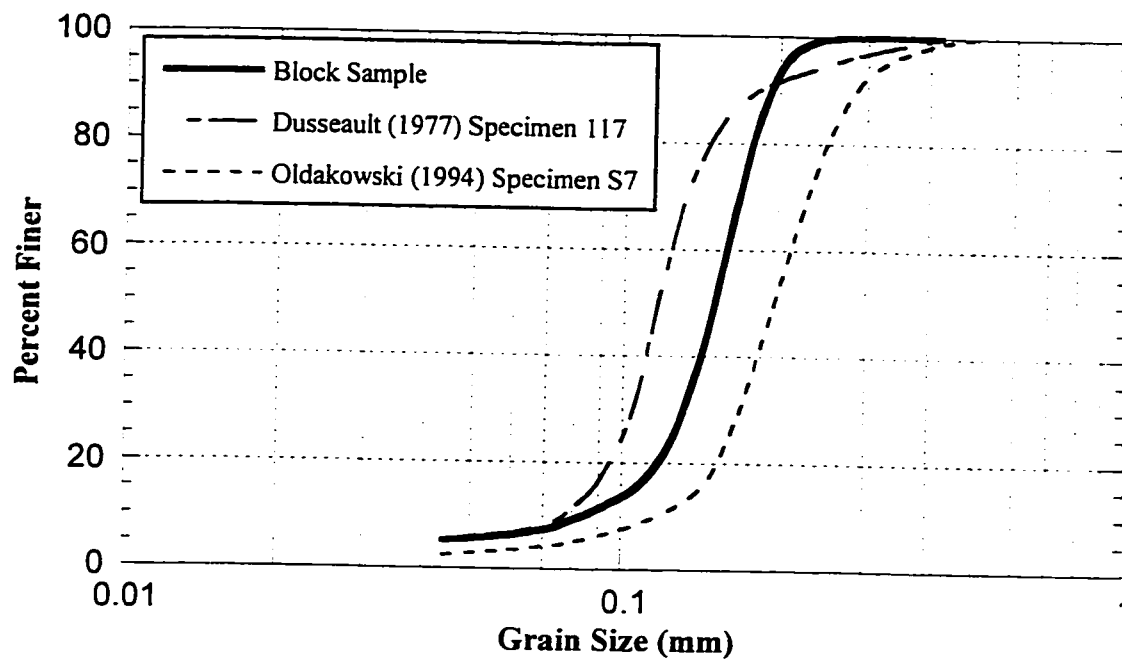
Figure 6.34 Grain size distribution of compared specimens

CHAPTER 7   NUMERICAL SIMULATION OF OIL SAND GEOMECHANICAL BEHAVIOR AT LOW CONFINING PRESSURES

7.1 Introduction

Triaxial drained compression tests on dense sand under low confining pressures typically show a response of the form illustrated in Figure 7.1. The specimen exhibits a marked peak in its deviatoric stress-axial strain curve, and, thereafter, deviatoric stress decreases and is continuing to decrease at the end of the test. Volumetrically, the specimen contracts slightly initially, but then expands or dilates strongly until the end of the test. Strain softening from a peak deviatoric stress is a familiar feature of the observed stress-strain behavior of dense sand, and it is important that this be incorporated into constitutive models.

This chapter describes a method whereby the type of response shown in Figure 7.1 can be reproduced. A numerical simulator, FLAC was chosen for the numerical simulation of oil sand geomechanical behavior at low confining pressures.

Several material input functions are necessary in order to simulate the strain softening and shear dilatancy with FLAC. Results from high quality triaxial experiments were used to provide these functions for the simulations. Using FLAC's built-in programming language, nonlinear compressibility of oil sands at low effective confining stresses was simulated. FLAC was used to simulate several triaxial tests on undisturbed McMurray Formation oil sand specimens. In these simulations the typical stress paths for the Steam Assisted Gravity Drainage Recovery Method (SAGD) were followed. The analyses depict the laboratory-measured relationships between deviatoric stress and axial strain, volumetric strain and axial strain. The simulation results were used to recommend proper functions for changes of stiffness, strength and shear-induced dilational properties. These functions can be used with FLAC for modeling the geomechanical response of oil sands subjected to other recovery processes.

7.2 FLAC

FLAC (Fast Lagrangian Analysis of Continua), is a two-dimensional explicit finite difference code which simulates the behavior of structures built of soil, rock or other materials which may undergo plastic flow when their yield limit is reached. Materials are represented by elements which form a grid that is adjusted by the user to fit the shape of the object to be modeled. Each element behaves according to a prescribed linear or nonlinear stress/strain law in response to the applied forces or boundary restraints. If stresses are high enough to cause the material to yield and flow, the grid can actually

deform (in large-strain mode) and move with the material which is represented. FLAC is based upon a "Lagrangian" calculation scheme which is well suited for modeling large distortions. The explicit, Lagrangian calculation scheme and the mixed discretization zoning technique used in FLAC ensures that plastic collapse and flow are modeled very accurately. Several built-in constitutive models are available that permit the simulation of highly nonlinear, irreversible response representative of geologic, or similar materials. Among them is Mohr-Coulomb plasticity and strain softening/hardening plasticity models. FLAC also contains a built-in programming language, FISH (short for FLACish). Details of FLAC, its capabilities and application examples can be found in Cundall and Board (1988) and Itasca (1991). FLAC version 3.0 was used in this thesis.

7.3 Constitutive model

For the present numerical study, a strain softening/hardening model was chosen. This model is a variant of the Mohr-Coulomb plasticity model. For both Mohr-Coulomb and strain-softening models, a shear yield function and a nonassociated shear flow rule are used. Selection of material properties required for geomechanical analysis depends on the chosen constitutive model. The following properties are required with the Mohr-Coulomb plasticity model:

(1) Modulus of elasticity, E
(2) Poisson's ratio, ν
(3) Cohesion, c'
(4) Maximum friction angle, ϕ'_{max}
(5) Dilation angle, ψ

A shear yield function is used in FLAC to detect the shear yield. Mohr-Coulomb criterion is used for this purpose and the shear yield function is defined as:

$$f_s = \sigma'_1 - \sigma'_3 N_\phi + 2c\sqrt{N_\phi}$$

[7.1]

Where:

$$N_\phi = (1 + Sin\phi')/(1 - Sin\phi')$$

[7.2]

σ'_1 = Major principal effective stress
σ'_3 = Minor principal effective stress
ϕ' = Effective friction angle
c' = Effective cohesion

If maximum friction angle obtained in a triaxial test is used in this criterion the resulting shear yield will correspond to the specimen's failure as defined in Chapter 6. However in order to be consistent with FLAC, the term shear yield is used in this chapter.

The shear potential function g_s corresponds to a nonassociated flow rule and has the form:

$$g_s = \sigma_1' - \sigma_3' N_\psi \qquad [7.3]$$

where:

$$N_\psi = (1 + Sin\psi)/(1 - Sin\psi) \qquad [7.4]$$

and ψ is the dilation angle.

The Mohr-Coulomb plasticity model only represents a material which yields in shear. This is the most conventional plasticity model chosen for analyzing soil and rock mechanics problems.

Using the FISH capabilities of FLAC, calculation of the following parameters were added to the program:

(1) Major and minor principal effective stresses
(2) Deviatoric stress
(3) Axial strain
(4) Volumetric strain

The Mohr-Coulomb model is an elastic-perfectly plastic model. The idealized relation and simulated behavior, based upon the Mohr-Coulomb failure surface, is shown for a triaxial test in Figure 7.2. The material simulated in these plots had the following typical properties of a dense sand under a confining pressure of $\sigma_3' = 1$ MPa:

$\phi'_{max} = 30°$
$E = 346$ MPa
$v = 0.3$
$c' = 0$
$\psi = 10°$

In FLAC the post peak volumetric response of a material is computed based on the concept of shear dilatancy. Shear dilatancy, or dilatancy, is the change in volume that occurs with shear distortion of a material. Dilatancy is characterized by a dilation angle, ψ, which represents the ratio of plastic volume change to plastic shear strain. Figure 7.2(b) shows both the idealized and simulated volumetric changes of the material based on Mohr-Coulomb model. Note that the initial slope for the plot in Figure 7.2(b) corresponds to the elastic regime while the slope used to measure the dilation angle corresponds to the plastic regime.

In the Mohr-Coulomb plasticity model, cohesion, friction and dilation are assumed to remain constant. Chlatumyk (1996) in his parametric analysis of SAGD process used FLAC with Mohr-Coulomb plasticity model. He noted that "the selection of an elastic-perfectly plastic model for an ideal analysis results in an underestimation of the shear induced volume changes occurring during SAGD processes". He concluded that "the primary reason for the model's inability to represent adequately the dilatant volume changes is related to the method used in computing volumetric strains. Plastic volume change is only computed when an element is at a state of yield. Below yield, the model only calculates elastic volume change". The SAGD stress paths obtained by Chalaturnyk (1996) show that the material reaches the peak failure envelope only briefly. The material then undergoes an increase in the mean normal effective stress causing a return to an elastic state with no further calculation of plastic volume changes. In reality, oil sand is a strain softening material and would continue to deform and soften once the peak failure envelope has reached.

In FLAC, shear hardening and softening is simulated by making Mohr-Coulomb properties (cohesion, friction and dilation angle), functions of plastic shear strain.

7.4 Strain-softening/hardening model

This constitutive model allows the user to represent arbitrary nonlinear material hardening and softening behavior based on the variation of the cohesion, friction, and dilatancy with plastic strain. The model is based on Mohr-Coulomb elasto-plasticity with a nonassociated flow rule. The difference, however, lies in the ability of the cohesion, friction and dilation to harden or soften after the onset of shear yield. In the Mohr-Coulomb plasticity model, the cohesion, friction and dilation are assumed to remain constant. Here, the user can define the cohesion, friction and dilation as functions of plastic shear strain. The code determines the total plastic strain at each time increment and causes the cohesion, friction and dilation to conform to the user-defined functions.

7.4.1 User defined functions for cohesion, friction and dilation

The user defines the cohesion, friction and dilation to be functions of the total plastic strain. Once shear yield begins, the code keeps track of the total plastic strain and determines the current values of cohesion, friction and dilation which correspond to this strain. In the next timestep, these values are used in the calculation of stress and strain. The cohesion, friction and dilation are defined as piecewise linear segments of a generally nonlinear function of the total plastic strain.

For example, assume a one-dimensional stress-strain curve which softens upon yield and attains some residual strength (Figure 7.3). The stress-strain curve is linear to the point of yield; in that range therefore, the strain will be elastic only: $\varepsilon = \varepsilon^e$. After yield, the total strain is composed of elastic and plastic parts: $\varepsilon = \varepsilon^e + \varepsilon^p$. In the softening/hardening model, the user defines the cohesion, friction and dilation variance as

a function of the plastic portion ε^p of the total strain. These functions which are illustrated in Figure 7.4, are approximated within FLAC as a set of linear segments, as shown in Figure 7.5. Hardening and softening parameters must be calibrated for each specific analysis and the values are generally back calculated from results of laboratory triaxial tests (Itasca 1991).

It is acknowledged that if the strain-softening model is used with a weakening material, the load/displacement relation generated by FLAC for a simulated test is strongly grid-dependent. The process of softening may be modeled, but it must be recognized that the grid size affects the results. Models must be calibrated for each grid used (Itasca 1991). Issues associated with the grid size are discussed in Section 7.6.1.

7.5 Material properties

The following sections describe the derivation of material properties for use in the numerical simulations. For simulations in this study, cohesion has been set zero and Poisson's ratio is 0.3.

7.5.1 Modulus of elasticity

A tangent modulus of elasticity for a given sand depends upon the level of confining stress. A standard "hyperbolic" function is typically chosen for defining this relationship:

$$E_i = K_E \, p_a \left(\frac{\sigma_3'}{p_a} \right)^n \qquad [7.5]$$

where:

E_i = modulus of elasticity at low strain level
K_E = modulus number
p_a = atmospheric pressure; and
n = modulus exponent

The modulus of elasticity E_i used in this thesis is the initial modulus of elasticity for the primary load.

Based on the results of triaxial shear tests (Chapter 6) the variation of tangent modulus of elasticity for effective confining stresses below 250 kPa was obtained for undisturbed oil sand specimens and reconstituted specimens (Figure 7.6). Using curve-fitting techniques the obtained hyperbolic expression for vertical and horizontal core specimens and the linear fit for reconstituted specimens are provided below:

Vertical cores: $E_i = 460 \, p_a \left(\dfrac{\sigma'_3}{p_a}\right)^{0.25}$ (MPa)   [7.6]

Horizontal cores: $E_i = 314 \, p_a \left(\dfrac{\sigma'_3}{p_a}\right)^{0.6}$ (MPa)   [7.7]

Reconstituted specimens (MS3): $E = 160 \, \sigma'_3$ (MPa)   [7.8]

7.5.1.1 Comparison with previous experimental studies

Byrne et al. (1987) provided guidelines for the selection of K_E and n in Equation 7.5 for sand. They mentioned that due to difficulty in obtaining undisturbed samples of granular materials, parameters were also assessed from back analysis of field measurements of foundation movements. Based on these field measurements and both static and dynamic laboratory test results, Byrne et al. (1987) developed a database of parameters for the above equation. For sands with relative densities of 100% they suggested that K_E ranges from 1500 to 3000 and $n = 0.5$. Selecting $K_E = 2000$, the resulting hyperbolic relationship is:

$$E_i = 2000 \, p_a \left(\dfrac{\sigma'_3}{p_a}\right)^{0.5} \text{ (MPa)}$$ [7.9]

Plot of this equation is produced in Figure 7.7.

Chalaturnyk (1996) reported substantial variation in modulus of elasticity values. Based on a data set of elasticity moduli for compression tests conducted on high quality oil sands, Chalaturnyk (1996) suggested the following power function which is also shown in Figure 7.7:

$$E = 343 \, \sigma'^{0.875}_3 \text{ (MPa)}$$ [7.10]

Samieh and Wong (1997) used drained compression tests to study the stress-strain response of Athabasca oil sand at low effective stresses. The oil sand specimens for their study were obtained from an exploration well approximately 10 km north of Fort McMurray, Alberta. Their experimental program included test on short specimens with lubricated ends configuration. These specimens were tested at effective confining stresses of 50 kPa to 750 kPa. Their use of lubricated ends and short specimens is similar to this study.

Samieh and Wong (1997) used Equation 7.5 to curve-fit the test data. For short specimens tested with lubricated ends, they suggested the values of $K_E = 950$ and $n = 0.5$. The resulting relationship is:

$$E_i = 950\, p_a \left(\frac{\sigma_3'}{p_a} \right)^{0.5} \text{(MPa)} \qquad [7.11]$$

This equation is plotted in Figure 7.7.

It is seen in Figure 7.7 that Equations 7.9, 7.10 and 7.11 do not display a fair match with test results. Equations 7.9 and 7.11 overestimate the modulus of elasticity for the specimens in this study.

It is important to realize that E_i calculated from the hyperbolic equation is a low strain level modulus of elasticity. The moduli of elasticity computed from a curve-fit through experimental data are lower due to the fact that they were calculated from stress-strain curves at a substantially higher axial strain.

Figures 7.6 and 7.7 show the variation of modulus of elasticity with effective confining pressures of up to 250 kPa. The equations suggested by Byrne et al. (1987) and Chalaturnyk (1996) are based on experimental results over a much wider range of confining pressures and extrapolating them to a very low range of confining pressures may not be justified. Figure 7.8 presents the elasticity moduli obtained by other researchers from compression tests conducted on high quality oil sands. These values were obtained under much higher effective confining pressures (up to 10 MPa). Equation 7.9 and Equation 7.10 are also plotted in Figure 7.8.

The Byrne et al. (1987) and Chalaturnyk (1996) relations show a good match for the whole range of confining pressures up to 10 MPa. Equations 7.6, 7.7 and 7.8 underestimate the modulus of elasticity in higher values of confining pressures. Therefore, use of these equations in circumstances where effective confining pressure is higher than 250 kPa is not recommended.

The plot based on the equation suggested by Samieh and Wong (1997) matches the results of vertical cores up to 20 kPa and overestimates them after that. This is probably due to the differences in the method of measuring the modulus of elasticity in a triaxial compression test. Also most of their data points were measured for confining pressures over 300 kPa.

Since the equation suggested by Chalaturnyk (1996), Equation 7.10, plots within the obtained data of the core specimens for confining pressures below 250 kPa (Figure 7.7), its use as an overall equation for the changes of modulus of elasticity of oil sand with confining pressure is reasonable. However since in the simulations the effective

confining pressure was equal or below 250 kPa, Equations 7.6, 7.7 and 7.8 were used in this study.

The nonlinear variation of modulus of elasticity with confining pressure, as described by Equations 7.6, 7.7 and 7.8, was employed in the numerical simulations of oil sands using FLAC's built-in programming language FISH.

7.5.2 Friction angle

The friction angle is not considered to be constant but decreases with increasing stress level. The correlation generally adopted in geotechnical work is that friction angle is a function of dimensionless confining stress:

$$\phi' = \phi'_0 - \Delta\phi'_0 \, Log\left(\frac{\sigma'_3}{p_a}\right) \qquad [7.12]$$

in which ϕ'_0 is the value of the friction angle at a confining stress of 1 atmosphere and $\Delta\phi'_0$ is the reduction in friction angle for a ten-fold increase in confining stress.

From the results of triaxial shear tests on undisturbed oil sand specimens and reconstituted specimens (Chapter 6) the value of maximum friction angle in each test ϕ'_{max} and the corresponding effective confining pressure were obtained. The variations of maximum friction angle with effective confining pressure for these materials are shown in Figure 7.9. Using curve-fitting techniques expressions similar to Equation 7.12 were produced for vertical and horizontal core specimens and reconstituted specimens. These equations are provided below:

Vertical cores: $\phi'_{max} = 60 - 15.6 \, Log\left(\frac{\sigma'_3}{p_a}\right)$ (Degrees) $\qquad [7.13]$

Horizontal cores: $\phi'_{max} = 50 - 14.25 \, Log\left(\frac{\sigma'_3}{p_a}\right)$ (Degrees) $\qquad [7.14]$

Reconstituted specimens (MS3): $\phi'_{max} = 45.4 - 4.5 \, Log\left(\frac{\sigma'_3}{p_a}\right)$ (Degrees) $\qquad [7.15]$

Similar correlation was suggested by Samieh and Wong (1997) which is also shown in Figure 7.9. Their friction angle values is lower than the friction angle of vertical cores but they start to converge as the confining pressure increases. The majority of the data points of Samieh and Wong (1997) were measured in confining pressures over 300 kPa.

The maximum friction angle, one of the inputs required by FLAC, separates the elastic region from the plastic region. After the peak friction angle has been reached the program will change the friction angle value according to the introduced variation of friction angle with plastic shear strain.

The triaxial shear strain is defined as (Muir Wood 1990):

$$\varepsilon_s = \frac{2}{3}\left(\varepsilon_1 - \varepsilon_3\right)$$ [7.16]

Figures 7.10, 7.11 and 7.12 show the incremental change in friction angle as a function of ε_s.

For each material only a single curve has been used to model the change in friction angle. It would be more appropriate to use a series of these functions, each for a specific effective confining stress. Conventional drained compression tests in which the effective confining pressure is kept constant throughout the test is most suitable for this purpose. To develop these functions would require a series of conventional drained compression tests to be conducted covering the effective confining stress range of interest. For this study however insufficient tests were conducted in order to develop separate functions for different confining pressures. Thus a single function for the variation of friction angle with plastic strain was used in the numerical modeling.

7.5.3 Dilation angle

Dilatancy may be described as the change in volume associated with shear distortion in the material. A parameter used for characterizing a dilatant material is the dilatancy angle ψ, defined as:

$$Sin\,\psi = -\frac{d\varepsilon_v}{d\gamma}$$ [7.17]

This angle sets the ratio of two plastic strain rates, namely the rate of plastic volumetric strain $d\varepsilon_v$ and the rate of plastic distortion $d\gamma$. Strictly speaking, this definition is only exact in the plane strain case of simple shear (Vermeer and de Borst 1984).

Angle of dilatancy has been used by many researchers (Bolton 1986) for plane strain but its definition was not extended to cover triaxial strain. A definition was presented by Schanz and Vermeer (1996) and is explained subsequently.

The mechanical significance of the dilation angle in a plane strain deformation can best be appreciated by considering the case of direct shear shown in Figure 7.13 (Bolton 1986). If rigid blocks of nonfailing soil are assumed to bound the thin uniformly

straining rupture zone ZZ, this must mean that for compatibility ZZ must be zero extension line so that: $d\varepsilon_z = 0$ within the rupture zone.

Also:

$$d\gamma_{yz} = \frac{dz}{y} \qquad\qquad [7.18]$$

$$d\varepsilon_y = -\frac{dy}{y} \qquad\qquad [7.19]$$

So in Figure 7.13(b):

$$\tan\psi = -\frac{d\varepsilon_y}{d\gamma_{yz}} = \frac{dy}{dz} \qquad\qquad [7.20]$$

The angle of dilation is then seen in Figure 7.13(b) to be equal to the instantaneous angle of motion of the sliding blocks relative to the rupture surface. It should be recognized that the angle of dilatancy becomes a meaningless parameter in an axisymmetric triaxial compression test, since the geometrical relationship of Figure 7.13 applies only to plane strain (Bolton 1986).

Several theories have been developed for predicting the volumetric strain in triaxial testing as a function of the axial strain. In particular, the applicability of Rowe's (1962, 1971) stress dilatancy theory has been widely recognized. Vermeer and de Borst (1984), using theory of plasticity, introduced an equation for the evaluation of the dilatancy angle ψ from triaxial test data. Also, Schanz and Vermeer (1996) used the concept of superposition to relate the angle of dilatancy to triaxial strain conditions. Only the latter method will be discussed in this thesis.

The stress dilatancy theory starts with an expression for plane states of strain:

$$D = R/K \qquad\qquad [7.21]$$

where $D = -d\varepsilon_3/d\varepsilon_1$, R is the stress ratio σ'_1/σ'_3 and K is a coefficient representing the internal friction. The parameter D can also be written as $D = 1 - d\varepsilon_v/d\varepsilon_1$ (Rowe 1962) and therefore is an indication of the dilation rate $d\varepsilon_v/d\varepsilon_1$.

On changing from a plane state of strain to triaxial testing conditions, the following two mechanisms must be considered (Figure 7.14):

- Mechanism A; sliding on a σ'_1-σ'_2 plane governed by the stress ratio σ'_1/σ'_2.
- Mechanism B; sliding on a σ'_1-σ'_3 plane governed by the stress ratio σ'_1/σ'_3.

Each sliding mechanism constitutes a planar deformation, and thus Equation 7.21 can be applied to each separate mechanism. This yields:

$$-\frac{d\varepsilon_2}{d\varepsilon_{1A}} = D_A = \frac{R_A}{K} \tag{7.22}$$

$$-\frac{d\varepsilon_3}{d\varepsilon_{1B}} = D_B = \frac{R_B}{K} \tag{7.23}$$

Where $R_A = R_B = R$ and $d\varepsilon_2 = d\varepsilon_3$ for triaxial testing conditions. There are two contributions to the axial strain, i.e.:

$$d\varepsilon_1 = d\varepsilon_{1A} + d\varepsilon_{1B} = -\frac{d\varepsilon_2}{D_A} - \frac{d\varepsilon_3}{D_B} \tag{7.24}$$

The angle of dilatancy is first examined in plane strain situations and its definition is then extended to include triaxial compression. For plane strain conditions, the definition is given in several textbooks by:

$$Sin\psi = -\frac{d\varepsilon_1 + d\varepsilon_3}{d\varepsilon_1 - d\varepsilon_3} \tag{7.25}$$

From the definition of D and the above equation, the following relationship can be obtained:

$$D_A = D_B = \frac{1 + Sin\psi}{1 - Sin\psi} \tag{7.26}$$

Combining Equations 7.24 and 7.26, yields the following expression for ψ:

$$Sin\psi = -\frac{d\varepsilon_v/d\varepsilon_1}{2 - d\varepsilon_v/d\varepsilon_1} = \frac{1}{1 - \frac{2}{(d\varepsilon_v/d\varepsilon_1)}} \tag{7.27}$$

Hence, a definition has been derived for the dilatancy angle that can be used to measure this angle in triaxial compression testing (Schanz and Vermeer 1996).

This equation can also be written as:

$$Sin\psi = \frac{d\varepsilon_v}{-2\,d\varepsilon_1 + d\varepsilon_v} \qquad [7.28]$$

For triaxial strain conditions;

$$d\varepsilon_v = d\varepsilon_1 + d\varepsilon_2 + d\varepsilon_3 = d\varepsilon_1 + 2\,d\varepsilon_3 \qquad [7.29]$$

and for plane strain conditions;

$$d\varepsilon_v = d\varepsilon_1 + d\varepsilon_3 \qquad [7.30]$$

Equation 28 holds for triaxial testing conditions as well as for plane strain conditions (Vermeer and de Borst 1984).

In order to determine the dilatancy angle from triaxial test results, a plot of volumetric strain versus axial strain is required. For any portion of an axial strain-volumetric strain curve that a slope for $d\varepsilon_v/d\varepsilon_1$ can be obtained, a corresponding ψ can be calculated by substituting this slope into Equation 7.27.

Figure 7.15 shows a typical plot of axial strain ε_1 with volumetric strain ε_v for a horizontal core specimen of oil sand. It is noted (Vermeer and de Borst 1984) that a material will not dilate infinitely and after intense shearing the dilatancy angle gradually vanishes. In most of the tests the relationship between ε_v and ε_1 could be reasonably approximated by a bilinear curve representing the regions of peak and residual dilation rates (Figure 7.15). A linear curve fit was used in this study for each region. Dilation angles were determined by substituting the slope of the line in the peak dilation rate region of each test in Equation 7.27. Figure 7.16 presents the obtained dilation angles. The variation of dilation angle with effective confining stress is clearly illustrated in Figure 7.16.

Although FLAC allows for the introduction of a change in dilation angle with plastic shear strain, the experimental results did not warrant the use of this feature. The approximation of the ε_1 versus ε_v plot with a straight line at the beginning of dilation (peak dilation rate region) was reasonable. This approximation is justifiable since the numerical simulations were conducted only to 5% axial strain.

Samieh and Wong (1997) also reported the variation of peak dilation rate of oil sand with confining pressure. The corresponding dilation angles were calculated by substituting the values of peak dilation rate obtained by Samieh and Wong (1997) in Equation 7.27. The resulting dilation angles are shown in Figure 7.16. In general, Samieh and Wong's (1997) angles are higher than the dilation angles obtained in this study. The reason for this difference is that the slope of the line in the peak dilation region

(Figure 7.15) represents an average of the dilation rate from the onset of dilation till the start of the residual region.

Expressions similar to Equation 7.12 can also be used to describe the variation of dilation angle with confining pressures. Using curve-fitting techniques expressions were obtained for vertical and horizontal core specimens and reconstituted specimens:

Vertical cores: $\psi = 26.6 - 17.5\,Log\left(\dfrac{\sigma_3'}{P_a}\right)$ (Degrees) [7.31]

Horizontal cores: $\psi = 25 - 6.6\,Log\left(\dfrac{\sigma_3'}{P_a}\right)$ (Degrees) [7.32]

Reconstituted specimens (MS3): $\psi = 17.2 - 5.2\,Log\left(\dfrac{\sigma_3'}{P_a}\right)$ (Degrees) [7.33]

7.6 Numerical analysis

Figure 7.17 shows the assumed boundary conditions for the numerical analyses. In the loading process, increments of vertical displacement (vertical velocity) were applied along the contact surfaces (rigid frictionless platens). As mentioned earlier numerical boundary conditions can influence the model response due to shear hardening/softening behavior. The rate of loading can also introduce inertial effects. This could be controlled with a servo-control function. With the use of a servo-control function, the applied vertical velocities can be adjusted as a function of the maximum unbalanced force in the model. By preventing the unbalanced forces from getting too high (i.e., controlling the inertial effects), the user has a better control over model behavior (Itasca 1991). However as an alternative method a very low vertical velocity with higher number of steps could be used. This way, there will be a consistency in loading conditions among the different analyses. The latter method was used in this study. Vertical velocities were chosen so that the specimens would undergo 5% axial strain in 250,000 steps.

It is convenient to have a prior knowledge of the effective confining stress at peak strength, where the material changes from elastic to plastic behavior. Some important input parameters like maximum friction angle and dilation angle are functions of this confining stress and in the case of FLAC, these functions must be introduced prior to any simulation. Thus in a reservoir simulation, the value of the effective confining stress at peak strength must be assumed at the beginning. This value is then adjusted after the first simulation.

Considering the simplicity of the boundary conditions for the particular case of an axisymmetric triaxial compression test, a simpler solution can be derived. However the

following method applies only to the instance of simulating a triaxial test and is presented here to clarify the presentation of the numerical results.

Instead of a time consuming iterative simulation of each case, iterations were done in a spreadsheet program using the following formulation.

Assume an initial effective confining stress as the current value for σ'_3, and an increment in the axial strain $\Delta\varepsilon_1$. Deviatoric stress is defined as $q = \sigma'_1 - \sigma'_3$. Increase in pore pressure is Δu. As was discussed in the previous chapter, the amount of increase in the pore pressure value depends on the desired stress path.

Iteration were done in the following order:

$$\varepsilon_1 = \varepsilon_1 + \Delta\varepsilon_1 \qquad [7.34]$$

As mentioned earlier, a nonlinear elastic behavior was assumed for the material prior to reaching a peak friction angle. Using Equations 7.6, 7.7 or 7.8 and the current value of σ'_3:

$$E = f(\sigma'_3) \qquad [7.35]$$

$$q = q + E\,\Delta\varepsilon_1 \qquad [7.36]$$

$$\Delta u = f(q) \qquad [7.37]$$

$$\sigma'_3 = \sigma'_3 - \Delta u \qquad [7.38]$$

$$\sigma'_1 = \sigma'_3 + q \qquad [7.39]$$

$$\phi'_{max} = Sin^{-1}\left(\frac{\sigma'_1 - \sigma'_3}{\sigma'_1 + \sigma'_3}\right) \qquad [7.40]$$

These steps were repeated with the new value of σ'_3 until the value for ϕ'_{max} converged to a constant value. The final σ'_3 was used to define the proper input value for the maximum friction angle (Equations 7.13, 7.14 and 7.15) and dilation angle (Equations 7.31, 7.32 and 7.33).

7.6.1 Grid size

In many physical situations, shear bands are observed. The deformation in the material is nonuniform and concentrated in narrow bands. The same process occurs in numerical

simulations. However, it is influenced to some extent by artificial conditions imposed by the numerical grid, both by the orientation and the element size.

FLAC is able to allow bands to develop and evolve. A strain softening material is more prone to produce bands. In reality, the thickness of a band is determined by internal features of the material, such as grain size. These features are not built into FLAC's constitutive models. Hence, the bands in FLAC collapse down to the smallest width that can be resolved by the grid, which is one grid width if the band is parallel to the grid, or about three grid widths if the band cuts across the grid at an arbitrary angle. Therefore if the strain softening model is used the stress-strain behavior simulated by FLAC is strongly grid dependent. It must be recognized that the grid size and angle affects the results. Models must be calibrated for each grid used.

To examine the grid size effects on the strain softening model chosen for the numerical simulations, three grid sizes were evaluated. Figure 7.18 shows the three grid size tested. Horizontal core material properties and a constant mean effective stress path (stress path 2) were chosen for this evaluation. Figures 7.19 and 7.20 illustrate the variation in stress-strain behavior for these grid sizes. The grid with 50 elements undergoes more softening than the other two while their volumetric strain changes are same. Based on these grid size simulations, a grid with 98 elements was chosen for the main study.

7.6.2 Results

The same stress paths utilized in the triaxial experiments were followed in the numerical simulations. This was done by adjusting the pore pressure within the model using the FISH capabilities of FLAC. Pore pressure was increased with an increase in the deviatoric stress in order to follow the desired stress path. The pore pressure remained constant as soon as the peak friction angle was reached or when the effective confining pressure reached 15 kPa. Figures 7.21 to 7.29 compare the stress paths followed in the numerical simulations and the actual experiments.

The predicted deviatoric stress and volumetric strain versus axial strain behavior is shown in Figures 7.30 to 7.53. The deviatoric stress increase up to the peak is simulated fairly well however in the post peak region the numerical model predicts increased softening. This could be due to the input function representing change in the friction angle with plastic shear strain. As it was mentioned earlier it is desirable to have a more precise definition of this function. The one which will account for different confining pressures. The simulation of the volumetric deformation is of more importance in this study as it is a controlling factor in the change of absolute permeability. The simulated volumetric behavior could be divided into two sections: elastic and plastic regions.

In the elastic region (before peak) the initial slopes of the volumetric strain-axial strain curve is only a function of Poisson's ratio as the material behaves in an entirely elastic manner at the onset of loading (Figure 7.2). The value Poisson's ratio of 0.3 was chosen

for the current simulations, however from the results it is obvious that a value lower than 0.3 is more appropriate. The volumetric behavior of numerical model in the post peak region is controlled mainly by the dilation angle. As explained earlier, change in dilation angle with plastic shear strain is not introduced in these analyses. The lack of these functions could explain the minor deviation of simulated behavior from the experimental results, although over all the simulation is good. It is apparent that the simulated volumetric behavior shows the correct trend.

As mentioned before, the required input data are extracted from triaxial experiments described in the previous chapter. In most of these tests the stress path imposed was not of the conventional drained compression test in which the effective confining pressure is kept constant. Since the effective confining pressure substantially affects the required input parameters, the conventional test is desirable in obtaining these parameters. It is recommended that a series of conventional triaxial tests should be conducted so that more accurate functions for input parameters could be obtained.

7.7 Summary

- The objective of this chapter is to describe the application of the laboratory results in simulation of oil sand using a strain softening constitutive model with FLAC.

- Several material input functions are necessary in order to simulate the strain softening and shear dilatancy with FLAC. Results from high quality triaxial tests were used to provide the required input data.

- The input functions included introduction of relationships for tangent modulus of elasticity. They were used to simulate the nonlinear compressibility of the material.

- Dilation angle was defined for the triaxial strain condition. The variation of maximum friction angle and dilation angle with confining pressure were obtained as input functions.

- Triaxial tests on undisturbed McMurray Formation oil sand specimens were simulated with strain softening plasticity constitutive model. In the simulations the stress paths for Steam Assisted Gravity Drainage Recovery Method (SAGD) were followed.

- The stress-strain behavior up to the peak was simulated fairly well however in the post peak region the numerical model showed more softening.

- It was suggested that it would be more appropriate to use a series of input functions, each showing the change in the friction angle for a specific effective confining stress.

- The numerical model showed potential in simulating the volumetric behavior of the material.

- It was found that a Poisson's ratio lower than 0.3 may be more appropriate for McMurray Formation oil sands.

- It is recommended that more accurate input parameter functions could be obtained from a series of conventional drained triaxial tests.
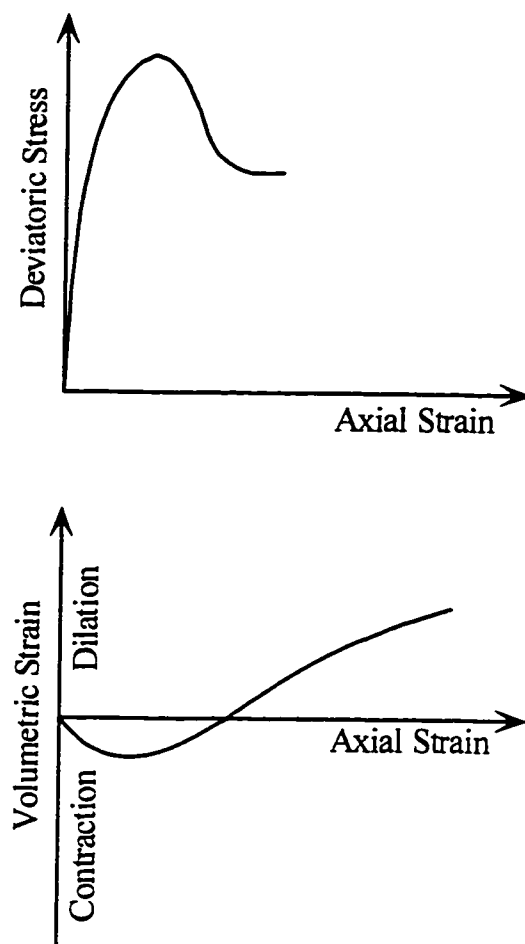
Figure 7.1 Typical results for triaxial drained test on dense sands
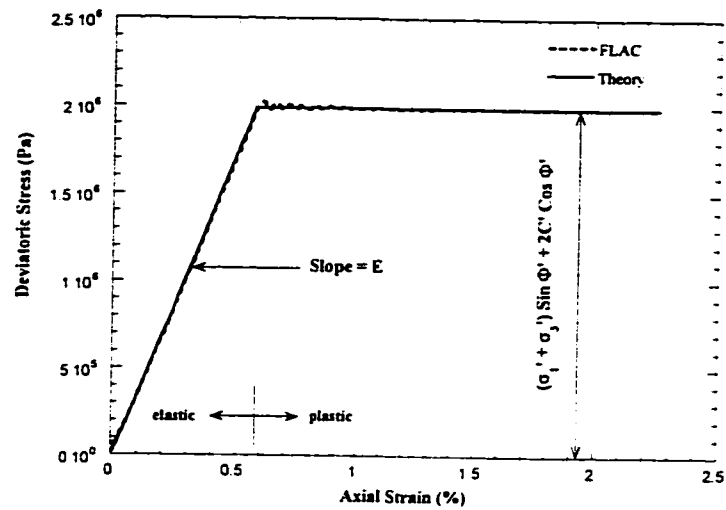
(a) Deviatoric Stress vs Axial Strain
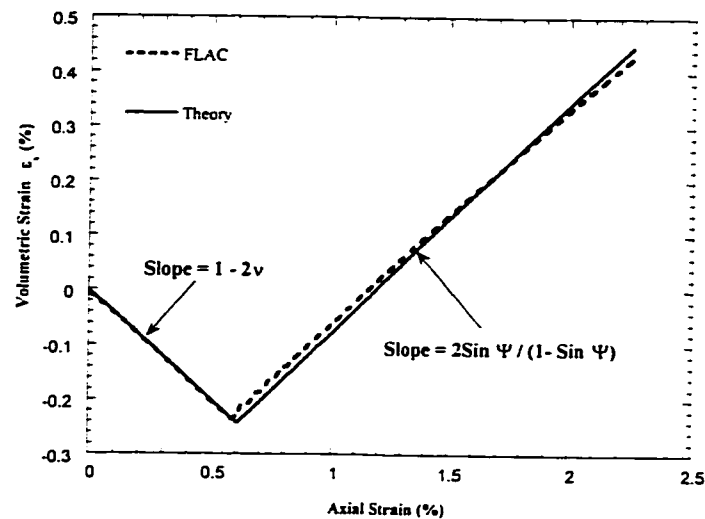
(b) Volumetric Strain vs Axial Strain

Figure 7.2 Bilinear idealization of triaxial test results based on Mohr-Coulomb plasticity model
(Vermeer and de Borst 1984)
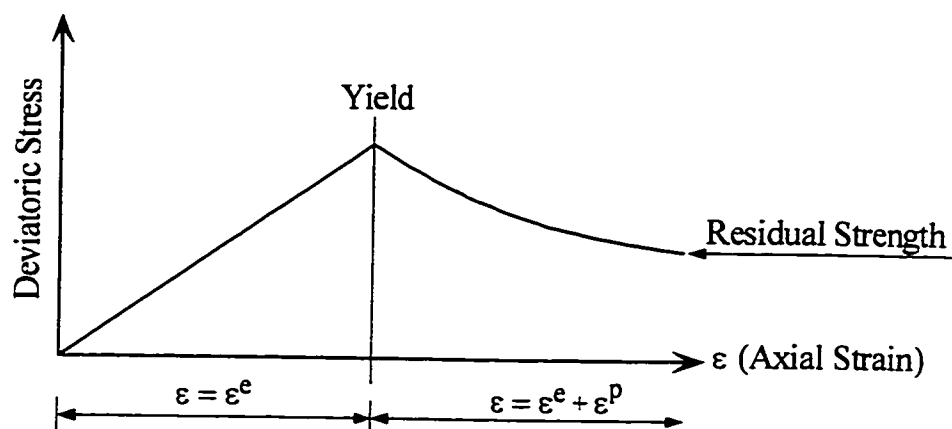
Figure 7.3 Example stress-strain curve
(Modified from Itasca 1991)
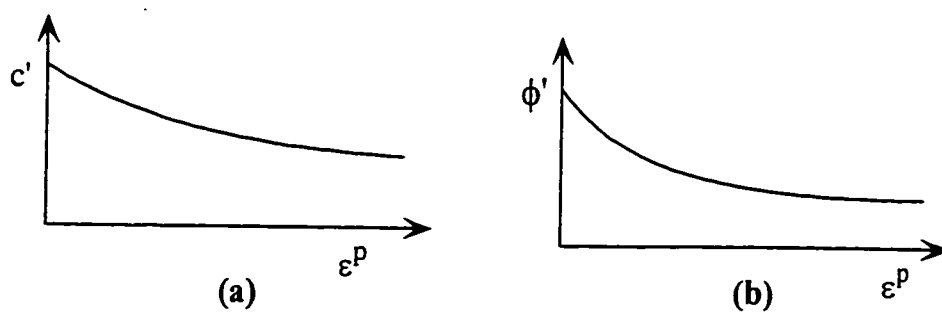
Figure 7.4 Variation of cohesion (a) and friction angle (b) with plastic strain ε^p
(Modified from Itasca 1991)
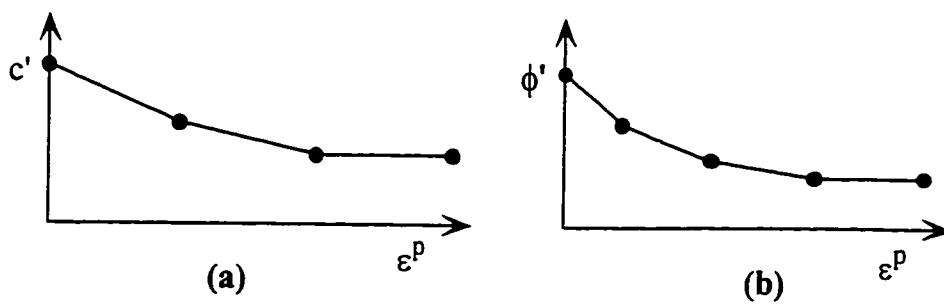
Figure 7.5 Approximation by linear segments
(Modified from Itasca 1991)
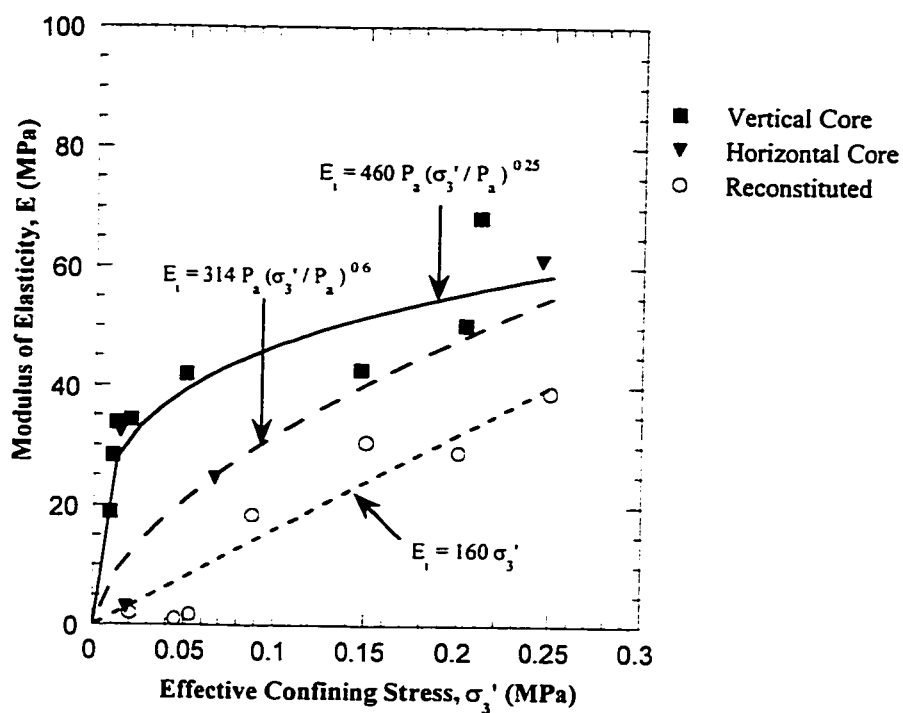
Figure 7.6 Variation of modulus of elasticity for effective confining stresses below 250 kPa

McMurray Formation oil sands
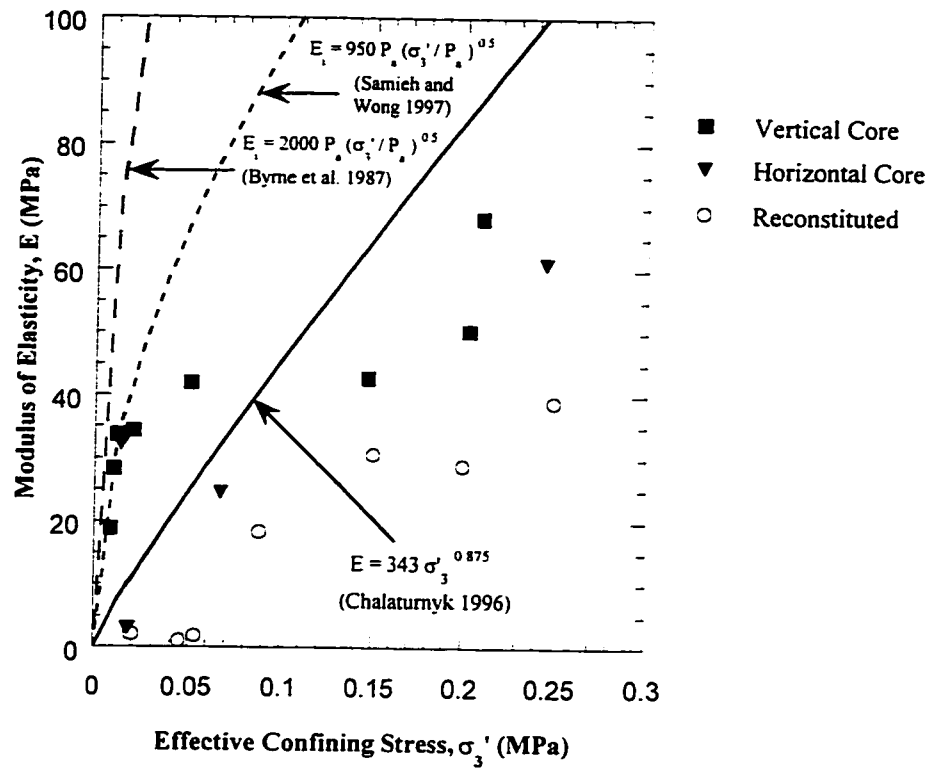
Figure 7.7 Variation of modulus of elasticity at low effective confining stresses McMurray Formation oil sands

$E_i = 2000 \, P_a \, (\sigma_3'/P_a)^{0.5}$
(Byrne et al., 1987)

$E = 343 \, \sigma_3'^{0.875}$
(Chalaturnyk, 1996)

O   Oldakowski (1994)

●   Agar (1984)

□   Chalaturnyk (1996)

△   Au (1984)

⊞   Plewes (1987)
     Conventional Platens

◩   Plewes (1987)
     Lubricated Ends

Modulus of Elasticity, E (Mpa)

Effective Confining Stress, σ_3' (MPa)
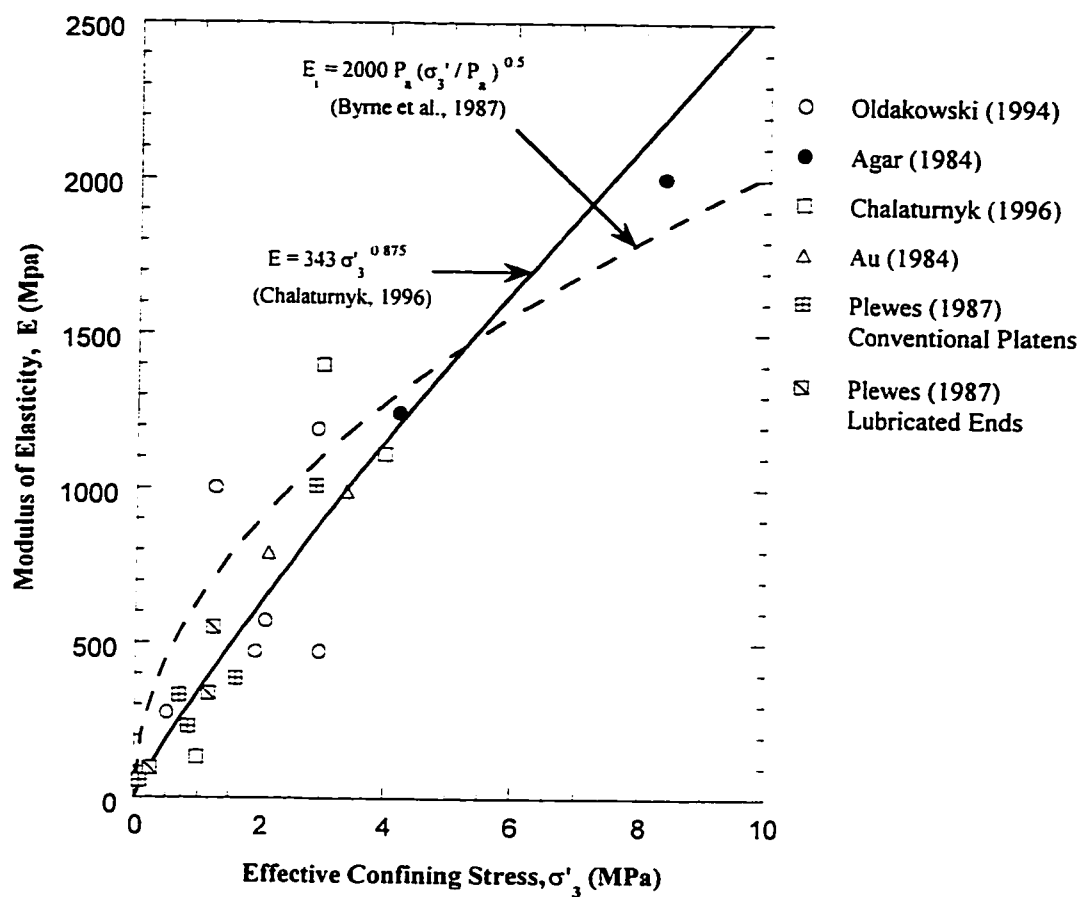
Figure 7.8 Variation of modulus of elasticity at high effective confining stresses McMurray Formation oil sands
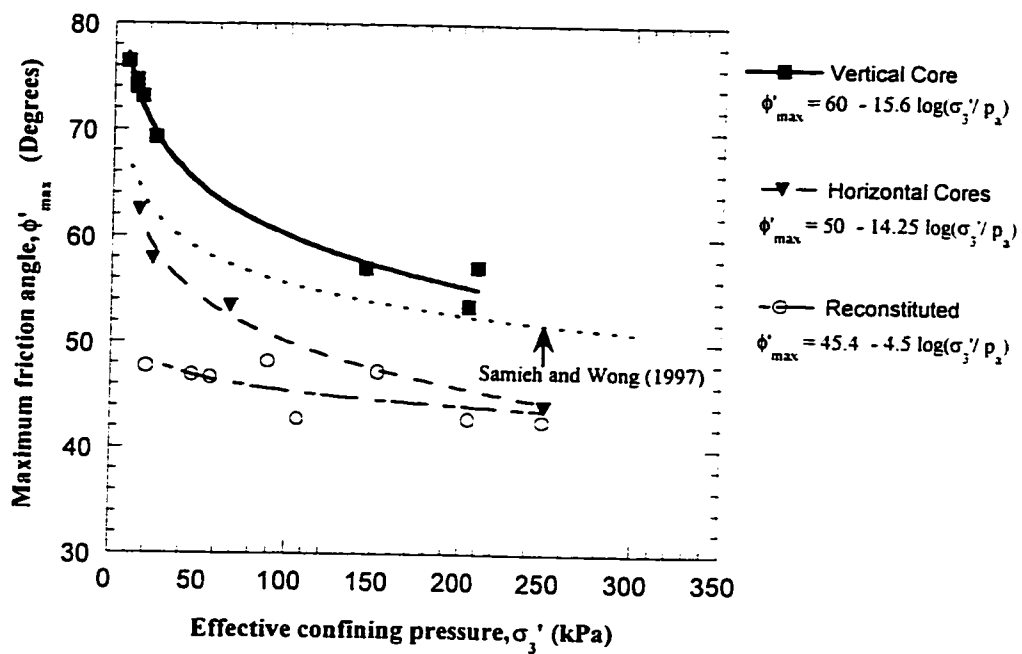
Figure 7.9 Variation of the maximum friction angle
with effective confining pressure
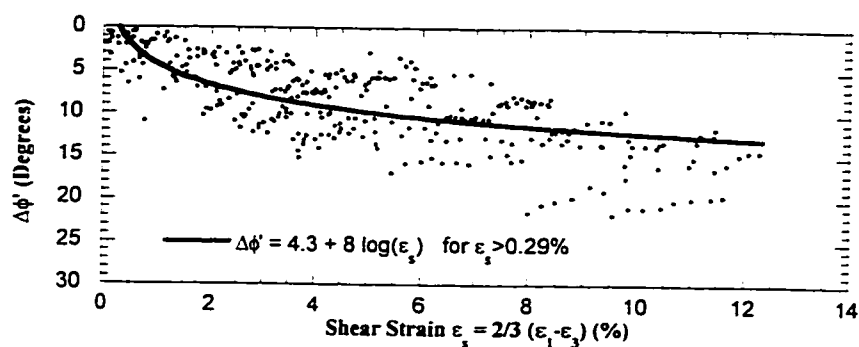
Figure 7.10 After peak changes in the friction angle with shear strain
Vertical cores

$\Delta\phi' = 4.3 + 8 \log(\varepsilon_s)$ for $\varepsilon_s > 0.29\%$
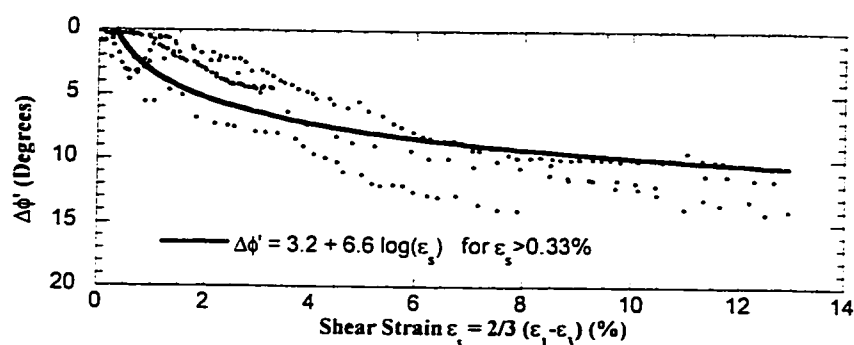
Figure 7.11 After peak changes in the friction angle with shear strain
Horizontal cores

$\Delta\phi' = 3.2 + 6.6 \log(\varepsilon_s)$ for $\varepsilon_s > 0.33\%$
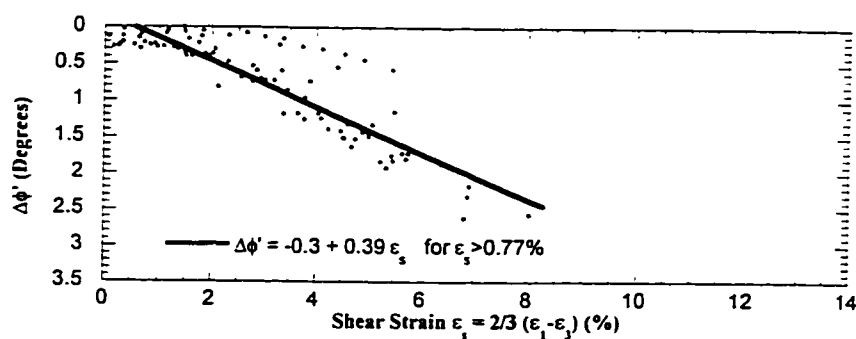
Figure 7.12 After peak changes in the friction angle with shear strain
Reconstituted specimens

$\Delta\phi' = -0.3 + 0.39\,\varepsilon_s$ for $\varepsilon_s > 0.77\%$
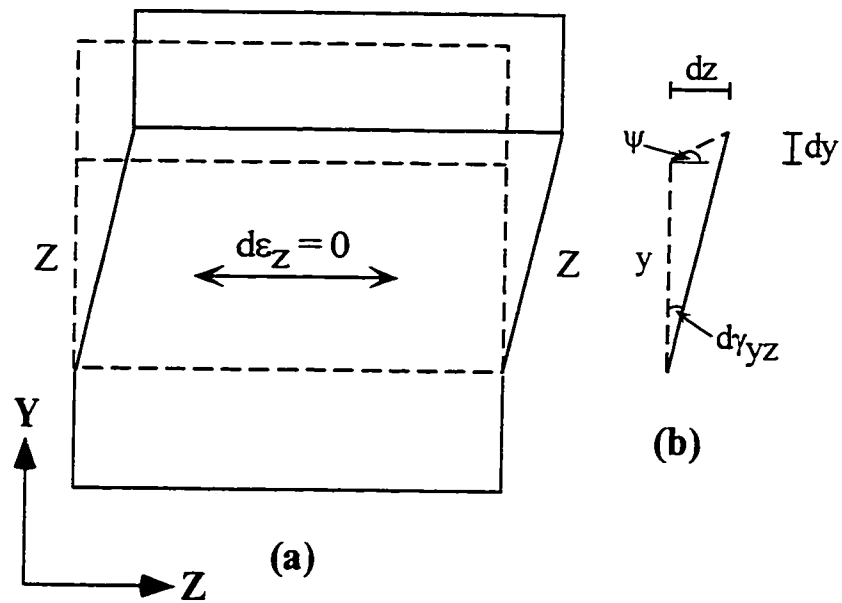
Figure 7.13 Angle of dilation y in plane shear
(Modified from Bolton 1986)
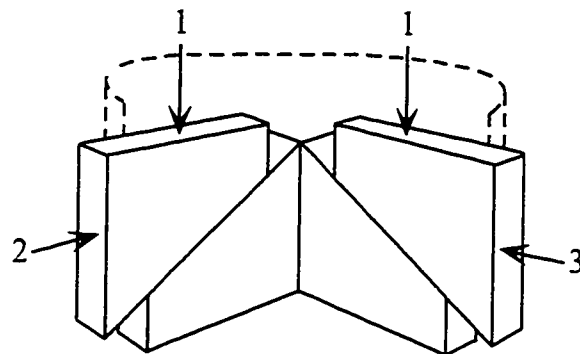
Figure 7.14 Derivation of triaxial dilatancy from biaxial state
(Modified from Schanz and Vermeer 1996)
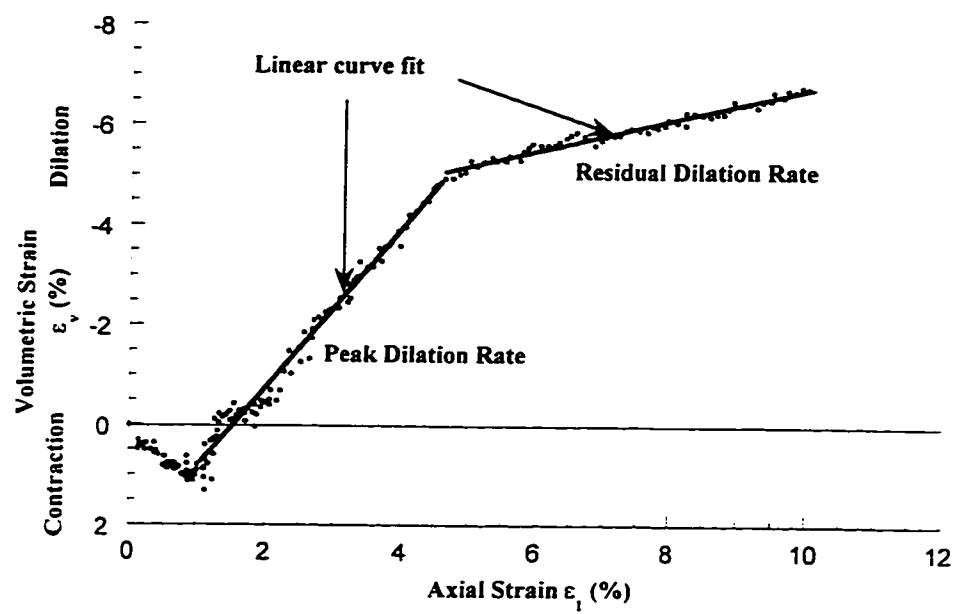
Figure 7.15 Typical triaxial test results
(Horizontal core, T41)
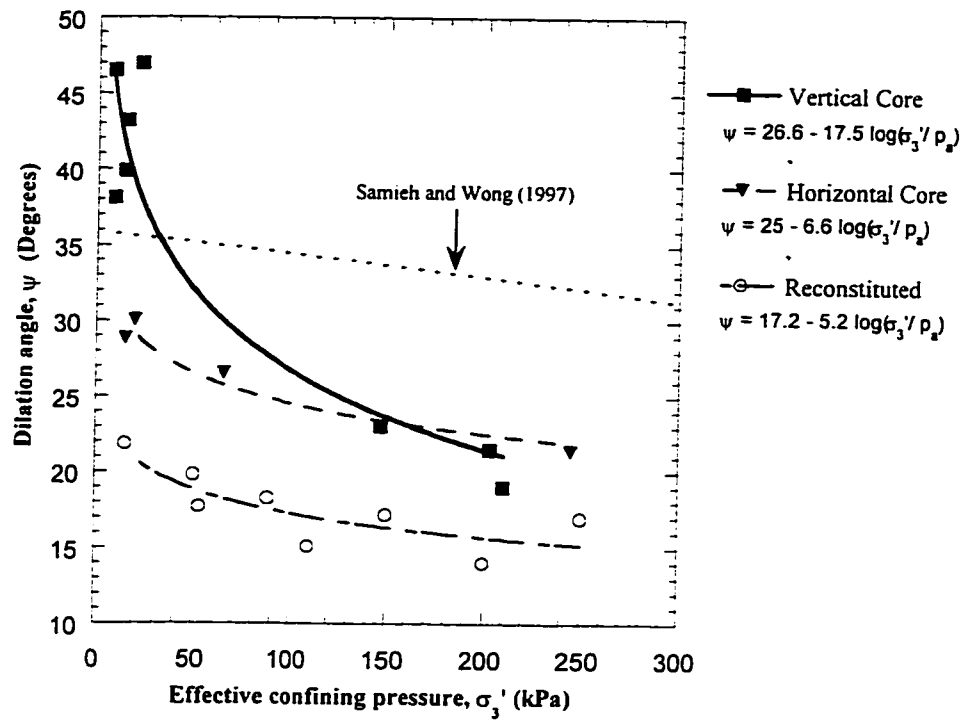
**Figure 7.16 Variation of the dilation angle
with effective confining pressure**
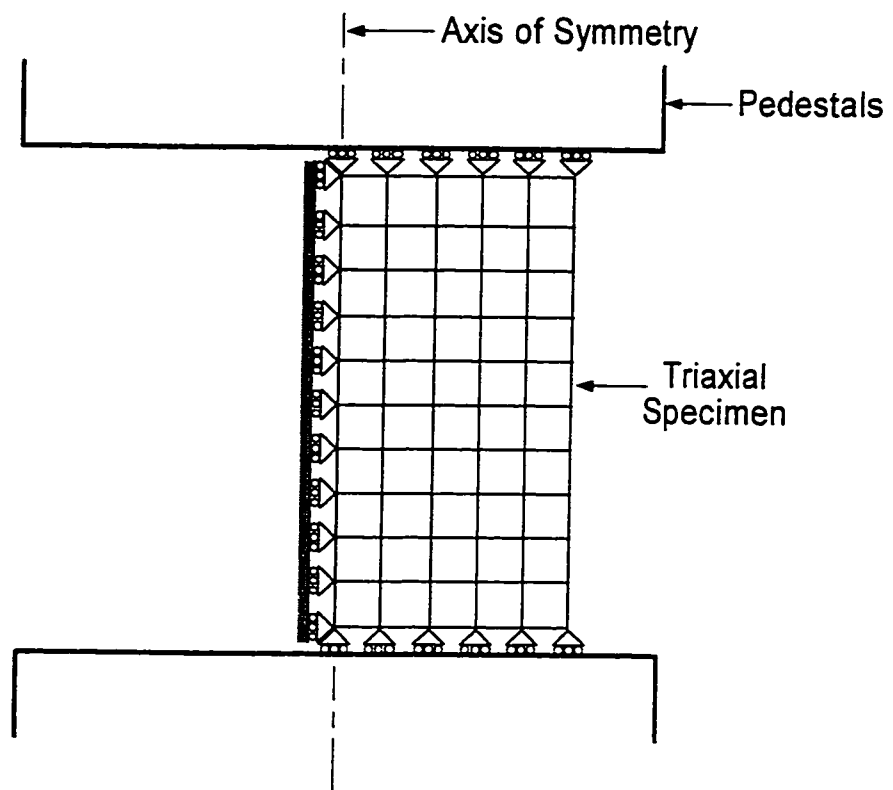
Figure 7.17 Boundary conditions of the numerical model
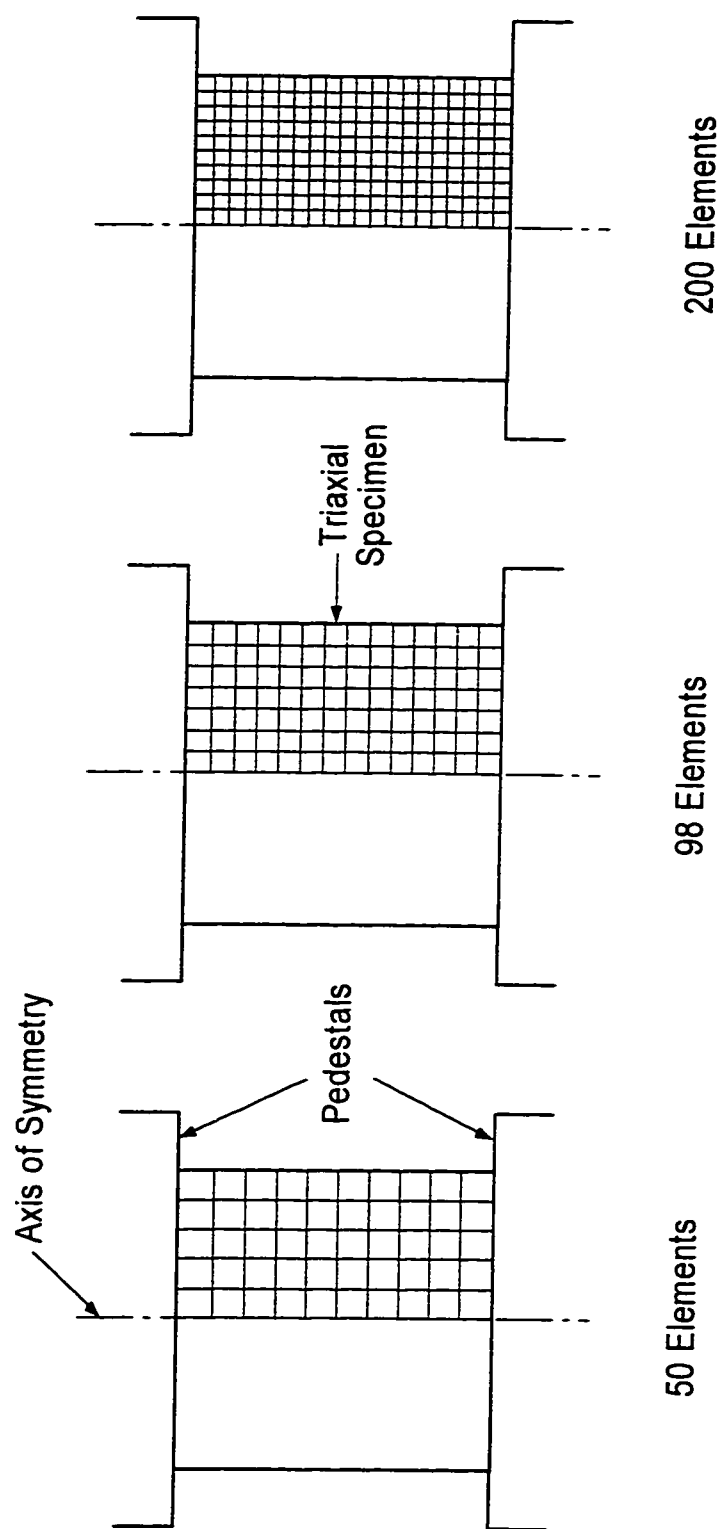
Figure 7.18 Geometry of the problem and the assumed grid sizes
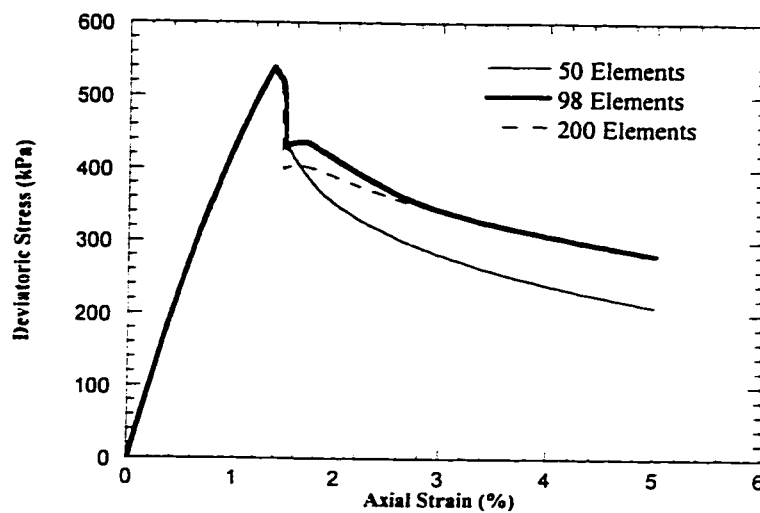
Figure 7.19 Deviatoric stress versus axial strain for different grid sizes
Horizontal Core
Stress Path 2 (Initial σ_3'=250 kPa)
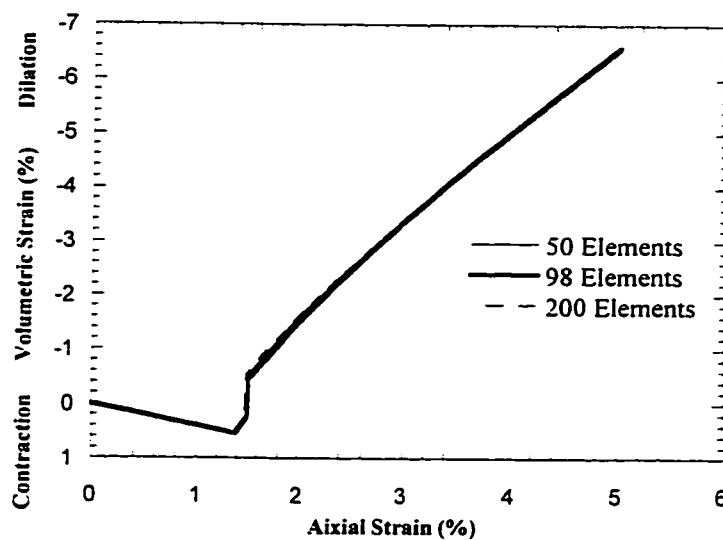
Figure 7.20 Volumetric strain versus axial strain for different grid sizes
Horizontal Core
Stress Path 2 (Initial σ_3'=250 kPa)
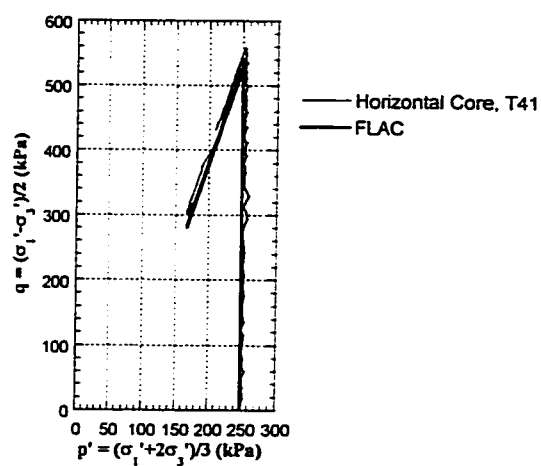
**Figure 7.21   Stress Path 2
Horizontal Core**
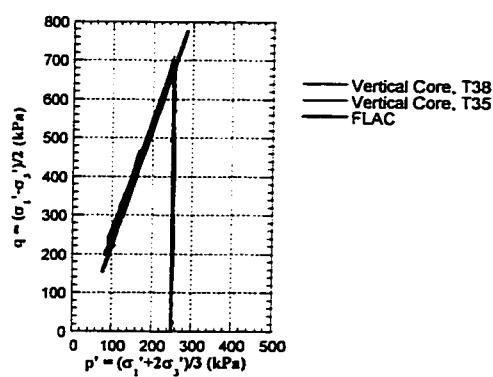
**Figure 7.22 Stress Path 2
Vertical Core**
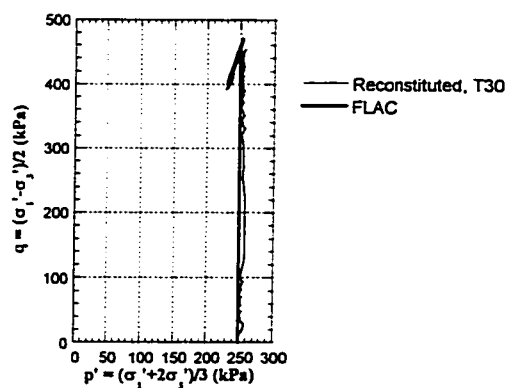
**Figure 7.23 Stress Path 2
Reconstituted Specimen**
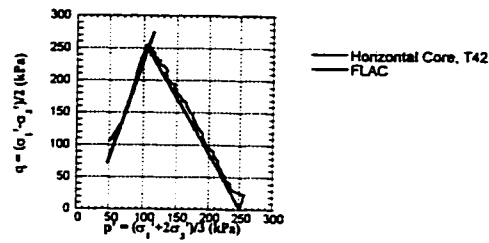
**Figure 7.24   Stress Path 3
Horizontal Core**
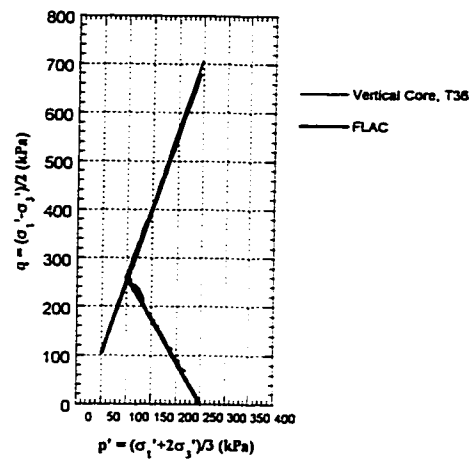
**Figure 7.25   Stress Path 3
Vertical Core**
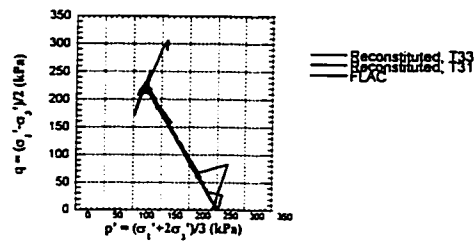
**Figure 7.26   Stress Path 3
Reconstituted Specimen**
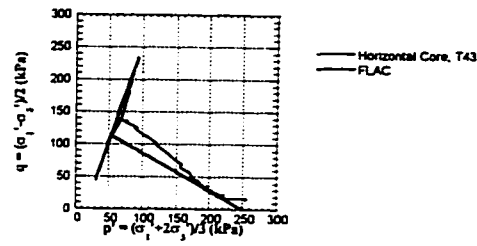
Figure 7.27 Stress Path 4
Horizontal Core
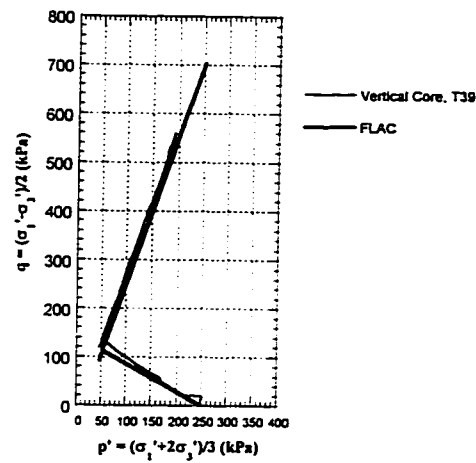
Figure 7.28   Stress Path 4
Vertical Core
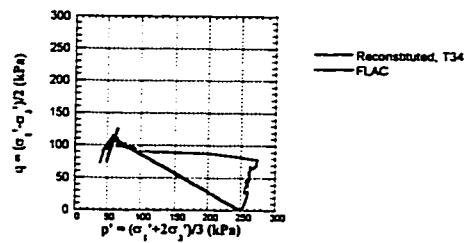
Figure 7.29   Stress Path 4
Reconstituted Specimen
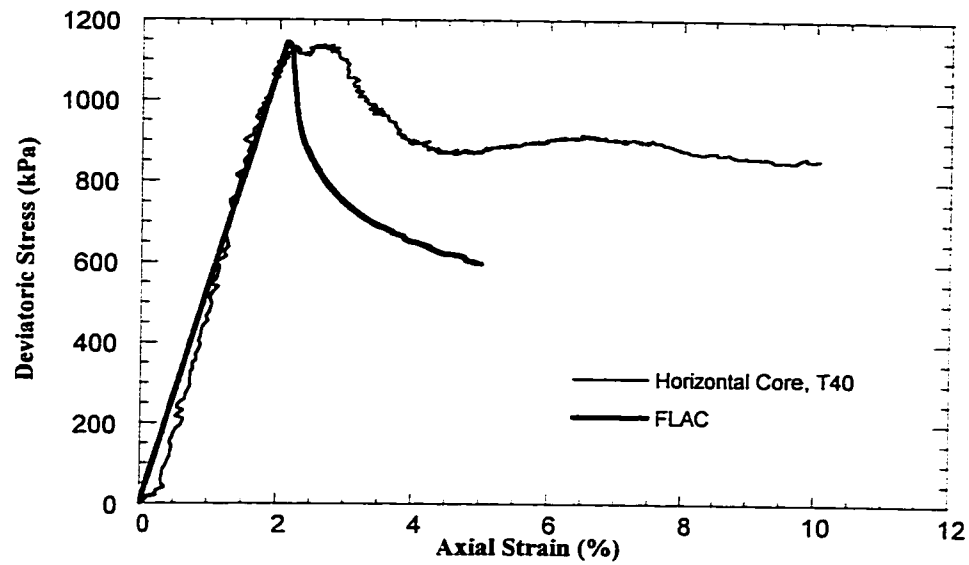
Figure 7.30   Deviatoric stress versus axial strain
Horizontal Core
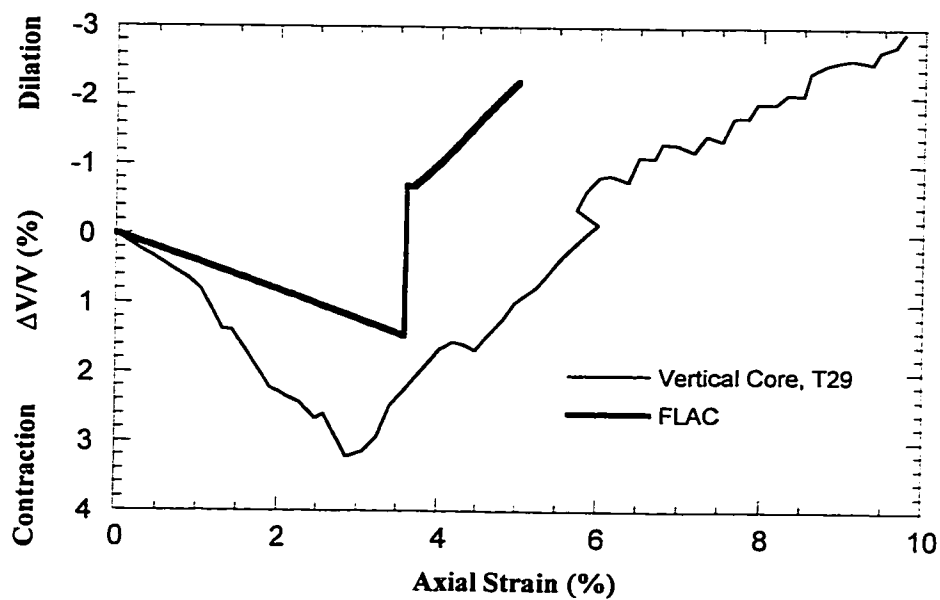**Stress Path 1 (σ_3'=250 kPa)**
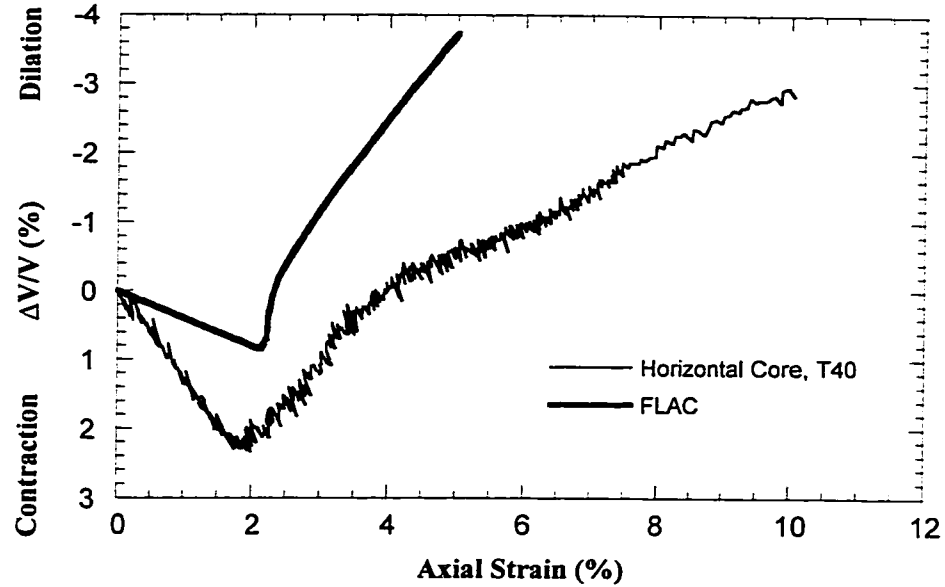
Figure 7.31 Volumetric strain versus axial strain
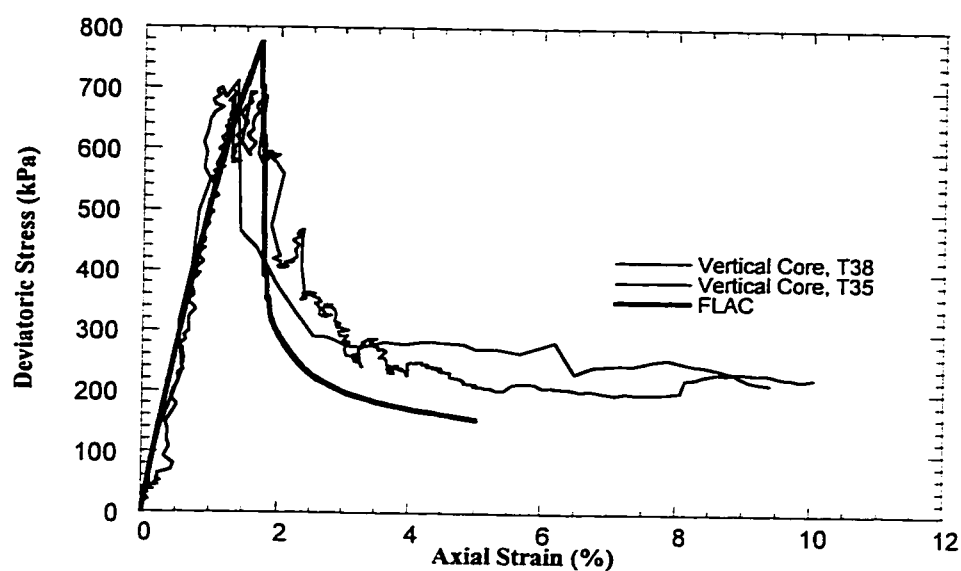**Horizontal Core**
Stress Path 1 (σ_3'=250 kPa)
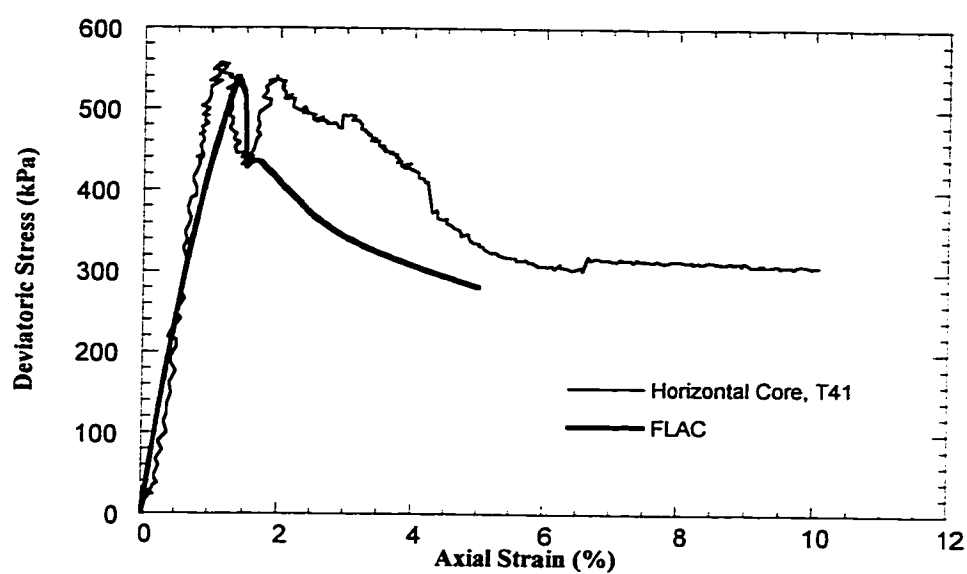
Figure 7.32   Deviatoric stress versus axial strain
Horizontal Core
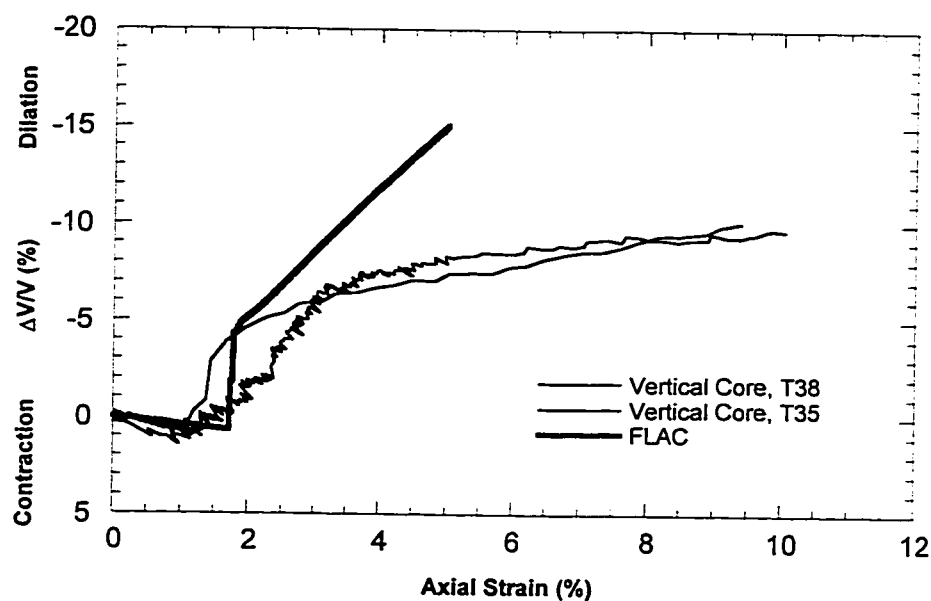**Stress Path 2 (Initial σ_3'=250 kPa)**
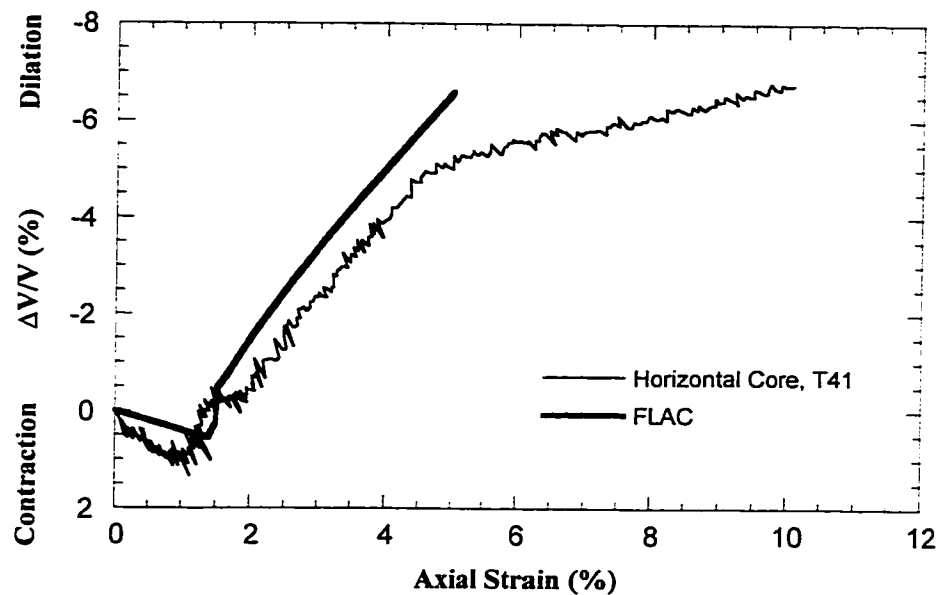
Figure 7.33 Volumetric strain versus axial strain
Horizontal Core
Stress Path 2 (Initial σ_3'=250 kPa)
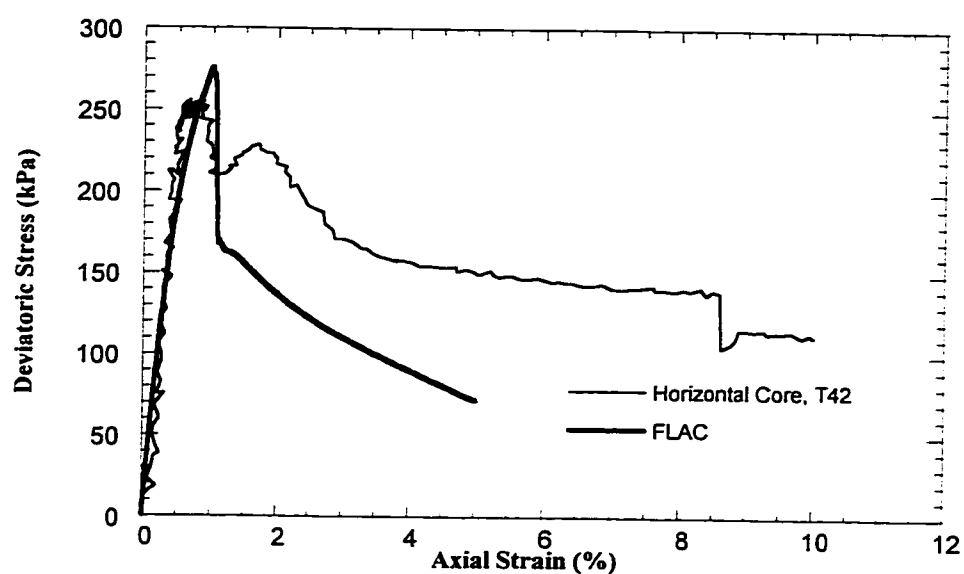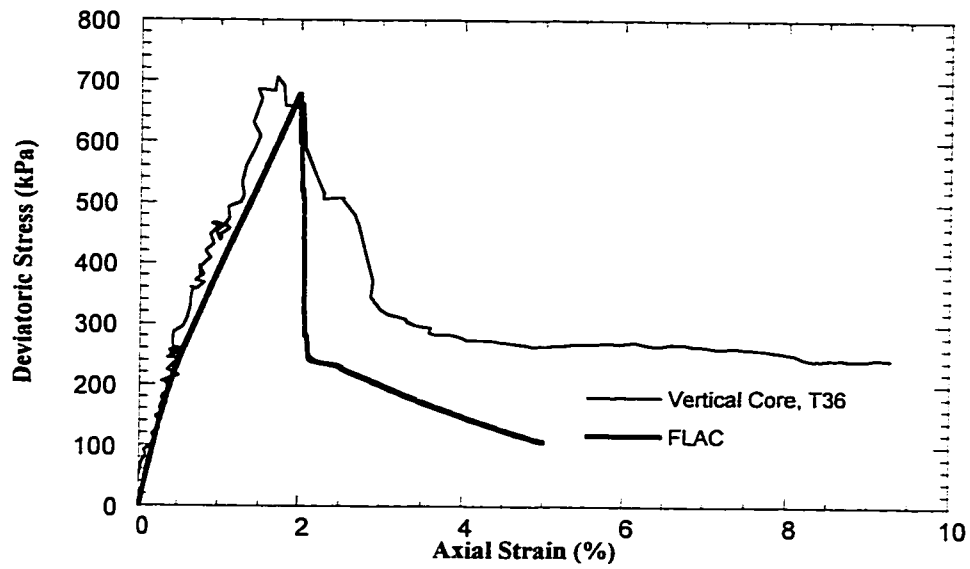
Figure 7.34   Deviatoric stress versus axial strain
Horizontal Core
Stress Path 3 (Initial σ_3'=250 kPa)
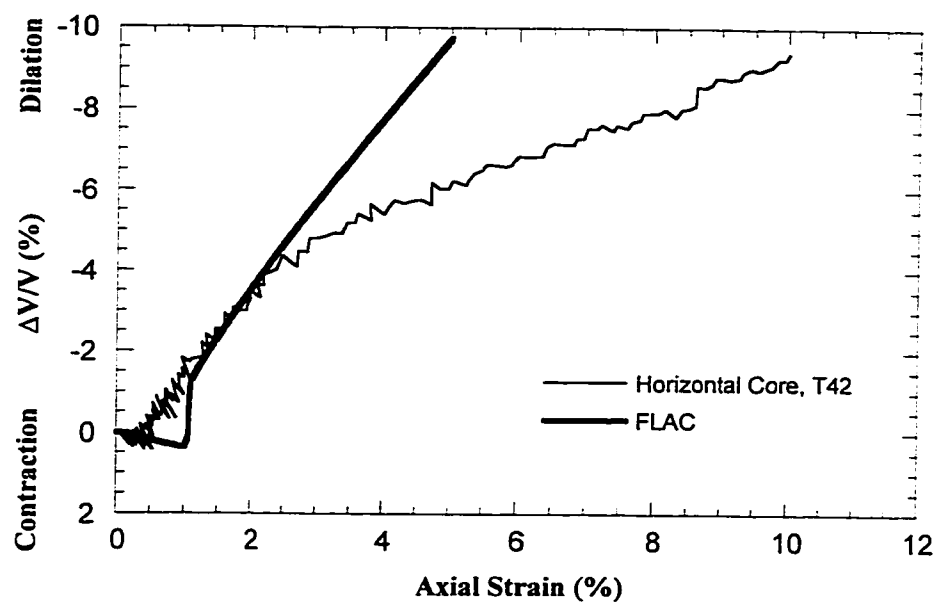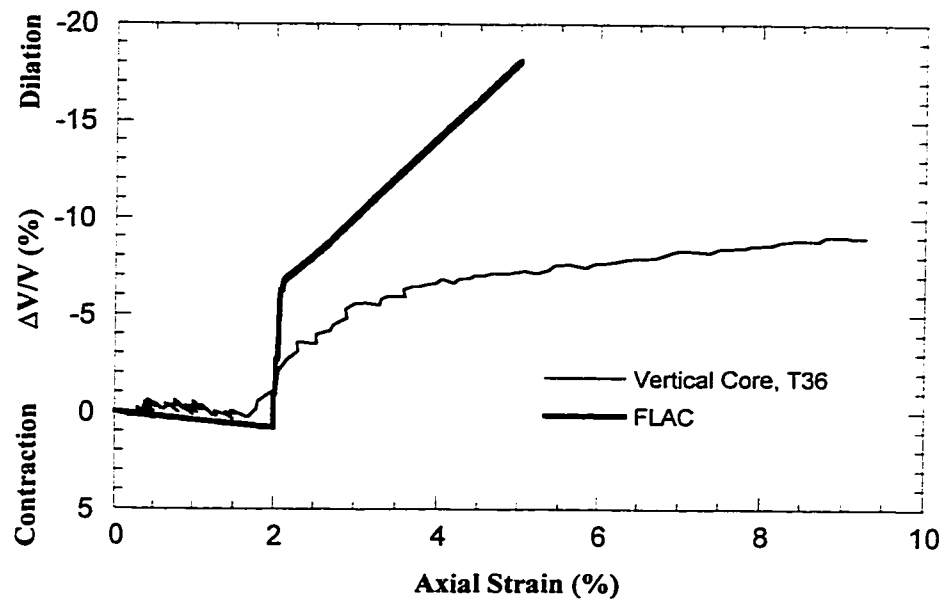

Figure 7.35 Volumetric strain versus axial strain
Horizontal Core
Stress Path 3 (Initial σ_3'=250 kPa)
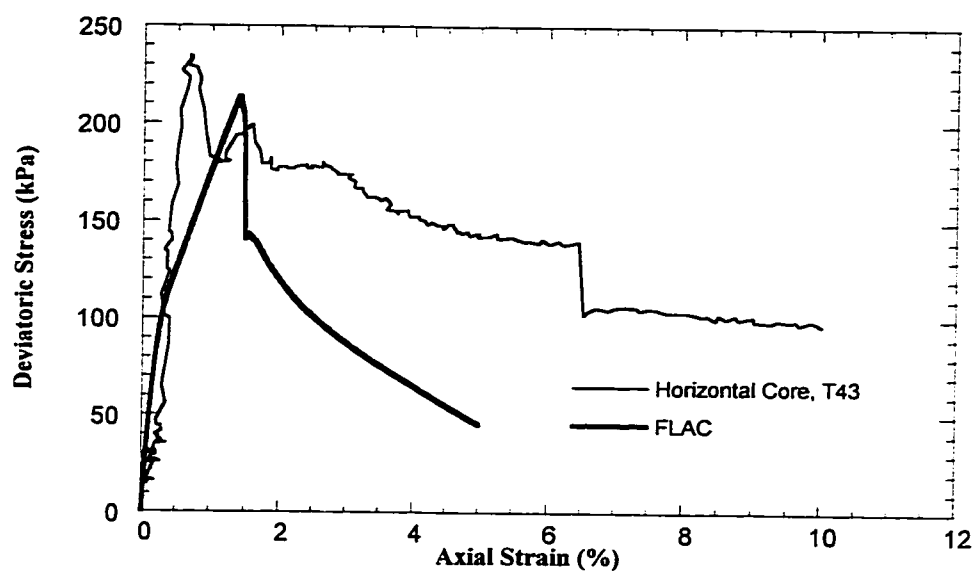
Figure 7.36   Deviatoric stress versus axial strain
Horizontal Core
Stress Path 4 (Initial σ_3'=250 kPa)
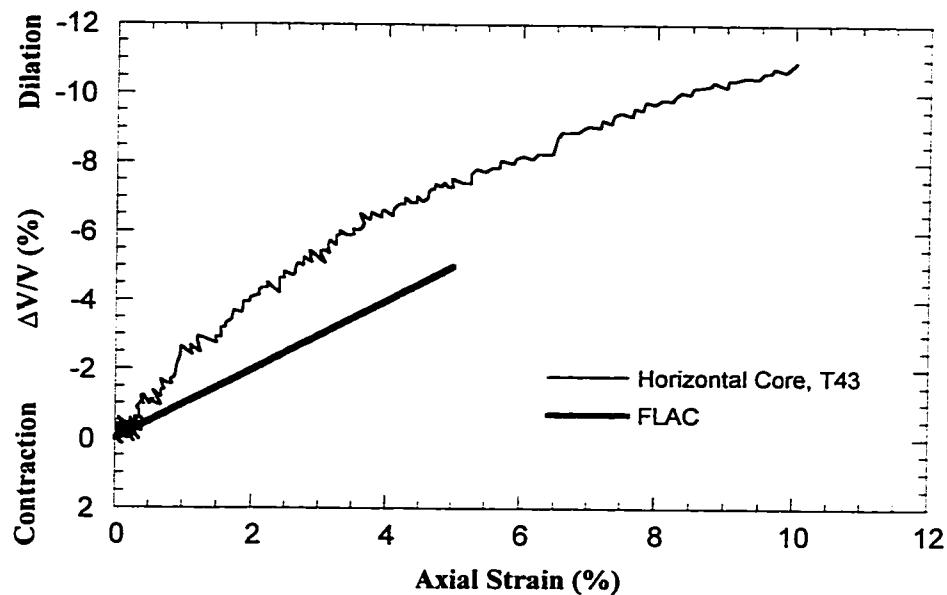
Figure 7.37 Volumetric strain versus axial strain
Horizontal Core
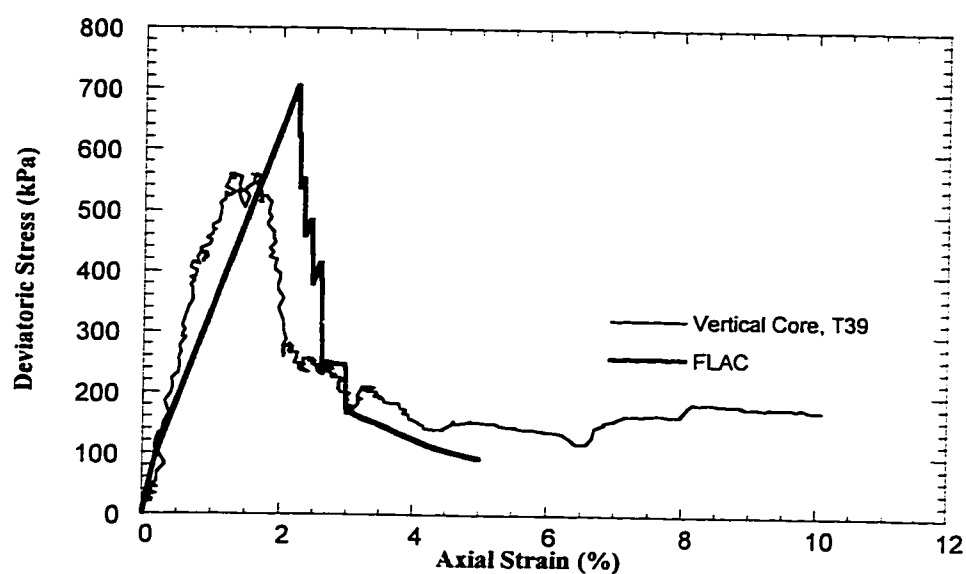**Stress Path 4 (Initial σ_3'=250 kPa)**
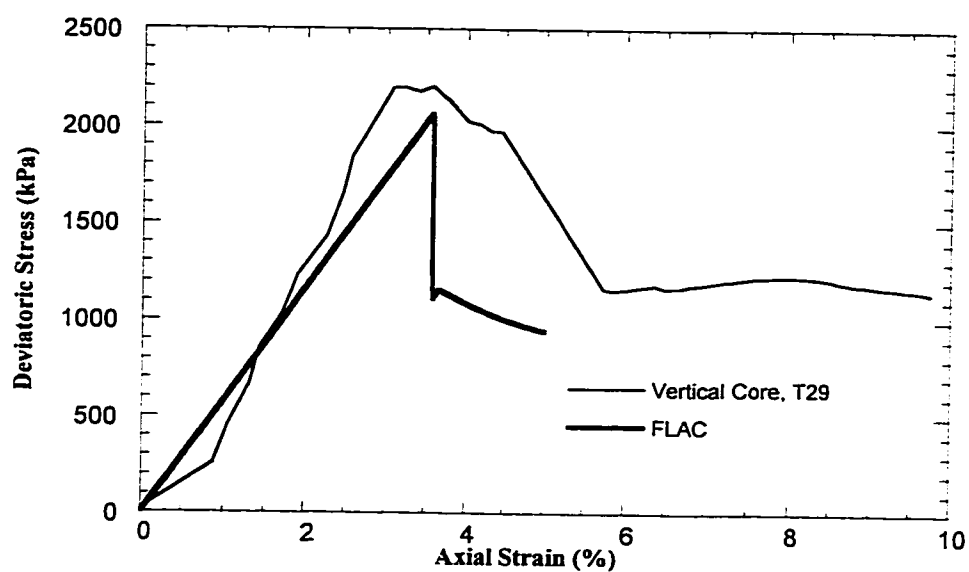
Figure 7.38   Deviatoric stress versus axial strain
Vertical Core
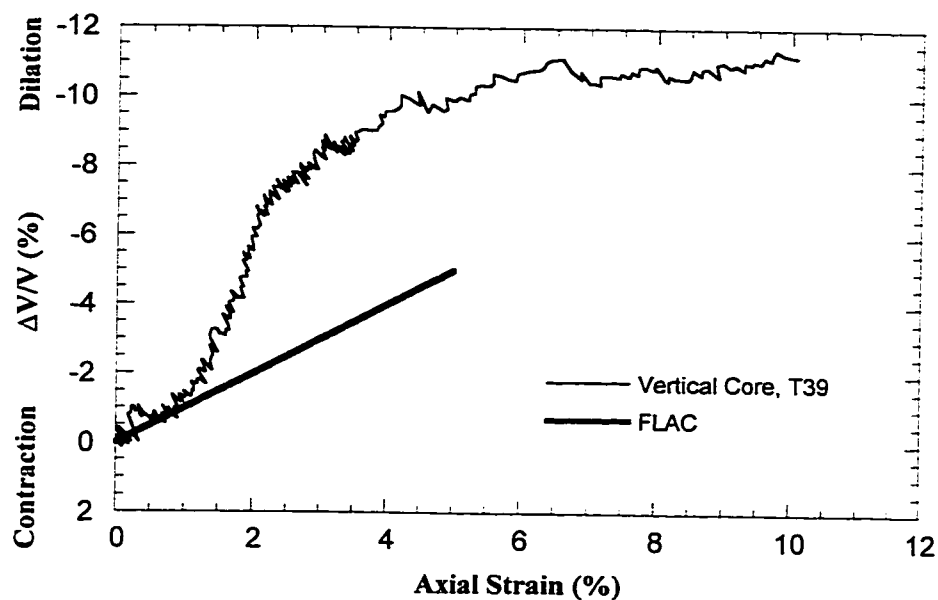**Stress Path 1 (σ_3'=250 kPa)**

Figure 7.39 Volumetric strain versus axial strain
Vertical Core
Stress Path 1 (σ_3'=250 kPa)

Figure 7.40   Deviatoric stress versus axial strain
Vertical Core
Stress Path 2   (Initial σ_3'=250 kPa)

Figure 7.41 Volumetric strain versus axial strain
Vertical Core
Stress Path 2 (Initial σ_3'=250 kPa)

Figure 7.42 Deviatoric stress versus axial strain
Vertical Core
Stress Path 3 (Initial σ_3'=250 kPa)

Figure 7.43 Volumetric strain versus axial strain
Vertical Core
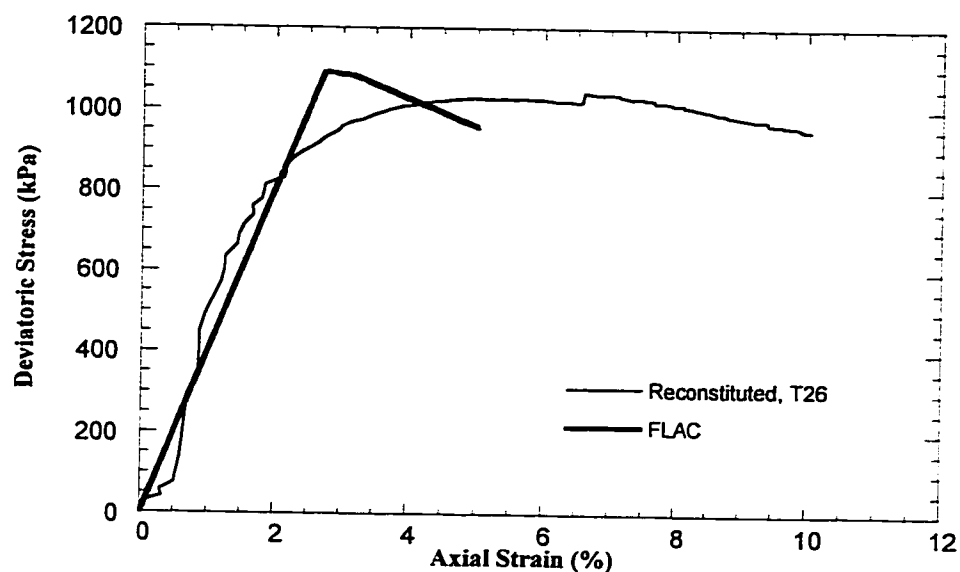**Stress Path 3 (Initial σ_3'=250 kPa)**

Figure 7.44   Deviatoric stress versus axial strain
Vertical Core
Stress Path 4 (Initial σ_3'=250 kPa)

Figure 7.45 Volumetric strain versus axial strain
Vertical Core
Stress Path 4 (Initial σ_3'=250 kPa)

Figure 7.46 Deviatoric stress versus axial strain
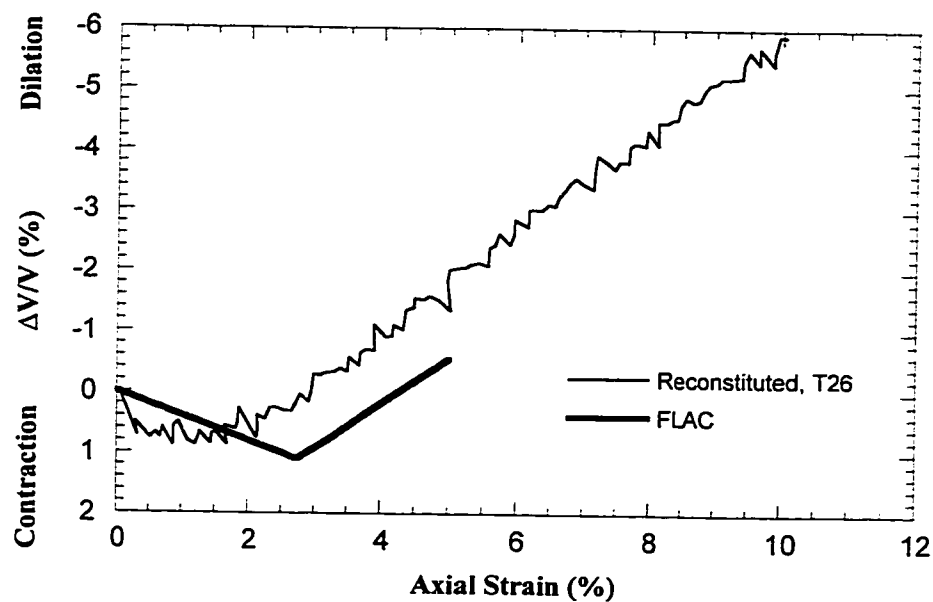**Reconstituted Specimen**
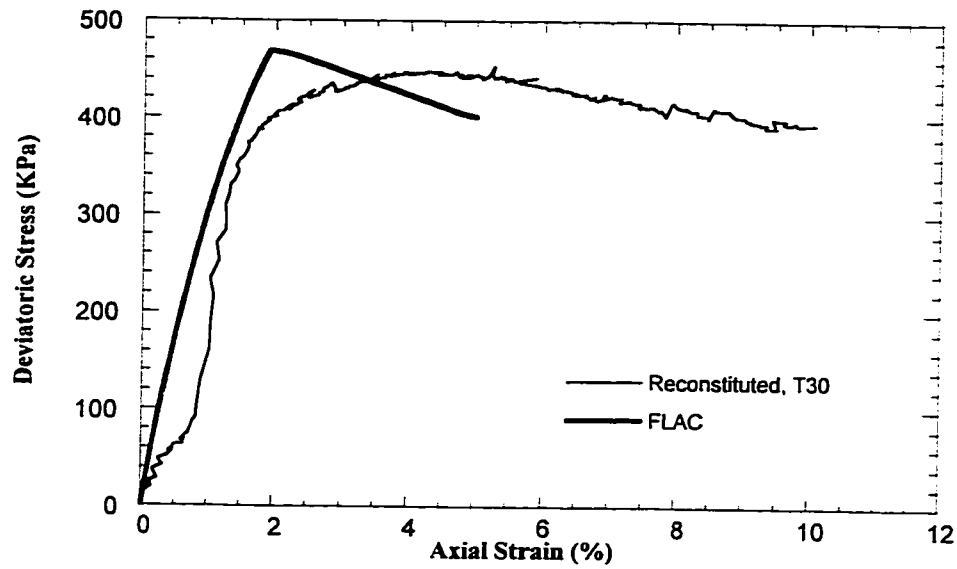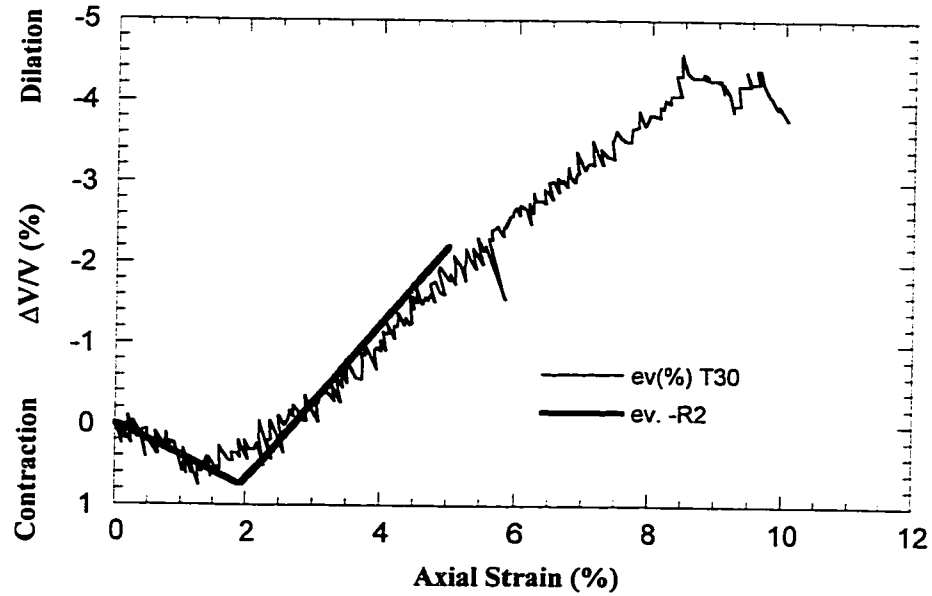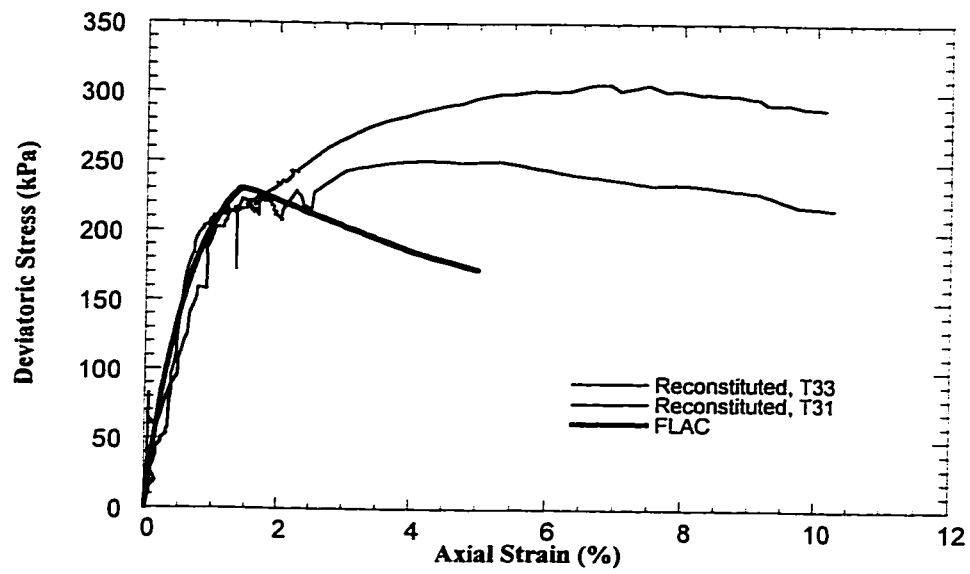**Stress Path 1 (σ_3'=250 kPa)**

Figure 7.47 Volumetric strain versus axial strain
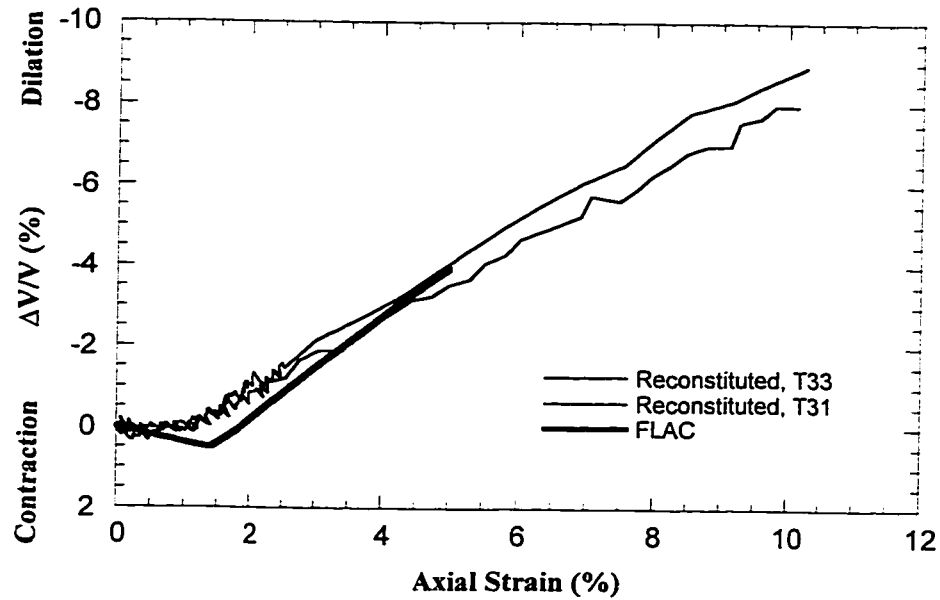**Reconstituted Specimen**
Stress Path 1 (σ_3'=250 kPa)

Figure 7.48   Deviatoric stress versus axial strain
Reconstituted Specimen
Stress Path 2   (Initial σ_3'=250 kPa)

Figure 7.49 Volumetric strain versus axial strain
Reconstituted Specimen
Stress Path 2 (Initial σ_3'=250 kPa)

**Figure 7.50   Deviatoric stress versus axial strain
Reconstituted Specimen
Stress Path 3   (Initial σ_3'=250 kPa)**

**Figure 7.51 Volumetric strain versus axial strain
Reconstituted Specimen
Stress Path 3 (Initial σ_3'=250 kPa)**

Figure 7.52   Deviatoric stress versus axial strain
Reconstituted Specimen
Stress Path 4   (Initial σ_3'=250 kPa)

Figure 7.53 Volumetric strain versus axial strain
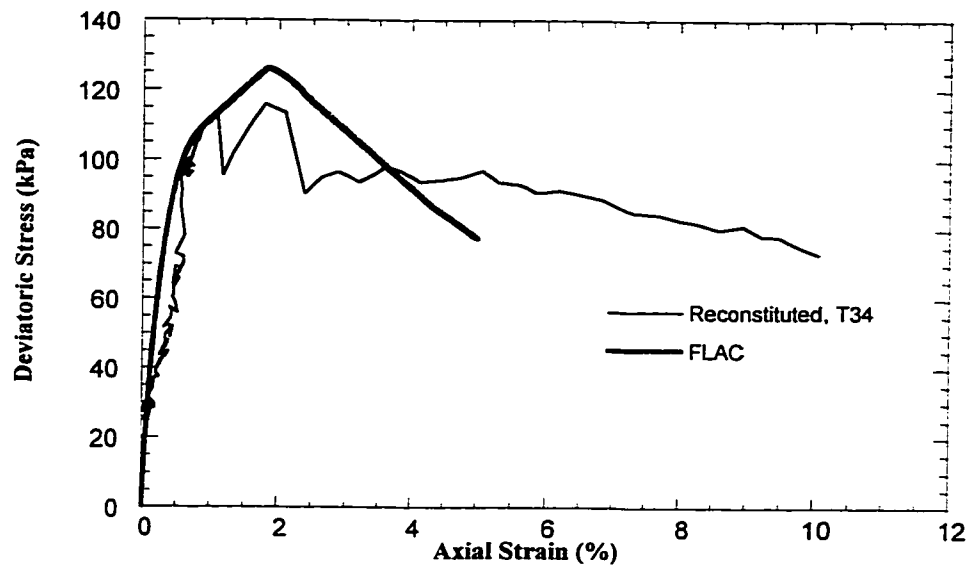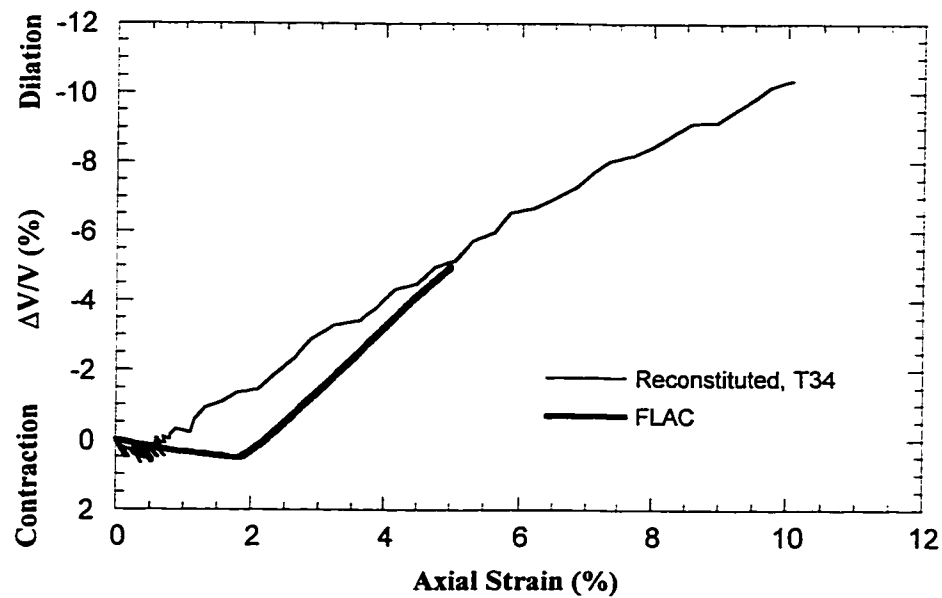**Reconstituted Specimen**
Stress Path 4 (Initial σ_3'=250 kPa)

CHAPTER 8   OIL SAND ABSOLUTE PERMEABILITY[2]

8.1 Introduction

Analyses of water flow in saturated soils are usually based on Darcy's law. Hydraulic conductivity or coefficient of permeability, k, is defined as the discharge velocity, v, through an unit area under an unit hydraulic gradient:

$$v = k\, i$$

[8.1]

where, i, the hydraulic gradient, equals $\Delta H/L$. ΔH is the head difference in the flow length L.

k in fact is the constant of proportionality, which is termed the hydraulic conductivity in most disciplines but is often termed the coefficient of permeability by civil engineers.

Permeability is one of the most intriguing properties of materials that engineers must deal with because it can vary over a very wide range. No other engineering property of soils is as variable as permeability.

In many of the engineering works involving drainage, permeability is detrimental to safety and performance. It is essential to specify the relation between porosity and permeability in the case of oil production where consolidation is a principal driving mechanism. Adequate modeling of consolidation means solving a coupled problem of solid and fluid phase in the two-phase media. The coupling variable is the pore pressure which in turn governs the solid phase through the well known Terzaghi's effective stress principle, as well as fluid flow through Darcy's law.

Performance of the gravity drainage recovery of bitumen in McMurray Formation oil sands is highly dependent on permeability, specifically absolute permeability, and its changes throughout the process. During steam assisted gravity drainage (SAGD) in situ thermal recovery of bitumen from oil sands, steam is injected at elevated temperatures and pressures. This results in high pore pressures, low vertical effective stress and an increase in horizontal effective stress (Chalaturnyk 1996). Shear deformation of oil sand under these conditions results in shear dilation and an increase in pore volume and, therefore, in permeability.

To understand this interrelationship, it is necessary to measure and monitor the permeability of oil sand when it undergoes changes in stress and strain. In this study, an extensive laboratory testing program was conducted to replicate the stress and pore pressure conditions simulating SAGD process.

The triaxial test equipment used in the experimental program provides facilities for maintaining a constant flow rate of permeant through a specimen while it is subjected to a controlled effective stress path. Special stress path triaxial permeability testing equipment was developed for this purpose and is described in detail in Chapter 2.

A test set up that ensured a uniform stress-strain condition in the triaxial specimen was necessary. Lubricated end platens for a specimen size of 38 mm by 38 mm were used to obtain these uniform conditions. The use of lubricated end configurations in a permeability test requires special permeability calculations. This issue was discussed in Chapter 3.

Both undisturbed and reconstituted oil sand specimens were tested. The undisturbed specimens were obtained by coring a block sample both vertically and horizontally (Chapter 6). Figure 6.6 shows the grain size distribution of the block sample and the reconstituted specimens (MS3). As it can be seen, these materials are uniform quartz sands with similar grain size distribution. Reconstituted specimens were made from McMurray Formation sand obtained from the trimmings of the block samples. This sand was sieved and blended in order to have a grain size distribution identical to that of the block sample. Dense reconstituted specimens were made by the wet vibration method (Chapter 4).

A series of triaxial shear and permeability tests were conducted on these oil sand specimens. Table 6.1 shows a summary of tests and specimen properties.

Results of the permeability tests are presented and an empirical relationship between changes in volumetric strain and absolute permeability is proposed. As the initial in situ absolute permeability varies because of geological details, the following discussion emphasizes changes to the initial absolute permeability rather than the determination of the true, in situ value of permeability.

8.2 Absolute permeability

A convenient form for representing the permeability of a medium independent of fluid properties is the absolute permeability. The relationship discovered by Darcy is concerned with the flow of water in sand. However a more generalized version of Darcy's law states that the discharge velocity of flow of fluid through a porous granular medium, under steady conditions, is proportional to the excess hydrostatic pressure causing the flow, and inversely proportional to the viscosity of the fluid. This can be expressed by the equation:

$$v = K \frac{1}{\eta} \frac{\Delta P}{L} \times 10^{-12} = K \frac{1}{\eta} \frac{\Delta H \rho g}{L} \times 10^{-12} = \frac{K \rho g i}{\eta} \times 10^{-12} \qquad [8.2]$$

where:

v is the discharge velocity in m/s,

η is the dynamic viscosity of the fluid in Pa.s,

ΔP is the pressure difference in Pa along the flow length L in m,

ΔH is the total head difference in m,

ρ is the density of fluid in kg/m^3,

g is the acceleration due to gravity in m/s^2 and

i is the hydraulic gradient equal to $\Delta H/L$.

K, is an empirical constant known as the absolute or intrinsic permeability, having the dimension of area (μm^2). The absolute permeability is constant for a given soil at a given porosity and is independent of the viscosity and density of the fluid.

In most engineering applications we are concerned with the flow of water. Considering the Equation 8.1 and Equation 8.2 the following relationship between, k, hydraulic conductivity and, K, absolute permeability is obtained:

$$k = \frac{\rho_w g}{\eta_w} K \times 10^{-12} \qquad [8.3]$$

Or:

$$K = \frac{\eta_w}{\rho_w g} k \times 10^{12} \qquad [8.4]$$

where:

k is the hydraulic conductivity in m/s,

ρ_w is the density of water in kg/m^3,

η_w is the dynamic viscosity of water in Pa.s and,

K is the absolute permeability in μm^2.

8.3 Triaxial permeability test results

Chapter 6 describes the triaxial shear test results conducted during this research. Figure 6.5 shows the stress paths implemented in this study. Permeability test results presented here includes both the vertical and horizontal specimens obtained from the block sample and the reconstituted MS3 specimens.

Lubricated end configuration with specimen size of 38 mm by 38 mm were used for the permeability tests. Initial effective confining pressures of 100 KPa to 250 KPa were applied (Table 6.1). Figures 6.8 to 6.10 display the attained stress paths.

Figure 8.1 shows the values of initial absolute permeability for all the tests. Results from previous researchers on similar material (Agar 1984, Oldakowski 1994) are also included for comparison. The variation in results can be explained by the fact that the specimens tested in this study have a smaller porosity and that the grain size distribution of sands tested by other researchers was different.

Figures 8.2 to 8.13 show the variation of volumetric strain and absolute permeability with axial strain for all the stress paths tested. Since most of the available studies describe a direct relationship between porosity and permeability it is appropriate to present the permeability results against porosity. Figures 8.14 to 8.17 show the variation of absolute permeability with changes in porosity during tests. A reduction in porosity due to contraction in volumetric strain at the beginning of shearing and then an increase in porosity with dilation afterwards is apparent. This however is anticipated in view of results presented in Figures 8.2 to 8.13.

It is worthwhile to reflect on the changes of permeability with volumetric strain during the initial phase of volumetric contraction and then during the dilation phase.

8.3.1 Absolute permeability change during contraction

Permeability test results in Figures 8.2 to 8.17 show that at the beginning of triaxial shear, when specimens experience contraction, there is almost no change in the absolute permeability. Figures 8.18 to 8.20 show the variation of absolute permeability of McMurray Formation oil sand when it was undergoing contraction. The permeability changes were insignificant. Other researchers have also reported similar results. It shows that the permeability reduction due to volume decrease is neutralized by the effects of shear displacement.

Mori and Tamura (1986) using triaxial compression tests investigated the relationship between the permeability and the dilatancy of medium-dense sands stabilized by chemical grout. They reported that the permeability of Toyoura sand specimens, a uniform sand with a grain size of 0.11 to 0.25 mm, similar to that of the oil sand used in this study, does not increase excessively as long as dilatancy does not occur. They observed that the coefficient of permeability begins to increase only when the axial strain is more than 2% which corresponds to the start of dilation in their tests. Mori and Tamura data show that in fact permeability does not change much when the specimen is experiencing contraction in the beginning of triaxial shear. This indicates that the development of flow channels caused by shearing and the volume contraction cancel each other at this stage. Fabric changes associated with shear distortion resulting in flow path and connectivity enhancement are critical factors which affect permeability. The onset of permeability increase, which is relatively abrupt, indicates that some level of path connectivity must be

attained before flow enhancement. Their data show that in the case of dense sands, the large dilation results in permeability enhancement. The volume increase from dilation has the effect of widening the flow paths rather than increasing connectivity, which is more shear related.

Also Mori and Tamura (1986) reported that in the case of Soma I and II sand specimens, both of which have larger grain size than Toyoura sand, the permeability increased significantly during shear even where the volumetric strain is contractive. It was therefore deduced that not only dilatancy but also grain size influences the development of new flow channels caused by shearing and subsequent changes in the permeability.

8.3.2 Absolute permeability change during dilation

The start of dilation is defined as the beginning of volume increase in the specimen. This is often after the specimen has experienced some reduction in the volume. Therefore dilation starts before the specimen reaches its original volume. Figures 8.21 to 8.23 show the variation of absolute permeability with volumetric strain from the start of dilation. As is expected the absolute permeability increases with an increase in the volume of the specimen. For a volumetric strain of 4% the absolute permeability of horizontal cores and reconstituted specimens has increased 50%, while with the same amount of volumetric strain, vertical cores show a permeability increase of 100%.

The triaxial test was continued beyond this volumetric strain, however due to the problem of fines migration there was an impediment to the further increase of absolute permeability in the later stages of the test. Chalaturnyk (1996) based on field measurements reported a maximum volumetric strain of 2.5% within the reservoir, as a result of the SAGD process. Therefore only the relevant portion of test results has been shown in Figures 8.21 to 8.23.

A simple relation for the prediction of changes in the absolute permeability during dilation is presented in Section 8.5.

8.4 Empirical correlations

Bear (1972) has provided a review of the different models that have been used to represent flow through porous media (Rajani 1988). The models cited by Bear are essentially classified into four different categories:

- capillary tube models
- fissure models
- hydraulic radius models and
- resistance to flow models.

All these models basically describe the different nature of flow in a real soil matrix. Rajani (1988) noted that all the different expressions for permeability could be expressed in the form:

$$K = f(n) \ g(s) \ D_s^2 = f(n) \ C \ D_s^2 = f(n) \ \bar{C}$$

[8.5]

where $g(s)$ is a constant C that is a function of the particle shape and pore shape, $f(n)$ is a function of porosity (packing characteristics) of the soil matrix and D_s is the mean size of the solid particles. The constant $\bar{C}$ incorporates the shape factor C and mean particle size D_s.

Rajani (1988) suggested a general relationship for the porosity function $f(n)$ with the form:

$$f(n) = \frac{n^a}{(1-n)^b} = \frac{e^a}{(1+e)^{a-b}}$$

[8.6]

where n is the porosity and is related to the void ratio e by $n = e/(1+e)$. Thus the following general equation for absolute permeability is defined:

$$K = C \ D_s^2 \ \frac{n^a}{(1-n)^b} = \bar{C} \ \frac{n^a}{(1-n)^b}$$

[8.7]

in which a and b are constants to be determined from experimental data. If $a = 3$ and $b = 2$ then Equation 8.7 will lead to the Kozeny-Carman equation:

$$K = \frac{C \ n^3 \ D_s^2}{(1-n)^2}$$

[8.8]

The Kozeny-Carman relation is popular and has been found particularly, applicable for sandy and silty soils. Carman (1939) suggested a value of $C = 1/180$ for uniform spherical particles. D_s, the mean particle size, is 0.155 mm for the oil sand tested. The resulting correlation is plotted in Figure 8.1. It overestimates the permeability values for oil sand. It is believed that Kozeny-Carman relation works better in a higher range of porosities (Rajani 1988).

Similarly, substituting $a = 2$ and $b = 1$ will lead to the relation suggested by Rumer and Drinker (1966). Now if we assume $a = b = B$ and $\bar{C} = A$ then Equation 8.7 will yield the following equation:

$$K = A \ e^B$$

[8.9]

This equation was proposed by Chardabellas as given by Kezdi (1974). The constant A represents the absolute permeability at a void ratio of 1 and shows the order of magnitude of K. The constant B is indicative of the rate of change of K with the change of e. B has values ranging from 2 to 5. Figure 8.1 shows the Chardabellas relation (Equation 8.9) for the oil sand for B values of 2 and of 5. The absolute permeability, A, at a void ratio of 1 or porosity of 50% is found with the use of the Kozeny-Carman equation (Equation 8.8). The correlation for $B = 5$ is better, however, it still somewhat overestimates the value of initial absolute permeability.

Previous researchers have tried to improve the prediction of this empirical correlation by adjusting the constants in the equations (Rajani 1988, Oldakowski 1994). This has been done mainly by performing regression analysis procedures on the permeability test results on a particular sand. However, in many instances, as in the case of McMurray Formation oil sand, initial absolute permeability can vary because of variation in geological facies. It is thus more important to have a relation describing the changes in the initial permeability when the material is going through changes in pore pressure and stress. In the following section, the derivation of an equation which describes the change in the original permeability rather than estimating its initial value is presented.

8.5 A simple relation for change in absolute permeability

It is recognized that in sandy soils porosity is the major factor controlling the permeability. In analytical methods, however, it is desirable that the volumetric strain instead of the porosity is used to directly calculate the changes in the permeability. The relation between porosity and volumetric strain is defined in the following:

The original porosity n_1 is defined as:

$$n_1 = \frac{V - V_S}{V} \qquad [8.10]$$

where V is the total volume of sand and V_S is the volume of solids. If there is a volume change of ΔV, then the new porosity n_2 is defined as:

$$n_2 = \frac{(V + \Delta V) - V_S}{(V + \Delta V)} \qquad [8.11]$$

the volumetric strain ε_v is defined as:

$$\varepsilon_v = \Delta V / V \qquad [8.12]$$

which leads to:

$$\Delta V = \varepsilon_v V \tag{8.13}$$

here for simplicity an increase in volume (dilation) is assumed to be positive. Substituting Equation 8.13 into Equation 8.11 will result:

$$n_2 = \frac{\varepsilon_v + n_1}{1 + \varepsilon_v} \tag{8.14}$$

Assuming the initial and current absolute permeabilities to be K_1 and K_2 respectively, the ratio of the new to original permeability is given by:

$$\frac{K_2}{K_1} = \frac{n_2^a}{(1 - n_2)^b} \times \frac{(1 - n_1)^b}{n_1^a} \tag{8.15}$$

Now by substituting Equation 8.14 into Equation 8.15 one can write:

$$\frac{K_2}{K_1} = \frac{\left(\dfrac{\varepsilon_v + n_1}{1 + \varepsilon_v}\right)^a}{\left[1 - \dfrac{\varepsilon_v + n_1}{1 + \varepsilon_v}\right]^b} \times \frac{(1 - n_1)^b}{n_1^a} \tag{8.16}$$

$$= \frac{(\varepsilon_v + n_1)^a}{(1 + \varepsilon_v)^a \dfrac{(1 - n_1)^b}{(1 + \varepsilon_v)^b}} \times \frac{(1 - n_1)^b}{n_1^a}$$

$$= \frac{(\varepsilon_v + n_1)^a}{(1 + \varepsilon_v)^{a - b} n_1^a}$$

$$= \frac{\left(1 + \dfrac{\varepsilon_v}{n_1}\right)^a}{(1 + \varepsilon_v)^{a - b}}$$

If the Kozeny-Carman values of $a = 3$ and $b = 2$ are substituted in the Equation 8.16, the resulting equation is:

$$\frac{K_2}{K_1} = \frac{\left(1 + \dfrac{\varepsilon_v}{n_1}\right)^3}{1 + \varepsilon_v} \tag{8.17}$$

Tortike and Farouq Ali (1991) suggested this equation as a first attempt at systematically incorporating volumetric strain into the changes of the absolute permeability.

Taking the natural logarithm on both sides of Equation 8.16 will result in:

$$Ln \frac{K_2}{K_1} = a \, Ln \left(1 + \frac{\varepsilon_v}{n_1}\right) - (a - b) \, Ln \left(1 + \varepsilon_v\right) \qquad [8.18]$$

Expressing the logarithmic terms in Taylor's series form:

$$Ln \frac{K_2}{K_1} = a \left[\frac{\varepsilon_v}{n_1} - \frac{1}{2}\left(\frac{\varepsilon_v}{n_1}\right)^2 + \frac{1}{3}\left(\frac{\varepsilon_v}{n_1}\right)^3 \right]$$

$$- (a - b) \left[\varepsilon_v - \frac{1}{2}\varepsilon_v^2 + \frac{1}{3}\varepsilon_v^3 \right] \qquad [8.19]$$

As the value of volumetric strain is fairly small, the 2nd, 3rd and higher order terms can safely be neglected. This leads to:

$$Ln \frac{K_2}{K_1} = a \frac{\varepsilon_v}{n_1} - (a - b)\varepsilon_v$$

$$= \left(\frac{a}{n_1} - a + b\right)\varepsilon_v$$

$$= \left[\frac{(1 - n_1)a + b \, n_1}{n_1}\right] \varepsilon_v \qquad [8.20]$$

Considering that the terms in bracket in Equation 8.20 are constants, the equation could be rewritten as:

$$Ln \frac{K_2}{K_1} = C_{n_1} \varepsilon_v \qquad [8.21]$$

Equation 8.21 is a linear semi-logarithmic expression. Most of available studies (Muskat 1937, Taylor 1948, Lambe and Whitman 1979) also describe a linear relationship between porosity and logarithm of hydraulic conductivity. The term C_{n1} in Equation 8.21 is a function of initial porosity of the formation.

By substituting the Kozeny-Carman values of $a = 3$ and $b = 2$ in Equation 8.20:

$$Ln \frac{K_2}{K_1} = \left(\frac{3}{n_1} - 1 \right) \varepsilon_v$$

[8.22]

Similarly by using the Chardabellas terms of $a = b = B$ in Equation 8.20:

$$Ln \frac{K_2}{K_1} = \frac{B}{n_1} \varepsilon_v$$

[8.23]

By choosing $B = 5$, Equation 8.23 yields:

$$Ln \frac{K_2}{K_1} = \frac{5}{n_1} \varepsilon_v$$

[8.24]

The interesting feature of Equation 8.23 is that it clearly shows that the rate of change in the absolute permeability is inversely proportional to the initial porosity. Other researchers (Oldakowski 1994) also have reported that smaller initial porosities lead to greater changes in the permeability.

It has been shown above that different correlations for permeability are in fact a variation of a general relationship (Equation 8.7) and that this can be reduced to a simple relation described by Equation 8.21. This equation describes the changes in the initial permeability with volumetric strain.

8.6 Analysis of experimental results

Figures 8.21 to 8.23 show the variation in the absolute permeability with changes in the volumetric strain from the start of dilation. With Equation 8.21 in mind a linear regression is applied to the test results and the obtained values of C_{n1} are reported in Figures 8.21 to 8.23 and Table 8.1. Plots of Equation 8.22 (Kozeny-Carman) and Equation 8.23 (Chardabellas, for both $B = 2$ and 5) are also shown on these figures. The corresponding values of C_{n1} are presented in Table 8.1.

It is seen that Equation 8.22 (Kozeny-Carman) and Equation 8.23 (Chardabellas) with $B = 2$ provide a good agreement with the experimental results for the horizontal core and reconstituted specimens while Equation 8.24 (Chardabellas) with $B = 5$ is close to the experimental results for the vertical core specimens. Since vertical core specimens display a much higher dilation (Figure 7.13) than horizontal core and reconstituted specimens it could be concluded that the relation based on the Chardabellas equation with $B = 5$ is more appropriate for material with a very high dilation rate while the

Kozeny-Carman relation and Chardabellas equation with $B = 2$ is suitable for dense sands with less but still significant dilative behavior.

It is apparent that by choosing the appropriate B value, between 2 to 5, the Chardabellas equation is capable of covering material behavior between these two cases.

With respect to these findings and discussion in Section 8.3.1, an idealized model for changes in the absolute permeability of McMurray Formation oil sand is presented in Figure 8.24. Based on this model new values of absolute permeability, K_2, can be calculated from the initial value of absolute permeability, K_1, and the measured rate of volumetric strain. Thus an accurate prediction of volumetric strain is very important in reservoir modeling. Laboratory tests to determine volumetric strain during shear require high quality undisturbed core and closely controlled experimental procedures.

8.7 Summary

- Reservoir modeling to estimate bitumen recovery by SAGD processes in oil sands is highly dependent on the absolute permeability values used in the modeling. It is essential to specify permeability changes throughout the process.

- Special stress path triaxial permeability testing equipment was developed (Chapter 2) and a series of triaxial permeability tests at low confining pressures have been performed. The changes in the permeability of oil sand specimens have been measured when they were undergoing changes in stress and pore pressure simulating SAGD conditions.

- The results of permeability tests were analyzed during the initial volumetric contraction and during the subsequent volumetric dilation. It was observed that when oil sand specimens experienced contraction, there was almost no change in the absolute permeability. It was assumed that permeability enhancement due to development of flow channels caused by shearing was taken back due to permeability reduction from volumetric contraction.

- A simple relation for the prediction of changes in the absolute permeability during dilation is presented. Emphasis is made on describing the changes in the initial permeability while the oil sand core is undergoing changes in applied stress and pore pressure. The proposed relation is a linear semi-logarithmic expression and includes a coefficient C_{n1}. Based on this equation values of absolute permeability can be obtained from its initial value and the volumetric strain.

- An appropriate value for C_{n1} has to be picked. Values of C_{n1} derived based on the Chardabellas equation with $B = 5$ is more appropriate for material with a very high dilation rate (vertical cores) while the Kozeny-Carman relation and Chardabellas

equation with $B = 2$ are suitable for dense sands with less but still significant dilative behavior (horizontal cores and reconstituted specimens). It is apparent that the Chardabellas equation is capable of covering material behavior between these two cases.

- An idealized simple model for obtaining the absolute permeability during shear induced dilation was suggested. It is apparent that having an accurate value for the volumetric strain is necessary to obtain a good estimate of the changes in the absolute permeability.

- It has been shown that smaller initial porosities lead to greater changes in permeability.

Table 8.1 Values of C_{n1} for McMurray Formation oil sand

Specimen Type	C_{n1}			
	Experiments	Kozeny-Carman	Chardabellas	
			$B = 2$	$B = 5$
Vertical cores	17.48	7.86	5.9	14.76
Horizontal cores	9.07	7.9	5.83	14.84
Reconstituted specimens	8.26	7.75	5.83	14.58
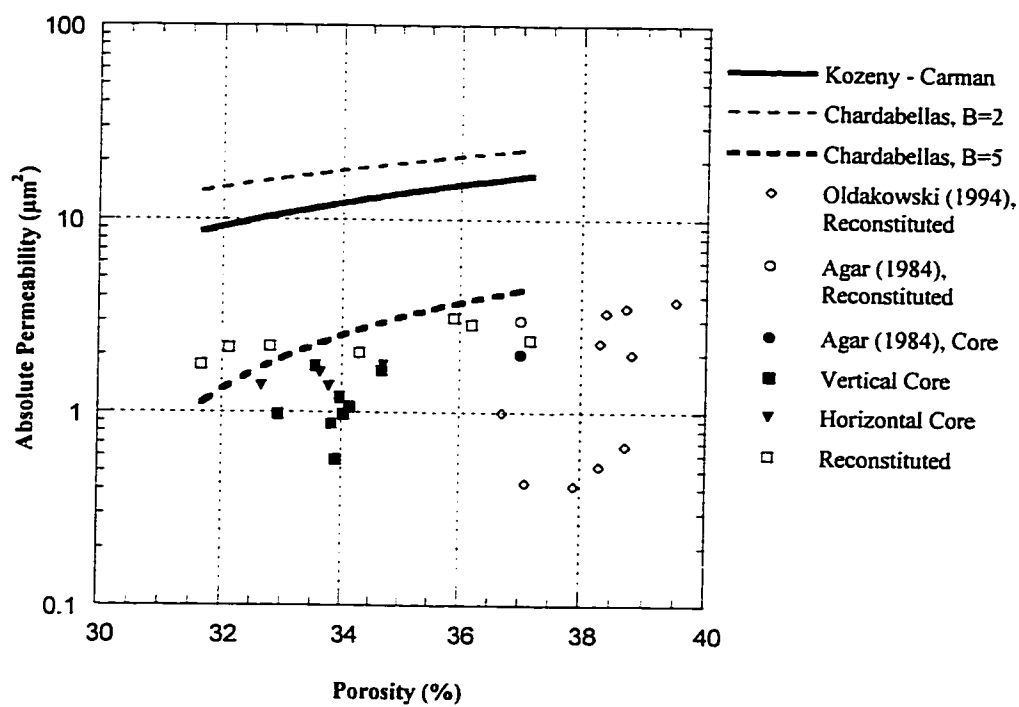
Figure 8.1 Initial absolute permeability of McMurray Formation oil sand
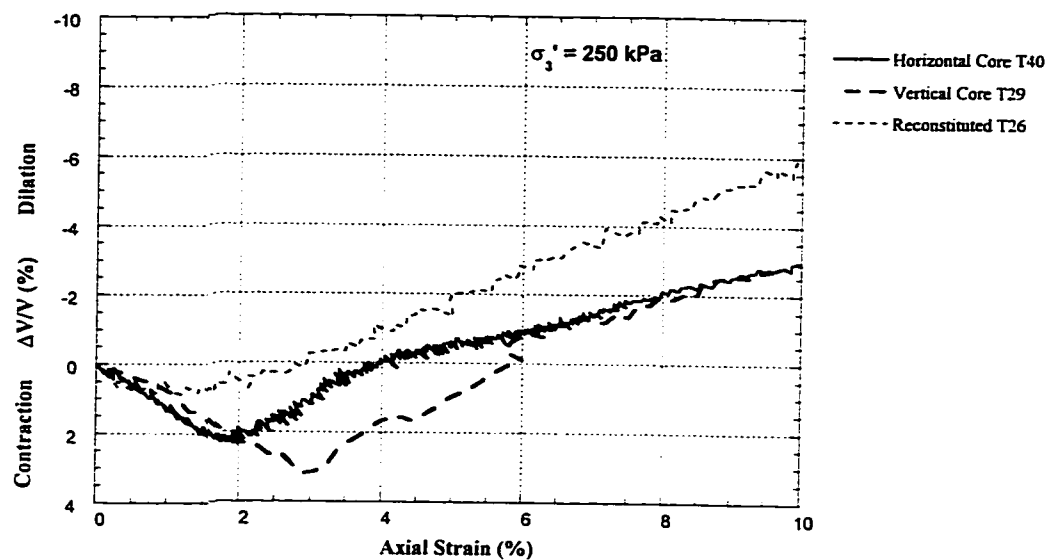
Figure 8.2 Volumetric strain versus axial strain
Stress Path 1 (σ_3' = 250 kPa)
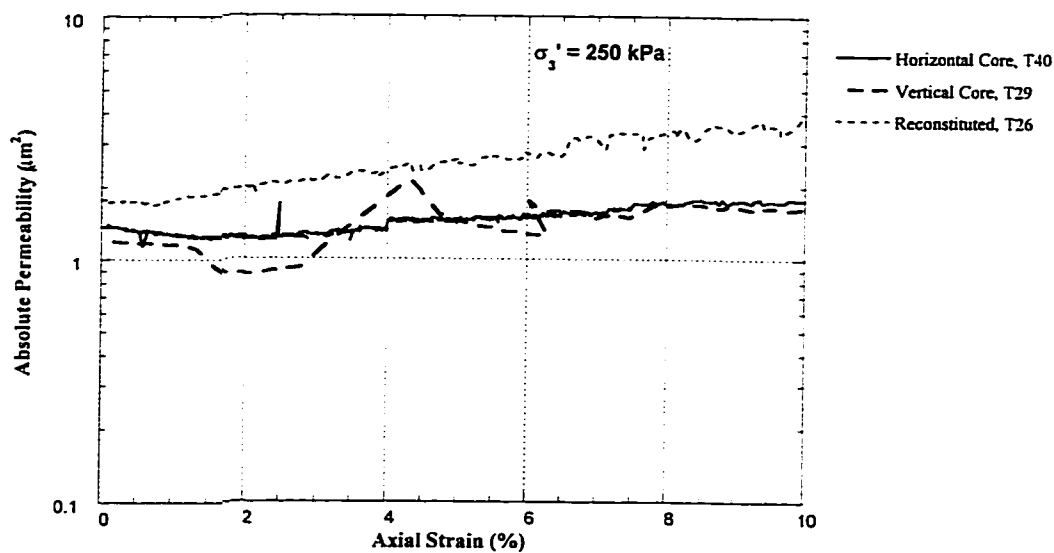
Figure 8.3 Absolute permeability versus axial strain
**Stress Path 1 (σ_3' = 250 kPa)**
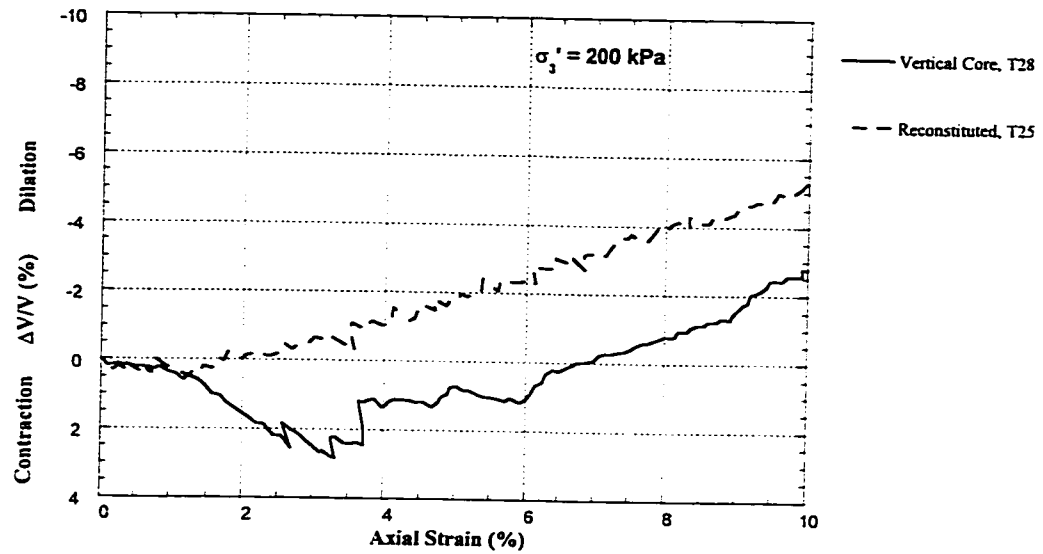
Figure 8.4 Volumetric strain versus axial strain Stress Path 1 (σ_3' = 200 kPa)
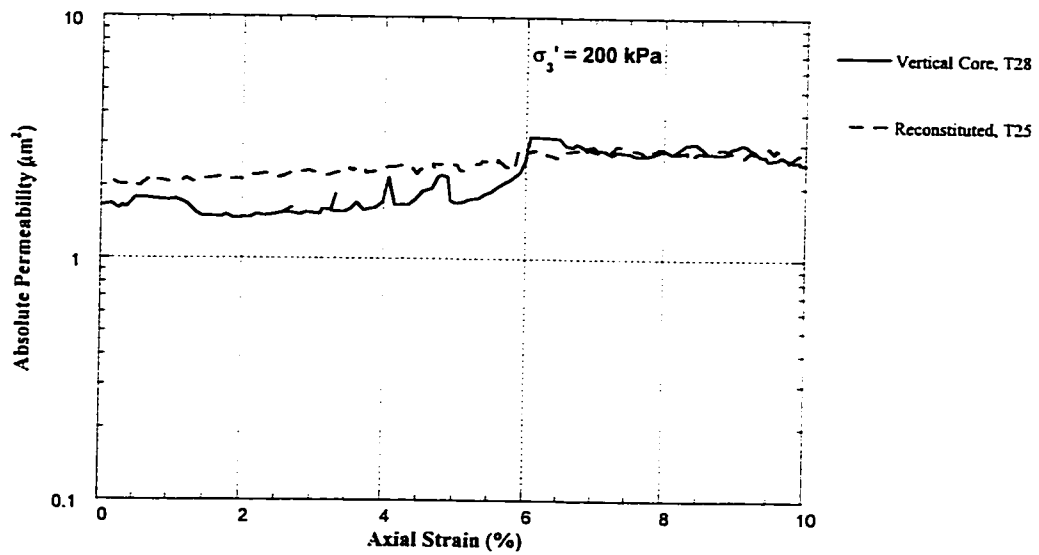
Figure 8.5 Absolute permeability versus axial strain Stress Path 1 (σ_3' = 200 kPa)
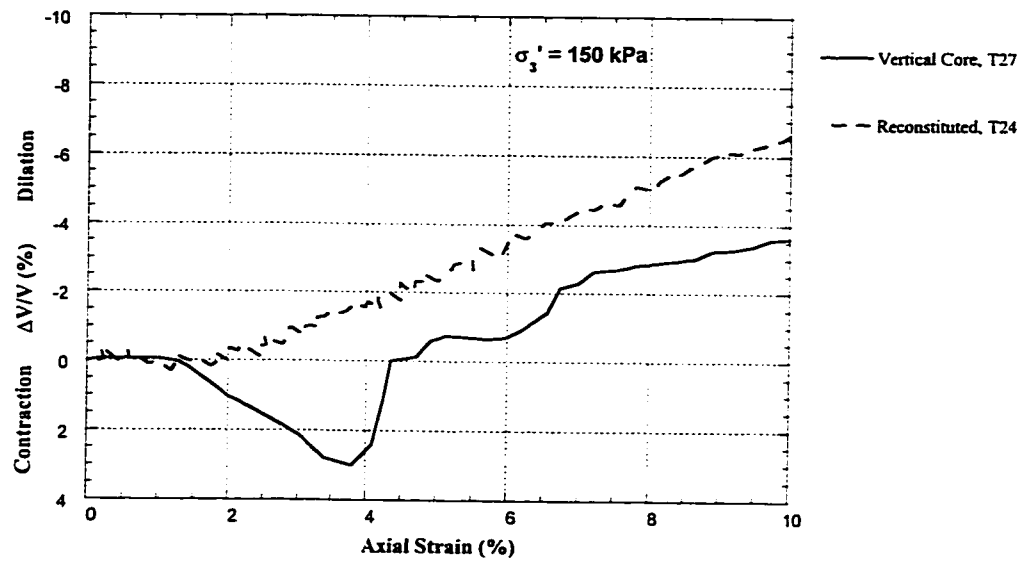
**Figure 8.6 Volumetric strain versus axial strain
Stress Path 1 ($\sigma_3' = 150$ kPa)**
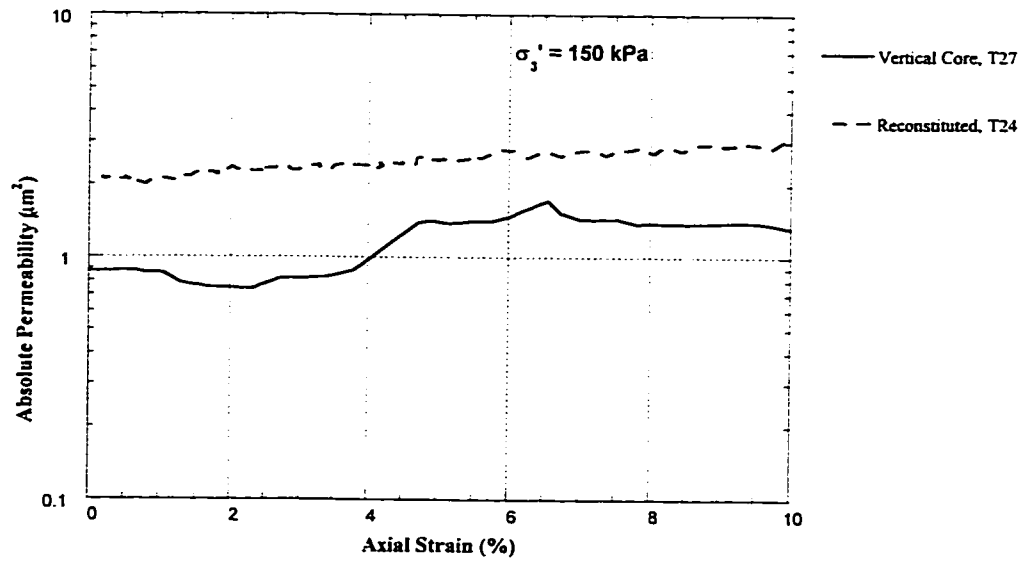
**Figure 8.7 Absolute permeability versus axial strain
Stress Path 1 ($\sigma_3' = 150$ kPa)**
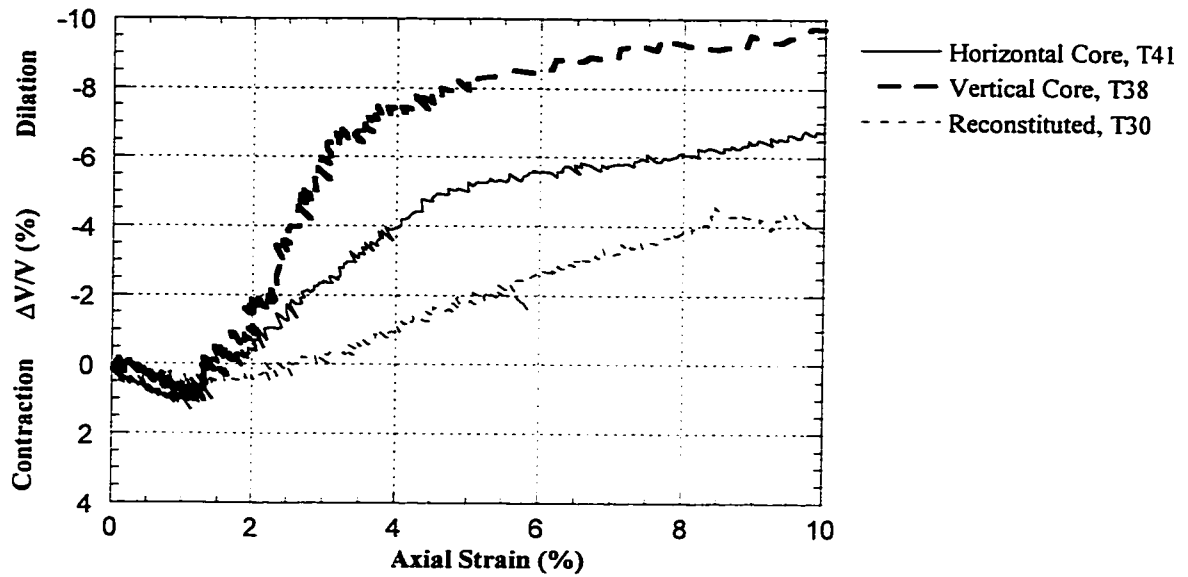
**Figure 8.8 Volumetric strain versus axial strain
Stress Path 2 (Initial σ_3' = 250 kPa)**
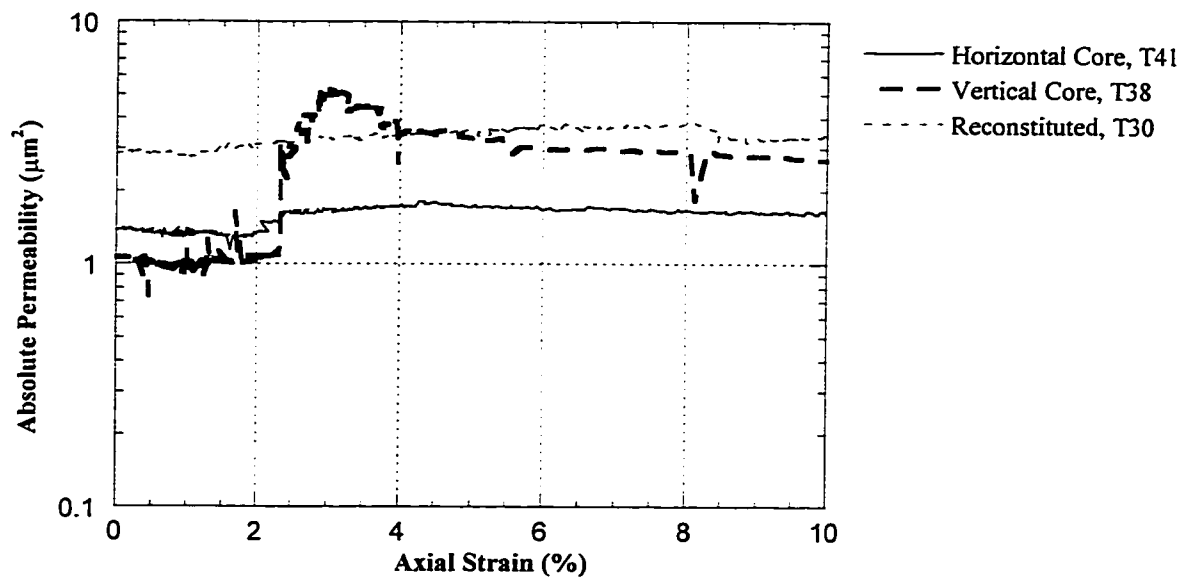
**Figure 8.9 Absolute permeability versus axial strain
Stress Path 2 (Initial σ_3' = 250 kPa)**
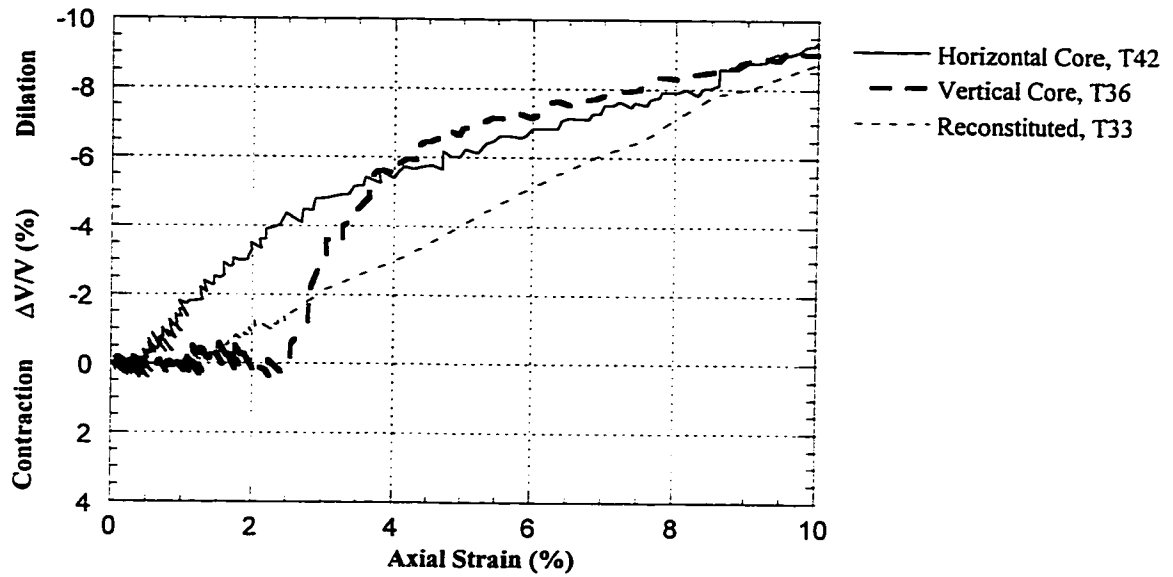
Figure 8.10 Volumetric strain versus axial strain
Stress Path 3 (Initial σ_3' = 250 kPa)
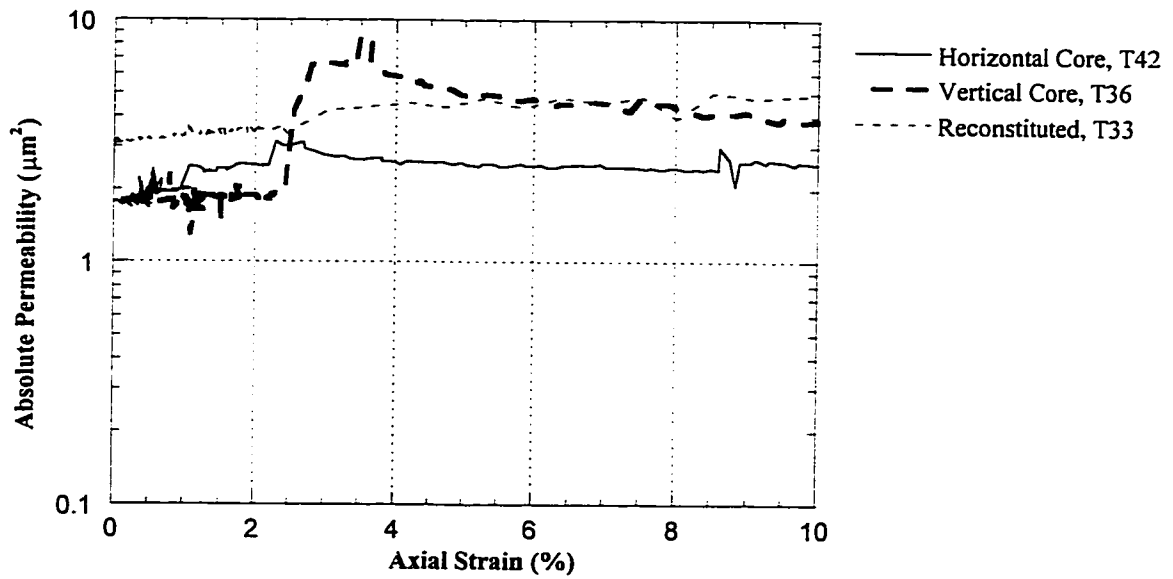
Figure 8.11 Absolute permeability versus axial strain
Stress Path 3 (Initial σ_3' = 250 kPa)
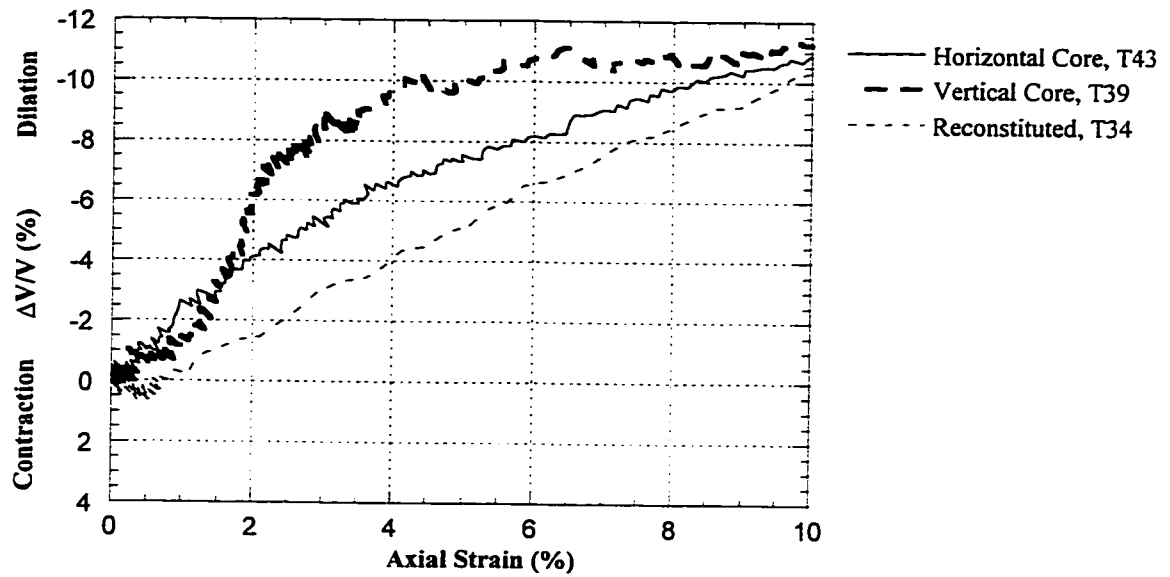
Figure 8.12 Volumetric strain versus axial strain
Stress Path 4 (Initial σ_3' = 250 kPa)
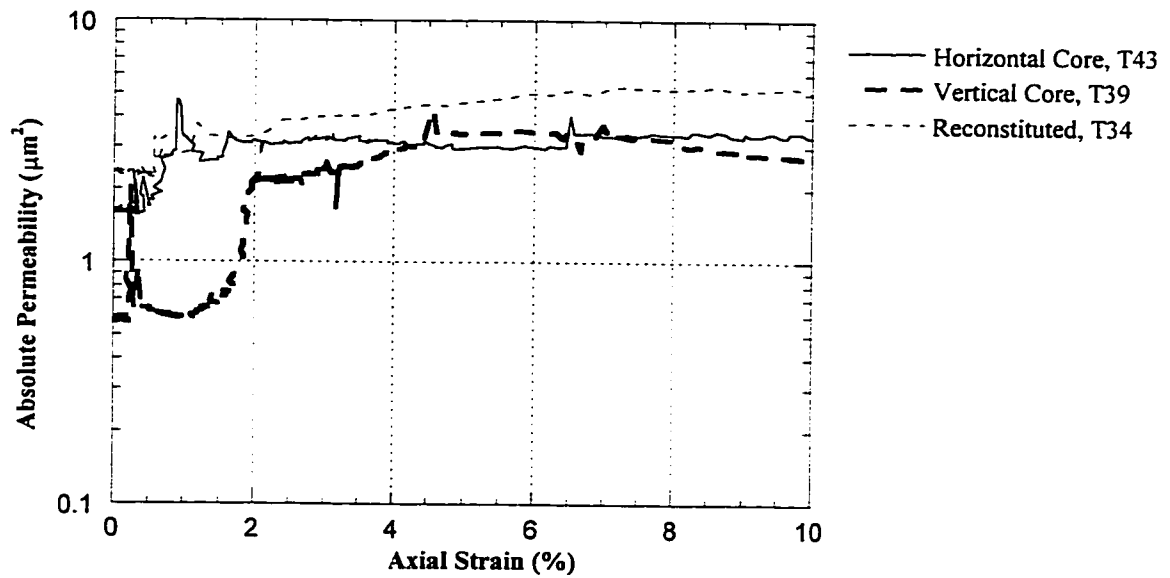
Figure 8.13 Absolute permeability versus axial strain
Stress Path 4 (Initial σ_3' = 250 kPa)
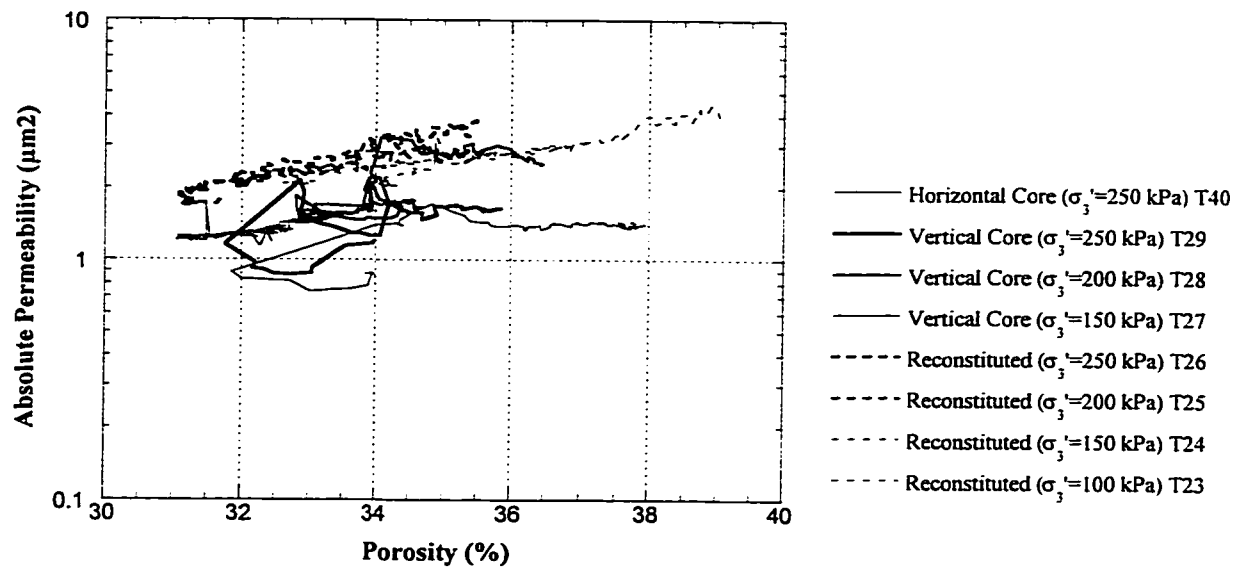
Fig 8.14 Absolute permeability versus porosity
Stress Path 1
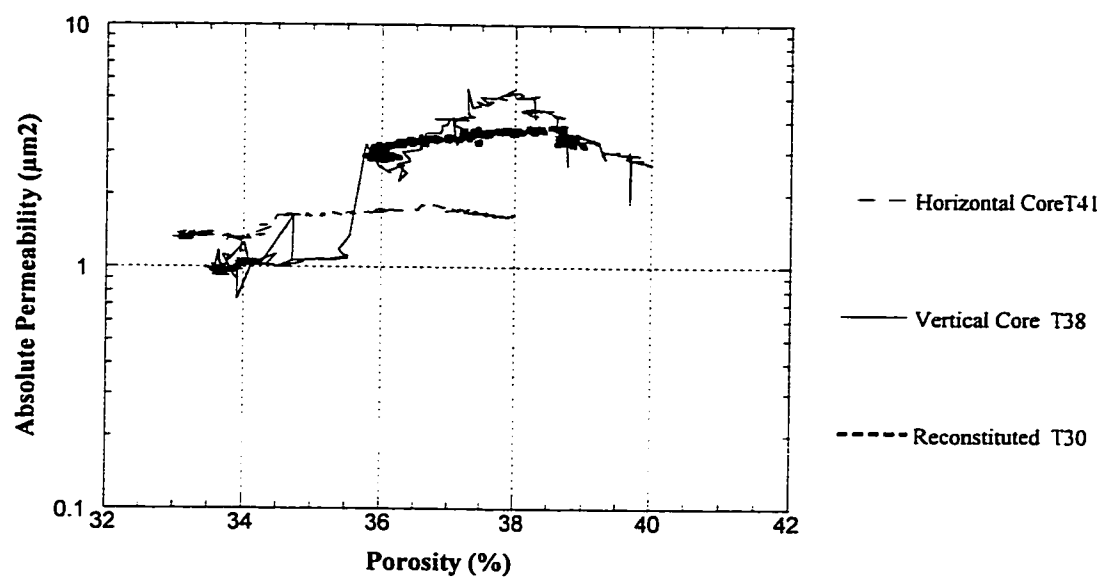
**Fig 8.15 Absolute permeability versus porosity
Stress Path 2**
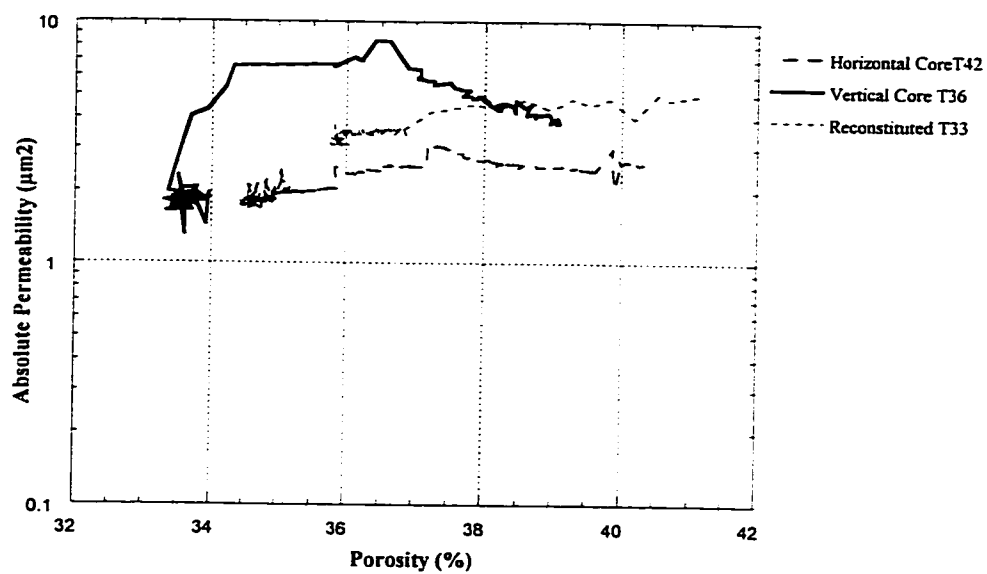
Fig 8.16 Absolute permeability versus porosity
Stress Path 3
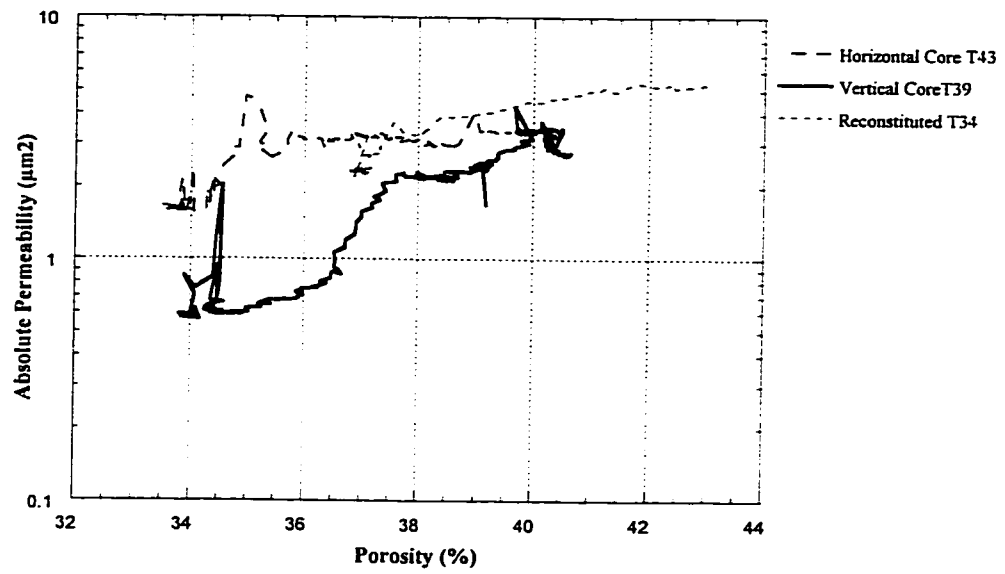
Fig 8.17 Absolute permeability versus porosity
Stress Path 4
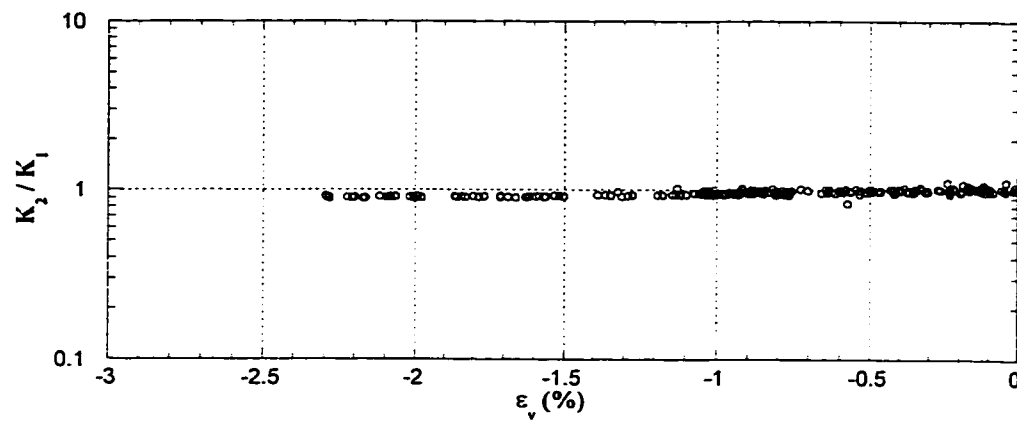
Figure 8.18 Variation of the absolute permeability in contraction Horizontal core specimens
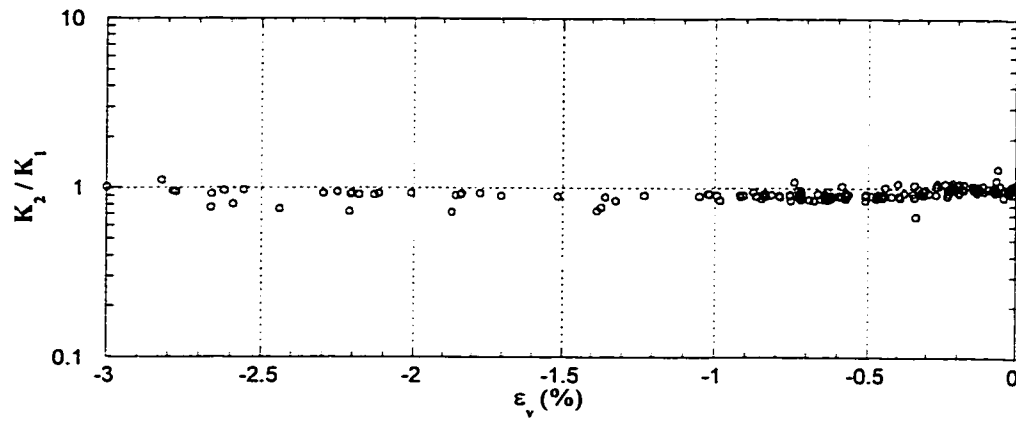
Figure 8.19 Variation of the absolute permeability in contraction Vertical core specimens
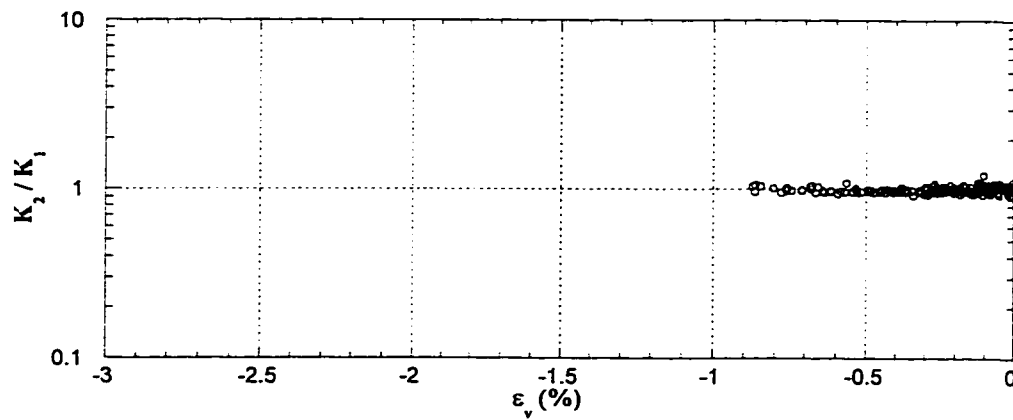
Figure 8.20 Variation of the absolute permeability in contraction Reconstituted specimens
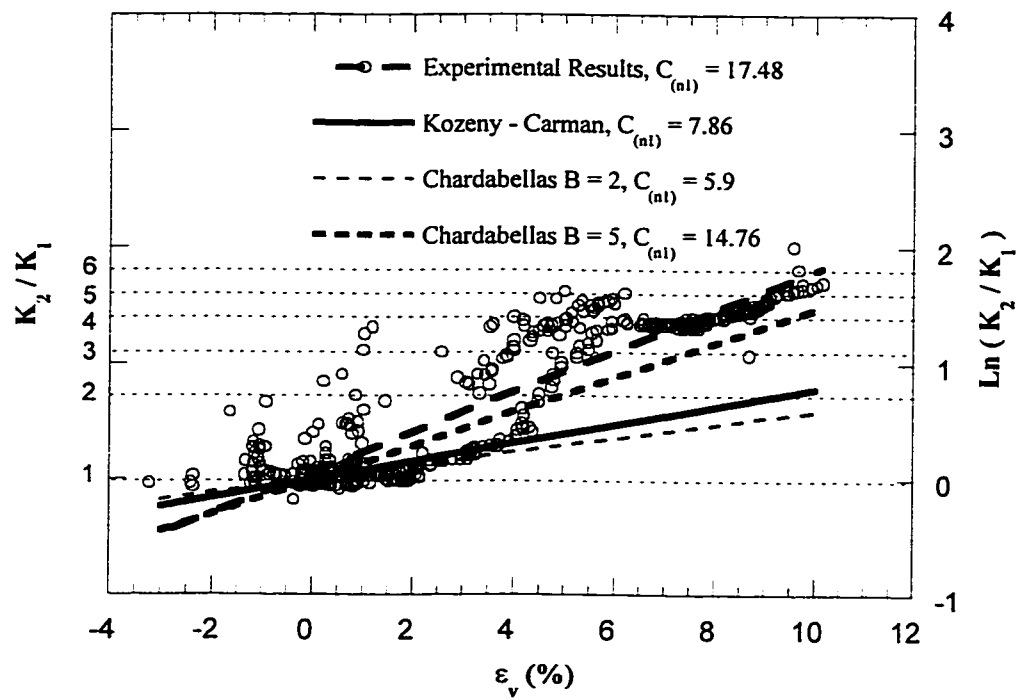
Figure 8.21 Variation of absolute permeability in dilation
Vertical core specimens, average porosity = 33.9%
(Dilation is assumed positive)
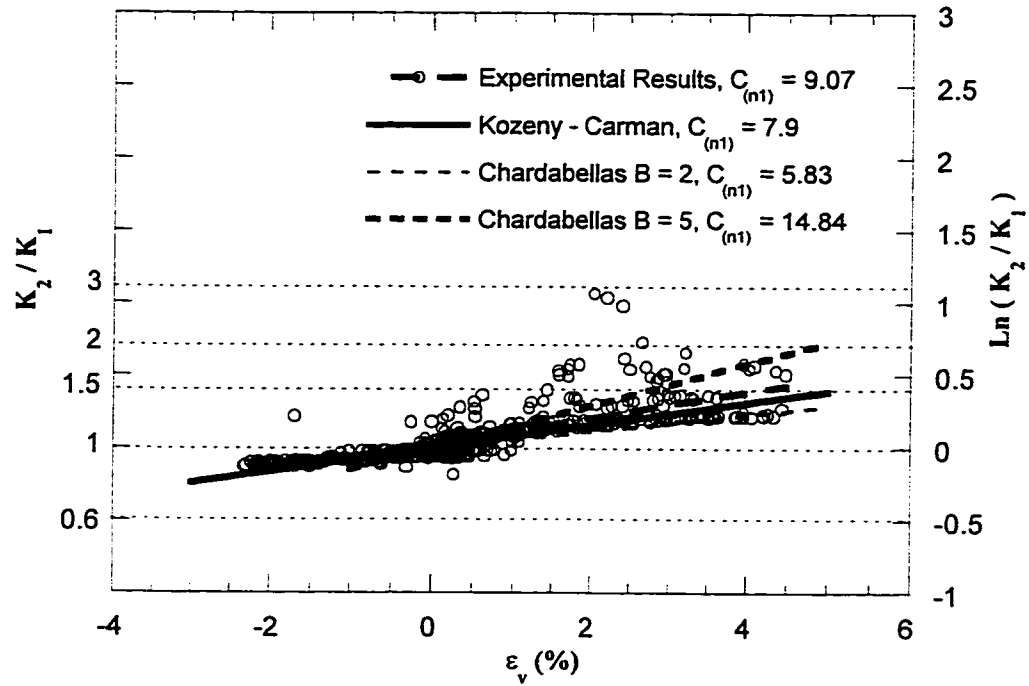
**Figure 8.22 Variation of absolute permeability in dilation
Horizontal core specimens, average porosity = 33.7%
(Dilation is assumed positive)**
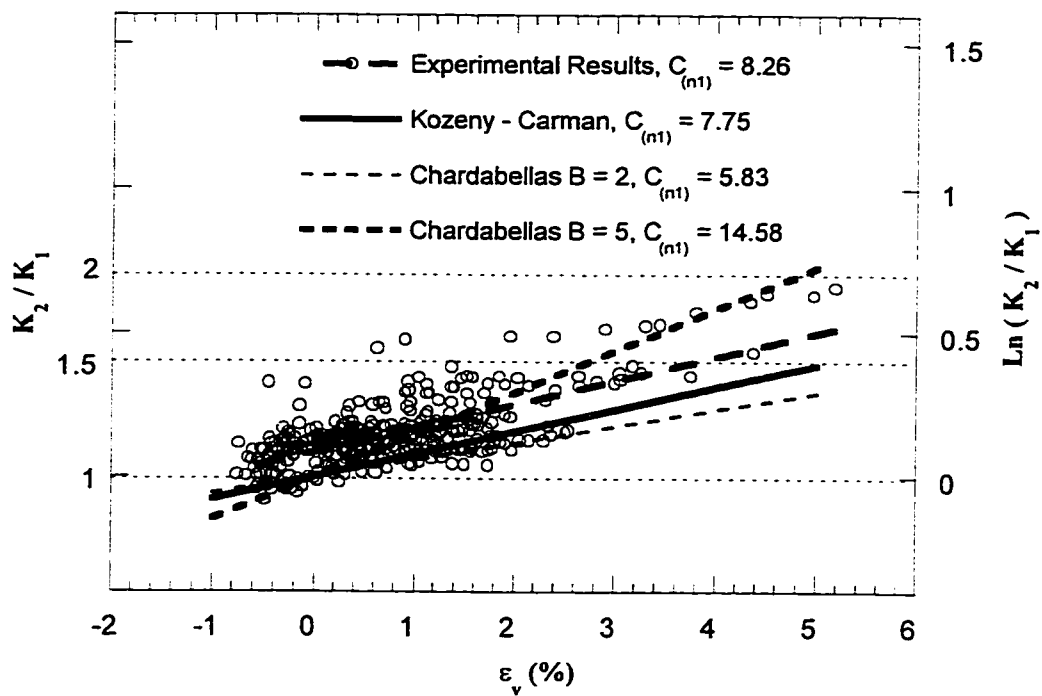
Figure 8.23 Variation of absolute permeability in dilation
Reconstituted specimens, average porosity = 34.3%
(Dilation is assumed positive)
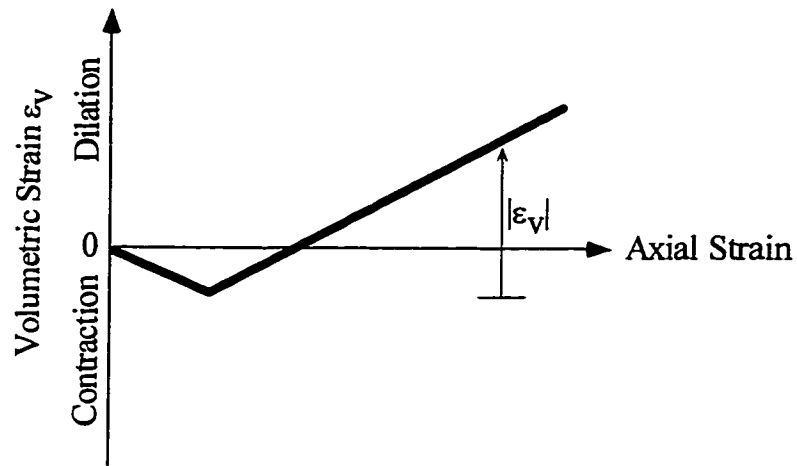
(a) Typical volumetric strain behavior
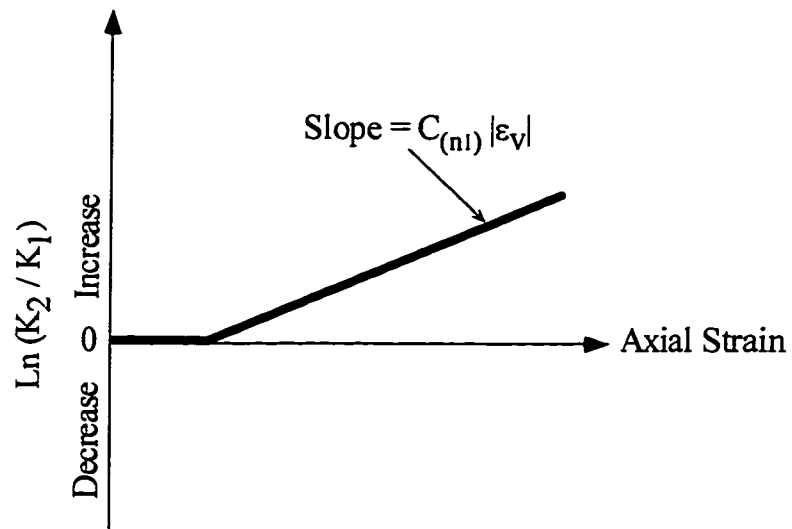
(b) Corresponding changes in the absolute permeability

**Figure 8.24 Suggested variation in the absolute permeability
of McMurray Formation oil sand during shear**

CHAPTER 9   CONCLUSIONS AND RECOMMENDATIONS

9.1 Summary

Experimental study of the geomechanical behavior of oil sand, specifically, the change in absolute permeability during shear at low confining pressures was the primary objective of this thesis. Specimens obtained from a block of bitumen-free oil sand along with reconstituted specimens were used in this research program. This block sample of bitumen-free sand was taken along the banks of the High Hill River, approximately 60 kilometers east of Fort McMurray, Alberta. Since this block of locked sand is bitumen-free, no disturbance to the fabric of the cored specimens was induced by having to clean and extract the bitumen. The fabric characteristics of oil sand specimens obtained from this block sample were also studied with the use of a scanning electron microscope.

The following sections summarize different components of this research.

9.1.1 Triaxial permeability testing of oil sand

- In order to improve the comparison of results between reconstituted and undisturbed specimens, a goal of this study was to prepare reconstituted sand specimens as dense as possible. To attain this goal different methods of preparing reconstituted triaxial sand specimens were evaluated. They included dry tamping, moist tamping, water pluviation, slurry deposition and wet vibration method. The wet vibration method was successful in producing dense uniform sand specimens. New procedures were developed for the wet vibration method. Special modifications were made to produce a fully saturated specimen.

- A new computer controlled stress path triaxial testing system with the capability of continuous measurement of permeability was developed for this study. For this triaxial apparatus, the desired stress paths could be implemented easily with most stress paths designed to follow the steam assisted gravity drainage (SAGD) process. The testing program consisted of stress-strain, strength and permeability tests.

- Measuring permeability during triaxial shear requires that the specimen deforms uniformly to ensure a representative measure of permeability. To achieve this condition, lubricated end platens were used in this study. Knowing that flow inside a cylindrical specimen with lubricated end platens was not rectilinear, special equations were developed for solving this problem under these boundary conditions.

9.1.2 Fabric of oil sand

- Oil sand is composed of a fabric of discrete particles whose shape and orientation are important factors in controlling its mechanical properties. In order to study the fabric of oil sand, images of bitumen-free, vertically and horizontally oriented oil sand specimens were analyzed with the use of a scanning electron microscope (SEM). As expected, the diagenetic interpenetrative structure of oil sand were clearly visible in the SEM images.

- Using image analysis software, the orientation of nonspherical particles were analyzed with a statistical examination of the SEM images. In vertical sections, particles had a strong preferred orientation with more particles oriented along the horizontal direction. Particles showed random orientations in the horizontal sections.

9.1.3 Geomechanical properties of oil sand

- Undisturbed specimens of McMurray Formation oil sand were tested along with reconstituted specimens. The undisturbed specimens were obtained by coring block samples both vertically and horizontally. A series of triaxial tests were performed to replicate stress path conditions associated with SAGD.

- Undisturbed specimens demonstrated higher dilation rates and higher strength than reconstituted specimens. This is due to the interlocking structure of undisturbed oil sand specimen. High density reconstituted specimens showed similar but a more ductile stress-strain behavior.

9.1.4 Numerical simulation of oil sand

- A numerical simulator, FLAC, was chosen for the numerical simulation of oil sand geomechanical behavior at low confining pressures. The intent was to illustrate a methodology in which the laboratory results could be implemented in numerical modeling of oil sands with a strain softening behavior incorporated into the constitutive model.

- Several material input functions are necessary in order to simulate the strain softening and shear dilatancy with FLAC. Results from high quality triaxial experiments were used to provide the following functions defining the relationships for tangent modulus of elasticity, E_i, maximum friction angle, ϕ'_{max}, and dilation angle, ψ.

Functions used to simulate nonlinear compressibility are:

Vertical cores: $$E_i = 460\, p_a \left(\frac{\sigma'_3}{p_a}\right)^{0.25} \quad \text{(MPa)} \qquad [9.1]$$

Horizontal cores: $\qquad E_i = 314\, p_a \left(\dfrac{\sigma'_3}{p_a}\right)^{0.6}$ (MPa) [9.2]

The functions for maximum friction angle and dilation angle are:

Vertical cores: $\qquad \phi'_{max} = 60 - 15.6\, Log\left(\dfrac{\sigma'_3}{p_a}\right)$ (Degrees) [9.3]

$$\psi = 26.6 - 17.5\, Log\left(\dfrac{\sigma'_3}{p_a}\right) \qquad \text{(Degrees)} \qquad [9.4]$$

Horizontal cores: $\qquad \phi'_{max} = 50 - 14.25\, Log\left(\dfrac{\sigma'_3}{p_a}\right)$ (Degrees) [9.5]

$$\psi = 25 - 6.6\, Log\left(\dfrac{\sigma'_3}{p_a}\right) \qquad \text{(Degrees)} \qquad [9.6]$$

- Care must be taken to ensure that the dilation angle computed from triaxial test results is derived using equations for triaxial boundary conditions. Use of plane strain assumptions will result in an error for the computed dilation angle.

- Using these material input functions, triaxial tests on undisturbed oil sand specimens were simulated with a strain softening plasticity constitutive model. Implementation of these functions in FLAC was straightforward. The simulations provided confirmation that the volumetric behavior of oil sand could be modeled.

9.1.5 Absolute permeability of oil sands

- A series of triaxial permeability tests at low confining pressures were performed. The test specimens included both vertical and horizontal undisturbed oil sand specimens and reconstituted specimens. Changes in the absolute permeability was measured when stress and pore pressure conditions simulated the steam assisted gravity drainage process.

9.2 Conclusions

The following are conclusions and recommendations regarding the stated objectives of this thesis.

9.2.1 Absolute permeability of oil sands

- The undisturbed specimens tested had initial porosities ranging from 32.7% to 34.7% with an average initial porosity of 33.8%. For these specimens the average initial absolute permeability in the vertical direction is 1.12 μm^2 and in the horizontal direction is 1.55 μm^2.

- The horizontal absolute permeability (parallel to the bedding planes), k_h was moderately higher than the vertical permeability (perpendicular to the bedding planes), k_v. The ratio of k_h to k_v was approximately 1.4. The anisotropic permeability of oil sand is therefore established. This is due to the structural anisotropy which provides flow paths that are shorter in the horizontal direction and consequently, a higher permeability.

- Absolute permeability of oil sand increased considerably during dilative shear. For a dilative volumetric strain of 2%, k_v increased 40% and k_h increased 20%. This has substantial impact on the in situ recovery process and must be considered in a reservoir simulation.

- The empirical relationships of Kozeny-Carman and Chardabellas overestimate the oil sand permeability. However when used to describes the change in the original permeability rather than estimating its absolute value, they showed a good agreement with the experimental results.

- When oil sand specimens experienced contraction at the beginning of shear, there was almost no change in the absolute permeability. This indicated that the permeability reduction due to volume decrease is neutralized by the permeability enhancement due to development of flow channels caused by shearing.

- The following relationship for the change in absolute permeability during dilation was developed:

$$Ln \frac{K_2}{K_1} = C_{n_1} \varepsilon_v \qquad [9.7]$$

Guidelines for the selection of C_{n1} were presented.

- An idealized model for the prediction of changes in the absolute permeability during shear was developed.

9.2.2 Fabric of oil sand

- The fabric characteristics of oil sand were studied with the use of a scanning electron microscope (SEM). The interpenetrative structure of the oil sand was intact, therefore it was concluded that the core specimens were undisturbed.

- The image analysis of obtained SEM images showed that the axial ratio for oil sand was between 0.68 to 0.71, showing the nonspherical grain shape of oil sand. These values fall in the typical range for natural sands mentioned by other researchers. Thus it could be concluded that the diagenetic processes have not significantly changed the overall grain shape of oil sand.

- Image analysis revealed that in vertical sections, particles had a strong preferred orientation toward the horizontal direction. Thus the inherent anisotropy of oil sand due to preferred particle orientation of particles was recognized.

9.2.3 Geomechanical properties of oil sand

- Vertical core specimens showed higher strength and dilation rates than horizontal core specimens. This is due to the preferred orientation of nonspherical particles parallel to the horizontal plane. The stress-strain behavior shows that increased shear strength and lower compressibility occurs in the direction perpendicular to the bedding plane.

- For the range of confining pressures applied in this study, failure envelopes were obtained for the specimens. Vertical core specimens showed a friction angle of 51° while horizontal cores had a friction angle of 41°.

- At an effective confining stress of 50 kPa, vertical specimens had a peak dilation angle of 32° while horizontal specimens had a peak dilation angle of 27°. At the same effective confining pressure the ratio of the tangent modulus of elasticity in the vertical direction to the tangent modulus of elasticity in the horizontal direction is 1.8.

- A noticeable contraction at the beginning of shear was observed for the core specimens. The amount of contraction decreased with the reduction in effective confining pressure. This was attributed to the specimen boundary condition, i.e. use of the lubricated end platens, which resulted in the participation of the whole volume of the specimen in shear deformation.

9.2.4 Triaxial permeability testing of oil sand

- Improper specimen boundary conditions result in an underestimation of the specimen's volumetric strain during a triaxial shear test.

- Where the flow inside a specimen is not rectilinear, special equations, derived in this study, should be used in the analysis of the permeability test. It was shown that if the solution method was not applied in the flow analysis, the resulting error in the permeability measurements could lead to an underestimation of permeability up to five times.

9.3 Recommendations for reservoir simulation

The following recommendations result from the above conclusions.

- Most reservoir models used in simulating the SAGD process do not account for the geomechanical response of oil sand and the resulting changes in the absolute permeability (Chalaturnyk 1996). A coupled or a decoupled approach should be adopted through which both fluid flow and geomechanical models are used in conducting a reservoir simulation.

- It is important that the geomechanical model simulates the dilative volumetric strain correctly. Volumetric strain is the controlling factor in changes in the absolute permeability.

- Anisotropy in strength and in dilation are integral parts of oil sand behavior and should be included in any reservoir simulation of oil sand.

9.4 Recommendations for future research

The following recommendations may be useful for future geomechanical studies of oil sands:

- Due to the continuous flow of water through the specimen during a permeability test, the specimen volume change was monitored on the cell pressure line. Measurements of the specimen volume change on a cell pressure line require several corrections and are consequently less accurate than volume change measurements made on a back pressure line. To overcome this problem a double wall triaxial cell as suggested by Bishop and Henkel (1962) could be used. The specimen in the inner wall is surrounded with mercury and its volume change during the test is monitored by observing the changes in the mercury level.

- It is recommended that additional triaxial testing be conducted to refine and confirm the relationship for the post peak changes in the friction angle with shear strain. The refinement of this relationship is vital in simulation of oil sand post peak behavior. Conventional drained compression tests are well suited for this purpose since the effective confining pressure is kept constant throughout the test.

- To confirm the actual ratio of k_h/k_v for oil sands further absolute permeability measurements are recommended on core from other sites.

- In order to reduce the problem of fines migration, tests with discrete measurement of permeability are suggested. In these tests a continuous flow through the specimen is not imposed but rather a series of short permeability tests would be conducted at

predetermined intervals. In order to monitor the changes in the permeability during shear these tests would have longer periods of shearing.

REFERENCES

Agar, J. R., 1984. Geotechnical behavior of oil sands at elevated temperatures and pressures. Ph.D. dissertation, Department of Civil Engineering, University of Alberta, 906 p.

Agar, J.G., Morgenstern, N.R. and Scott, J.D. 1987. Shear strength and stress-strain behaviour of Athabasca oil sands at elevated temperatures and pressures. Canadian Geotechnical Journal, Vol. 24, No. 1, pp. 1-10.

Anderson, S.H., Peyton, R.L., Wigger, J.W. and Gentzer, C.J. 1992. Cautionary notes for the automated analysis of soil pore-space image. Geoderma, 53, pp. 399-415.

Arthur, J.R.F. and Menzies, B.K. 1972. Inherent anisotropy in a sand. Geotechnique, 22, NO. 1, pp. 115-128.

Arthur, J.R.F. and Phillips, A. B. 1975. Homogeneous and layered sand in triaxial compression. Geotechnique, 25, NO. 4, pp. 799-815.

Barsvary, A. K., Klym, T. W. and Franklin J. A. 1980. Lists of terms, symbols, and recommended SI units and multiples for geotechnical engineering. Canadian Geotechnical Journal, Vol. 17, pp. 89-96.

Bear, J. 1972. Dynamics of fluids in porous media. American Elsevier Publishing Co., Inc., New York.

Bishop, A.W. and Henkel, D.J. 1962. The measurement of soil properties in the triaxial test. Edward Arnold Pub. LTD.

Bishop, A.W. 1973. The influence of an undrained change in stress on the pore pressure in porous media of low compressibility. Geotechnique, Vol. 23, No. 3, pp. 435-442.

Bishop, A. W. and Wesley, L.D. 1975. A hydraulic triaxial apparatus for controlled stress path testing. Geotechnique, 25, No. 4, pp. 657-670.
London.

Black, D. K. and Lee, K. L. 1973. Saturating laboratory samples by back pressure. Proceedings Paper 9484. Journal of the Soil Mechanics and Foundations Division, Proceedings of the American Society of Civil Engineers, Vol. 99, No. SM1, pp. 75-93.

Bolton, M.D. 1986. The strength and dilatancy of sands. Geotechnique, Vol. 36, No. 1, pp. 65-78.

Brewer, R. 1964. Fabric and mineral analysis of soils. John Wiley and Sons, Inc., pp. 129-158.

Byrne, P. M., Cheung, H. and Yan, L. 1987. Soil parameters for deformation analysis of sand masses. Can. Geotech. Journal, Vol. 24, No. 3, pp. 366-376.

Carman, P.C. 1939, Permeability of saturated sands, soils and clays. J. Agr. Sci. 29. pp. 262-273.

Casagrande, A. and Carillo, N. 1994. Shear failure of anisotropic materials. Proc. Boston Soc. Of Civ. Engrs, 31, pp. 74-87.

Chalaturnyk, R.J., Scott, J.D. and Yang, G. 1991. Geomechanical modelling of Phase A at the AOSTRA Underground Test Facility. Proceedings, Petroleum Society of CIM and AOSTRA Technical Conference, Banff, Alberta, Vol. 1, pp.91-07 to 91-07-16.

Chalaturnyk, R.J. 1996. Geomechanics of the steam assisted gravity drainage process in heavy oil reservoirs. Ph.D. dissertation, Department of Civil Engineering, University of Alberta, 576 p.

Chaney, R. C., Stevens, E., and Sheth, N. 1979. Suggested test method for determination of degree of saturation of soil samples by B value measurement. Geotechnical Testing Journal, GTJODJ, Vol. 2, No. 3, pp. 158-162.

Cundall, P. and Board, M. 1988. A microcomputer program for modeling large-strain plasticity problems. Proc. 6th Int. Conf. Num. Methods in Geom., Vol.3, pp. 2101-2108.

Curray, J. R. 1956. The analysis of two-dimensional orientation data. Jour. Geol., Vol. 64, pp. 117-131.

Dusseault, M.B. 1977. The geotechnical characteristics of the Athabasca oil sands, Ph.D. dissertation, Department of Civil Engineering, University of Alberta, 472p.

Dusseault, M.B. and Morgenstern, N.R. 1978. Shear strength of Athabasca oil sands. Canadian Geotechnical Journal, Vol. 15, No.2, pp. 216-218.

Dusseault, M.B. and Morgenstern, N.R. 1979. Locked sands. Quarterly Jour. Eng. Geol., Vol. 12, No. 2, pp. 117-131.

Edmunds, N.R. 1987. UTF Gravity drainage process development. Advances in Petroleum Recovery and Upgrading Technology, AOSTRA, Edmonton, Alberta, 11p.

GEO-SLOPE International Ltd. 1991. SEEP/W. Calgary, Alberta, Canada.

Goto, S. and Tatsuoka, F. 1988. Effects of end conditions on triaxial compressive strength for cohesionless soil. Advanced Triaxial Testing of Soil and Rock. ASTM STP 977, Robert T. Donaghe, Ronald C. Chaney, and Marshall L. Silver, Eds., American Society for Testing and Materials, Philadelphia, pp. 692-705.

Griffiths, D.V. 1984. Rationalized charts for the method of fragments applied to confined seepage. Geotechnique 34, No. 2, pp. 229-238.

Head, K.H. 1980,1982 and 1986. Manual of soil laboratory testing. Vol. 1-3. John Wiley and Sons, New York-Toronto, 1238 p.

Harr, M.E. 1962. Ground water and seepage. McGraw-Hill, New York.

Ishibashi, I., Chen, Y.C. and Chen, M.T. 1991. Anisotropic behavior of Ottawa sand in comparison with glass spheres. Soils and Foundations, Vol. 31, No.1, pp. 145-155.

Itasca, 1991. FLAC: Fast Lagrangian Analysis of Continua. Volume I User's Manual.

Kezdi, A. 1974. Handbook of soil mechanics. Volume 1. Soil Physics. Elsevier Scientific Publishing Co., New York.

Kosar, K.M. 1989. Geotechnical properties of oil sands and related strata. Ph.D. dissertation, Department of Civil Engineering, University of Alberta, 795 p.

Kuerbis, R. and Vaid, Y.P.1988. Sand sample preparation- the slurry deposition method. Soils and Foundations, Vol. 28, No.4, pp.107-118.

Kwan, M. Y., Cullen, M. P., Jamieson, P. R. and Fortier, R. A. 1988. A study of fines migration related permeability damage in extracted cold lake heavy oil cores. Paper No. 59, presented at the 39th Annual Technical Meeting of the Petroleum Society of CIM, Calgary, June 12-16, pp. 59-1 to 59-18.

Lade, P.V. 1982. Localization effects in triaxial tests on sand. IUTAM Conference on Deformation and Failure of Granular Materials, Delft, 31 Aug. - 3 Sep. 1982, pp. 461-471.

Lade, P. V. and Wasif, U. 1988. Effects of height-to-diameter ratio in triaxial specimens on the behavior of cross-anisotropic sand. Advanced Triaxial Testing of Soil and Rock, ASTM STP 977, Robert T. Donaghe, Ronald C. Chaney, and Marshall L. Silver, Eds., American Society for Testing and Materials, Philadelphia, 1988, pp. 706-714.

Lambe, T.W. and Whitman, R.V. 1979. Soil mechanics. SI Version. John Wiley, New York.

Lee, K.L. 1978. End restraint effects on undrained static triaxial strength of sand. J. Geot. Eng. Div., ASCE, 104, GT6, pp. 687-704.

Lowe, J. and Johnson, T. C. 1960. Use of back pressure to increase degree of saturation of triaxial test specimens. ASCE Research Conference on Shear Strength of Cohesive Soils, Boulder, Colorado, USA, pp. 819-836.

McKay, J.G. 1989. Undisturbed oil sand sampling and sample quality evaluation. M.Sc. dissertation, Department of Civil Engineering, University of Alberta, Edmonton, Alberta, 227 p.

Morgenstern, N.R., Fair, A.E. and McRoberts, E.C. 1988. Geotechnical engineering beyond soil mechanics – a case study. Canadian Geotechnical Journal, Vol. 25, pp. 637-661.

Mori, A. and Tamura, M. 1986. Effects of dilatancy on permeability in sands stabilized by chemical grout. Soils and Foundations, Vol. 26, No. 1, March, pp. 96-104.

Mossop, G.D. 1980. Geology of the Athabasca oil sands. Science, Vol. 207, No.11, January, pp. 145-152.

Muir Wood, D. 1990. Soil behaviour and critical state soil mechanics. Cambridge University Press.

Muskat, M. 1937. The flow of homogeneous fluids through porous media. McGraw-Hill, New York.

National Instruments Corporation. 1993. Lab VIEW 3. Austin, TX, USA.

Nicholson, P.G., Seed, R.B. and Anwar, H.A. 1993. Elimination of membrane compliance in undrained triaxial testing. Canadian Geotechnical Journal, Vol. 30, pp. 727-738.

NIH, 1997, Software Program, "Image", Version 1.6, National Institute of Health, Bethesda, MD.

Norris, G.M. 1981. Effect of end membrane thickness on the strength of frictionless cap and base tests. Laboratory Shear Strength of Soils. ASTM STP No. 740, pp. 303-314, Am. Soc. for Testing and Materials, Philadelphia, USA.

Ochiai, H. and Lade, P.V. 1983. Three-dimensional behavior of sand with anisotropic fabric. Journal of Geotechnical Engineering, American Society of Civil Engineers, Vol. 109, No. 10, pp.1313-1328.

Oda, M. 1972. Initial fabrics and their relations to mechanical properties of granular material. Soils and Foundations, Vol. 12, No.1, pp. 17-36.

Oda, M. 1972. The mechanism of fabric change during compressional deformation of sand. Soils and Foundations, Vol. 12, No.2, pp. 1-18.

Oda, M. and Koishikawa, I. 1977. Anisotropic fabric of sands. Proc. 9th ICSMFE, Vol. 1, pp. 235-238.

Oda, M., Koishikawa, I. and Higuchi, T. 1978. Experimental study of anisotropic shear strength of sand by plane strain test. Soils and Foundation, Vol. 18, No. 1, pp. 25-38.

Oda, M. 1981. Anisotropic strength of cohesionless sands. J. Geotech. Engrg., ASCE, 107(9), pp. 1219-1231.

Oda, M., Nemat-Naser, S., and Konishi, J. 1985. Stress-induced anisotropy in granular masses. Soils and Foundations, 25(3), pp. 85-97.

Oda, M. and Nakayama, H. 1989. Yield function for soil with anisotropic fabric. Journal of Engineering Mechanics, Vol, 115, NO. 1, pp. 89-104.

Oldakowski, K. 1994. Stress induced permeability changes in Athabasca oil sands. M.Sc. dissertation, Department of Civil Engineering, University of Alberta, 227 p.

Olsen, H.W. 1966. Darcy's law in saturated kaolinite. Wat. Resour. Res. 2, No. 6, pp. 287-295.

Olsen, H.W., Nichols, R.W. and Rice, T.L. 1985. Low gradient permeability measurements in a triaxial system. Geotechnique 35, No.2, pp. 145-157.

Plewes, H.D. 1987. Undrained strength of Athabasca oil sands. M.Sc. dissertation, Department of Civil Engineering, University of Alberta, 428 p.

Protulipac, D.G. 1991. Comparing strength characteristics of St. Peter sandstone and oil saturated McMurray sand. M.Sc. thesis, University of Waterloo, Waterloo, Ontario.

Rajani, B.B. 1988. A simple model for describing variation of permeability with porosity for unconsolidated sands. In Situ, Vol. 12, No. 3, pp. 209-226.

Raju, V.S., Sadasivan, S.K. and Venkataraman, M. 1972. Use of lubricated and conventional end platens in triaxial tests on sands. Soils and Foundations, Vol. 12, No. 4, pp. 35-43.

Rottenfusser, B.A., Dexter, S. and Alwast, N.K. 1988. Initial analyses of cores from UTF Phase A. Alberta Research Council report submitted to AOSTRA.

Rottenfusser, B.A., Palfreyman, J.E. and Alwast, N.K. 1988. Geology of the AOSTRA Underground Test Facility site. The Fourth UNITAR/UNDP International Conference on Heavy Crude and Tar Sands, Vol. II, Paper No. 115, 21p.

Rowe, P.W. 1962. The stress-dilatancy relation for static equilibrium of an assembly of particles in contact, Proc. R. Soc., A269, pp. 500-527.

Rowe, P.W. and Barden, L. 1964. Importance of free ends in triaxial testing. Journal of Soil Mechanics and Foundations Division, American Society of Civil Engineers, Vol. 90, No. SM1, Jan., pp. 1-27.

Rowe, P.W. 1971. Theoretical meaning and observed values of deformation parameters for soil. Proceedings of Roscoe Memorial Symposium, pp. 143-194. Henley-on-Thames: Foulis.

Rumer, R.R. and Drinker, P.A. 1966. Resistance to laminar flow through porous media. Proc. Amer. Soc. Civil Eng., Vol. 92, No. HY 5, pp. 155-164.

Samieh, A. M. and Wong, R.C.K. 1997. Deformation of Athabasca oil sand at low effective stresses under varying boundary conditions. Canadian Geotechnical Journal, Vol. 34, pp. 985-990.

Sarsby, R.W., Kalteziotis, N. and Haddad, E.H. 1980. Bedding error in triaxial tests on granular media. Technical Note, Geotechnique 30,No. 3, pp. 302-309.

Schanz, T. and Vermeer, P. A. 1996. Angles of friction and dilatancy of sand. Geotechnique, Vol. 46, No. 1, pp. 145-151.

Scott, J.D., Proskin, S.A. and Adhikary, D.P. 1994. Volume and permeability changes associated with steam stimulation in an oil sands reservoir. Journal of Canadian Petroleum Technology, Vol. 33, No. 7, pp. 44-52.

Skempton, A. W. 1954. The pore pressure coefficient A and B. Geotechnique, Vol. 4, No. 4, pp. 143-147.

Taylor, D.W. 1948. Fundamentals of soil mechanics. John Wiley, New York.

Tortike, W.S. and Farouq Ali, S.M. 1991. Prediction of oil sand failure due to steam-induced stresses. The Journal of Canadian Petroleum Technology, Vol. 30, No. 1, pp. 87-96.

Vaid, Y.P. and Negussey, D. 1984. Relative density of pluviated sand samples. Soils and Foundations, Vol. 24, No. 2, pp. 101-105.

Vaid, Y. P. and Negussey, D. 1988. Preparation of reconstituted sand specimens. Advanced Triaxial Testing of Soil and Rock, ASTM STP 977, Donaghe, R.T., Chaney, R.C. and Silver, M.L, Eds. American Society for Testing and Materials, Philadelphia, pp. 405-417.

Vermeer, P.A. and de Borst, R. 1984. Non-associated plasticity for soils, concrete and rock. Heron 29, No. 3.

Wightman, D., Rottenfusser, B., Kramers, J. and Harrison, R. 1989. Geology of the Alberta oil sands deposits, AOSTRA technical handbook on oil sands, bitumens and heavy oils. L.G. Hepler and Ch. Hsi Ed. AOSTRA Technical Publication, Series No.6, pp. 1-9.

Wissa, A. E. Z. 1969. Pore pressure measurement in saturated stiff soils. Proceedings Paper 6670. Journal of the Soil Mechanics and Foundations Division, Proceedings of the American Society of Civil Engineers, Vol. 95, No. SM4, pp. 1063-1073.

APPENDIX A SCANNING ELECTRONIC MICROSCOPE IMAGES

This appendix contains all the images of oil sand structure obtained in this study with the use of a scanning electron microscope (SEM). These images were obtained from a block sample of bitumen-free McMurray Formation oil sand. A measured white bar is placed in each image to show the scale.

A total of 9 undisturbed specimens were prepared for the scanning electron microscope (Figure A1). They were cut out from three locations on the oil sand block sample (a block of 22 cm by 22 cm by 15 cm dimension). On each location two horizontal specimens at perpendicular directions and one vertical specimen were prepared. Figure A2 shows the schematic of the specimen preparation. The reference axes, X, Y and Z are selected as shown. The axis Z is selected as the vertical direction and the axes X and Y as the horizontal directions. One of the horizontal directions corresponded to a plane parallel to the face of slope from which the block sample was obtained.

Some of the images were analyzed with NIH Image 1.6 digital image analysis software (NIH, 1997). The analyzed images were four vertical sections and two horizontal sections (Figures A3, A5, A7, A9, A9, A11 and A13). The resulted binary images of these analyzed images are presented in Figures A4, A6, A8, A10, A12 and A14. All these images have the same magnifications.
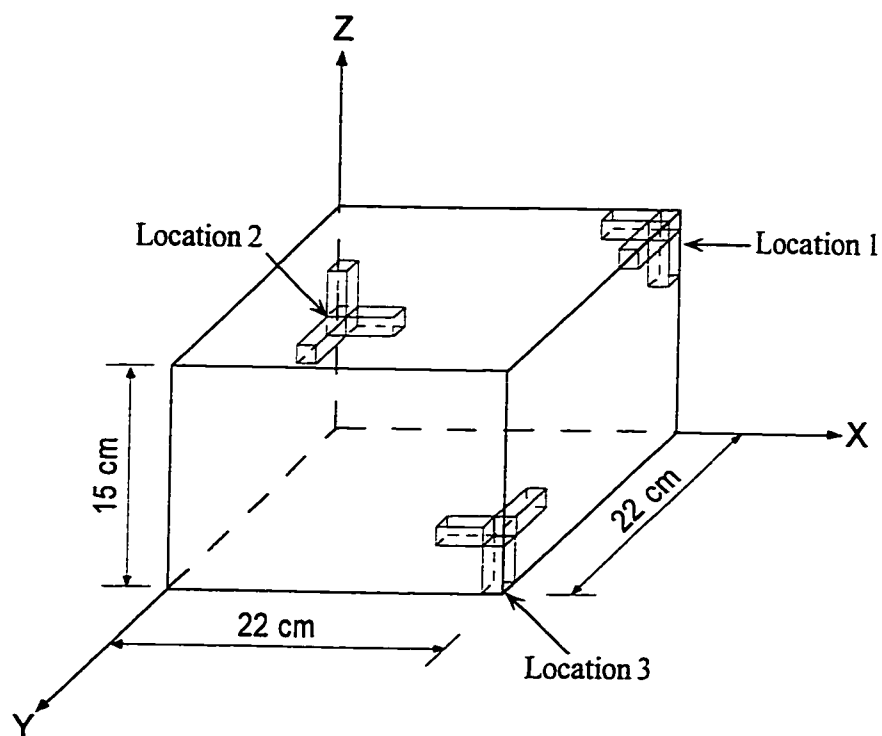
**Figure A1 Schematic of block sample and
locations where specimens were obtained**
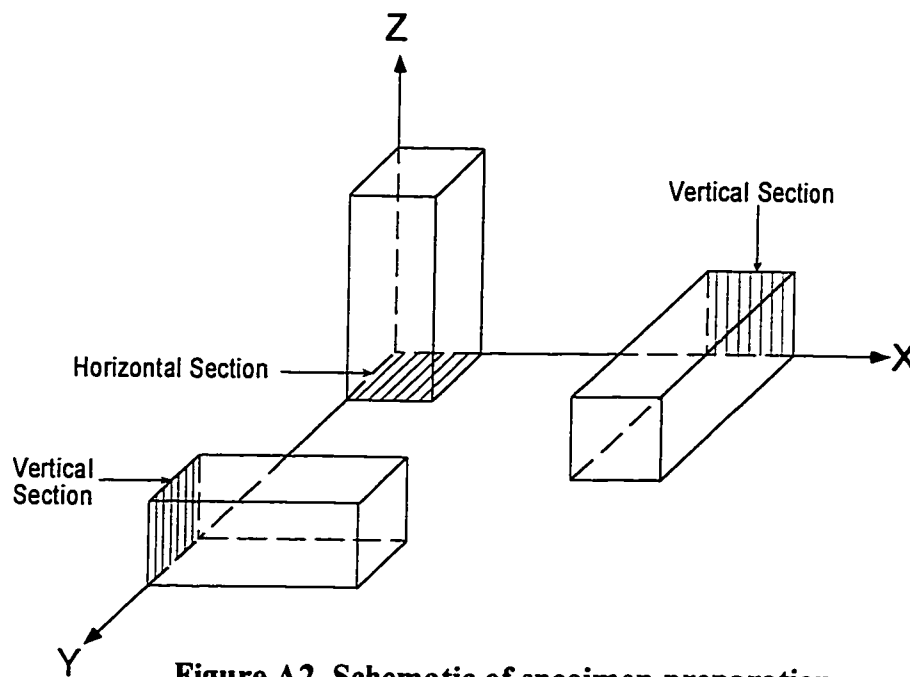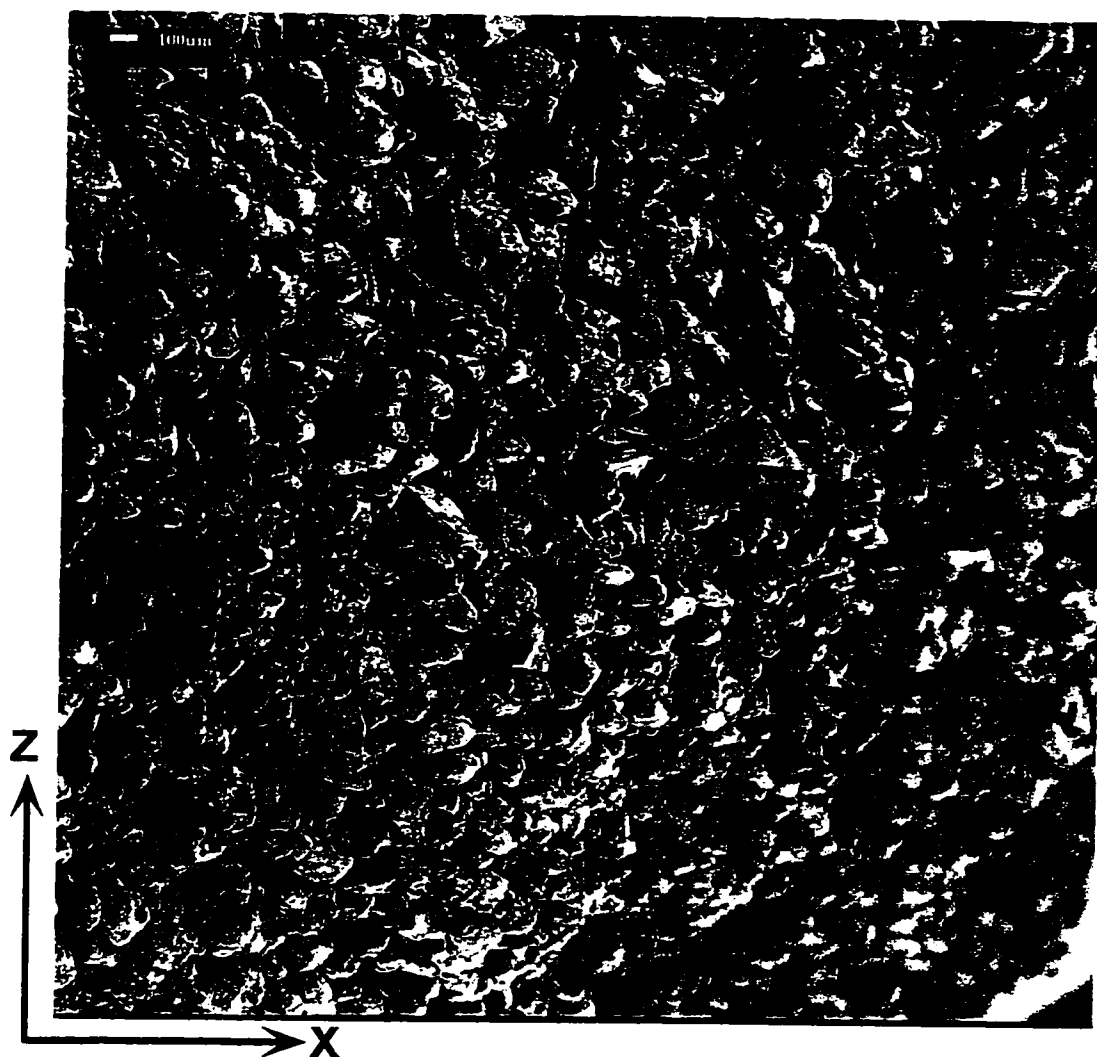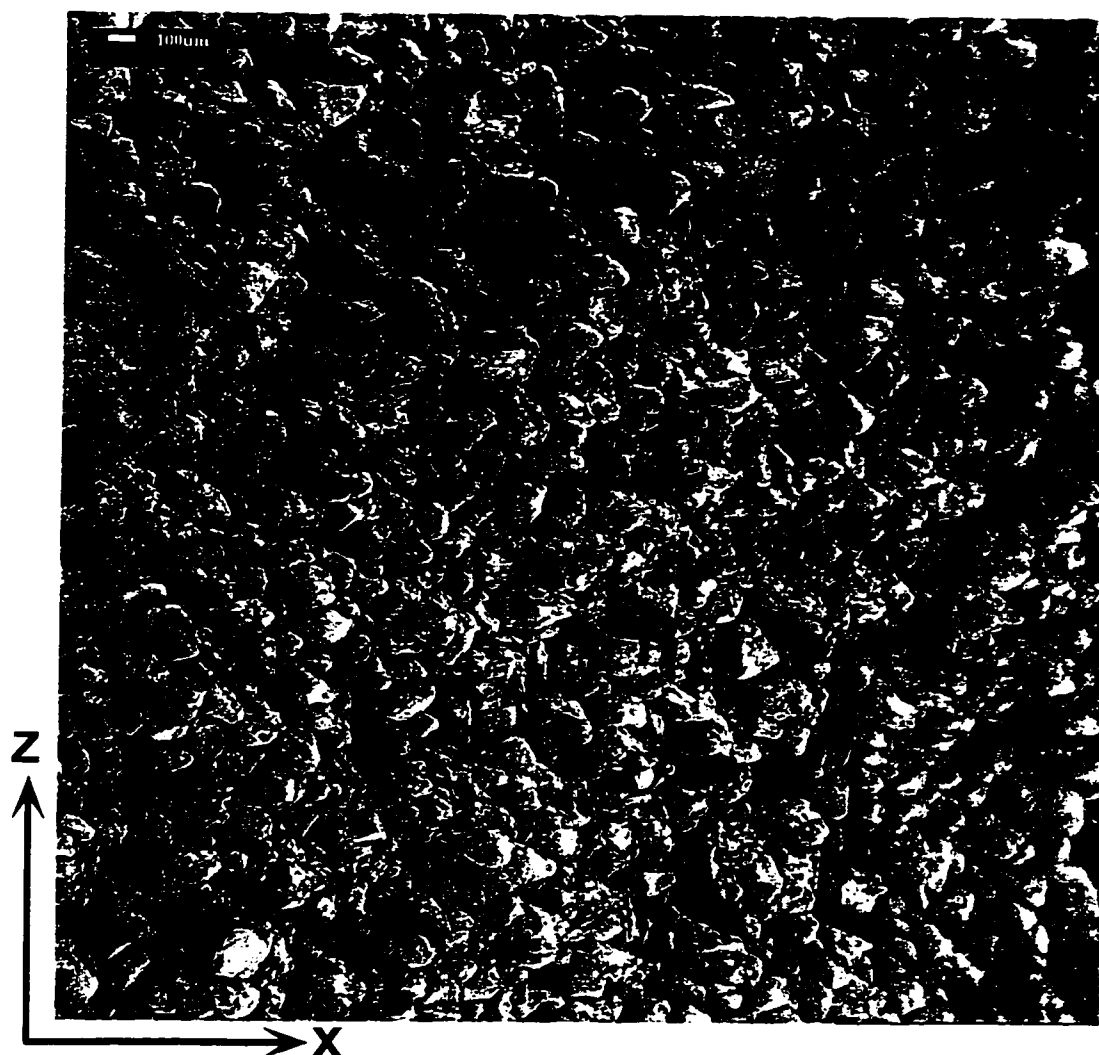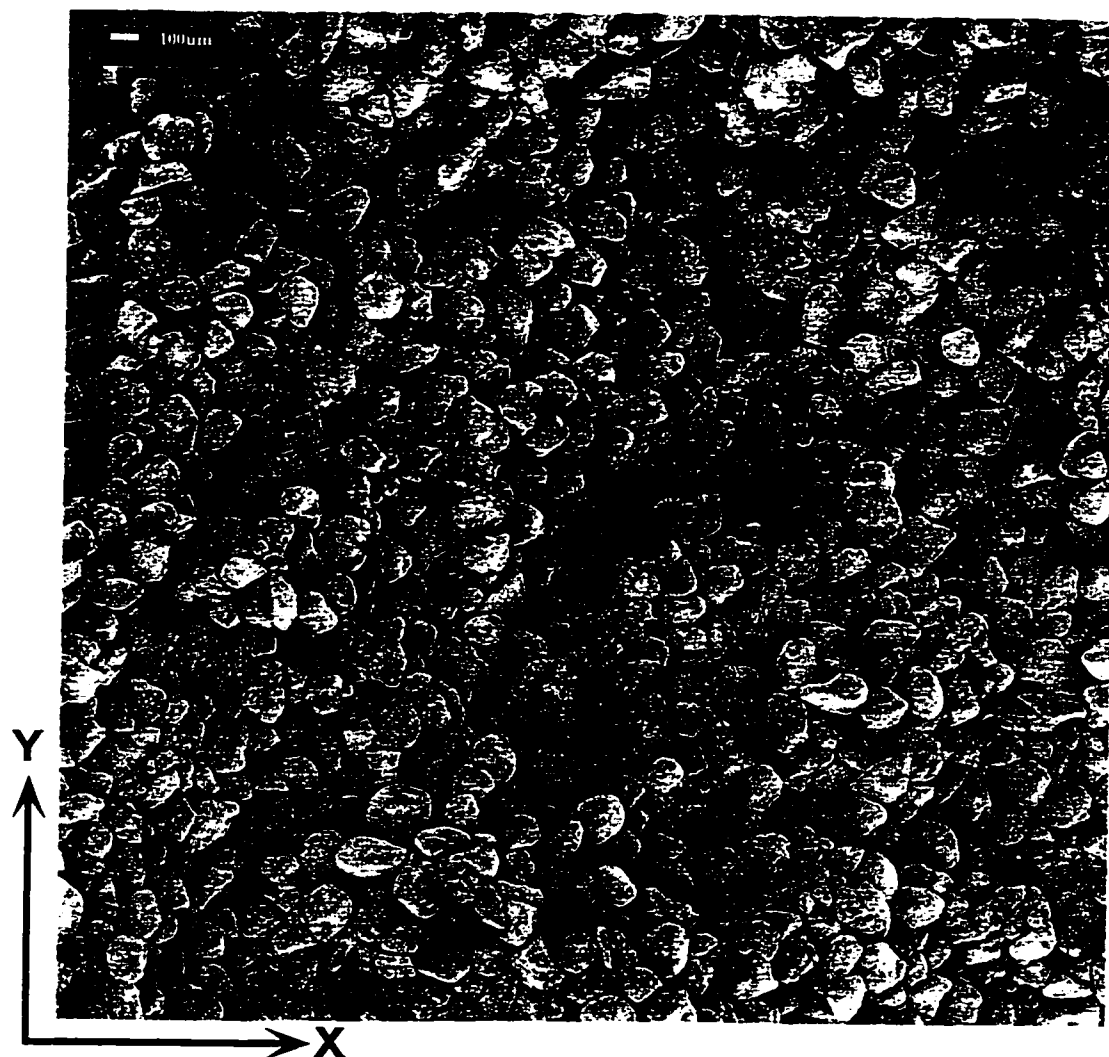

Figure A2 Schematic of specimen preparation
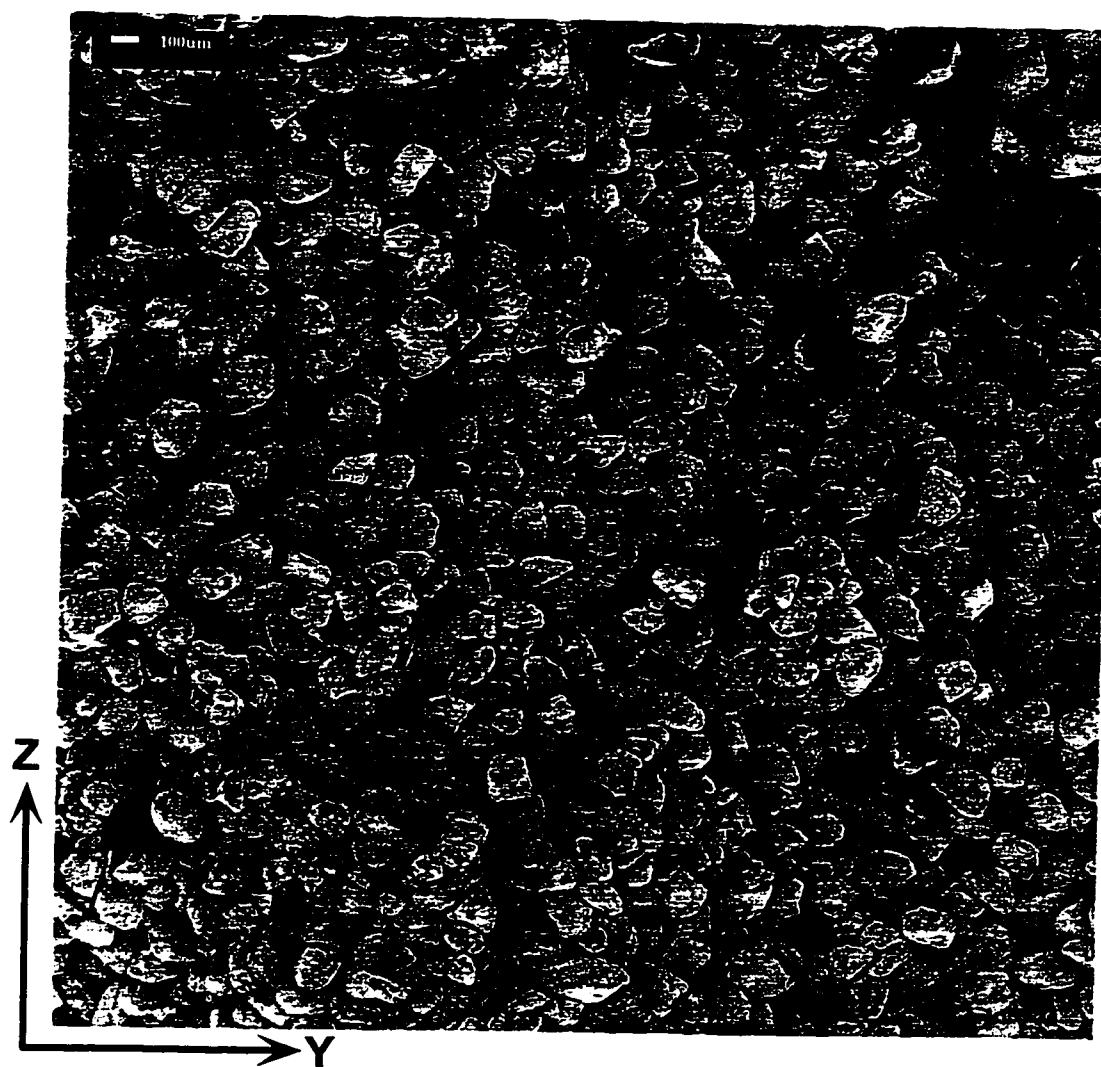
Figure A3 Scanning electron microscope of a vertical section of bitumen-free
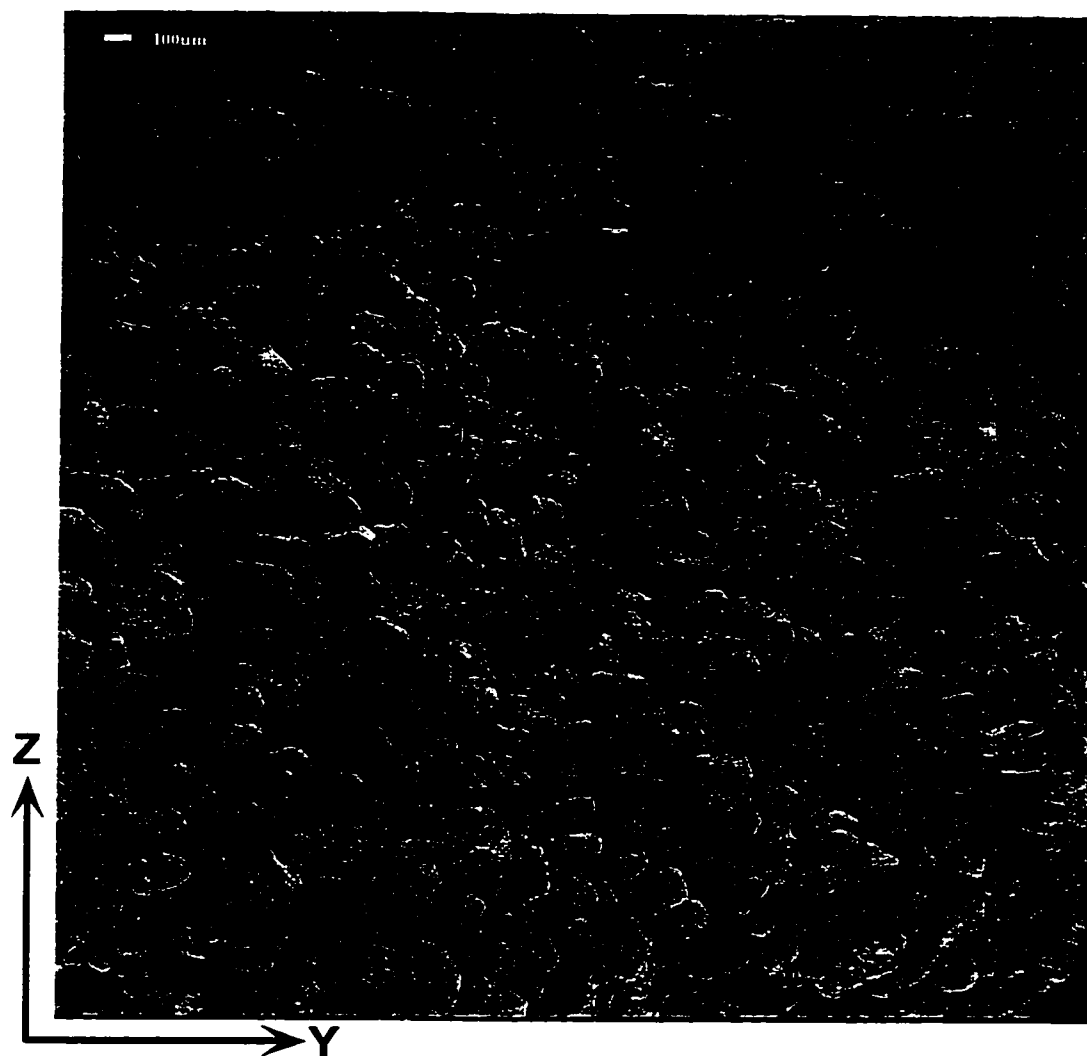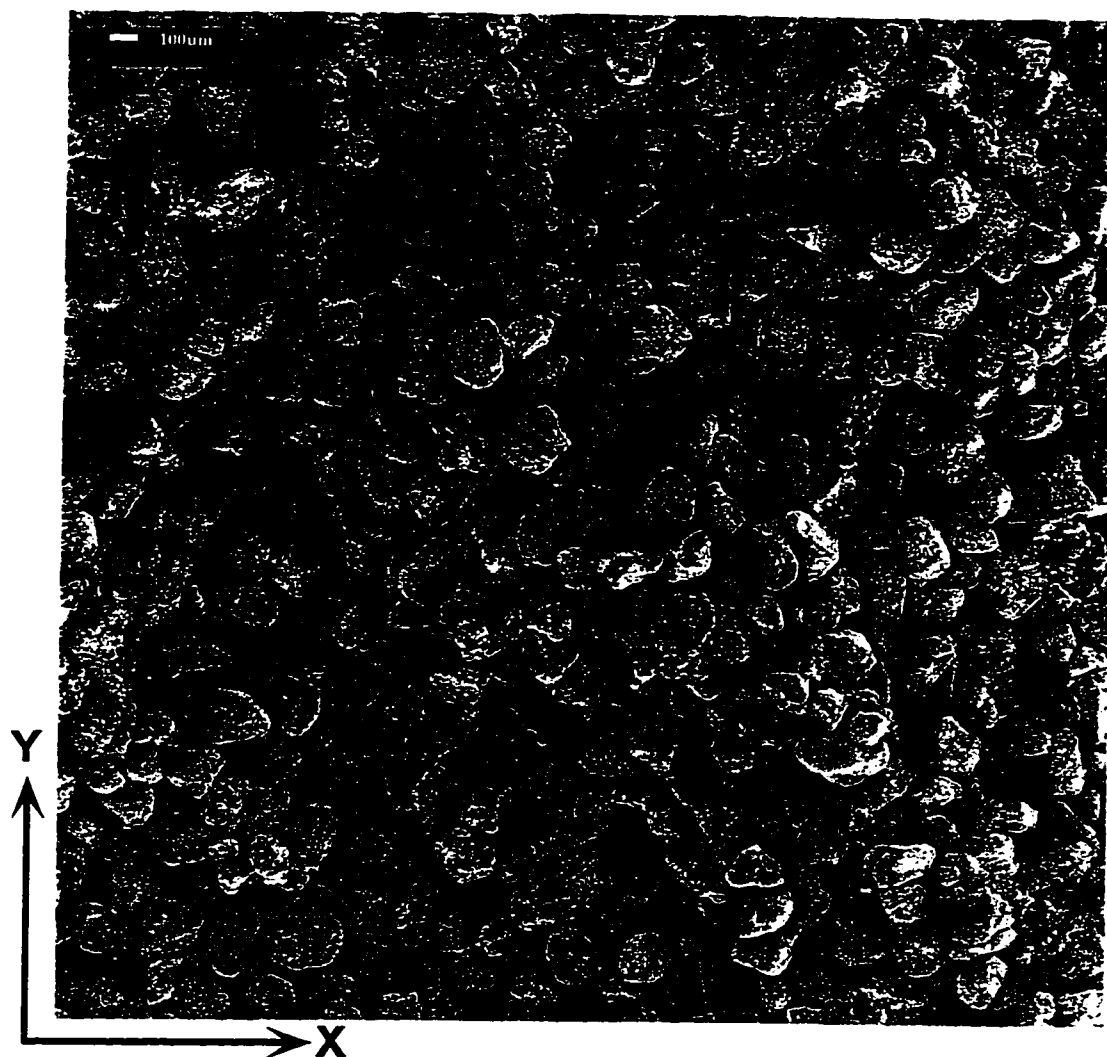McMurray Formation oil sand (Z-Y plane)
Location 2
(White bar is 100 μm)
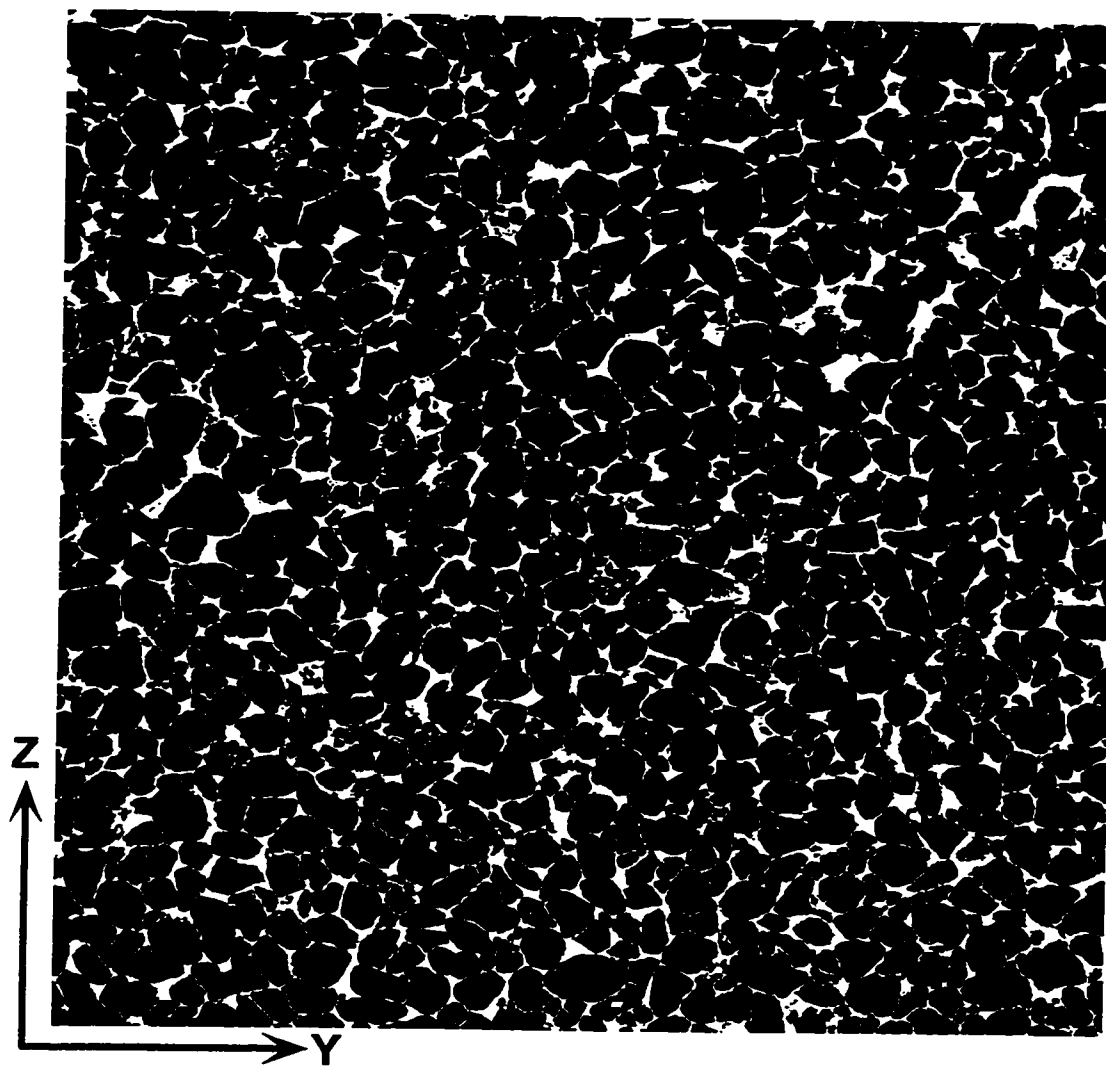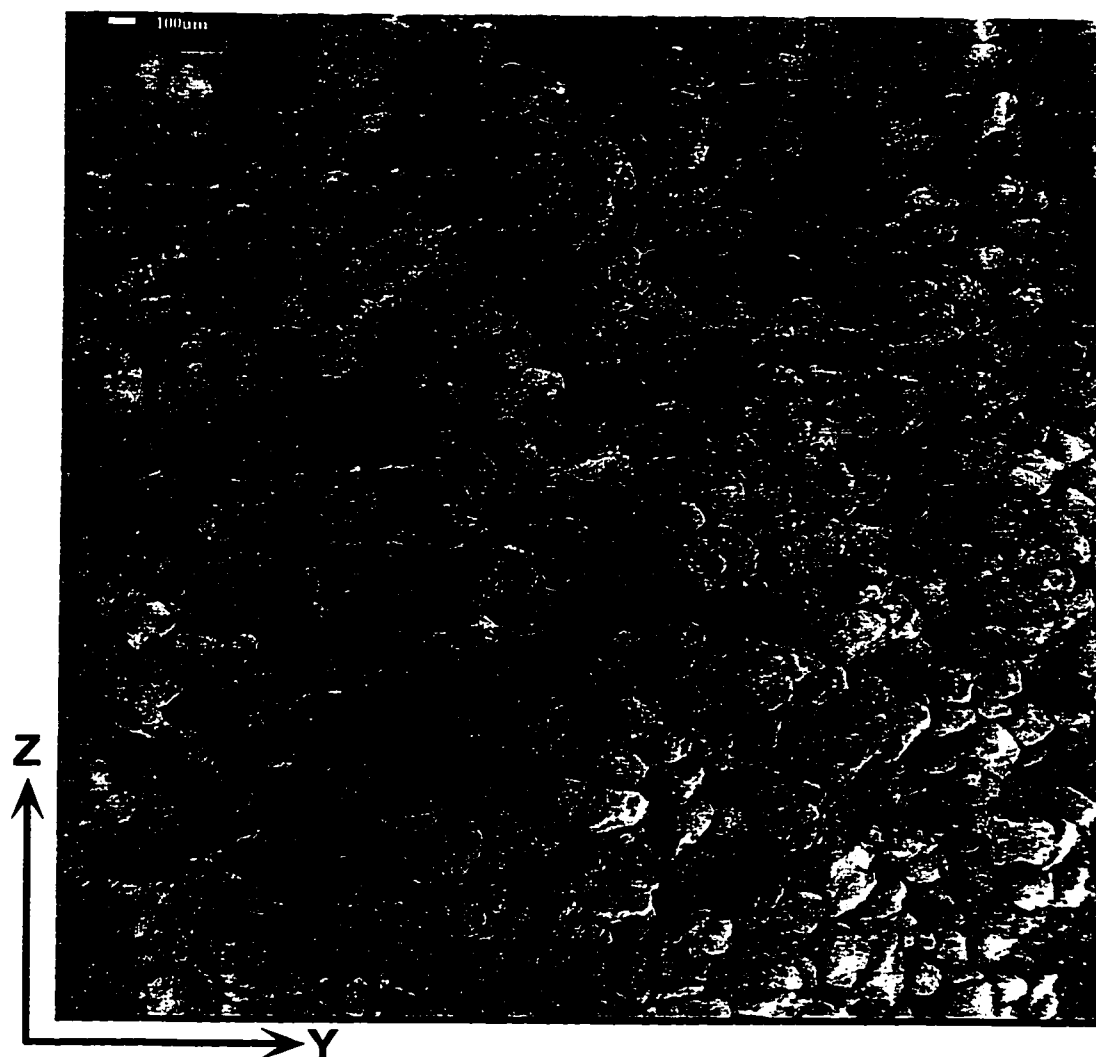
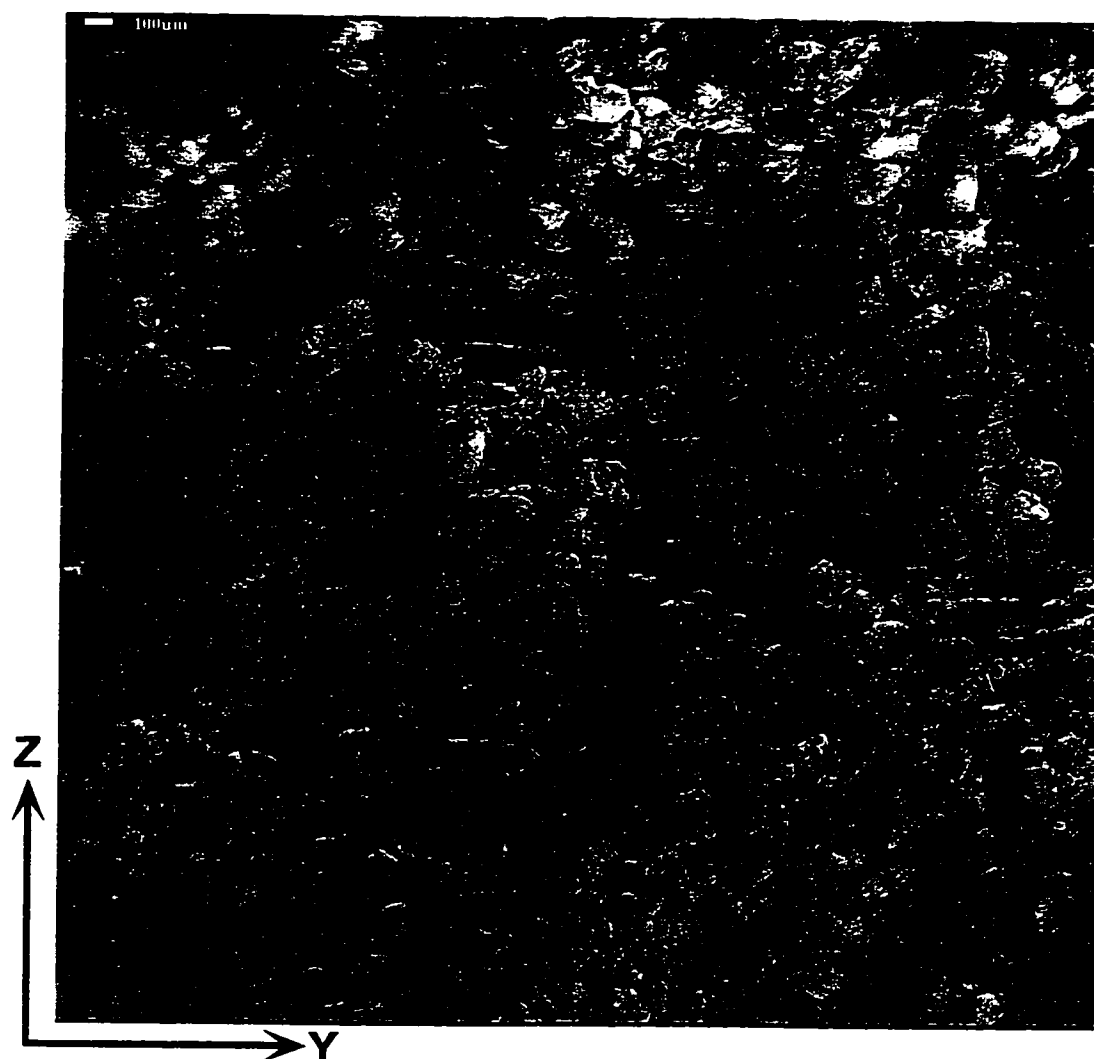**Figure A4 Binary image produced by delineating particles in Figure A3**
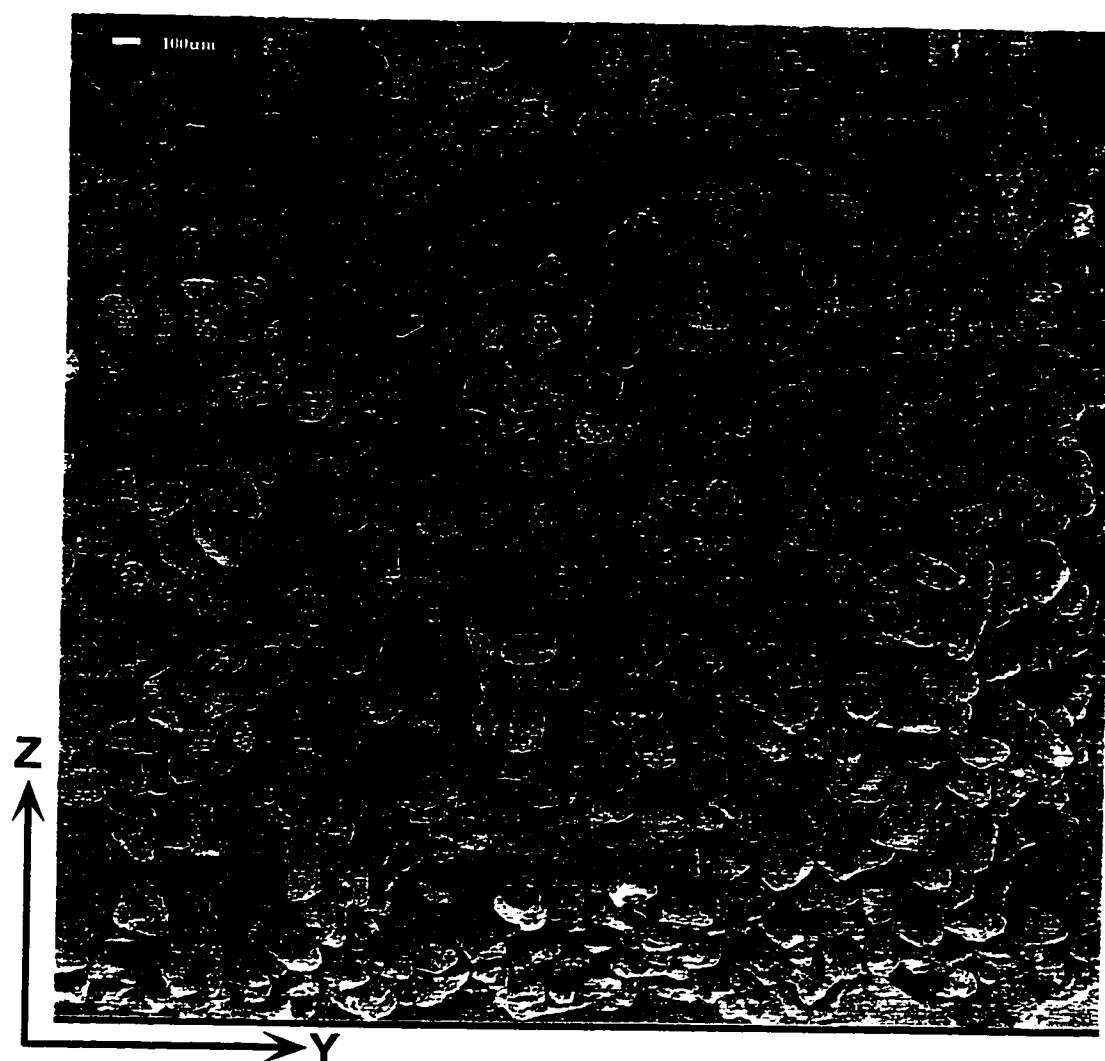
**Figure A5 Scanning electron microscope of a vertical section of bitumen-free McMurray Formation oil sand (Z-Y plane)
Location 2
(White bar is 100 μm)**
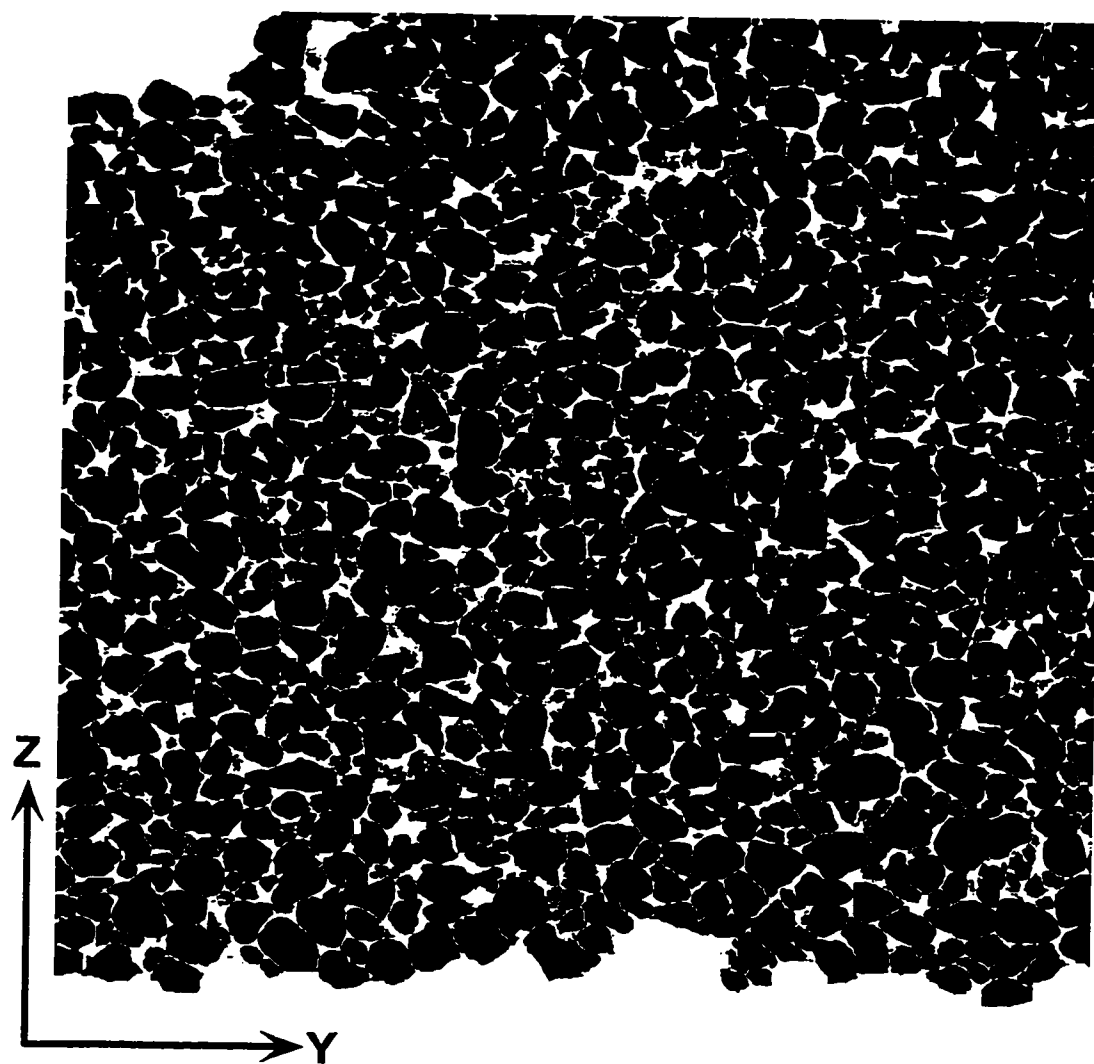
Figure A6 Binary image produced by delineating particles in Figure A5
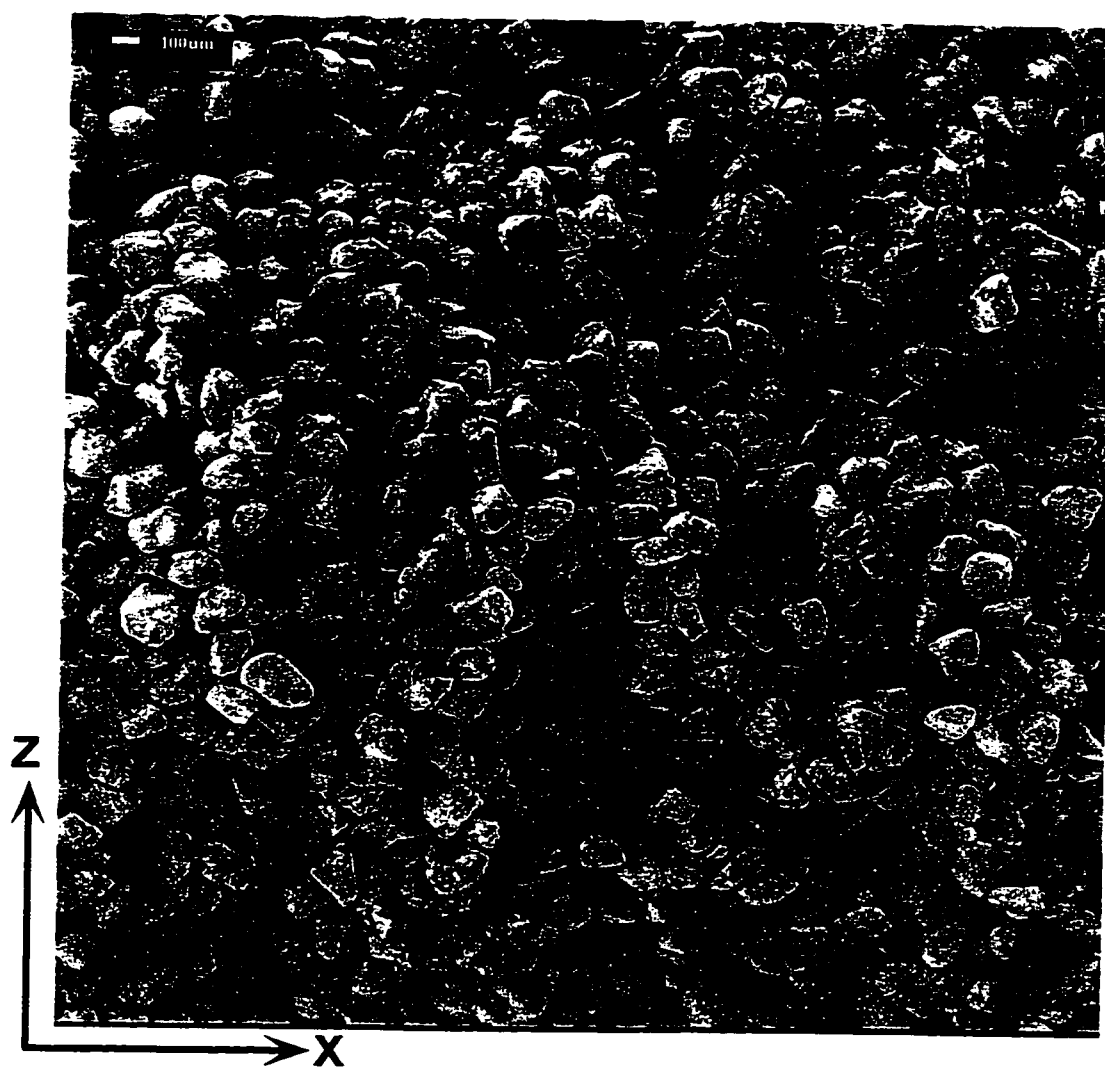
Figure A7 Scanning electron microscope of a vertical section of bitumen-free
McMurray Formation oil sand (Z-X plane)
Location 3
(White bar is 100 μm)
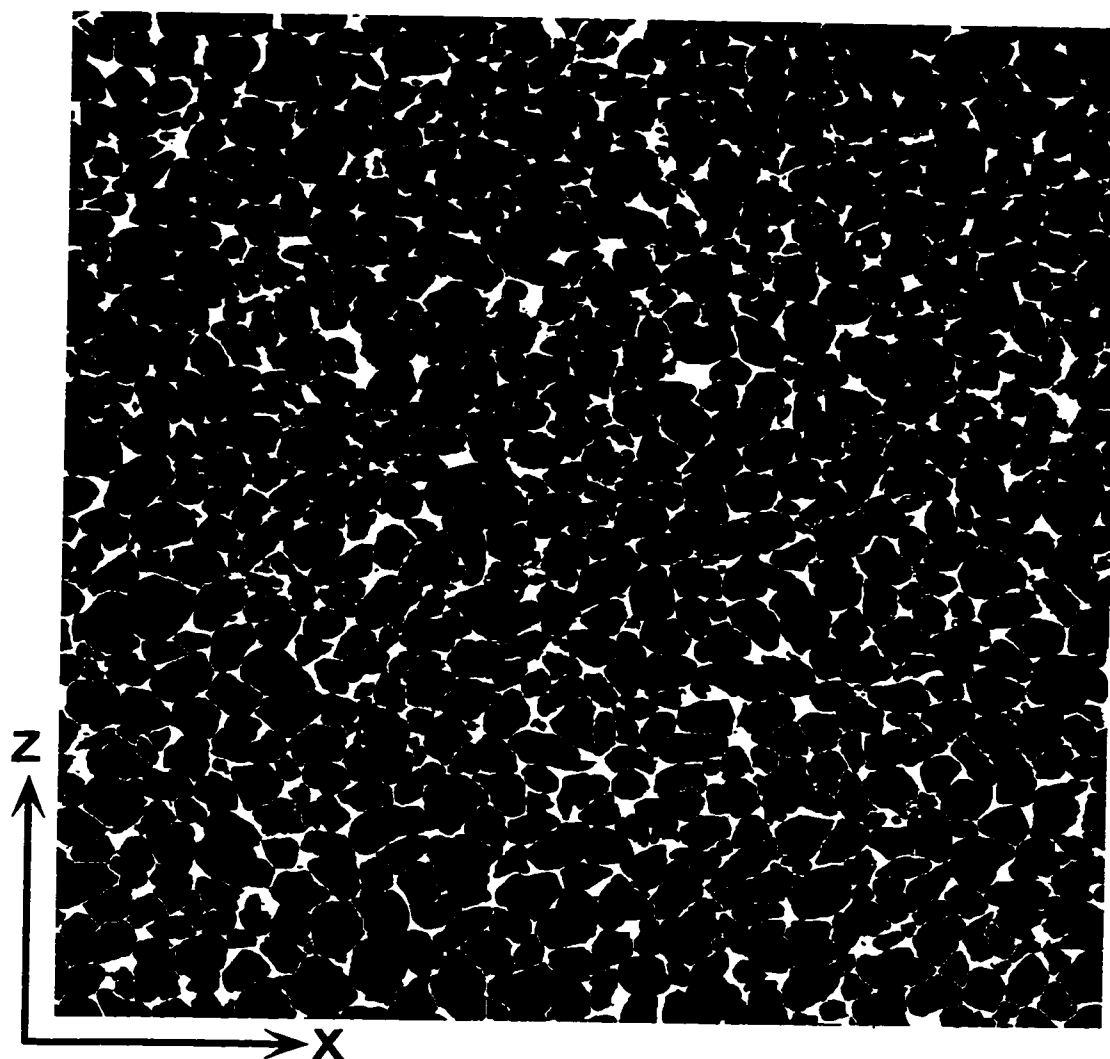
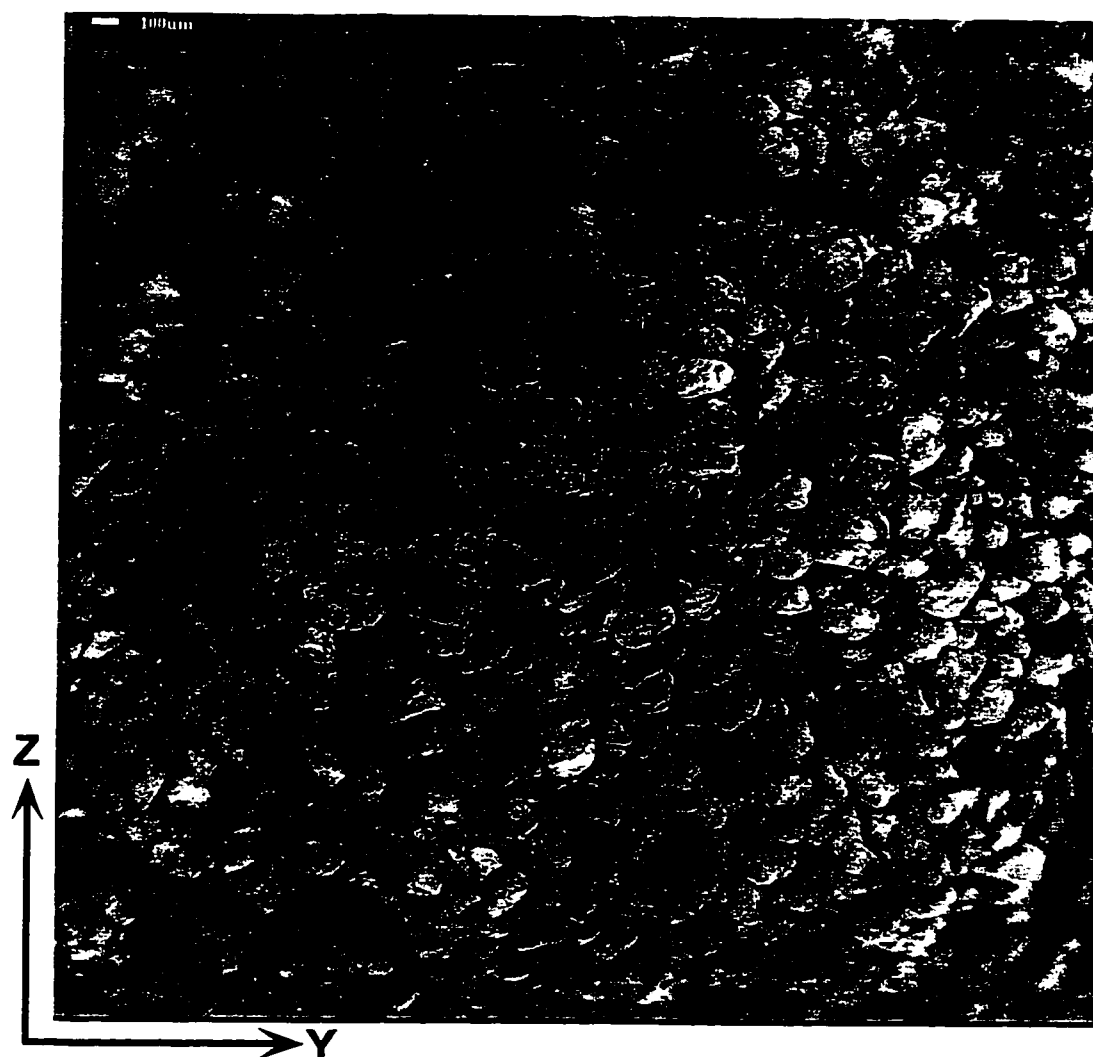**Figure A8 Binary image produced by delineating particles in Figure A7**
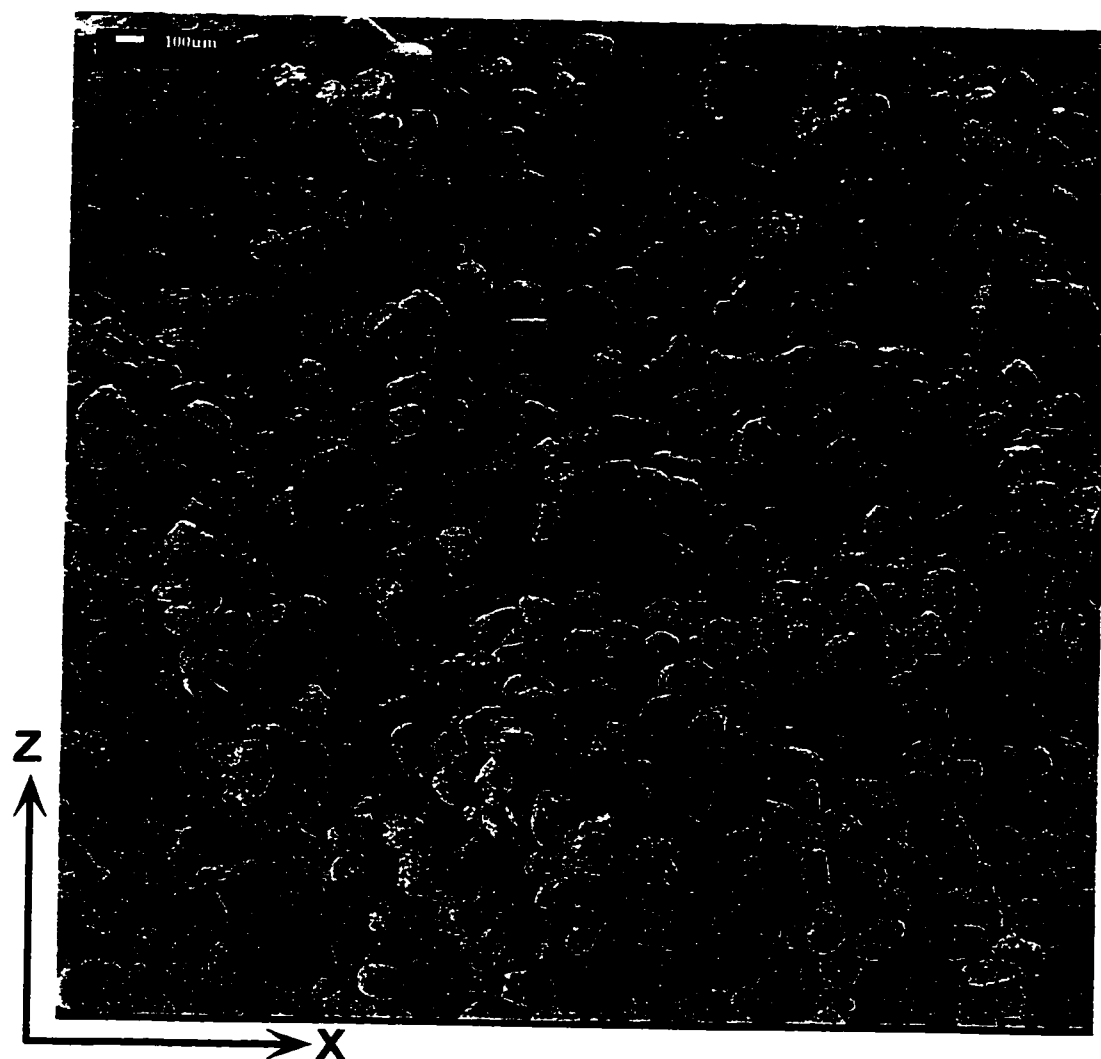
**Figure A9 Scanning electron microscope of a vertical section of bitumen-free
McMurray Formation oil sand (Z-X plane)
Location 3
(White bar is 100 μm)**
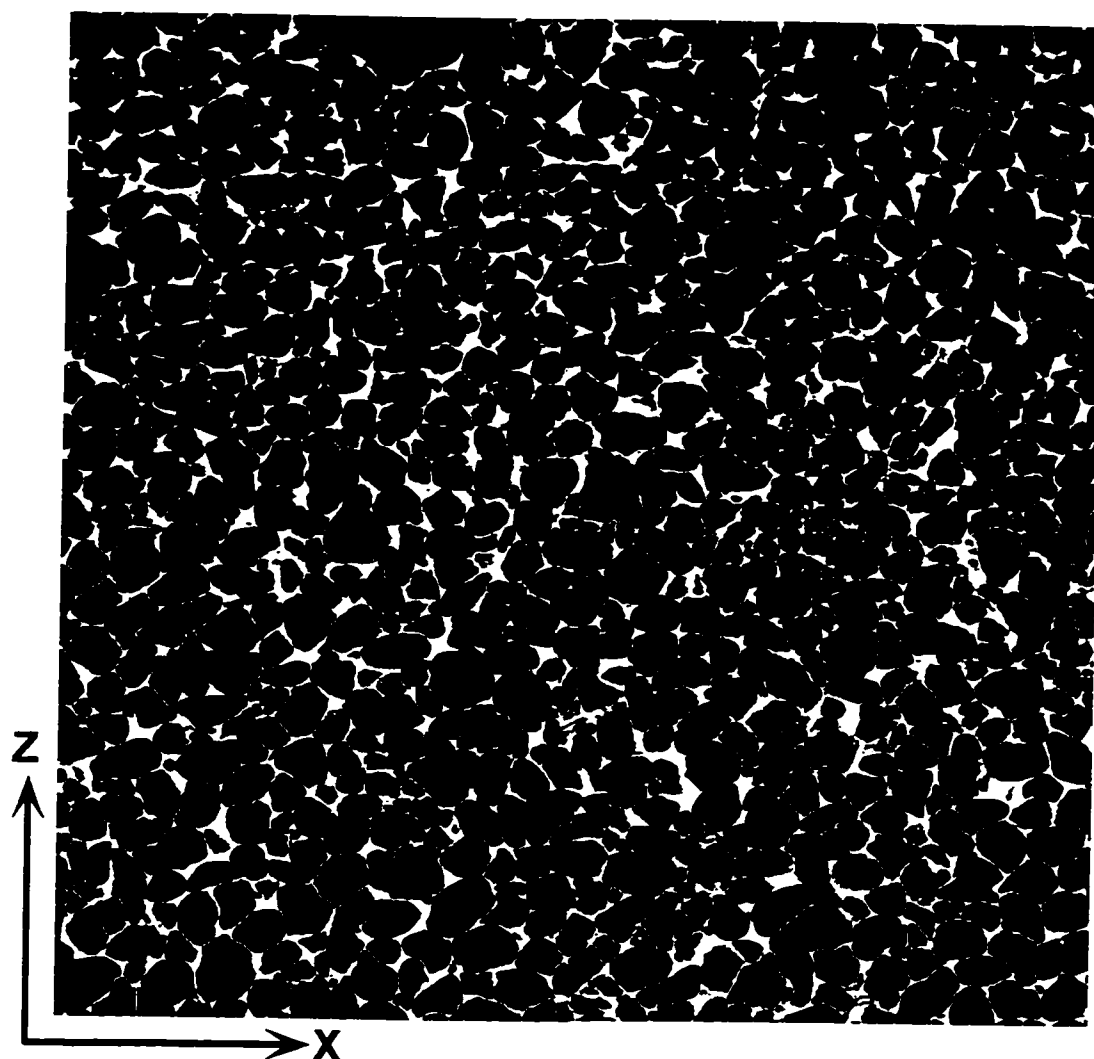
Figure A10 Binary image produced by delineating particles in Figure A9
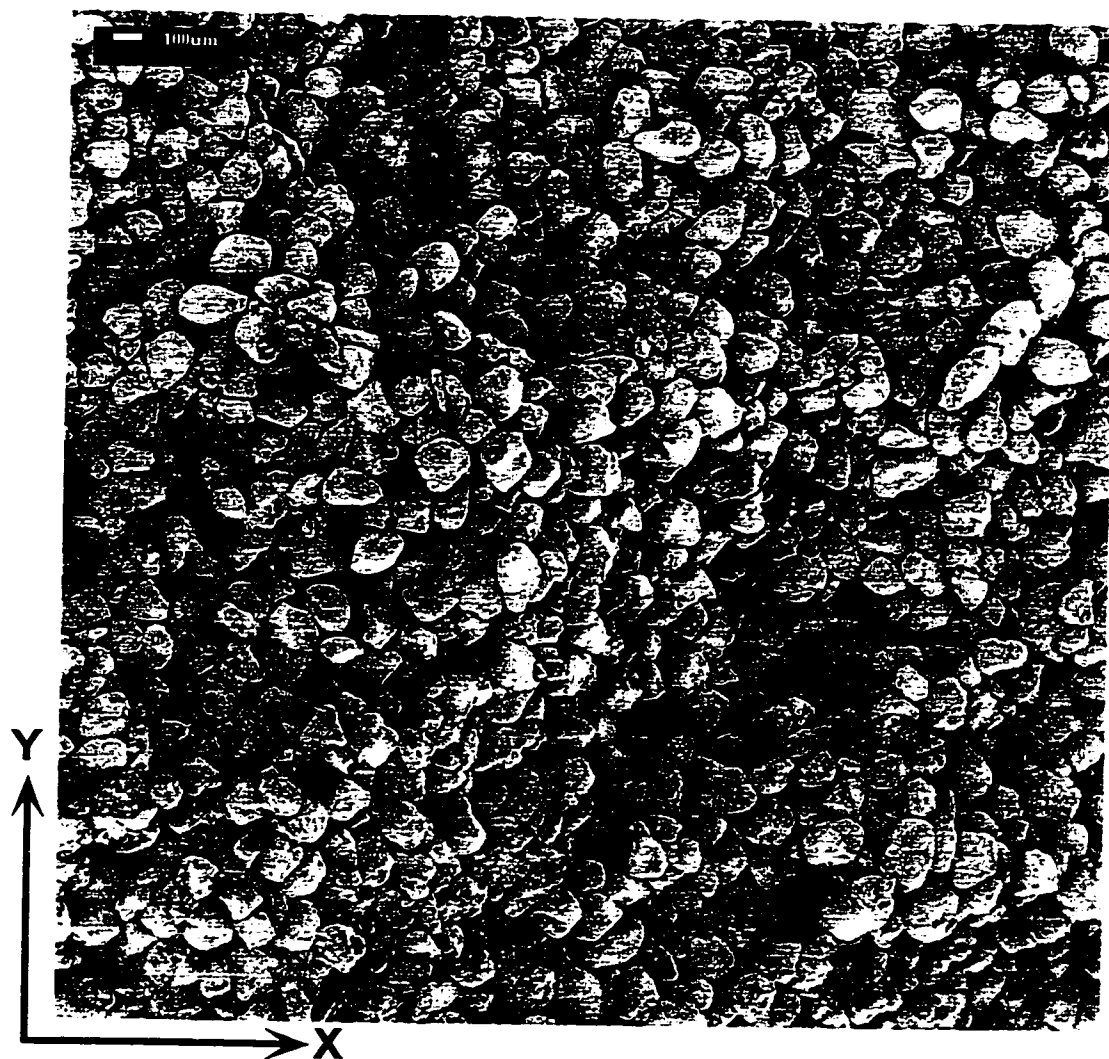
Figure A11 Scanning electron microscope of a horizontal section of bitumen-free
McMurray Formation oil sand (Y-X plane)
Location 2
(White bar is 100 μm)
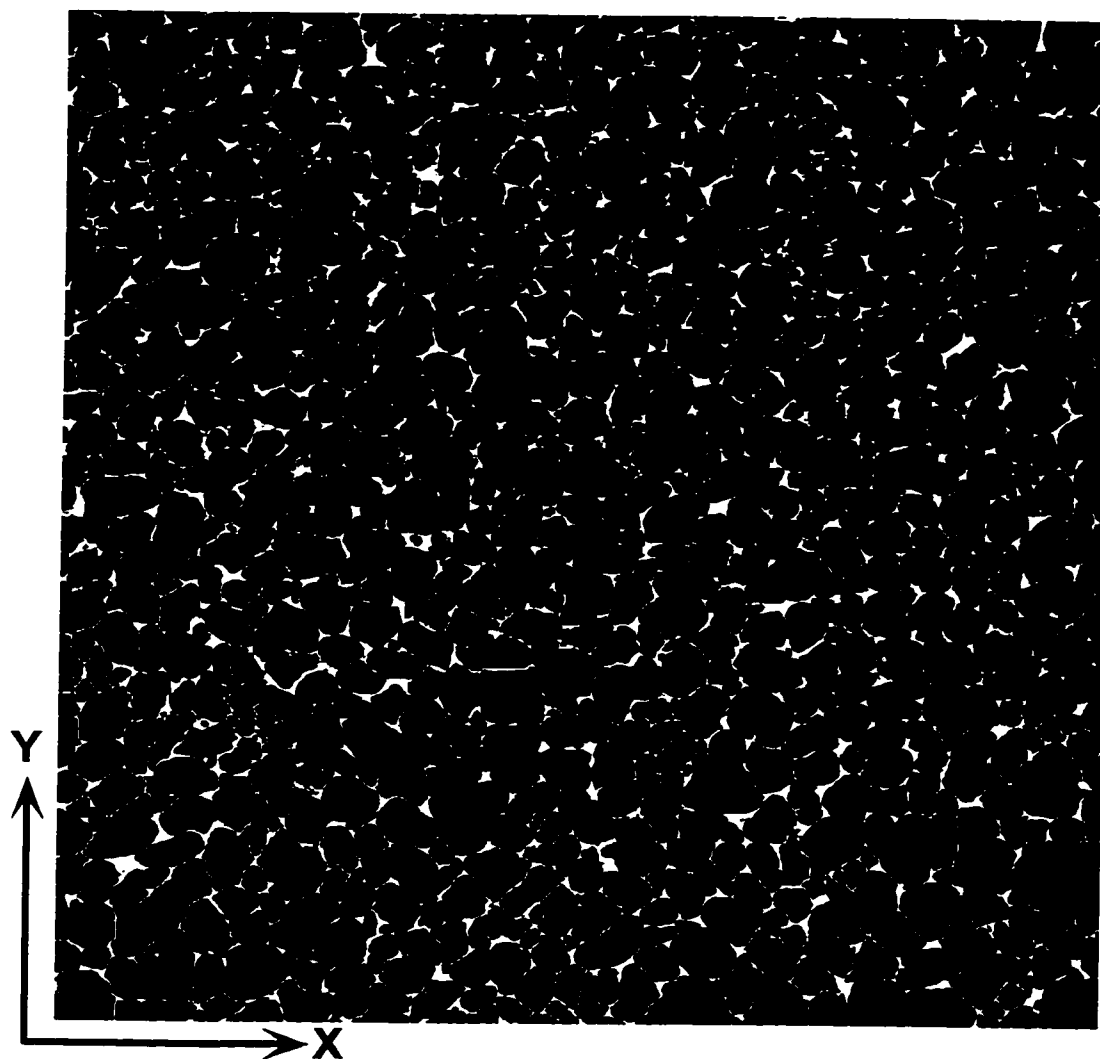
Figure A12 Binary image produced by delineating particles in Figure A11
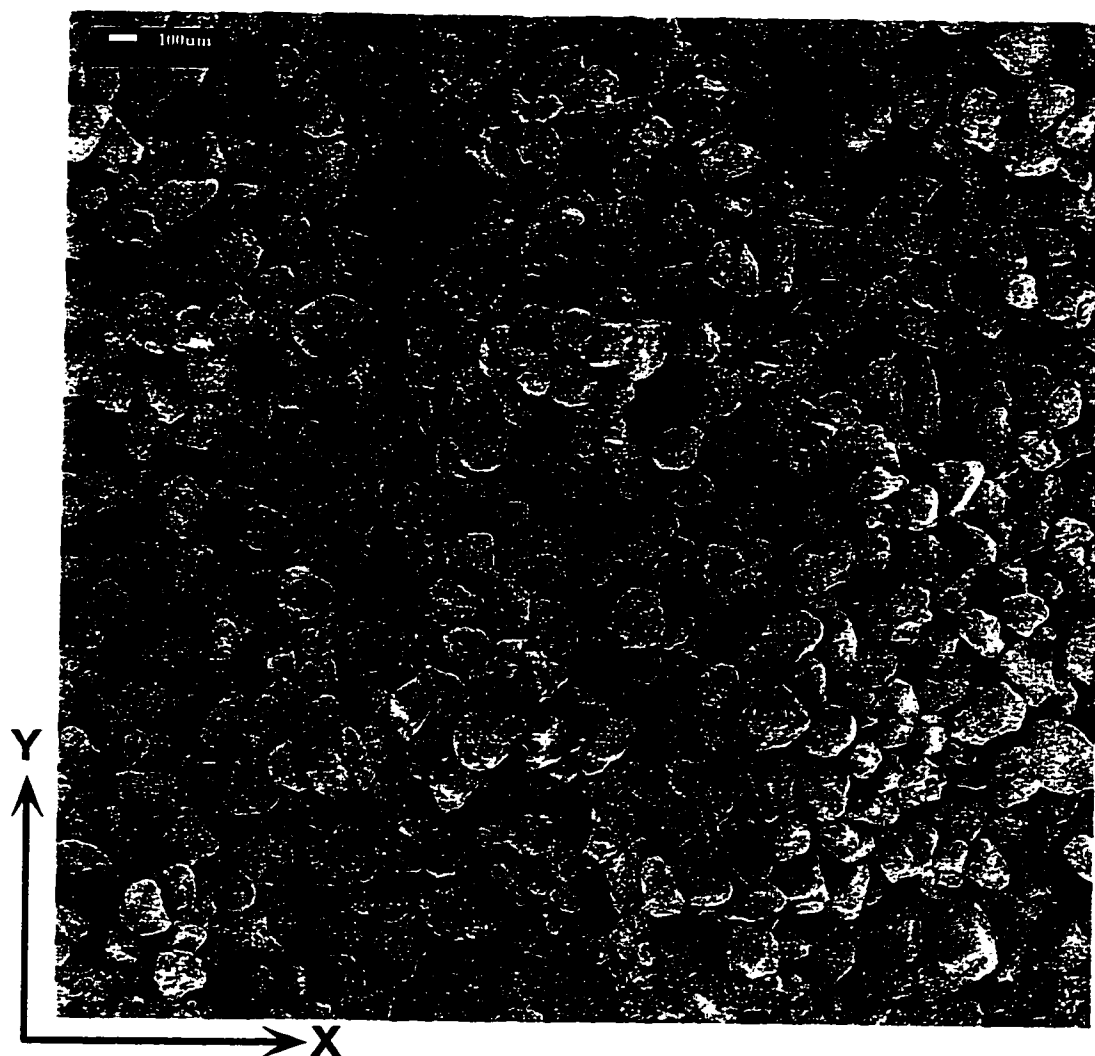
Figure A13 Scanning electron microscope of a horizontal section of bitumen-free McMurray Formation oil sand (Y-X plane)
Location 3
(White bar is 100 µm)
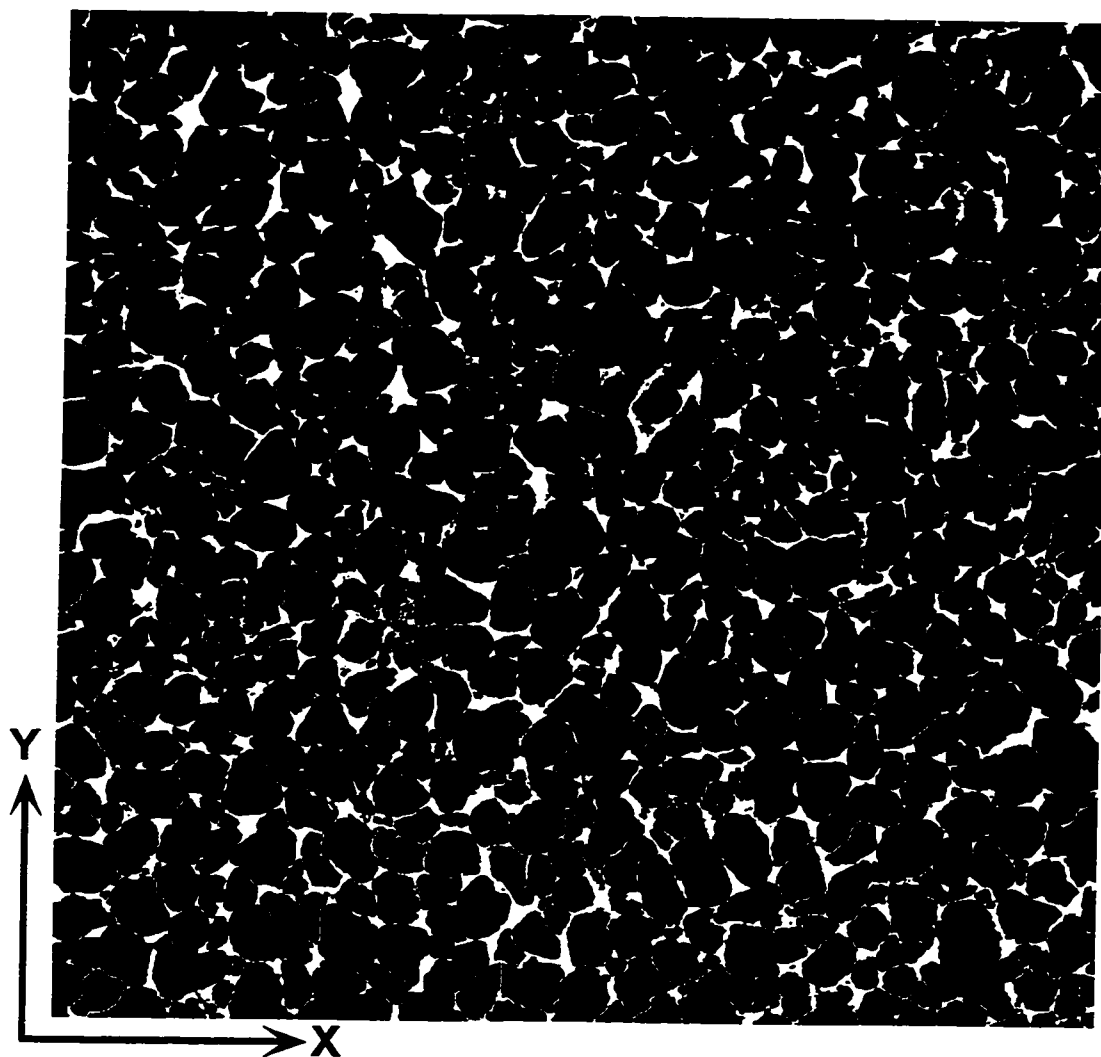
Figure A14 Binary image produced by delineating particles in Figure A13
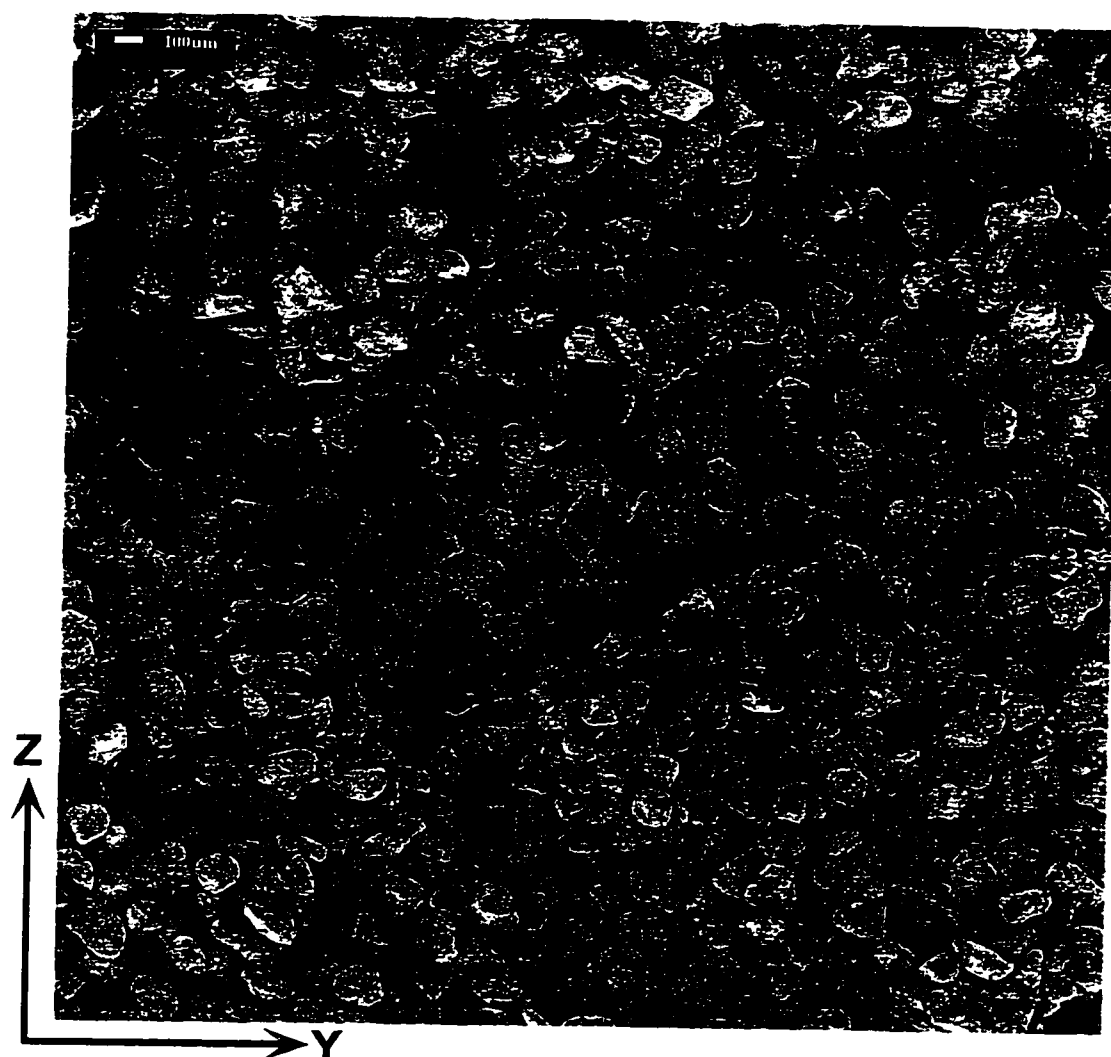
**Figure A15 Scanning electron microscope of a vertical section of bitumen-free
McMurray Formation oil sand (Z-Y plane)
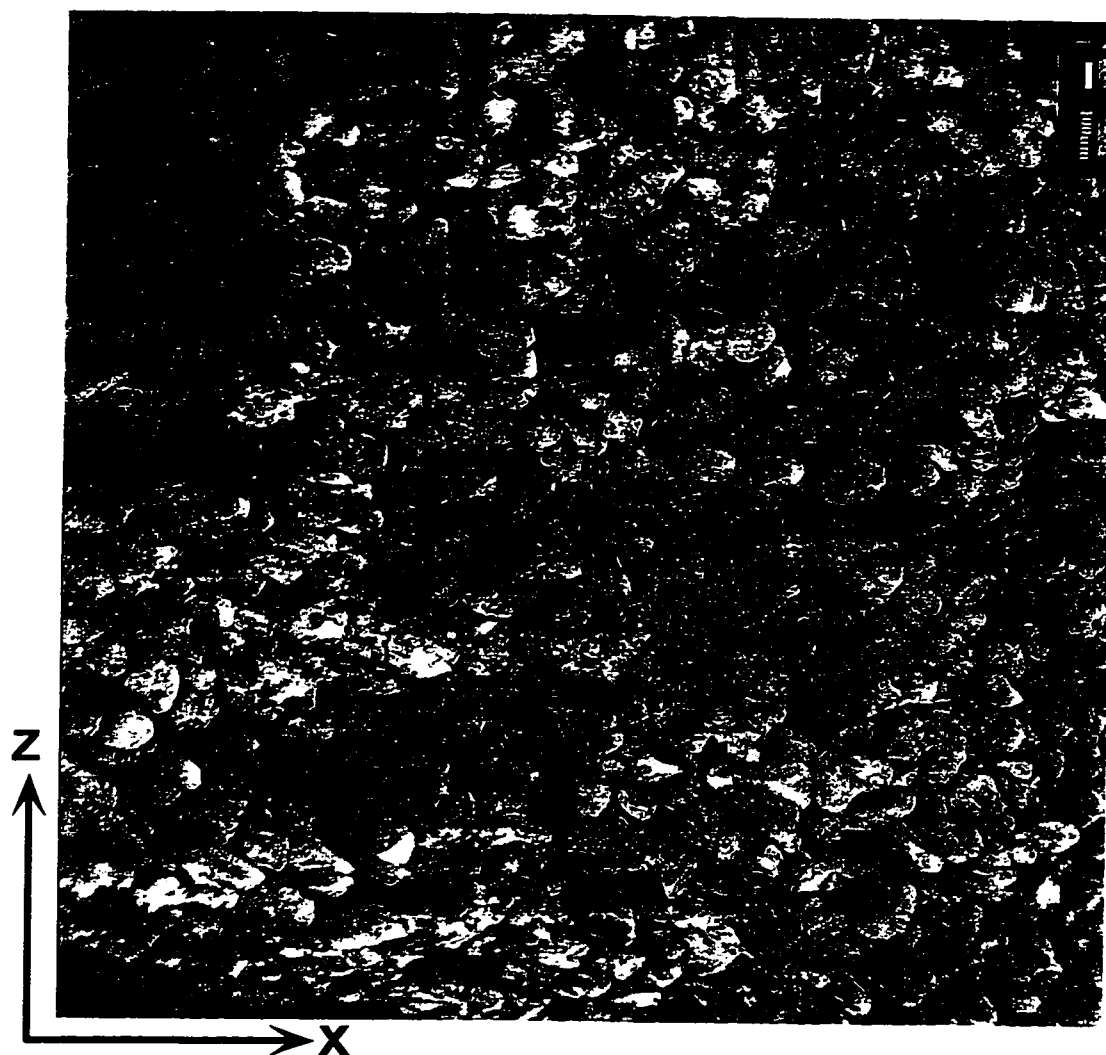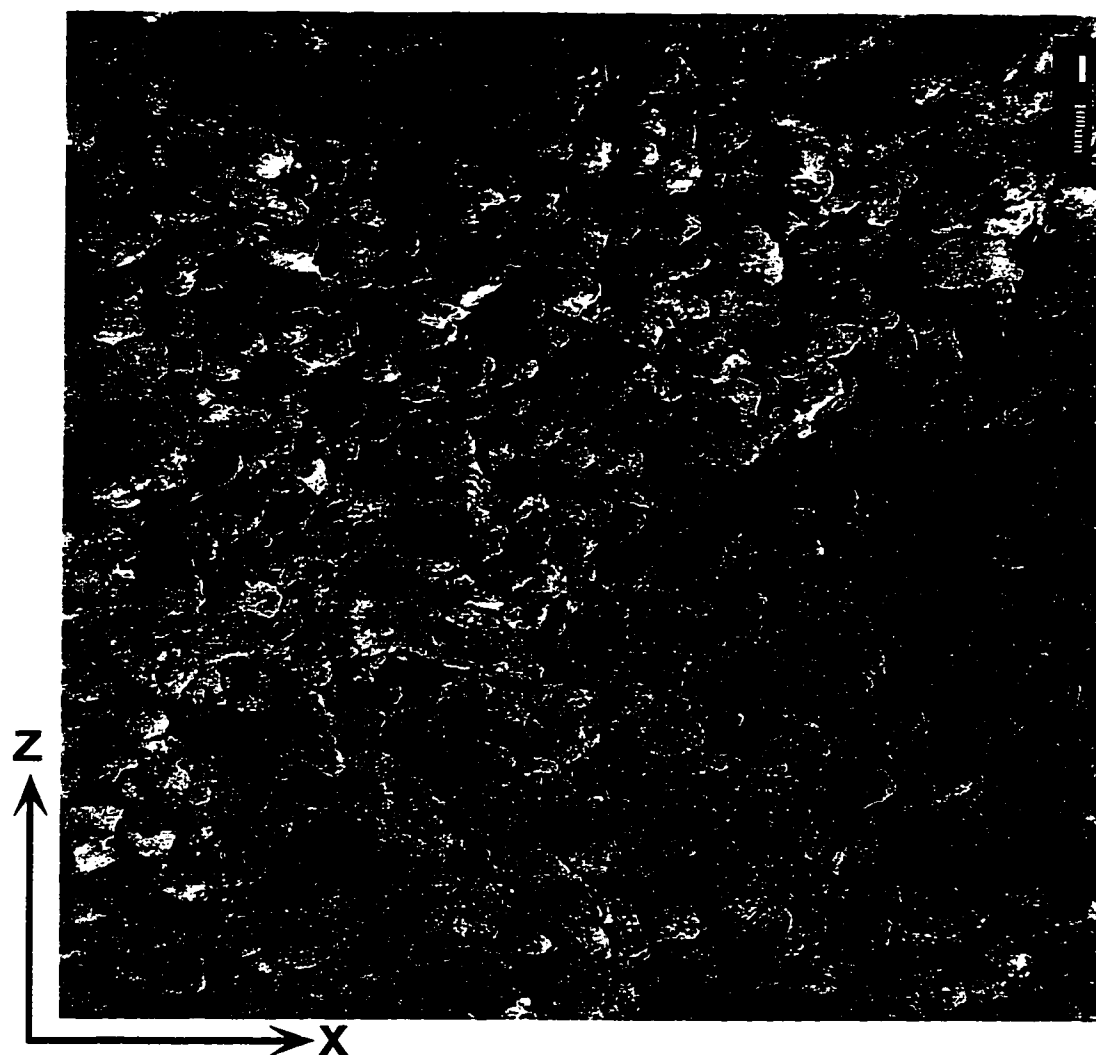Location 2
(White bar is 100 μm)**
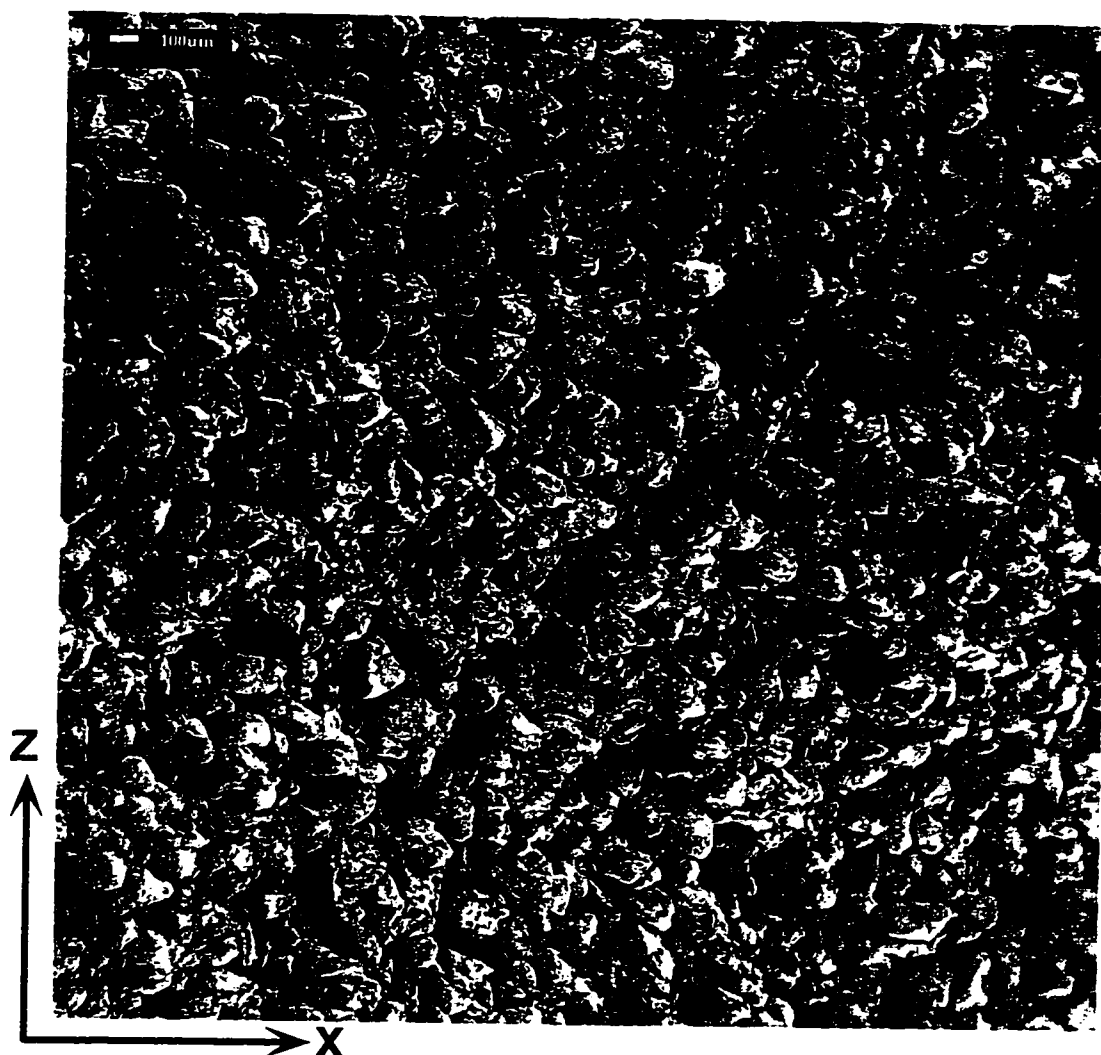
Figure A16 Scanning electron microscope of a vertical section of bitumen-free McMurray Formation oil sand (Z-X plane)
Location 2
(White bar is 100 μm)

Figure A17 Scanning electron microscope of a vertical section of bitumen-free
McMurray Formation oil sand (Z-X plane)
Location 2
(White bar is 100 μm)

**Figure A18 Scanning electron microscope of a vertical section of bitumen-free
McMurray Formation oil sand (Z-X plane)
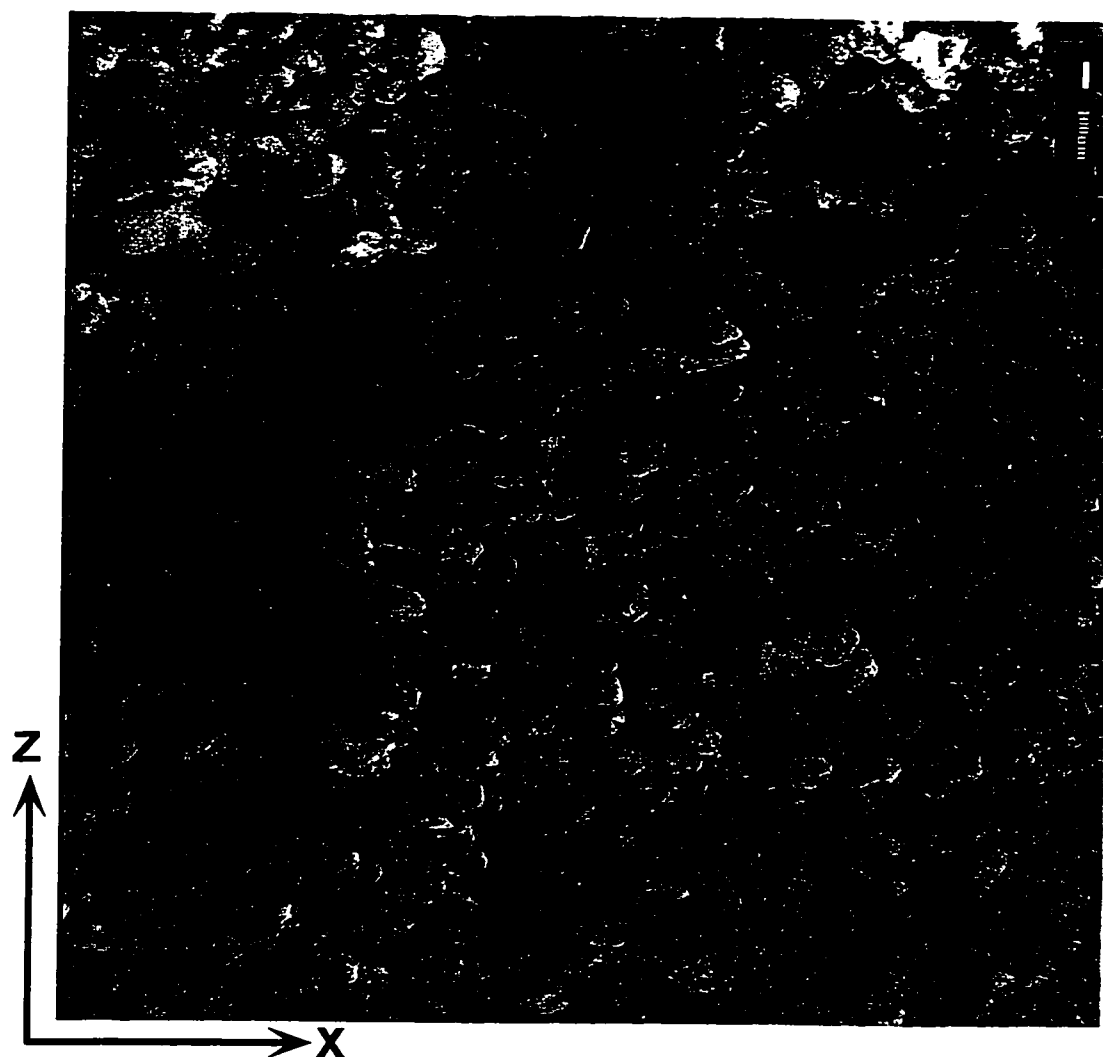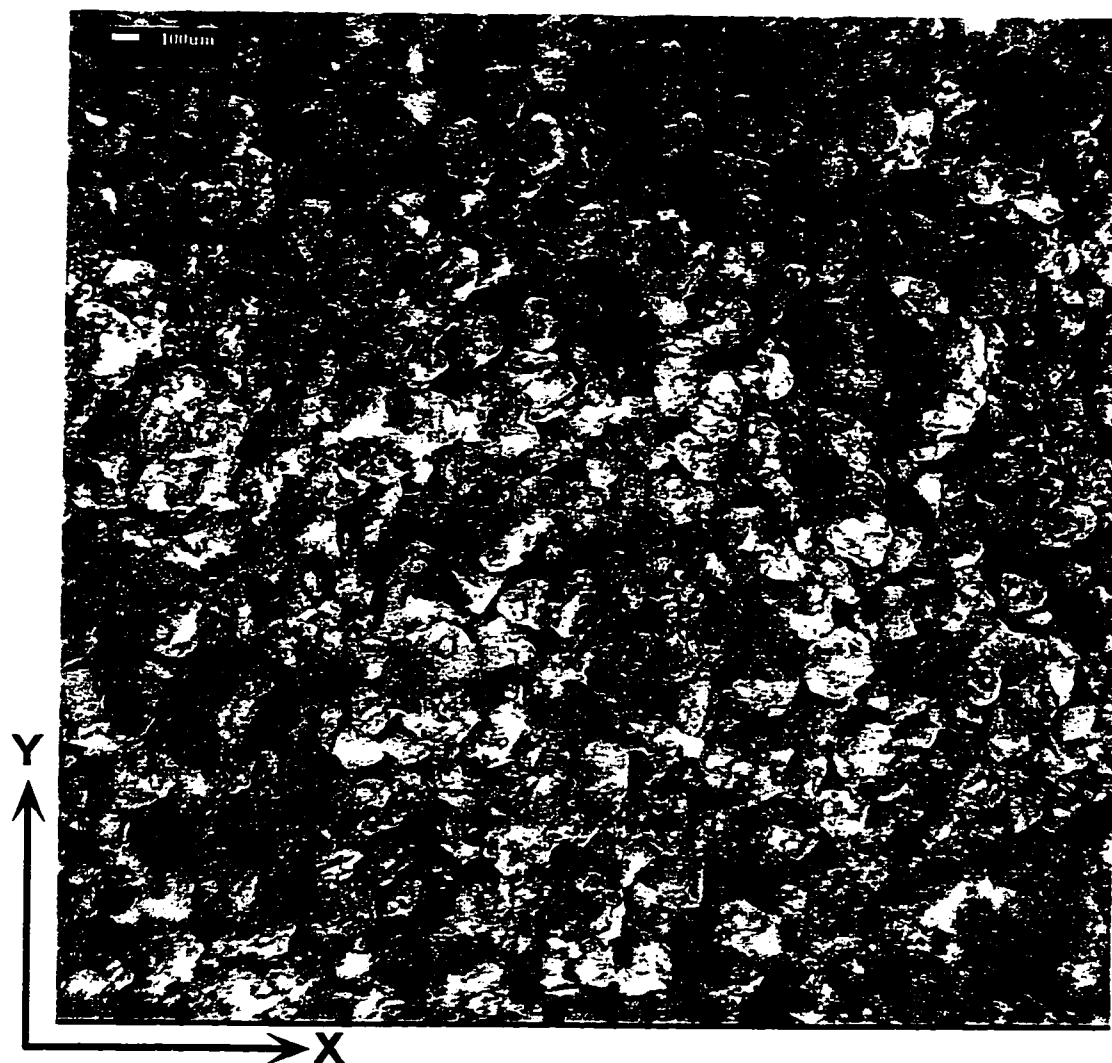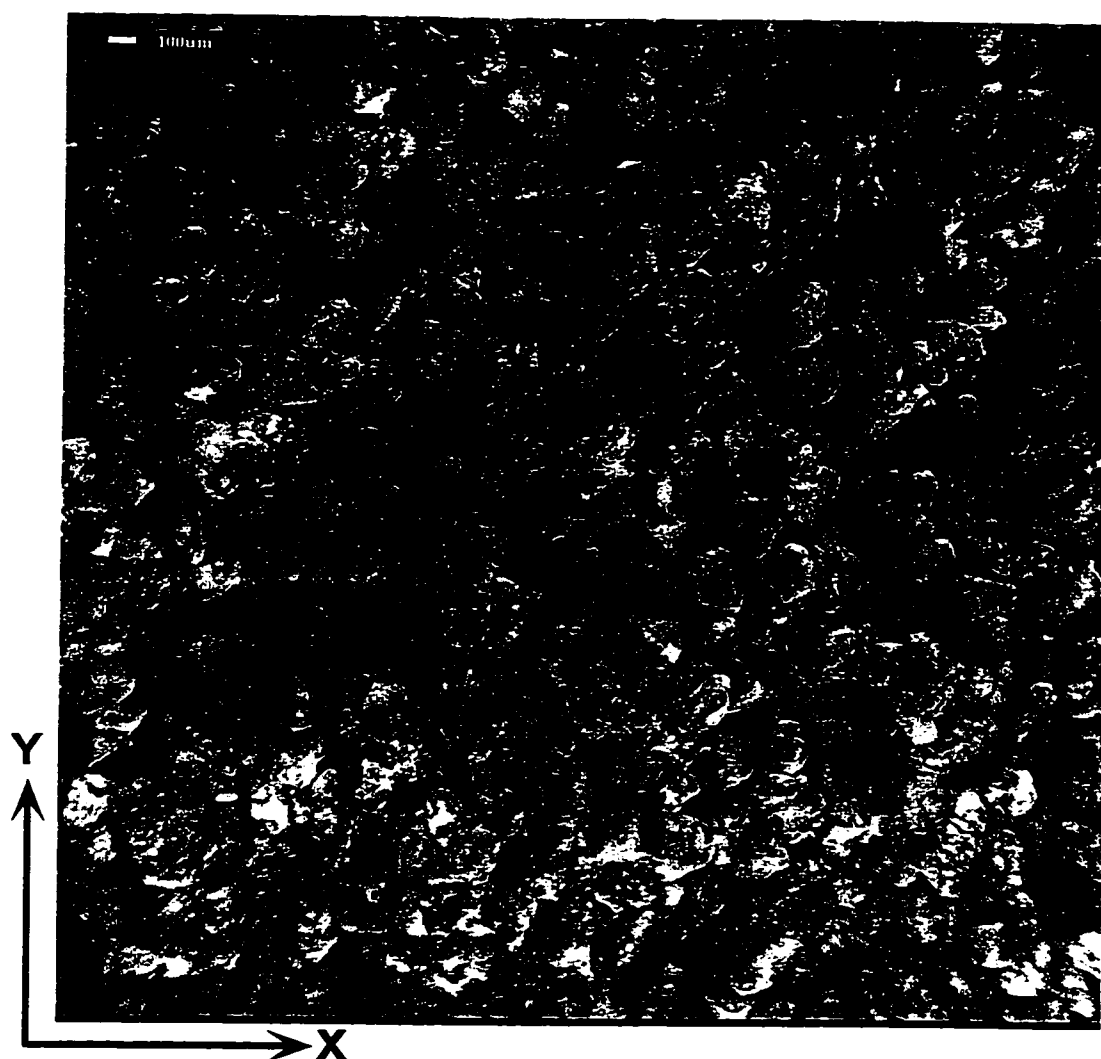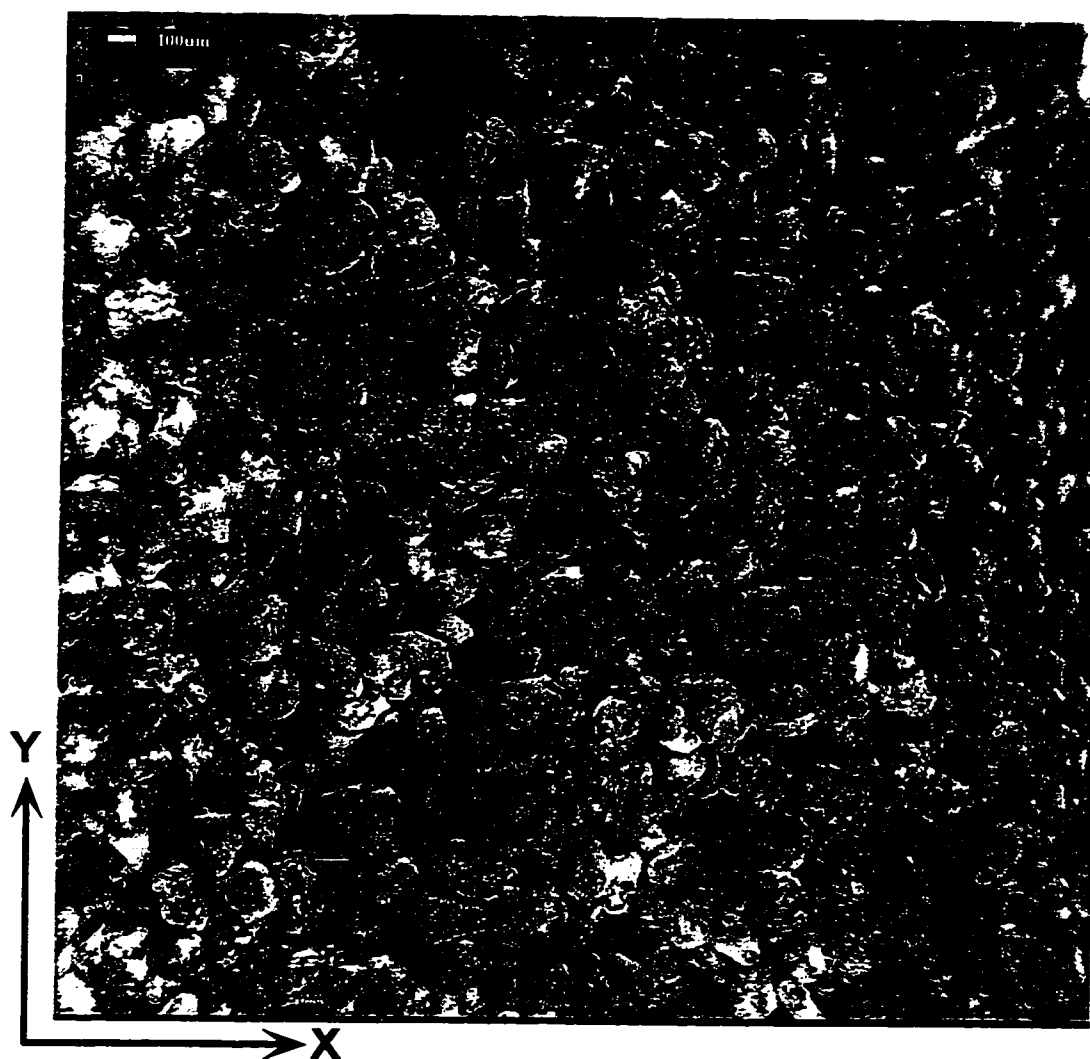Location 2
(White bar is 100 μm)**

Figure A19 Scanning electron microscope of a horizontal section of bitumen-free
McMurray Formation oil sand (Y-X plane)
Location 2
(White bar is 100 μm)

**Figure A20 Scanning electron microscope of a vertical section of bitumen-free McMurray Formation oil sand (Z-Y plane)
Location 3
(White bar is 100 μm)**

**Figure A21 Scanning electron microscope of a vertical section of bitumen-free McMurray Formation oil sand (Z-Y plane)
Location 3
(White bar is 100 μm)**

Figure A22 Scanning electron microscope of a horizontal section of bitumen-free
McMurray Formation oil sand (Y-X plane)
Location 3
(White bar is 100 μm)

Figure A23 Scanning electron microscope of a vertical section of bitumen-free
McMurray Formation oil sand (Z-Y plane)
Location 1
(White bar is 100 µm)

**Figure A24 Scanning electron microscope of a vertical section of bitumen-free
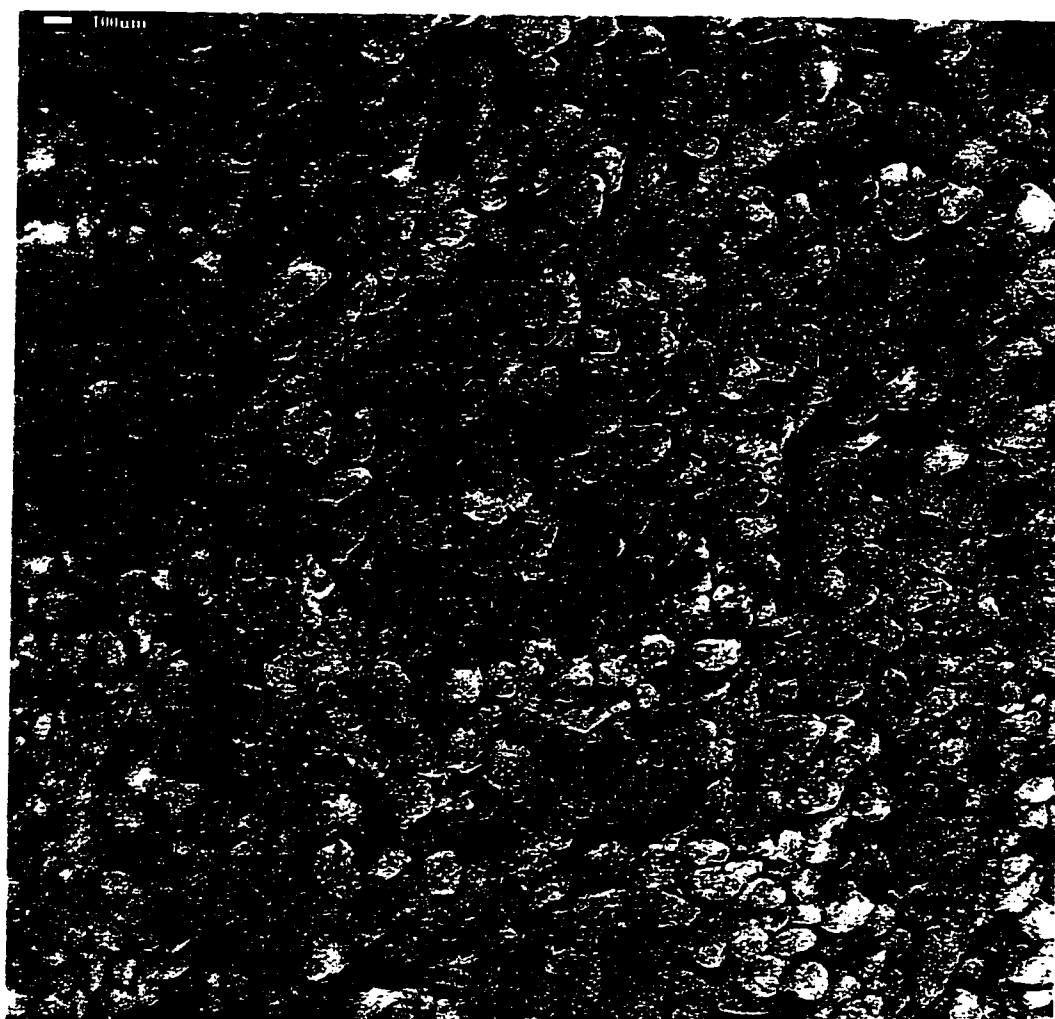McMurray Formation oil sand (Z-Y plane)
Location 1
(White bar is 100 μm)**

**Figure A25 Scanning electron microscope of a vertical section of bitumen-free
McMurray Formation oil sand (Z-Y plane)
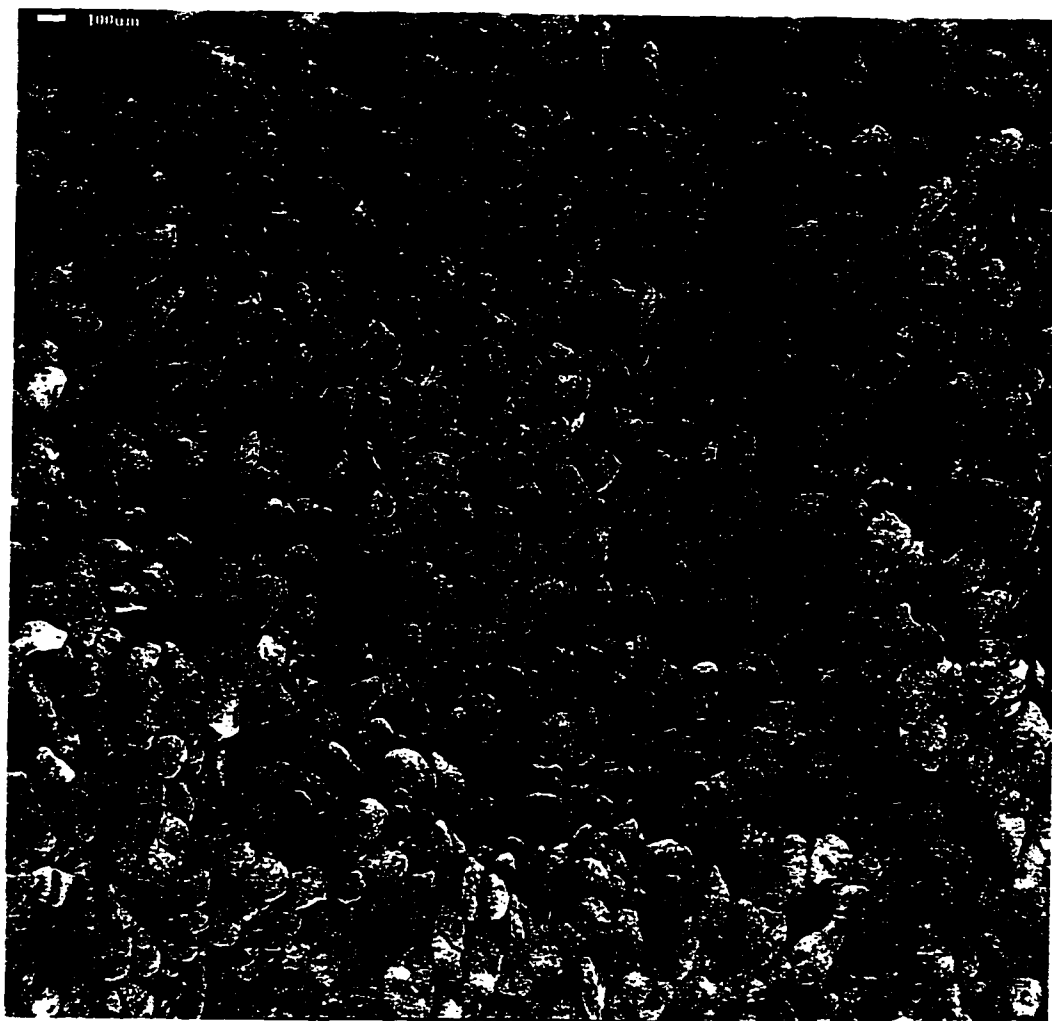Location 1
(White bar is 100 μm)**

**Figure A26 Scanning electron microscope of a vertical section of bitumen-free
McMurray Formation oil sand (Z-Y plane)
Location 1
(White bar is 100 μm)**

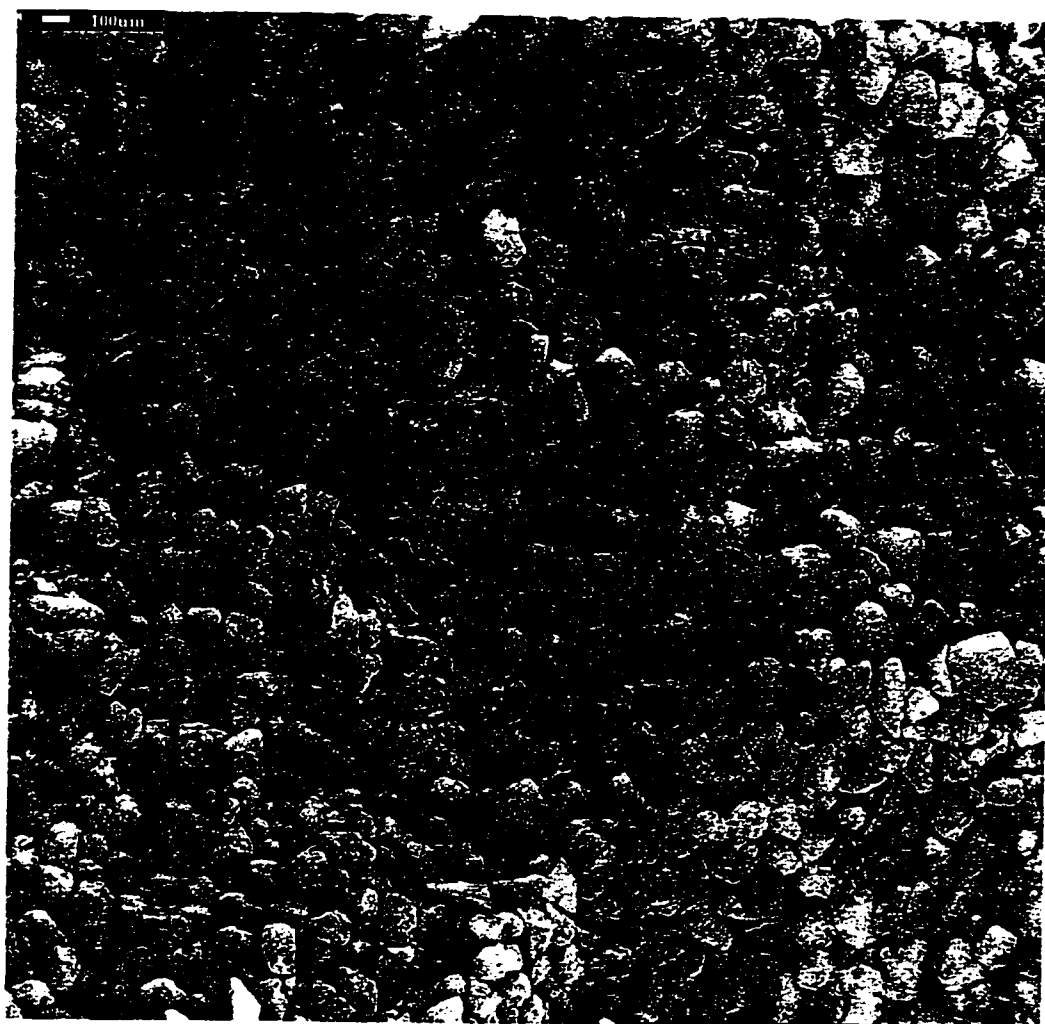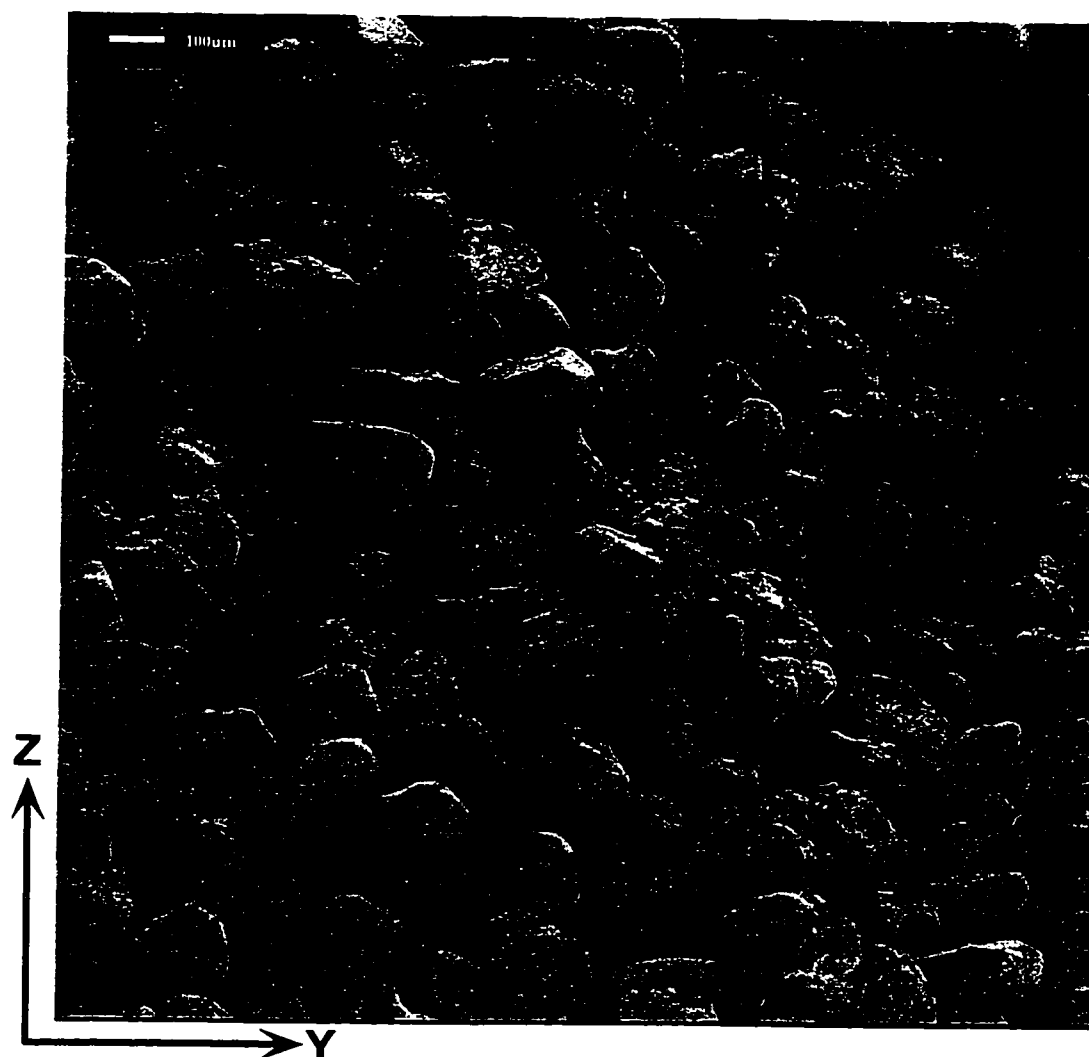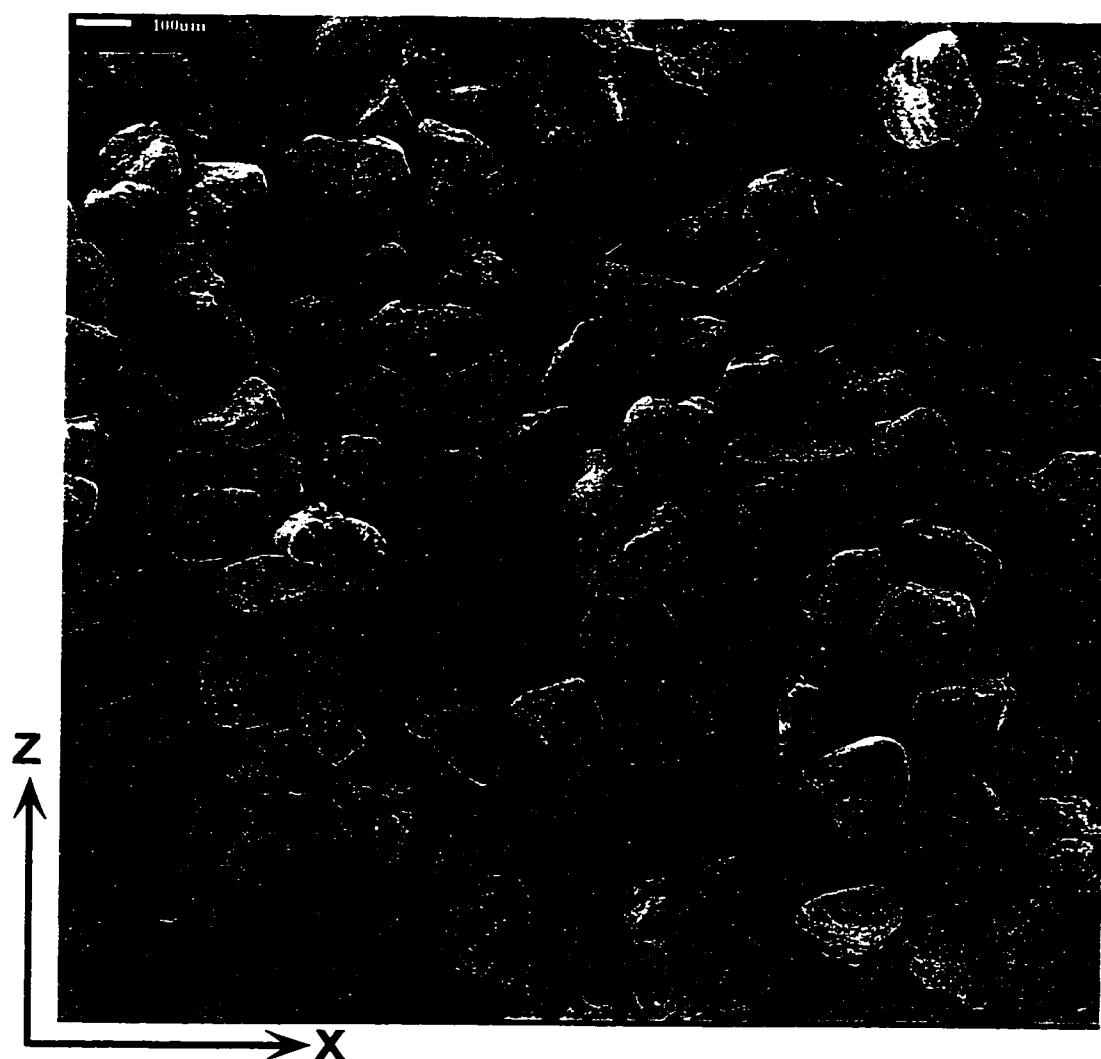**Figure A27 Scanning electron microscope of a vertical section of bitumen-free
McMurray Formation oil sand (Z-X plane)
Location 1
(White bar is 100 μm)**

**Figure A28 Scanning electron microscope of a vertical section of bitumen-free
McMurray Formation oil sand (Z-X plane)
Location 1
(White bar is 100 μm)**

**Figure A29 Scanning electron microscope of a vertical section of bitumen-free
McMurray Formation oil sand (Z-X plane)
Location 1
(White bar is 100 μm)**

**Figure A30 Scanning electron microscope of a horizontal section of bitumen-free
McMurray Formation oil sand (Y-X plane)
Location 1
(White bar is 100 μm)**

Figure A31 Scanning electron microscope of a horizontal section of bitumen-free McMurray Formation oil sand (Y-X plane)
Location 1
(White bar is 100 μm)

**Figure A32 Scanning electron microscope of a horizontal section of bitumen-free
McMurray Formation oil sand (Y-X plane)
Location 1
(White bar is 100 μm)**

**Figure A33 Scanning electron microscope of a vertical section of bitumen-free
McMurray Formation oil sand (Z-Y plane)
(orientation of this image is not known)
Location 1
(White bar is 100 μm)**

Figure A34 Scanning electron microscope of a vertical section of bitumen-free McMurray Formation oil sand (Z-X plane) (orientation of this image is not known) Location 1 (White bar is 100 μm)
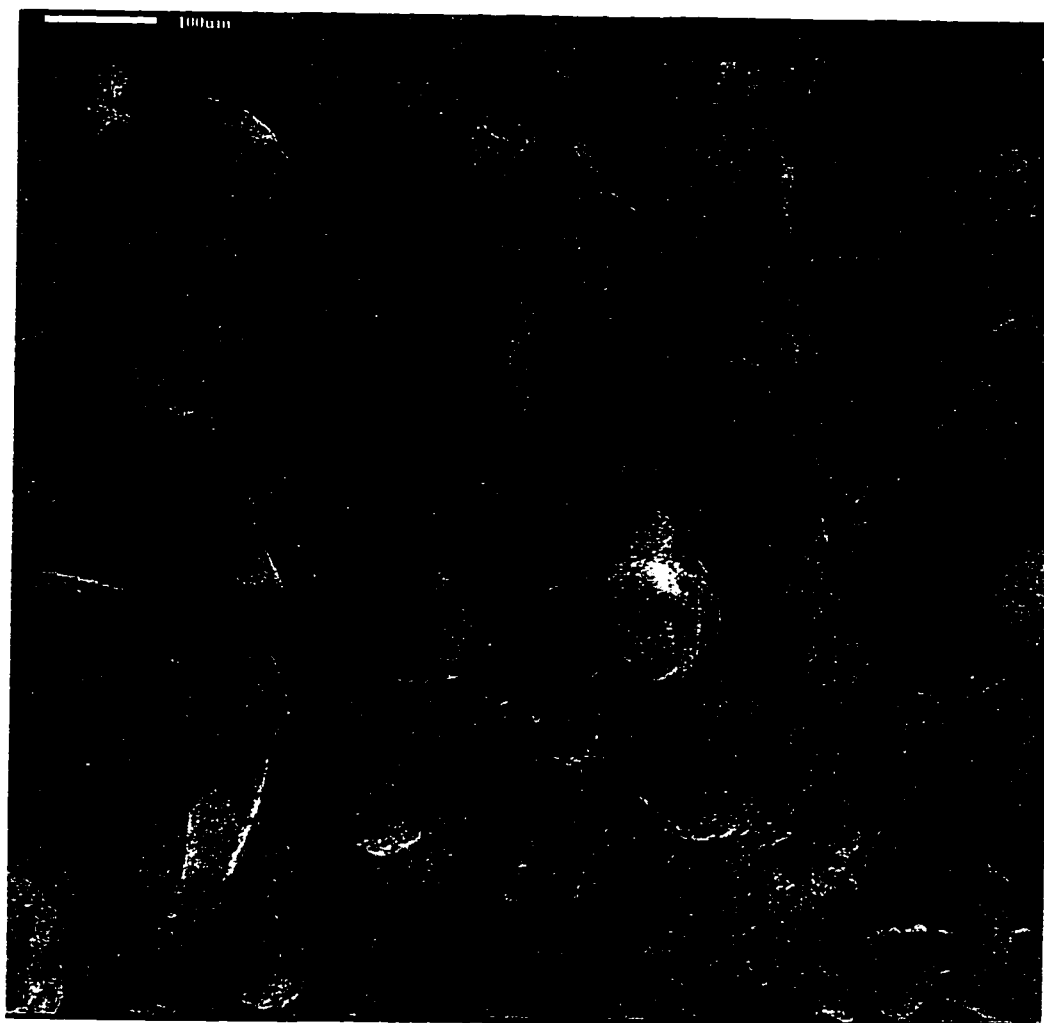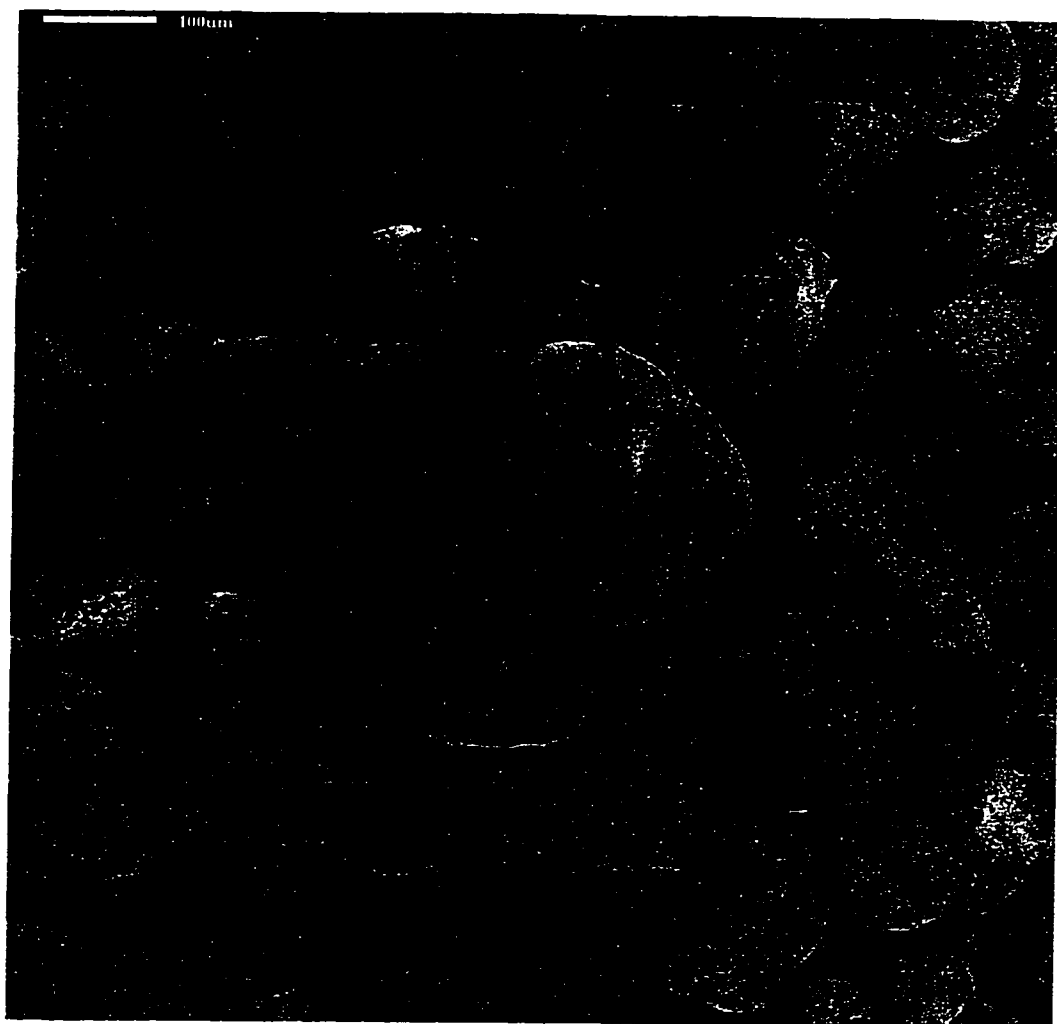
**Figure A35 Scanning electron microscope of a horizontal section of bitumen-free
McMurray Formation oil sand (Y-X plane)
(orientation of this image is not known)
Location 1
(White bar is 100 μm)**

**Figure A36 Scanning electron microscope of a vertical section of bitumen-free McMurray Formation oil sand (Z-Y plane)
Location 3
(White bar is 100 μm)**

Figure A37 Scanning electron microscope of a vertical section of bitumen-free McMurray Formation oil sand (Z-X plane)
Location 3
(White bar is 100 μm)

Figure A38 Scanning electron microscope of a vertical section of bitumen-free McMurray Formation oil sand (Z-Y plane)
(orientation of this image is not known)
Location 1
(White bar is 100 μm)

**Figure A39 Scanning electron microscope of a vertical section of bitumen-free
McMurray Formation oil sand (Z-Y plane)
(orientation of this image is not known)
Location 1**
(White bar is 100 μm)

**Figure A40 Scanning electron microscope of a vertical section of bitumen-free
McMurray Formation oil sand (Z-Y plane)
(orientation of this image is not known)
Location 1
(White bar is 100 μm)**

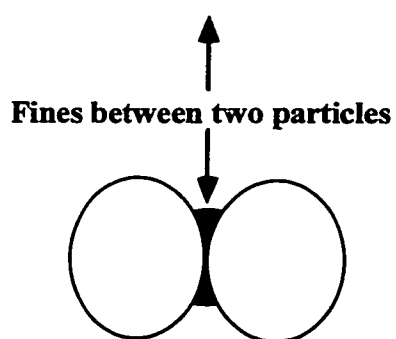**Figure A41 Scanning electron microscope of a vertical section of bitumen-free
McMurray Formation oil sand (Z-X plane)
(orientation of this image is not known)
Location 1
(White bar is 100 μm)**

**Figure A42 Scanning electron microscope of a vertical section of bitumen-free
McMurray Formation oil sand (Z-X plane)
(orientation of this image is not known)
Location 1
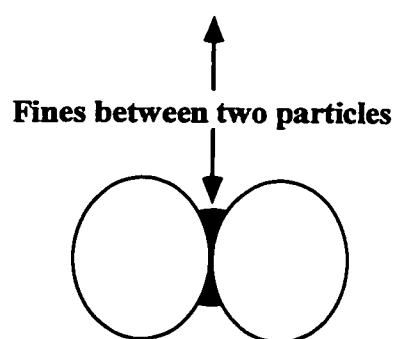(White bar is 100 μm)**

Figure A43 Scanning electron microscope of a vertical section of bitumen-free
McMurray Formation oil sand (Z-X plane)
(orientation of this image is not known)
Location 1
(White bar is 100 μm)

Figure A44 **Scanning electron microscope of a horizontal section of bitumen-free**
McMurray Formation oil sand (Y-X plane)
(orientation of this image is not known)
Location 1
(White bar is 100 μm)

**Figure A45 Scanning electron microscope of a horizontal section of bitumen-free
McMurray Formation oil sand (Y-X plane)
(orientation of this image is not known)
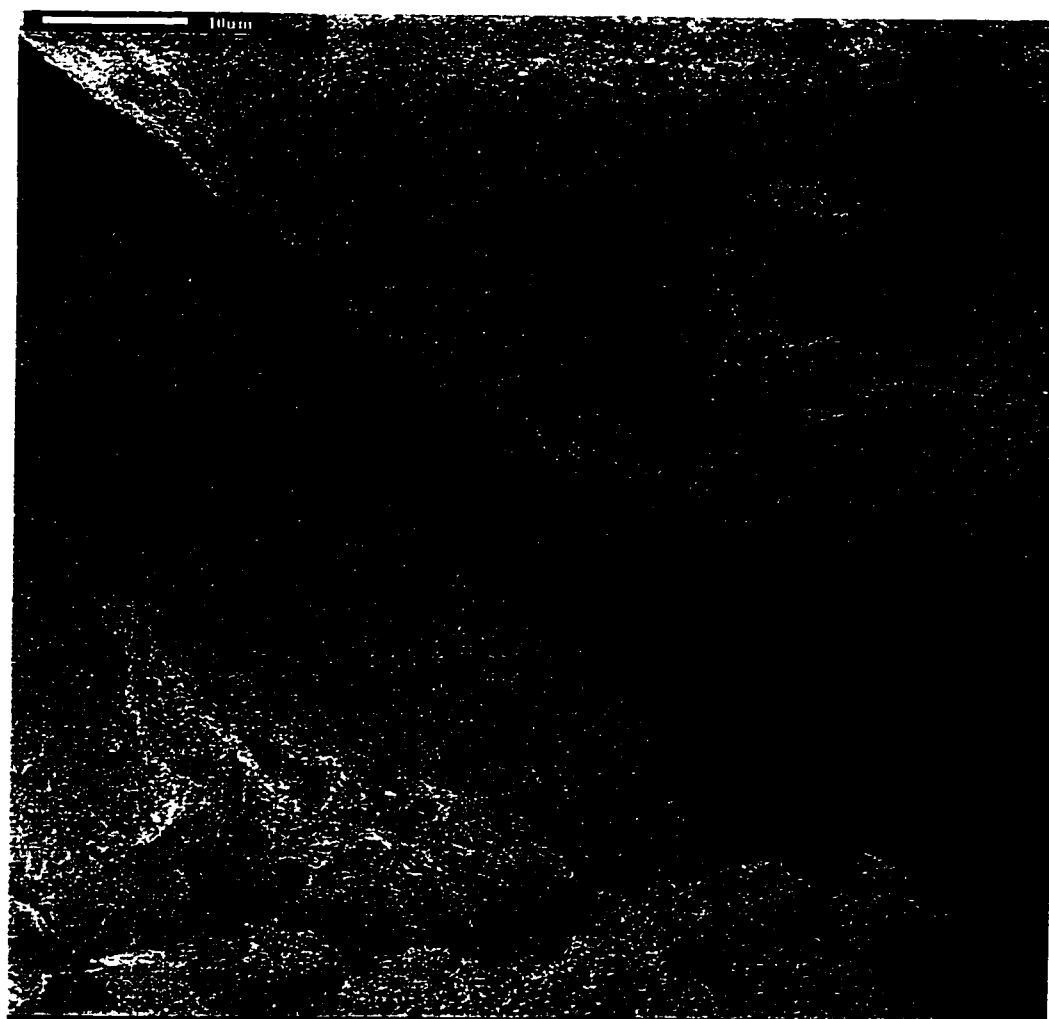Location 1
(White bar is 100 μm)**

**Figure A46 Scanning electron microscope of a horizontal section of bitumen-free McMurray Formation oil sand (Y-X plane)
(orientation of this image is not known)
Location 1
(White bar is 100 μm)**

**Figure A47 Scanning electron microscope of a vertical section of bitumen-free
McMurray Formation oil sand (Z-X plane)
(orientation of this image is not known)
Location 1
(White bar is 10 μm)**

Figure A48 Scanning electron microscope of a horizontal section of bitumen-free McMurray Formation oil sand (Y-X plane)
**(orientation of this image is not known)**
Location 1
(White bar is 10 μm)

Figure A49 Scanning electron microscope of a horizontal section of bitumen-free
McMurray Formation oil sand
Location 3
(White bar is 10 μm)

Fines between two particles
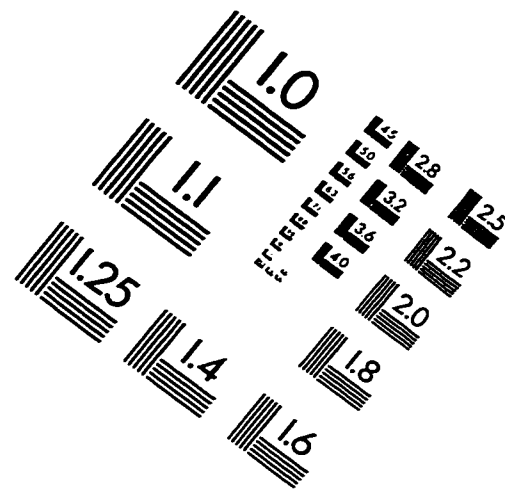
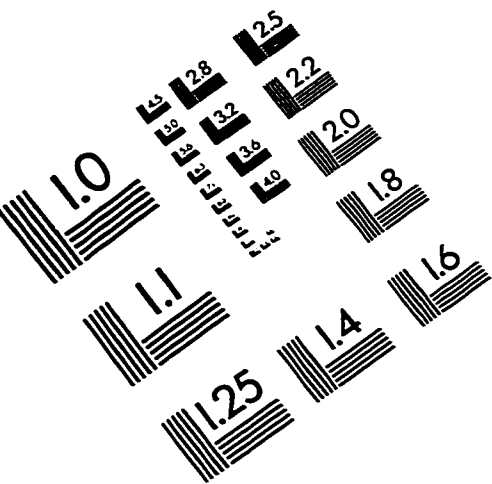Figure A50 Scanning electron microscope of a horizontal section of bitumen-free
McMurray Formation oil sand
Location 1
(White bar is 10 μm)

Figure A51 Scanning electron microscope of a horizontal section of bitumen-free
McMurray Formation oil sand
(clay particles)
Location 1
(White bar is 1 μm)

IMAGE EVALUATION
TEST TARGET (QA-3)

150mm

6"
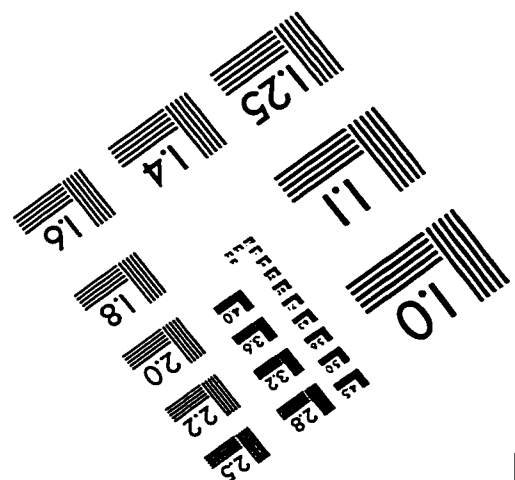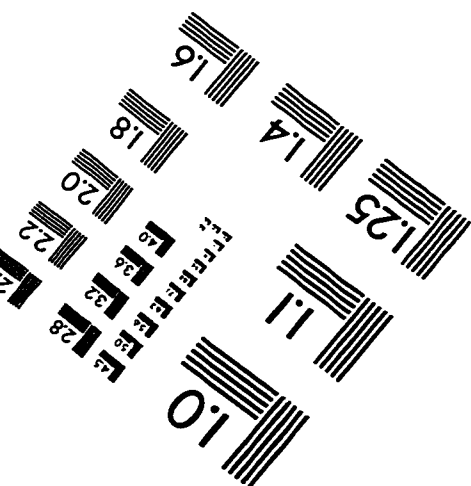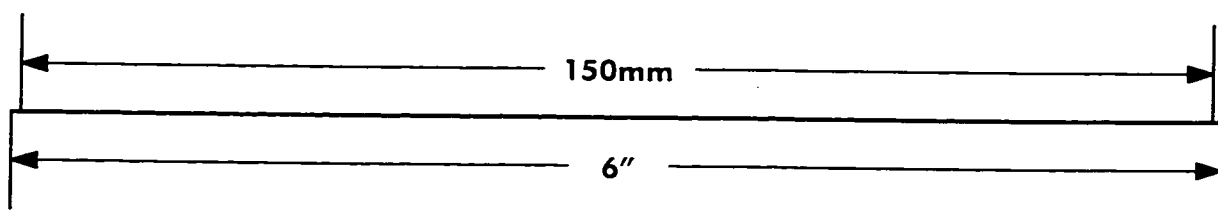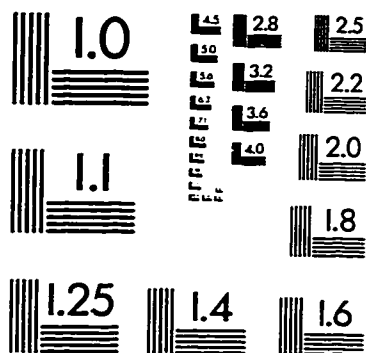
APPLIED IMAGE . Inc
1653 East Main Street
Rochester, NY 14609 USA
Phone: 716/482-0300
Fax: 716/288-5989

© 1993, Applied Image, Inc., All Rights Reserved